



City Research Online

City, University of London Institutional Repository

Citation: Miah, S. (2018). A low-cost intelligent localisation system to improve cyclist safety. (Unpublished Doctoral thesis, City, University of London)

This is the accepted version of the paper.

This version of the publication may differ from the final published version.

Permanent repository link: <https://openaccess.city.ac.uk/id/eprint/19873/>

Link to published version:

Copyright: City Research Online aims to make research outputs of City, University of London available to a wider audience. Copyright and Moral Rights remain with the author(s) and/or copyright holders. URLs from City Research Online may be freely distributed and linked to.

Reuse: Copies of full items can be used for personal research or study, educational, or not-for-profit purposes without prior permission or charge. Provided that the authors, title and full bibliographic details are credited, a hyperlink and/or URL is given for the original metadata page and the content is not changed in any way.

A Low-Cost Intelligent Localisation System to Improve Cyclist Safety

by

Shahjahan Miah (MEng)

A thesis submitted
in fulfilment of the requirements for the degree
of

Doctor of Philosophy

in

Systems and Modelling

at

Research Centre for Systems & Control

Department of Electrical & Electronic Engineering

City, University of London



London
April 2018

Declaration

The author grants powers of discretion to the University Librarian to allow this thesis to be copied in whole or in part without further reference to the author. This permission covers only single copies made for study purposes, subject to normal conditions of acknowledgement.

Abstract

Cycling is an increasingly popular mode of travel in cities owing to the great advantages that it offers in terms of space consumption, health and environmental sustainability, and it is therefore favoured and promoted by many city authorities worldwide. A large number of recently introduced cycling-related schemes in many cities demonstrates this trend. However, the relatively low safety of pedal cycles as perceived by the users currently presents itself as a hurdle, and therefore cycling has yet to be adopted to a wider extent by users as a true alternative to the private car. Rising accident numbers, unfortunately, confirm this perception as reality, with a particular source of hazard appearing to originate from the interaction of cyclists with motorised traffic at low speeds in urban areas. Technological advances in recent years have resulted in a number of attempts to develop systems to prevent cyclist-vehicle collisions, but they have generally stumbled upon the challenge of accurate cyclist localisation and tracking, which can enable predicting a collision within a short-term time-horizon (5-10 seconds). Indeed, cyclist positioning accuracy is essential for any collision avoidance system, not only to ensure the effective operation of the system but also to minimise the occurrence of false alerts. Thus, motivated by the poor safety record, the research reported here involves the development and testing of an innovative technological solution for accurately localising and tracking cyclists, where the ultimate aim is to utilise the techniques in a concept called Cyclist 360° Alert to avoid collisions.

The overarching innovation of this PhD is the development of the instrumented bicycle system, called iBike, which can be employed to track cyclists' positions more precisely. The system relies on bicycles being instrumented with low-cost Micro-electromechanical systems (MEMS) sensors, and utilises multiple Kalman filters, which were developed from the geometrical and kinematics modelling of the bicycles, to conduct a multi-sensor fusion on the iBike acquisition data with the measurements from the Global Positioning System, Wi-Fi hotspots and mobile communication systems. Apart from the above, the thesis also reports on the results obtained from a number of field trials where an enhanced off-the-shelf positioning system was employed to validate the developed system. The overall results from the field experiments demonstrate that, on average with an 80% probability, the iBike system can be used to estimate a position with less than 0.5 m error compared to a 16.2 m error from the enhanced positioning system under the same circumstances. Thus, the results from the field trials using the iBike have shown successful outcomes for the developed methodologies. This means that the iBike can be used to predict a collision more precisely. These results are presented in detail together with the hardware and software of the iBike system in this thesis.

To my son, Ehsan.

Acknowledgement

I would like to take this opportunity to acknowledge my appreciation of the support that I have received from the following people throughout this research study:

First and foremost, I would like to gratefully and sincerely thank my supervisors, Dr Ioannis Kaparias, Dr Efstathios Milonidis, Prof Nickolas Karcanias, and Prof Panos Liatsis for their guidance, invaluable advice and financial support throughout the course of this study. Whilst providing me with the freedom to develop my own concept and approach, they have always given critical and invaluable feedback. Thus, without their knowledge and wisdom, this thesis would not have been completed.

Secondly, I would like to thank Mr Richard Leach and Mr Keith Pamment for their critical assistance with the instrumentation of the bicycle and the development of a test rig. I would also like to thank Mr Donald Stirling and Mr Jim Hooker for their invaluable assistance with the topographical surveys of the routes around the university. I would also like to express thanks to Dr Khalid Nur from Imperial College London for his advice and for lending us the Cricket Indoor Location System for an experiment with the bicycle.

Thirdly, I would like to extend my sincere gratitude to my family, my wife and a special friend, Mr Stephen Jasper, who encouraged, inspired and motivated me throughout some difficult times, and pushed me to complete and deliver this thesis on time.

Finally, but not least, I would like to thank my colleagues, friends and the entire staff of SMCSE for their direct and indirect support of this PhD and for making it a joyful experience, which I will remember for the rest of my life. Furthermore, I would also like to thank Transport for London for supplying a Cycle Hire bicycle used in this study.

Table of Contents

<i>List of Tables</i>	<i>viii</i>
<i>List of Figures</i>	<i>ix</i>
<i>Acronyms and Abbreviations</i>	<i>xv</i>
<i>System Parameters and Notation</i>	<i>xviii</i>
Chapter 1: Introduction	1
1.1 Research Motivation	1
1.2 Brief Historical Overview of Bicycle’s Evolution	3
1.3 Problem Statement, Project Vision and Challenges	6
1.4 Aim and Objectives of this Research.....	8
1.5 Structure of the Thesis	10
1.6 Contribution of the Research.....	11
Chapter 2: Background to the Problem & Challenges	12
2.1 Introduction	12
2.2 Review of Cycle Collisions and Trends	12
2.3 Understanding the Causes and Key Characteristics of Cyclist Casualties	16
2.4 Technical Limitations and Human Factor.....	20
2.5 Review of Current ITS Solutions	22
2.6 Conclusions	25
Chapter 3: Formulation of Cyclist 360° Alert	26
3.1 Introduction	26
3.2 Overall System Architecture & Design Requirements.....	26
3.3 Review of Localisation Techniques	29
3.4 Review of Common Localisation Technologies	35
3.5 Summary of Localisation Technologies	46
3.6 Proposed Approach for Cyclist 360° Alert System.....	47
3.7 Implementation Strategy	51
3.8 Conclusions	52
Chapter 4: Bicycle Positioning Models & Algorithms	54

4.1	Introduction	54
4.2	The Unique Characteristics of a Bicycle	54
4.3	Transformation of Bicycle Motions.....	57
4.4	Sensor Data Fusion	66
4.5	Datum Conversions.....	75
4.6	Design of the Post-Processing Algorithms.....	77
4.7	Conclusions	78
Chapter 5: Development of iBike Prototype System.....		80
5.1	Introduction	80
5.2	iBike Measurement Sensors.....	80
5.3	Individual Subsystems.....	93
5.4	The Instrumented Bicycle.....	108
5.5	Development of Software and Database	110
5.6	Conclusions	122
Chapter 6: Validation of the Developed System.....		124
6.1	Introduction	124
6.2	Initial Experiment with Total Station.....	125
6.3	Fusion with Survey Points	130
6.4	Fusion with GPS, WiFi and Cell Towers.....	136
6.5	Conclusions	147
Chapter 7: Conclusions and Future Work		149
7.1	Summary of the Chapter Findings.....	149
7.2	Summary of Contributions.....	152
7.3	Reflection on Overall Work.....	153
7.4	Scope for Further Work.....	155
Publications Relating to this Research		160
References.....		162
Appendix A: Additional Materials on the Development of the iBike System		178
A.1	Brief Operating Principle of iBike Components.....	178

A.2	Configuration of the A2K Encoder	186
A.3	Design and Implementation of the Hardware.....	188
A.4	Electrical Connections of the Complete iBike System	193
Appendix B: Development of Test Rig.....		194
B.1	Design of the Test Rig.....	194
B.2	Implementation of Hardware and Software.....	196
Appendix C: Additional Experimental Results and Field Trial Data		198
C.1	Experimental Data from the Test Rig.....	198
C.2	Sample Data from GPS (GPSLogger app) and Spatial INS.....	199
C.3	Sample Data from the Field Trials	201
C.4	Approximation of Yaw Rate and Angle for the Kalman Filter	204
C.5	Comparison of Yaw Angles	205
C.6	Computation of GPS Mean Error.....	206
C.7	Cumulative Distribution of the Localisation Error	207
C.8	Cricket System Experimental Setup	209
References.....		210

List of Tables

Table 3.1: Summary of common localisation technologies including UWBPS.	47
Table 5.1: Five essential commands of the iBike measurement system.	102
Table 5.2: Spatial breakout cable connector pinout.	106
Table 5.3: Design of the file structure and storage of the Journey Details table..	115
Table 6.1: Mean, standard deviation and maximum values of the DR and fused	135
Table 6.2: Comparison of FPE of each system with 9 separate trials around the route.....	143
Table 6.3: The t-test results of the trials with the decision.....	145
Table 6.4: Comparisons of the probability of the positional error for each of the respective systems.....	146
Table C.1: Extracted coordinates of Trial 1	202
Table C.2: Computed errors of the coordinates for Trials 1-3.	203

List of Figures

<i>Figure 1-1: Early evolution of bicycles: illustration of Jacques’s design (left) [14], and development of modern bicycles (right) [15].</i>	3
<i>Figure 1-2: Copenhagen Wheel [20] – (a) Smartphone, (b) the hub of the Copenhagen Wheel and (c) a retrofit wheel with essential electrical and mechanical components.</i>	5
<i>Figure 1-3: Copenhagen City Bike [21] – (a) a tablet computer on the hub of the bike and (b) the Pedelec e-bikes.</i>	5
<i>Figure 1-4: Typical warning signs for cyclists appear on the back of HVs.</i>	6
<i>Figure 1-5: (a) Blind spots surrounding a lorry, (b) Cyclist 360° Alert driver’s display view and (c) predicted trajectories for vehicles and an indication of a danger.</i>	7
<i>Figure 1-6: (a) Minimum safe passing distance and (b) minimum dynamic width required [22].</i>	8
Figure 2-1: Reported cyclists killed or seriously injured between 2005 and 2015 (adapted from [30]).	14
Figure 2-2: Casualty and Fatality rates per billion passenger miles by road user type [28].	15
Figure 2-3: Reported pedal cyclist casualties in Greater London between 2005 and 2014 (adapted from [33]).	16
Figure 2-4: A typical fatal collision scenario for a cyclist with a lorry (adapted from [34]).	17
Figure 2-5: The most common conflict between Pedal Cycle and Other Vehicles [36].	18
Figure 2-6: Cyclist Casualties by Day and Light Conditions (adapted from [38]).	19
Figure 2-7: Cyclists Casualties by Month and Light Conditions (adapted from [38]).	19
Figure 2-8: Left turn blind spots for an articulated lorry [41].	20
Figure 2-9: Illustration of mirrors on a truck [40].	21
Figure 2-10: Volvo’s pedestrian and cyclist detection system [48].	23
Figure 2-11: (a) Backwatch’s blind spot detection system [55]; (b) Trixi traffic light mirrors (right) [41]; (c) Blaze Laserlights [58]	24
Figure 3-1: Overall system architecture of the Cyclist 360° Alert system.	27
Figure 3-2: Classification of localisation techniques.	32

Figure 3-3: Triangulation approach.	33
Figure 3-4: Trilateration approach – Intersection of circles.	34
Figure 3-5: (a) Satellite Constellation and (b) Intersection of the spheres.....	37
Figure 3-6: DGPS operation principal.	39
<i>Figure 3-7: Wi-Fi network configuration.</i>	<i>40</i>
<i>Figure 3-8: (a) 802.11 MAC frame format [75], (b) WPS operation principle.....</i>	<i>43</i>
<i>Figure 3-9: (a) Typical cells arrangement in a cellular network and (b) CTPS operation principle.....</i>	<i>45</i>
Figure 3-10: Hybrid localisation approach.....	48
Figure 3-11: Block diagram of position fusion system.	50
Figure 3-12: Collision prediction & warning system block diagram.	51
<i>Figure 4-1: components of a modern bicycle [97].</i>	<i>55</i>
<i>Figure 4-2: Illustration of a typical right turn with countersteering [101].</i>	<i>56</i>
Figure 4-3: A simple kinematic bicycle model of a vehicle.	58
<i>Figure 4-4: Turning geometry of a bicycle.....</i>	<i>59</i>
Figure 4-5: Top view of geometric bicycle model.	60
Figure 4-6: Geometric relationship from the previous location to current location.	61
Figure 4-7: Approximation with a two-step DR method.	63
Figure 4-8: Bicycle geometric relationship with body and global coordinates system.	64
Figure 4-9: Approximation with simplified positioning model.....	65
Figure 4-10: Design of the yaw angle Kalman filter.....	68
Figure 4-11: Design of the multi-system yaw angle fusion.	71
Figure 4-12: (a) Modelled trajectories based on DR algorithm and GPS; (b) Equivalent representation of the points with vector quantities.....	71
Figure 4-13: Design of the position Kalman filter.....	73
Figure 4-14: Design of the multi-system position fusion.....	75
Figure 4-15: Datum conversion software [128].....	76
Figure 4-16: Design of the overall algorithms.....	77
Figure 5-1: Hall Effect geartooth sensor [130].....	81
Figure 5-2: Hall Effect - Open Collector Sinking Block Diagram [129].....	82
Figure 5-3: Installation of spoke magnets	83

Figure 5-4: (a) Spoke magnets arrangement, (b) pulses to distance algorithm design.	84
Figure 5-5: US digital A2K absolute encoder.	85
Figure 5-6: Raw value into steering angle algorithm design.....	85
<i>Figure 5-7: (a) L3G4200D pinout description and (b) direction of the detectable angular rates [134].</i>	<i>87</i>
Figure 5-8: Raw value to angles algorithm design.	89
Figure 5-9: (a) ADXL345 pinout configuration and axes of acceleration sensitivity [139].	90
Figure 5-10: Accelerometer output response versus its orientation to gravity [139].	91
Figure 5-11: Design of the complementary filter.....	93
Figure 5-12: Arduino Mega 2560 R3 Front [144].	95
Figure 5-13: (a) Arduino Mini front without headers; (b) pin annotation of a typical board.	96
Figure 5-14: iBike measurement system architecture.	97
Figure 5-15: Schematic circuit diagram of the seat tube sensors.....	98
Figure 5-16: (a) Design of the top layer routing and (b) the bottom layer routing of the seat tube sensors PCB.....	99
Figure 5-17: (a) Developed PCB; (b) GY291 breakout board with header pins; (c) GY50 breakout board.	99
Figure 5-18: (a) the CAD design of the housing and (b) the 3D printed part installed on the bicycle.	100
Figure 5-19: Flowchart design of the main program within the firmware	101
Figure 5-20: Screenshot of the Arduino's IDE.	101
Figure 5-21: (a) Samsung S6 edge; (b) screenshot of Google maps app; (c) screenshot of GPS logger app.	103
Figure 5-22: the architecture of data storage system from a smartphone.	104
Figure 5-23: Spatial INS Cube [156].	105
Figure 5-24: The data collection and storage system for the INS.....	106
Figure 5-25: (a) Surface Pro Tablet PC; (b) the real-time data acquisition system.	107
Figure 5-26: (a) GoPro Camera; (b) data acquisition system.....	108

Figure 5-27: The Prototype Instrumented Bicycle (iBike).	109
Figure 5-28: Outputs data field of the overall system.	110
Figure 5-29: The overall system architecture.	111
Figure 5-30: The data acquisition tab of the developed software.	112
Figure 5-31: The data management tab of the developed software.	113
Figure 5-32: Entity relationship diagram of the iBike database.	114
Figure 5-33: Implementation of the Journey Details table using MySQL Workbench.	116
Figure 5-34: EER model of the database structure.	117
Figure 5-35: Sample dataset of the journey table.	118
Figure 5-36: Process and storage of the smartphone GPS data.	119
Figure 5-37: Process and storage of the Spatial INS data.	120
Figure 5-38: MATLAB Post-processing GUI.	120
Figure 5-39: Process and storage of the iBike measurement data via the post-processing software.	121
Figure 6-1: (a) Instrumented bicycle with the reflector; (b) total station instrument.	126
Figure 6-2: Initial experimental setup map.	127
Figure 6-3: A comparison of DR trajectory and TS points.	128
Figure 6-4: The maximum tolerable positional error from the actual location	129
Figure 6-5: Histogram and the mean error for the extrapolated points of the DR trajectory	130
Figure 6-6: The new iBike configuration.	131
Figure 6-7: (a) Topographical surveying techniques; (b) location of the control stations of the survey	132
Figure 6-8: (a) Satellite view of the experimental route; (b) (b) illustration of three surveyed points along the route.	133
Figure 6-9: Comparison of the trajectories	135
Figure 6-10: Comparison of the DR and Fused positional error	136
Figure 6-11: (a) OS map of the experimental route; (b) The first two control points along the survey route	137
Figure 6-12: Survey points versus Spatial INS trajectory	138
Figure 6-13: Survey points versus GPS trajectory	139

Figure 6-14: Selection of GPS points below the threshold limit.....	139
Figure 6-15: Survey points versus Fused trajectory	140
Figure 6-16: The process of data extraction and extrapolation	141
Figure 6-17: Survey points versus extrapolated points	142
Figure 6-18: Comparison of mean error for each trial with the respected system	144
Figure 6-19: Comparison of fused, GPS and INS average positional error	147
Figure 7-1: Sensor modules of GY80 with possible outputs from sensor fusion .	156
Figure 7-2: MATLAB's AI Neural Network [179].....	158
Figure 7-3: Survey points versus Fused trajectory with GPS data only.....	158
Figure A-1: The Hall Effect and Lorentz force [A1].....	179
Figure A-2: Hall Effect sensor operation principle diagram [A2].....	179
Figure A-3: Typical Hall Effect sensor diagram [A2].....	180
Figure A-4: (a) Optical Rotary Encoder [A3]; (b) Two-Channel Encoder [A4]	182
Figure A-5: Absolute Optical Encoder Simplified Structure [A5].....	182
Figure A-6: A typical mechanical Gyroscope [A6]	183
Figure A-7: A simple Accelerometer Device.....	184
Figure A-8: A sketch of a capacitive MEMS accelerometer [A7]	185
Figure A-9: Mechanical drawings of the steering hub	187
Figure A-10: Plates and shaft installed on the steering hub of the bicycle	187
Figure A-11: (a) Installation of the base and the optical disk; (b) top cover of the sensor	188
<i>Figure A-12: Schematic circuit diagram of the handlebar sensors.</i>	188
Figure A-13: (a) Design of the top layer routing and (b) the bottom layer routing of the handlebar sensors PCB.	189
<i>Figure A-14: (a) Developed PCB with the components</i>	189
<i>Figure A-15: (a) the CAD design of the housing; (b) the 3D printed part installed on the bicycle.</i>	189
Figure A-16: Schematic circuit diagram of the main control box	190
Figure A-17: (a) Design of the top layer routing and (b) the bottom layer routing of the main control box PCB.	191
Figure A-18: (a) Developed PCB for the main control box with the components and wiring.....	191

Figure A-19: (a) Top cover and (b) the base of the enclosure for the main control box.	192
<i>Figure A-20: (a) Hall Effect sensor bracket; (b) Seat tube enclosure brackets....</i>	192
Figure A-21: Electrical connections of the iBike system.....	193
Figure B-1: Closed-loop motor control system	194
Figure B-2: Block diagram of the control and data acquisition system.....	195
Figure B-3: Mechanical drawings of the test rig	195
Figure B-4: The developed test rig	196
Figure B-5: Motor control interface.....	197
Figure B-6: Data visualisation interface.....	197
Figure C-1: (a) Accelerometer raw data; (b) Gyroscope raw data from the test rig	199
Figure C-2: A sample GPS data collected via the smartphone app.	199
Figure C-3: Filtered GPS data.....	200
Figure C-4: A sample Spatial INS data loaded on the Grid InQuestII software ...	200
Figure C-5: Data settings used to transform the coordinates	201
Figure C-6: Sample raw data from the iBike measurement sensors	201
Figure C-7: Gyroscope yaw rate while bicycle is orthogonal to the ground	204
Figure C-8: Yaw Angle while pushing the bicycle in a straight path	204
Figure C-9: DR versus Fused yaw angle	205
Figure C-10: DR versus Fused yaw angle between 7 and 8 seconds.....	205
Figure C-11: GPS positions with respect to a known location	206
Figure C-12: Displacement from the known location.....	206
Figure C-13: Comparison of Spatial INS positional error	207
Figure C-14: Comparison of smartphone GPS positional error.....	208
Figure C-15: Comparison of fused positional error.....	208
Figure C-16: (a) Listener and laptop; (b) beacons used in the experiment	209
Figure C-17: DR versus Fused yaw angle between 7 and 8 seconds.....	209

Acronyms and Abbreviations

ADC	Analogue to Digital Converter
AI	Artificial Intelligence
AOA	Angle of Arrival
AP	Access Point
API	Application Programming Interface
BS	Base Station
C2V	Cycle-to-Vehicle
CAD	Computer-Aided Design
CDF	Cumulative Distribution Function
CDMA	Code-Division Multiple Access
C-iTag	Cycle-iTag
CPaWS	Collision Prediction and Warning System
CPU	Central Processing Unit
CSV	Comma-Separated Values
CTPS	Cell Towers Positioning System
dB	Decibels
DBMS	Database Management Systems
DfT	Department for Transport
DGPS	Differential Global Positioning System
DMP	Digital Motion Processor
DR	Dead-Reckoning
DSRC	Dedicated Short-Range Communication
e-bike	Electric Bicycle
ECF	European Cyclists' Federation
EEPROM	Electrically Erasable Programmable Read-Only Memory
EER	Enhanced Entity–Relationship
EIRP	Equivalent Isotropically Radiated Power
ESA	European Space Agency
EU	European Union
FPE	Filtered Positional Error
FSPLM	Free Space Path Loss Model
GNSS	Global Navigation Satellite System

GPIO	General Purpose Input-Output
GPS	Global Positioning System
GPX	GPS Exchange Format
GSM	Global System for Mobile Communications
GUI	Graphical User Interfaces
HGVs	Heavy Goods Vehicles
HVs	Heavy Vehicles
iBike	Instrumented Bicycle
IDE	Integrated Development Environment
IEEE	Institute of Electrical and Electronics Engineers
IIC	Inter-Integrated Circuit
IMU	Inertial Measurement Unit
INS	Inertial Navigation System
IoT	Internet of Things
ISM	Industrial, Scientific and Medical
ISR	Interrupt Service Routine
iTag	Wireless Communication Tag
ITS	Intelligent Transport Systems
LAN	Local Area Network
LOS	Line-of-sight
LSB	Least Significant Bit
MAC	Media Access Control
MEMS	Micro-electromechanical systems
MIT	Massachusetts Institute of Technology
MPU	Motion Processing Unit
OSGB36	Ordnance Survey of Great Britain 1936
OSNG	Ordnance Survey National Grid
PCBs	Printed Circuit Boards
RDBMS	Relational Database Management System
RFID	Radio-frequency identification
RSS	Received Signal Strength
RSSI	RSS indicator
RTOF	Roundtrip-time of Flight

SAD	Slave Address
SDK	Software Development Kit
SNRs	Signal-to-Noise Ratios
SPI	Serial Peripheral Interface
SRAM	Static Random Access Memory
SSID	Service Set Identifiers
TDOA	Time Difference of Arrival
TfL	Transport for London
TOA	Time of Arrival
TOF	Time of Flight
TRL	Transportation Research Laboratory
TRS	Terrestrial Reference System
TS	Total Station
UWB	Ultra-wideband
UWBPS	Ultra-wideband Positioning System
V-iTag	Vehicle-iTag
WAN	Wide Area Network
WCT	Wireless Communication Technologies
WGS84	World Geodetic System 1984
WLAN	Wireless Local Area Network

System Parameters and Notation

The main parameters used to analyse and model the bicycle system are as follows:

x, y and z	Global coordinate system
\tilde{x} and \tilde{y}	Body-fixed coordinate system
W	Wheelbase
R	Rear wheel turning radius
D	Rear wheel diameter
d_r	Travelled distance of the rear wheel
η	Caster angle
ϕ	Rear-frame roll or tilt or bank angle
$\dot{\phi}$	Roll rate
ψ	Rear frame yaw angle or azimuth or heading
$\Delta\psi$	Instantaneous central turning angle
ω or $\dot{\psi}$	Yaw rate
δ	Steering angle
β	Effective steering angle
P_f	Front wheel ground contact point
P_r	Rear wheel ground contact point
v_r	Rear wheel longitudinal velocity
v_f	Front wheel longitudinal velocity
P_c	Instantaneous centre of rotation
k	Time step in the algorithm
Δt	Time interval between two measured samples

Chapter 1: Introduction

1.1 Research Motivation

Cycling is an increasingly popular mode of travel in cities owing to the great advantages that it offers in terms of space consumption, health and environmental sustainability, and is therefore favoured and promoted by many city authorities worldwide. A large number of recently introduced schemes in many cities (such as the Santander Cycle Hire scheme and the Cycle Super-Highway in London) demonstrate this trend. For instance, in London in 2015, there were 670,000 cycle stages on an average day, a cycle stage being that part of a journey which is accomplished on a bicycle. This is a 3.5% increase from 2014. This follows a 10.3% increase from the previous year, with an overall 61% increase in cycle stages since 2005 [1].

Although the bicycle originally was invented for the benefit of travelling from point A to point B to replace animals for transport [2] cycling now offers many other benefits [3] [4] [5]:

- It promotes exercise and has low running costs.
- It is sustainable and does not consume natural resources.
- It does not harm the environment and improves air quality.
- It reduces motor traffic volumes and therefore traffic noise, pollution and congestion.

As cycling offers many benefits, city planners in recent years have been promoting cycling in the cities and the number of cyclists has increased dramatically and they plan to increase this number even more. For instance, the European Cyclists' Federation (ECF) is working on tripling cycling in Europe by 2020 [6].

Furthermore, bicycles occupy an important place in the context of smart cities because they improve the health and well-being of cyclists as well as being energy efficient. It is predicted that more than 60% of the world's population will live in a city

by 2030 [7] and by 2050, more than 6 billion people will be in urban areas [8]. As a result, for travel to work and short journeys, cycling occupies an important share in the modal split in many cities.

However, the relatively low perceived safety of cyclists from the users' side currently presents itself as a hurdle in achieving the desired uptake of cycling as a viable alternative to the private car, with a particular source of hazard appearing to originate from the interaction of cyclists with cars, Heavy Vehicles (HVs), i.e. buses, coaches, and lorries, at low speeds in urban areas. Accident numbers, unfortunately, confirm this perception as reality: the latest accident statistical figures released by the Department for Transport (DfT) for 2015 [9] show that cyclists are 17 times more likely to be killed and 21 times more likely to be seriously injured in road traffic accidents than car occupants in Great Britain. Furthermore, although the number of cyclists killed is slightly down since 2008, the reported cyclist casualties still stand at the staggering total figure of 18,845 for 2015. As a result, many authorities are trying to tackle this rising issue. Moreover, numerous studies have shown that fear of limited traffic safety for cyclists is a significant disincentive and reduces people's likelihood to cycle [10] [11] [12].

Until a few years ago, the only options for actively tackling such a problem would have been drawn from the domain of "hard" traffic engineering measures, (usually cost-intensive and disruptive, such as segregated lanes or vehicle type bans in certain streets). However, developments of ubiquitous computing and sensor technologies now offer ways to increase the use of smaller, more accurate and durable tools to support traffic safety interventions, and put Intelligent Transport Systems (ITS) in a prominent role with respect to improving the safety of cyclists. Thus, this research study formulates an innovative low-cost technological solution based on a hybrid localisation system and develops a prototype instrumented bicycle system that can be ultimately utilised to improve the safety of cyclists and promote the use of bicycles in urban areas. The term "iBike" was chosen to denote this new system.

1.2 Brief Historical Overview of Bicycle's Evolution

In the late 17th century, Ozanam illustrated the theoretical advantages of a human-powered carriage “in which one can drive oneself wherever one pleases, without horses” [13]. Ozanam’s publication featured a design for a four-wheeled carriage which could be pedal-driven and an illustration of the design is presented in Figure 1-1 left. This predecessor of the modern bicycle lasted for more than 100 years without significant modification.

It was not until 1817 when Karl von Drais, a German baron from a distinguished family in Karlsruhe, made an improvement to his early version of a four-wheeled pedal vehicle and he introduced what became known as Draisienne or the Dandy horse, which made use of the two-wheeler principle and it is the earliest form of the modern bicycle. The dandy horse was a slender vehicle made almost entirely of wood except for the iron tires which were positioned in a straight line. The rider sat almost completely erect and drove the device forward by pushing against the ground with one foot, then the other, as if walking or running. As illustrated in Figure 1-1 right, for the next few decades, inventors continued to improve the dandy horse and made many modifications as the technology evolved.

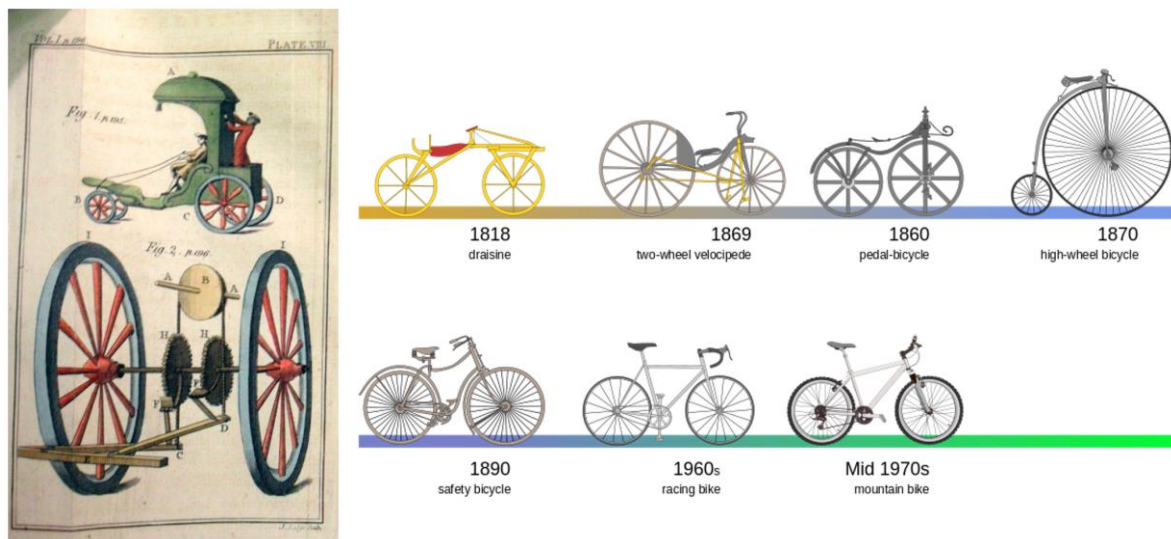


Figure 1-1: Early evolution of bicycles: illustration of Jacques’s design (left) [14], and development of modern bicycles (right) [15].

Finally, in the mid-1860s, the basic bicycle emerged in Paris. The brainchild of Pierre Lallement, a mechanic who specialised in baby carriages, it demonstrated the

principle that a vehicle with two wheels in a line could be indefinitely balanced and propelled by means of a mechanical drive, such as a gear, rather than by human propulsion alone [13]. This removed the principle objection to the dandy horse and opened a promising path for development. The inventors successfully made one of the world's masterpieces, which still puzzles many mathematicians on the theoretical principle, and introduced the term "bicycle" in the late 1860s [16]. In the 21st century, the bicycle continues to evolve as the technology advances and more and more bicycles are given the term "e-bike" or "smart bicycle".

An electric bicycle (e-bike) is a bicycle with an integrated electric motor that can be powered by electricity as well as propelled by pedals. Not to be confused with mopeds, the e-bikes retain the ability to be pedalled by the rider and therefore they are not classed as electric motorcycles. There are many different types of e-bikes available worldwide but in the scope of this project, the only one discussed is Pedelec e-bikes, which are bicycles with a small electric motor to assist the rider's pedalling. The acronym Pedelec comes from the words 'pedal electric cycle' and they are classified as conventional bicycles by the authorities in many countries. In Europe, a bicycle is considered a Pedelec if it is intended to cover electrically power-assisted cycles of a type which has a maximum continuous rated power of 0.25 kW, of which the output is progressively reduced and finally cut off as the vehicle reaches a speed of 25 kmph, or sooner, if the cyclist stops pedalling [17].

A smart bicycle, on the other hand, integrates the above feature with the additional onboard intelligent system, where it is utilised to manage power intelligently based on the local sensory information about the environment and the inputs from the rider. An example of a smart bicycle includes the Copenhagen Wheel [18] in Figure 1-2, which was developed at Massachusetts Institute of Technology (MIT) together with the city of Copenhagen.

The Copenhagen Wheel is a retrofit wheel for an ordinary bicycle that works as an electric hybrid system [19]. The hub of the Copenhagen Wheel contains all the necessary electronics and components including motor, removable batteries, wireless connectivity, smart locking, multiple sensors and an embedded control system. Riders control the functionality of the wheel using an app on their smartphone which communicates with the Wheel via Bluetooth technology. In

addition, the smart wheel learns how the rider pedals and integrates with the rider's motion. It also has a system similar to a regenerative braking system such that dissipated energies while cycling and braking are captured and later used to assist the rider whenever they require.

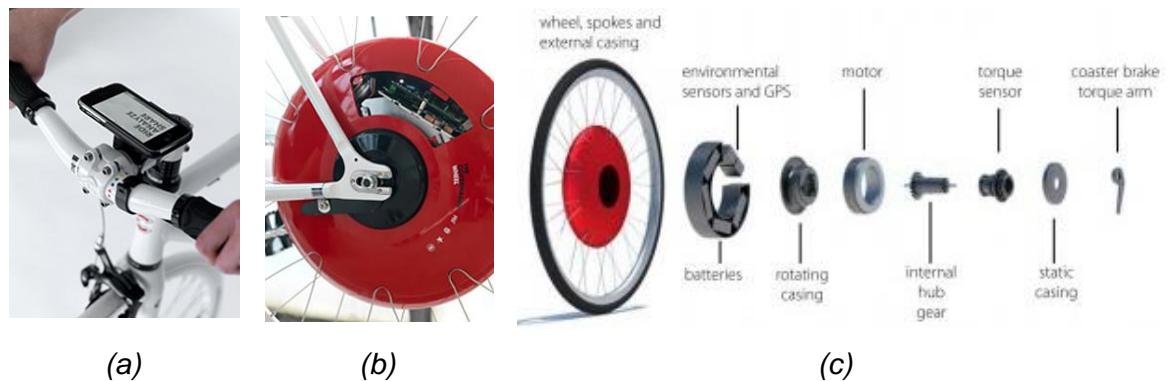


Figure 1-2: Copenhagen Wheel [20] – (a) Smartphone, (b) the hub of the Copenhagen Wheel and (c) a retrofit wheel with essential electrical and mechanical components.

Moreover, in Copenhagen the bike sharing scheme, which allows the public to hire a bicycle for shared use on a short-term basis, utilises Pedelec e-bikes with a tablet computer on board that is used to hire the bicycle shown in Figure 1-3.



Figure 1-3: Copenhagen City Bike [21] – (a) a tablet computer on the hub of the bike and (b) the Pedelec e-bikes.

In conclusion, bicycles have evolved dramatically in recent years, and this is mainly due to the advances in technologies. However, one of the issues that remain is the safety of the cyclists, especially in congested cities such as London, and this research study focuses on improving the safety of riders through technology.

1.3 Problem Statement, Project Vision and Challenges

The problem of cyclist and motorised vehicle accidents is well-defined, and it is acknowledged by drivers, as many of them display a warning sign at the rear of their vehicles, such as the ones shown in Figure 1-4, to alert the cyclists and other road users. Thus, it is not a new issue that has been elevated but rather a well-defined concern. On the other hand, many of the cyclists are not aware of the vehicles' blind spot, which is an area around the vehicle that cannot be directly observed by the driver (refer to Figure 1-5a), and the cyclists might be in danger if they are close to a vehicle which intends to turn. Although one of the warning signs says, "if you can't see my mirrors I can't see you", on most occasions the other road users might well see the mirrors but the drivers might not see them due to blind spot which is not covered by the mirrors, or is distracted by other events on the roads.



Figure 1-4: Typical warning signs for cyclists appear on the back of HVs.

The solution to the problem of bicycle-vehicle collisions proposed in this study is to:

- (1) Provide the ability to monitor the blind spots and to detect cyclists in their vicinity.
- (2) Provide the ability to take preventive action if a collision scenario is detected based on predicted trajectories of the vehicles.

The complete system is called Cyclist 360° Alert. One way of implementing the system could be to utilise the methodologies, which will be developed in this study, as tools for a collision avoidance system, where a vehicle would automatically react in a bicycle-vehicle conflict scenario. Another could be a collision warning system where a vehicle could avoid a collision with the cyclist by making the driver of the vehicle aware of the cyclist's location. For example, a warning message can be displayed through an in-vehicle or portable display unit, such as a smartphone,

allowing the driver to perceive potential hazards earlier, hence be prepared to stop, if necessary, to prevent a collision. This concept of operation is illustrated in Figure 1-5 (b) and (c). More details are given in chapter 3. In order for this concept to work, the system must be able to function in all traffic scenarios and environmental settings as well as being able to localise the position of the vehicles with a non-line-of-sight technology so that obscured regions in traffic conditions can be sensed.

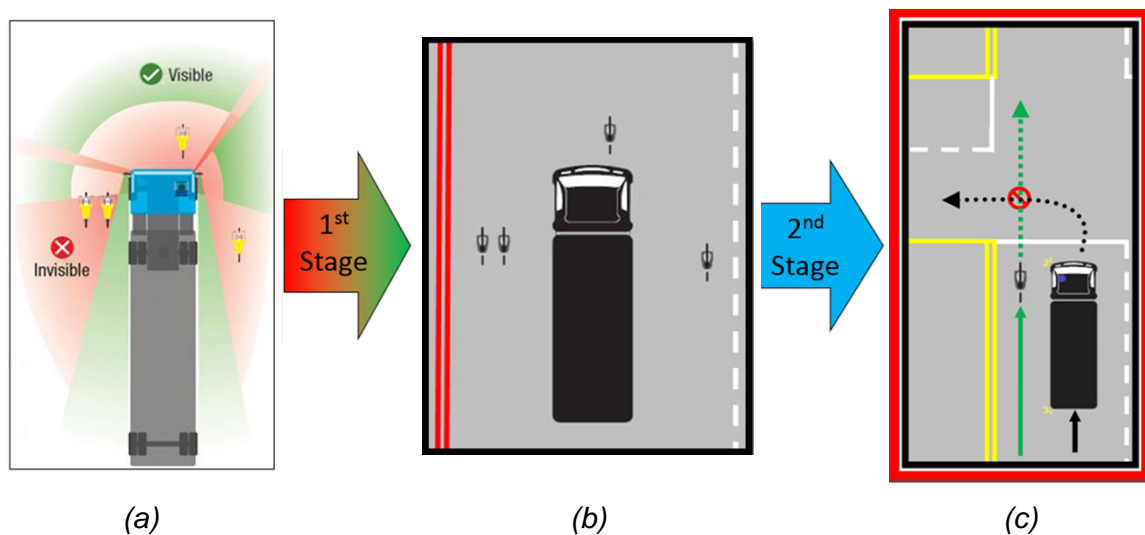


Figure 1-5: (a) Blind spots surrounding a lorry, (b) Cyclist 360° Alert driver's display view and (c) predicted trajectories for vehicles and an indication of a danger.

The Cyclist 360° Alert system requires the localisation and tracking of bicycles, as well as vehicles, in real-time, in order to deliver the proposed concept. One of the main challenges associated with the idea is the required level of high positioning accuracies for the vehicles and bicycles so that accurate collision prediction algorithms can be developed to provide drivers with more reliable warning messages and positioning of the cyclists.

According to Sustrans Handbook for cycle-friendly design [22] drivers overtaking cyclists should give clearances of at least 1 m and 1.5 m at 20 mph (32 kmph) and 30 mph (48 kmph) respectively and this is illustrated in the diagram in Figure 1-6(a), which comes from the Handbook. These distances are widely adopted throughout Europe. For example, it is written into French law. Thus, from the technical design in the Handbook, the minimum dynamic width required by the cyclist is 1 m as illustrated in Figure 1-6(b). Hence, localisation accuracy for Cyclist 360° Alert system should be at least ± 0.5 m at 32 kmph.

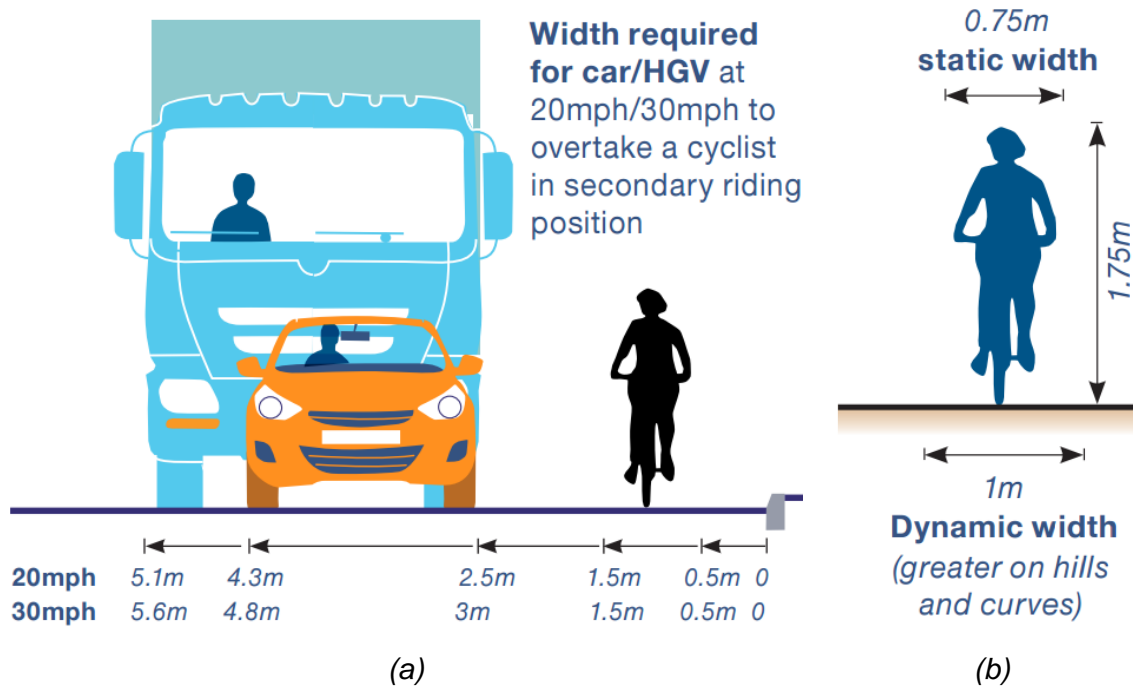


Figure 1-6: (a) Minimum safe passing distance and (b) minimum dynamic width required [22].

The main challenge is that bicycles are significantly smaller in comparison to vehicles, only occupy a small amount of space and are able to move more freely than vehicles on the road, which makes their real-time tracking to the desired accuracy a very difficult task. Although very few systems exist for tracking vehicles such as the iBus tracking system in London [23], yet there is no system specifically designed for tracking cyclists. Moreover, to the best of the author's knowledge, no single system based on non-line-of-sight technology currently fulfils the required localisation accuracy for the proposed system. As a result, a new approach is needed to achieve this. This should rely on existing technology, with cost being a major constraint on the development, as Cyclist 360° Alert needs to be a cheap solution that can eventually be integrated into all bicycles and vehicles. Since bicycles are significantly more complex to track than vehicles, this research focuses on the development of a prototype localisation system for cyclists that could be eventually employed for Cyclist 360° Alert system.

1.4 Aim and Objectives of this Research

The proposed research fits within the wider aim of exploring ways to prevent accidents involving vehicles and pedal cycles in space-congested cities, by

developing an advanced ITS architecture between the cyclists, vehicles and other road users. As mentioned in the previous section, no single system currently exists that is specifically designed for tracking cyclists with ± 0.5 m localisation accuracy and that could be employed within Cyclist 360° Alert concept formulated in Chapter 3 as part of this research study.

Therefore, the main aim of this work is to develop and implement a low-cost high-accuracy localisation method for cyclists that can be utilised to track bicycles in urban areas, including complex traffic situations such as intersections, and that can be integrated within a collision prediction and warning system for future development. The formulation of the sensor architecture, methodologies and the prototype system developed as part of this study will be the basis for future research in this field.

The objectives of the study are as follows:

1. To review analysis of accident data related to cyclists in order to systematically understand the scale and the causes of the problem, and to review current ITS solutions available to drivers.
2. To study the communication technologies widely found in smart devices that could be utilised for real-time localisation of cyclists and to formulate the system architecture of the novel methodology called “Cyclist 360° Alert”.
3. To develop innovative multi-level sensor fusion methodologies and algorithms to achieve the design requirement of ± 0.5 m positioning accuracy for cyclists.
4. To identify and develop iBike sensor system architecture to support the mapping algorithms and to develop a prototype iBike system with the proposed methodologies.
5. To test and validate the prototype iBike system through field experiments in urban areas with real-world traffic conditions, and to present the outcomes of the results through evaluating the positioning accuracy of the iBike system with an existing off-the-shelf enhanced positioning system.

1.5 Structure of the Thesis

This thesis consists of five main chapters: Chapters 2 and 3 present a broad analysis of existing literature in the context of cyclist-related collision and localisation systems; Chapters 4, 5, and 6 describe the contributed elements devoted to this research study. Each chapter beginnings with a short introduction, followed by several different sections and then endings with a summary of the chapter findings.

Chapter 2 introduces an overview of the problem by analysing accident statistics concerning cyclists, and this is followed by some of the key characteristics of cyclist accidents found in literature and a review of the existing ITS solutions to address the problem.

Chapter 3 formalises the overall problem and discusses an ITS solution that could prevent future accidents by providing the drivers with the ability to monitor the obscured regions of their vehicles. In this chapter, an investigation of the available communication technologies which could be utilised for localisation systems has been conducted together with some of the methodologies for localisation systems. This leads to a novel system creation.

Chapter 4 presents novel multi-sensor fusion algorithms, firstly by studying the characteristics of a bicycle. Then through the understanding of bicycle geometry and kinematics, it presents a simplified model which is used to derive the relevant parameters of a Kalman filter for multi-sensor fusion and it illustrates the design of the novel mapping algorithms using block diagrams.

Chapter 5 discusses the development of the iBike system, in which the main components of the system are described briefly along with the selected sensors. This chapter also describes the acquisition and processing of the data as well as the development of a database to store raw and processed data from field trials.

Chapter 6 reports on the validation of the iBike system through field experiments conducted on the roads around the university's campus. The report includes experimental setup, statistical analysis, as well as the presentation and discussion of the results obtained from experiments.

Chapter 7 concludes this thesis and identifies areas of potential further research.

1.6 Contribution of the Research

A number of contributions, mainly falling in the subject areas of ITS, Sensor Fusion and Signal Processing, have emerged from this research project. The overarching innovation of this thesis is the development of an iBike system that could be employed to track cyclists' positions more accurately. Specifically, the contributions of the thesis are summarised below:

- **An Innovative Concept for Tracking Cyclists** – Firstly, a concept named “Cyclist 360° Alert” is formalised from the understanding of the main causes of bicycle-vehicle related collisions. Secondly, a novel approach is proposed to fuse multi-sensor data to improve the localisation accuracy based on existing technologies and sensors widely found on smart devices and in urban areas.
- **Sensor Fusion Algorithms for Pedal Cycles** – Bicycle dynamics is an immensely complex subject. Nevertheless, a simplified positioning model is developed, and sensor fusion algorithms are applied to reconstruct the bicycle's trajectories and to improve the localisation accuracies respectively.
- **Instrumentation and Validation of an Instrumented Bicycle** – A number of kinematics measurement parameters and bicycle design parameters are defined from the design of the sensor fusion algorithms. Based on the design, a Santander Bicycle Hire cycle is instrumented with various low-cost sensors. A pioneering method is then proposed and utilised to validate the iBike measurement system using real-world data.
- **A State-of-the-art Database of Cyclist Trajectories** – A relational database is designed and developed to structurally store the raw and processed data collected via the iBike measurement system, Global Positioning System, Spatial Inertial Navigation System and data from a camera.

In addition, the results from the field experiments show that the iBike system can indeed be employed to estimate the position of a cyclist more accurately than what is currently offered by freely available global positioning systems or even commercially available enhanced positioning systems. Thus, from the trials, it is concluded that these innovative solutions can assist industries to develop accurate and more reliable safety for transport systems in society.

Chapter 2: Background to the Problem & Challenges

2.1 Introduction

To understand the scale of the issues, their main causes and the importance of this research, this chapter briefly presents the broad understanding of why cyclist casualties occur by studying accident statistics concerning cyclists. Section 2.2 reports on the newest available accident statistics on the national level and then on urban regions. Section 2.3 studies some of the key characteristics of cyclist accidents found in literature and specifically reports on the most common conflict types resulting in cyclists either being killed or seriously injured between 2011 and 2013. Section 2.4 summarises and highlights two common factors contributing to bicycle-related collisions. Section 2.5 briefly evaluates some of the existing ITS solutions developed to mitigate the issue of cyclist-vehicle related collision and Section 2.6 concludes this chapter.

There is also an important scientific challenge relating to data fusion, but this subject is dealt with in more detail in Chapters 3 and 4.

2.2 Review of Cycle Collisions and Trends

This section reports accident statistics for cyclists on the national and urban level.

2.2.1 Latest Accident Numbers on National Level

In Britain every year approximately 19,000 cyclists are killed or injured in road accidents. Of these around 3,000 are killed or seriously injured [24]. In the DfT's latest "Reported road casualties in Great Britain" statistical release [9], in 2015, there were 100 cyclist fatalities in the whole of Britain. This number suggests a slightly decreasing trend compared to previous years (118 in 2012 and 113 in 2014) but the report points out that the decrease is insignificant in statistical terms. The main

report includes the number of people killed¹, seriously injured² and slightly injured³ (a full list of definitions can be found in DfT - Reported Road Casualties in Great Britain: notes, definitions, symbols and conventions [25]) in accidents on public roads as reported to the police within 30 days, in Great Britain. Similar trends can be observed in other countries worldwide. For instance, in 2015, 2,043 cyclists were killed in road accidents in the EU countries [26] and 817 bicyclists were killed in the United States [27]. Thus, these accident statistics demonstrate that this is very much a global issue, not confined to a specific country or region.

However, it is well established that many cyclist casualties are not reported to the police, even when the cyclist is injured badly enough to be taken to the hospital. The report [28] which was prepared for Transport for London (TfL) by the Transportation Research Laboratory (TRL), indicates this issue by illustrating the data from police and hospital casualty records, which do not all coincide. Although the number of deaths is accurate, there could be two or three times as many seriously injured and double the number of slightly injured cyclists. The authors of a BioMed Central article [29] restricted their analysis to fatal collisions only due to the possibility of less severe crashes being under-reported. The cyclist casualties have risen in recent years as the amount of cycling has increased and the accident data for serious and slight injuries could be double the number reported.

Furthermore, it is clear from the graph in Figure 2-2 that the number of cyclists killed or seriously injured has steadily been rising over the past years and there has been 49% increase between the year 2005 and year 2014. Even though there was a fall of 5% to 3,239 serious injuries in 2015, this is still the second highest year for pedal cycle accidents since 1997 according to DfT report [28].

¹ Human casualties who sustained injuries which caused death less than 30 days after the accident.

² An injury for which a person is detained in hospital as an “in-patient”, or any of the following injuries whether or not they are detained in hospital: fractures, concussion, internal injuries, crushings, burns (excluding friction burns), severe cuts, severe general shock requiring medical treatment and injuries causing death 30 or more days after the accident.

³ An injury of a minor character such as a sprain (including neck whiplash injury), bruise or cut which are not judged to be severe, or slight shock requiring roadside attention. This definition includes injuries not requiring medical treatment.

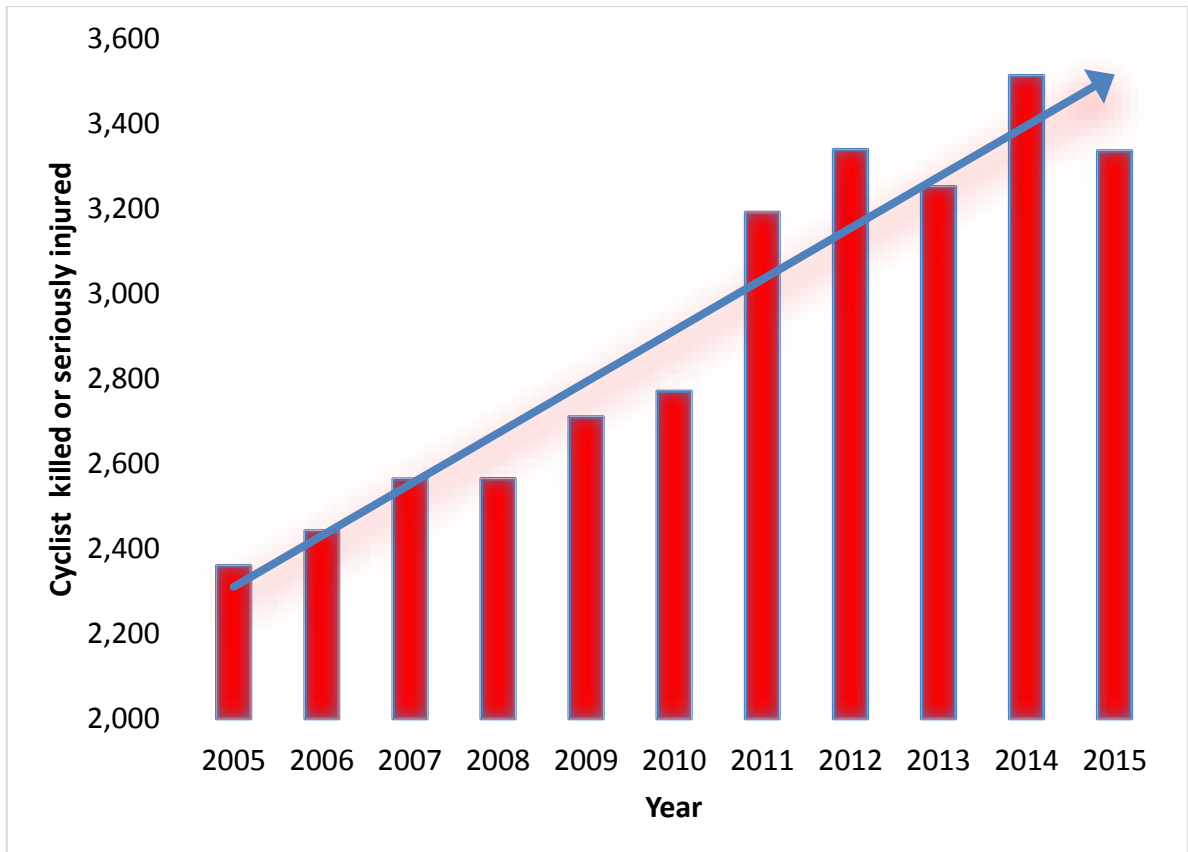


Figure 2-1: Reported cyclists killed or seriously injured between 2005 and 2015 (adapted from [30]).

Figure 2-2 provides a comparison of reported causality and fatality rates per billion passenger miles by road user type for 2015. The road user type includes pedestrians, cyclists, motorcyclists, car occupants and other vehicle users. The graph clearly indicates the much higher casualty rates for cyclists and motorcyclists in comparison to other vehicle users. Moreover, according to TRL Report PPR 445 [31], around 75 % of fatal or serious cyclist accidents occur in urban areas, hence, the next section looks into the studies and analyses accident statistics for London, mainly due to the availability of statistical data.

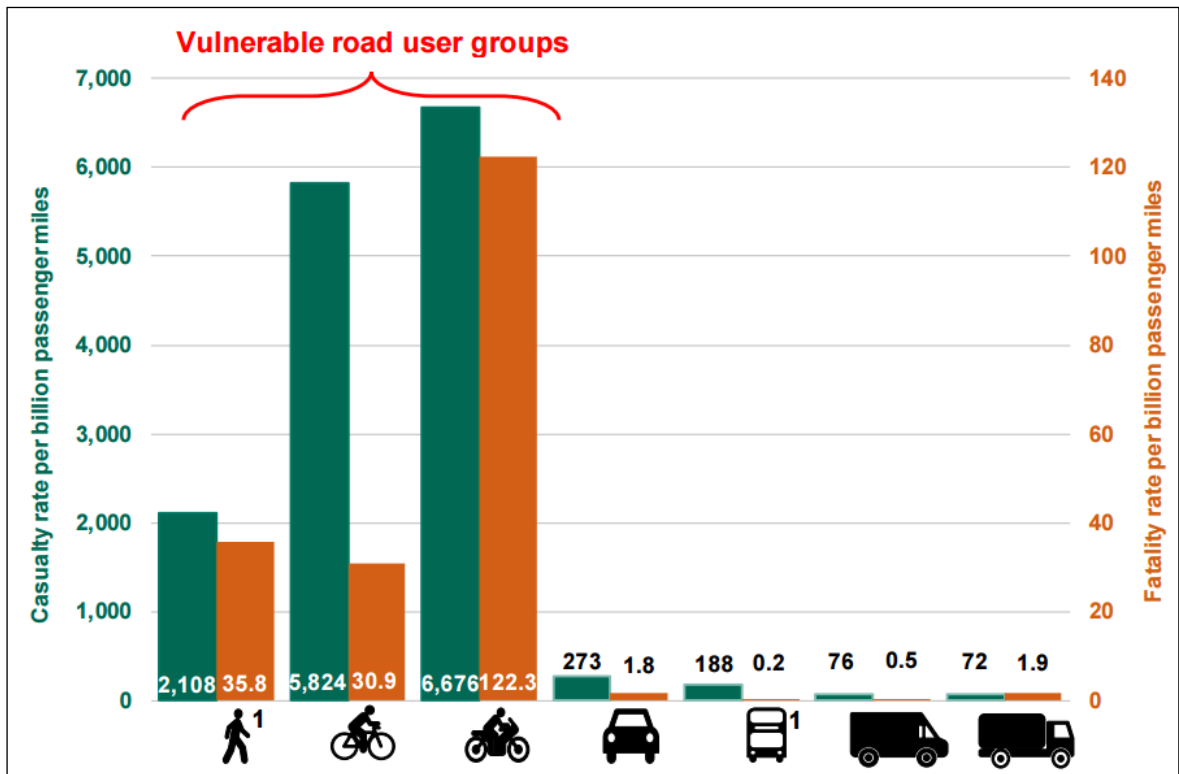


Figure 2-2: Casualty and Fatality rates per billion passenger miles by road user type [28].

2.2.2 Previous Studies and Urban Regions Accident Statistics

The results of the BMC research article referred to 2.2.1 [29] show that from 1992 to 2006 there was a mean of 16 cycling fatalities per year in London. In this period 60% of these deaths occurred in inner London and the rest were in outer London. However, there has been no indication of a decline over time other than a dip in 2004 when there were only 8 fatalities. (Adverse weather conditions in 2004 led to fewer bicycles on the road). The report also reveals an important figure - which is that freight vehicles were involved in 43% of all incidents and over 53% of these incidents took place when the vehicle was making a left turn. The study also shows that freight vehicles are disproportionately involved in collisions fatal to cyclists: approximately 24 times more likely to be involved in a fatal incident than cars, 4 times as likely as buses and 8.5 times as likely as motorcycles.

Recently, between 2008 and 2012, HVs were involved in 53% of London cyclist deaths despite making up only 4% of the traffic [32]. In 2013, the number of cyclists who died as a result of collisions with HVs had increased to 64%. In other words, 9 out of 14 cyclist fatalities in the capital were with HVs. The analysis of the road traffic

collisions and casualties in Greater London shown in Figure 2-3 also clearly indicates the rise of pedal cyclist casualties over the past years.

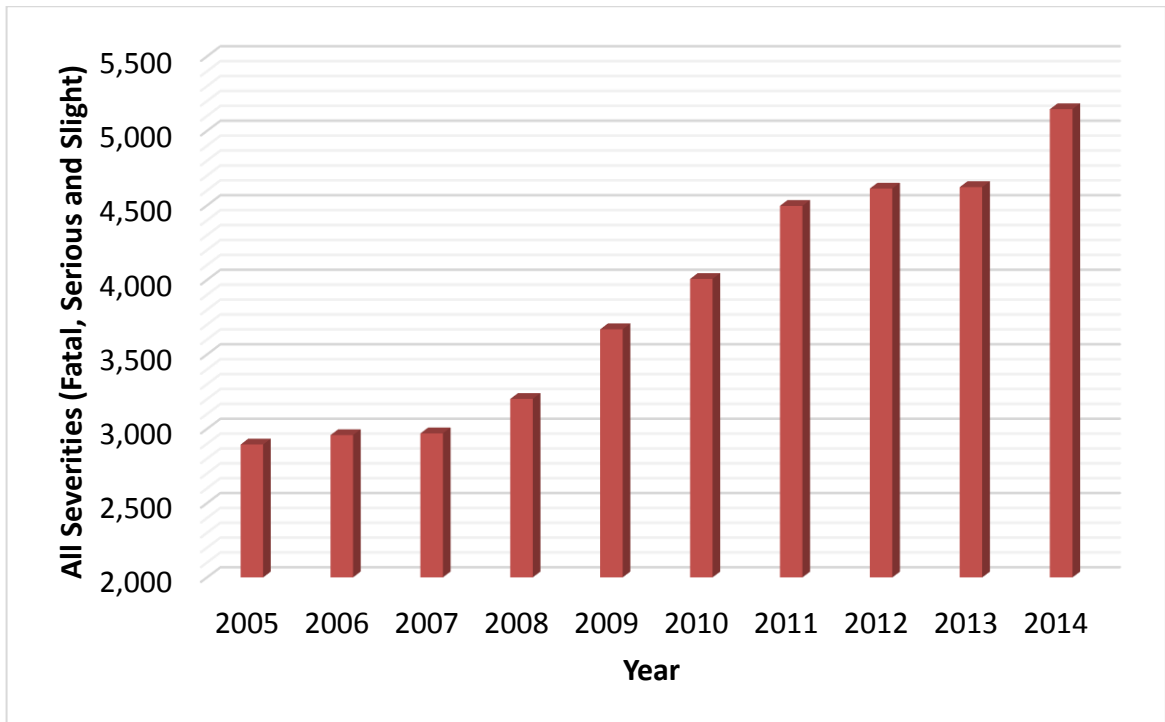


Figure 2-3: Reported pedal cyclist casualties in Greater London between 2005 and 2014 (adapted from [33]).

Overall the problem of cyclists' casualties is not confined to a single locality such as London, but it is an issue for many cities around the world. Therefore, as illustrated above, cyclists' casualties are a serious and growing problem, when many authorities are promoting cycling through a number of cycle-related schemes. As a result, the ECF asks for a set of measures to be implemented to halve injury and fatality rates by 2020 [6]. Thus, many stakeholders are keen to find a better solution that can improve the safety of cyclists, reduce the danger and promote the use of bicycles, especially in towns and cities.

2.3 Understanding the Causes and Key Characteristics of Cyclist Casualties

Analysis of accident data reveals that complex scenarios are involved in an accident between cyclists and other vehicles. In a collision scenario, cyclists are vulnerable because they are exposed to potential collisions and the bicycles, with their two wheels, are unstable. Bicycles are physically small in comparison with vehicles and

they are able to move more freely in traffic situations. Therefore, from the drivers' point of view, the movements of cyclists are unpredictable, even erratic. In some cases, cyclists cannot prevent an accident taking place even if they are aware that the vehicle is about to crash into them, as in the scenario illustrated in Figure 2-4 where the cyclist was unable to inform the driver of the danger.

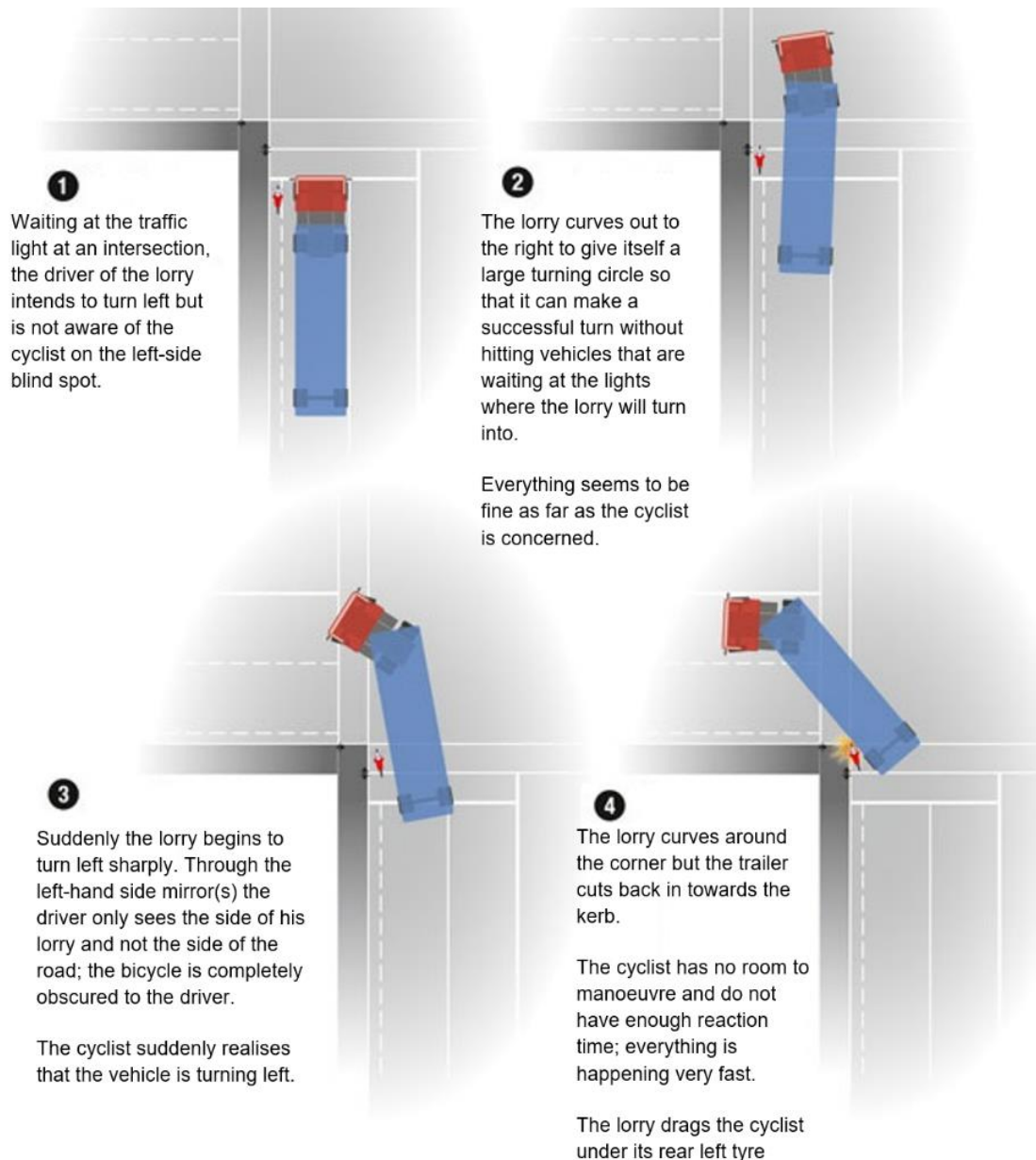


Figure 2-4: A typical fatal collision scenario for a cyclist with a lorry (adapted from [34])

There are many types of conflict scenarios between pedal cycle and other road users. TfL Surface Transport Factsheet [35] illustrates different types of conflict occurring in 2011. TfL's Cycle Safety Action Plan [36] shows the five most common conflict types, as illustrated in Figure 2-5, resulting in cyclists either being killed or

seriously injured from 2011 to 2013. The indicative diagram shows the direction of the cyclist with a dotted line and the other vehicle with a solid line. The report also states that the conflicts ranked 1, 4 and 5 are three of the most common collision scenarios resulting in serious injury to cyclists. However, collisions involving vehicles turning left and cyclists going straight ahead usually have serious consequences for the cyclist. The cyclist, who has right of way, is often unnoticed by the drivers and despite a variety of measures, blind spot crashes continue to occur.

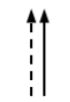
Conflict rank	Indicative diagram	Manoeuvre description	Seriously injured casualties (% of total)	Fatal casualties (% of total)
1		Other vehicle turns right across path of cyclist	243 (14%)	2 (5%)
2		Cyclist hits open door / swerves to avoid open door of other vehicle.	160 (10%)	2 (5%)
3		Cyclist and other vehicle travelling alongside each other.	146 (9%)	4 (9%)
4		Other vehicle turns left across the path of cyclist	125 (9%)	11 (25%)
5		Other vehicle fails to give way or disobeys junction control and collides with cyclist	96 (6%)	1 (2%)

Figure 2-5: The most common conflict between Pedal Cycle and Other Vehicles [36].

Figure 2-6 and Figure 2-7 below illustrate the number of cyclist casualties in Greater London in 2010 by day of the week and by month respectively. Both figures also indicate that most collisions take place in broad daylight. In addition, Figure 2-6 highlights that most accidents occur during weekdays while Figure 2-7 indicates that most of the accidents take place during summer months in Britain, which is when cycling activity also increases. A similar pattern is also illustrated in a report from Monash University [37] which describes the characteristics of crashes involving bicycles and motor vehicles in Victoria, Queensland, Western Australia and South Australia based on the accident data from the police between 2000 and 2004.

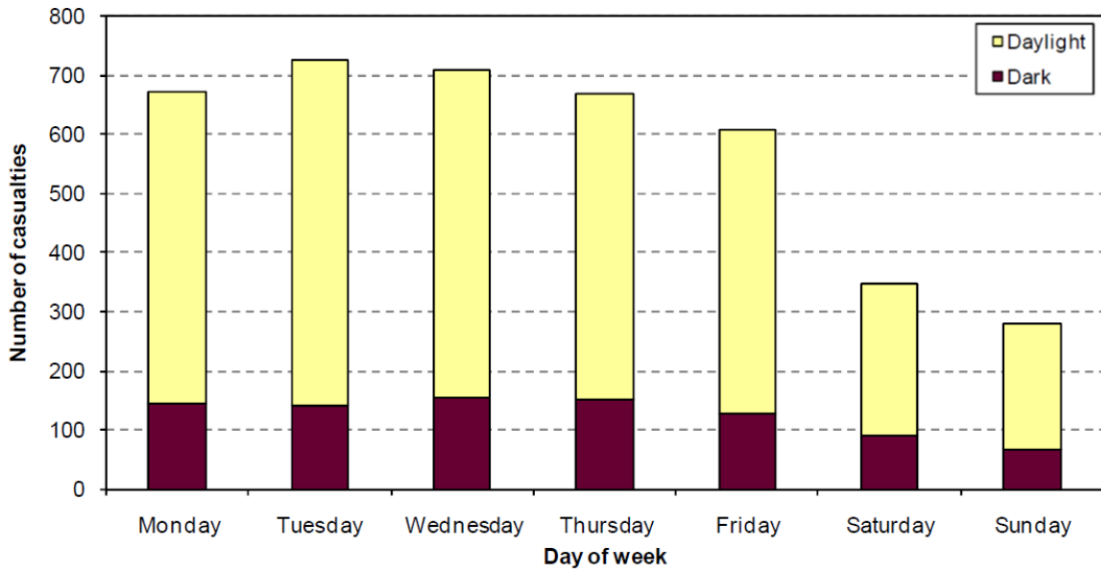


Figure 2-6: Cyclist Casualties by Day and Light Conditions (adapted from [38]).

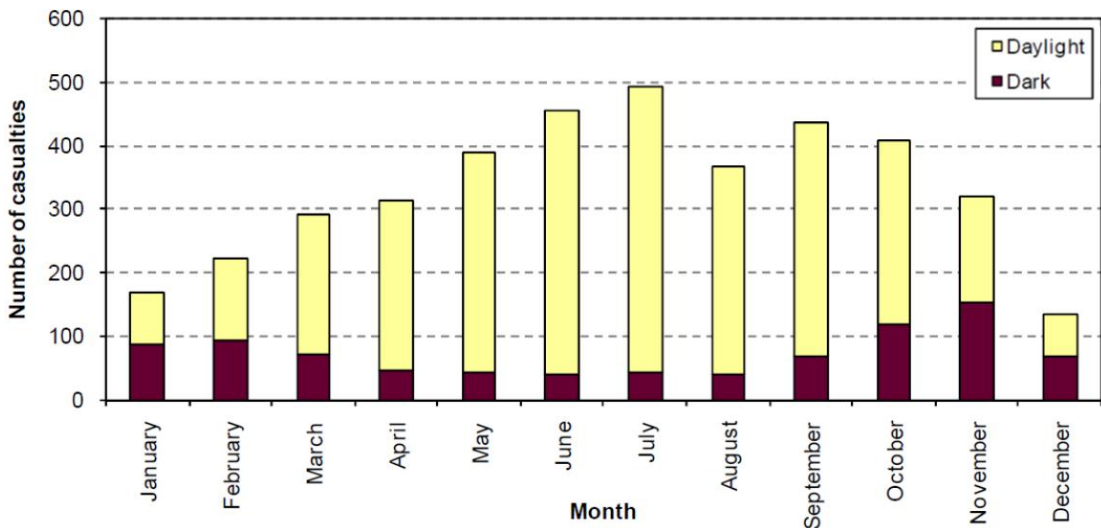


Figure 2-7: Cyclists Casualties by Month and Light Conditions (adapted from [38]).

Overall, According to Shooter and Reeve [39], depending on country and region, between 30% and 60% of all injury accidents and about 16% to 36% of fatalities are related to intersections. This is because accident scenarios at intersections are the most complex traffic situations and often involve a variety of road users. Analysis of blind-spot junctions by the Dutch SWOV group (Institute for Road Safety Research) [40] describes patterns of collisions involving turning HVs and cyclists colliding with them, usually leading to serious consequences for the cyclists. In addition, according to TfL’s report [36], in London over 80 % of cyclists injured in 2013 occurred at or within 20 metres of a junction with most casualties occurring at ‘T’ and staggered junctions.

In summary, many issues are associated with a collision but two common contributory factors with bicycle-related collisions are discussed below.

2.4 Technical Limitations and Human Factor

The first problem is blind spots around large vehicles - these are regions of the road that the driver is not able to see by looking directly or through a mirror. Blind spots are also created by the chassis of the vehicle, and especially the windscreen pillars and the area under the windscreen, because of the driver's higher seat position. Typical regions of blind spots surrounding a lorry are illustrated in Figure 1-5(a), where the pink-shaded regions on the figure are the blind spots. For example, the four cyclists in the figure are completely obscured by the blind spots, and so drivers would not see them from their normal driving position, as only the green-shaded areas are visible to the driver. In particular, the left-hand-side blind spot in the UK (right-hand-side in Continental Europe and North America) is most hazardous to the cyclists, because the driver sits on the opposite side and is unable to observe the blind spot area by looking down through the window directly.



Figure 2-8: Left turn blind spots for an articulated lorry [41].

Furthermore, as illustrated in Figure 2-8 above, the side mirrors of an articulated lorry become even less beneficial when the vehicle is partially turned, such as at an intersection where the lorry needs to turn left. This is where the most common type of fatal collisions for cyclists could take place. Moreover, despite measures to

improve the HV driver's field of vision, there is still an area around the vehicle that the driver is unable to see through the windows or with the help of mirrors and cameras. In addition, the mirrors may not always be adjusted properly, which unnecessarily increases the area not visible to the driver. Above all, HV drivers have to contend with a heavy mental burden when they want to turn: the driver must keep an eye on all the traffic at the junction by looking through the windows and in all mirrors. However, not all the mirrors are in the same direction of view and the eyes take time to change between the mirrors and this may give rise to a situation where a cyclist is overlooked [40]. Although the common perception is that the cyclist-HV related accidents can be solved by utilising more mirrors, this observation is not reflected in the accidents statistics [42]. Instead, the installation of different mirror configurations to tackle the problem was found to be complex and impractical [40].

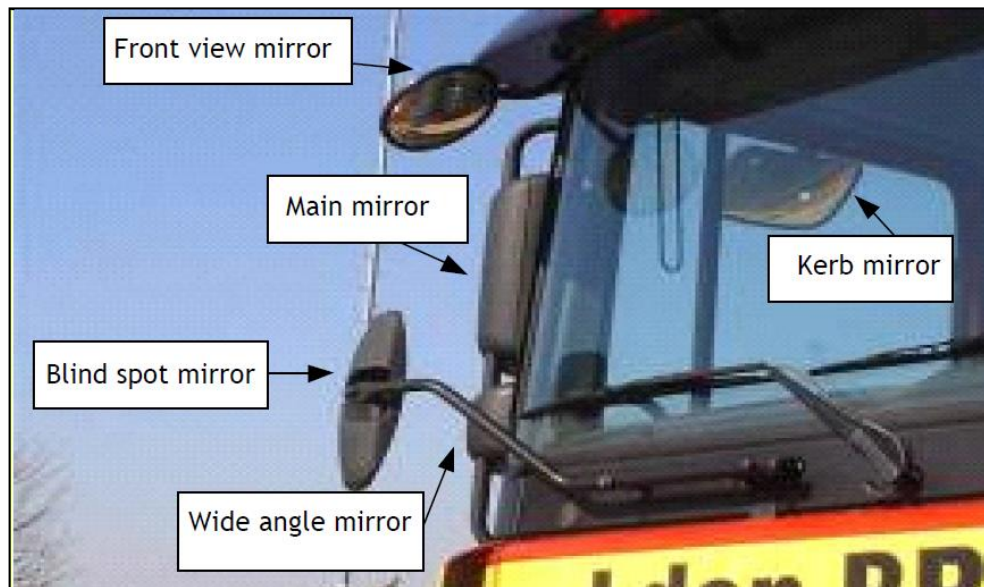


Figure 2-9: Illustration of mirrors on a truck [40].

The second problem is careless driving which could be the result of overloaded information and distractions. Figure 2-9 illustrates the fact that the HV drivers might have too many mirrors or instruments to observe. In addition, in urban areas, drivers also have to pay particular attention to busy roads ahead. As a result, drivers could fail to see a hazard in time to avoid a collision with a vehicle as small as a bicycle, especially in an urban environment. On the other hand, some cyclists do also ride their bicycles carelessly, for instance, riding through red lights, overtaking dangerously and not obeying all the Highway Code rules [43]. There are also some inexperienced cyclists who might not be aware of the dangers surrounding HVs.

However, in most scenarios, the cyclists cannot do much to prevent the accidents [44] because they are exposed to potential collisions and the bicycles, with their two wheels, are unstable and vulnerable.

For both of these problems indicated above, if a driver had an alternative way of observing the side roads surrounding the vehicle and alerting them of a danger, then the potential collisions with vulnerable road users could be prevented. Thus, this concept is used to formulate a solution in this thesis.

2.5 Review of Current ITS Solutions

The safety of cyclists has also been the objective of several international collaborative projects. For example, the European-Commission-funded project WATCH-OVER [45] focused on road accidents involving vulnerable users and attempted to design and develop an efficient and low-cost vehicle-VRU (Vulnerable Road User) cooperative system; this was to be based on an on-board platform and a VRU module, communicating with the on-board system wirelessly using standard technologies such as IEEE802.11 (Wi-Fi). INTERSAFE-2 [46] on the other hand, also sought to contribute to the desired reduction of injuries and fatalities at intersections, and investigated a series of vehicle-based safety technologies by bringing together a number of vehicle manufacturers. Similar investigative work was carried out by the COOPERS project [47], where the scope was to develop and demonstrate a system that links vehicles with road infrastructure via continuous wireless communication. However, their results have not been taken up due to limitations in methodology and technology.

Industrial research has also been conducted, with the most notable example being Volvo's pedestrian and cyclist detection system [48]. The system consists of a forward-facing high-resolution camera positioned ahead of the inside rear-view mirror, as well as a grille-mounted radar unit and a central controller that uses a constant data stream from both sensors to monitor and evaluate traffic ahead of the vehicle. If any potential collision with cyclists ahead of the vehicle is detected and the driver does not respond in time, the vehicle can automatically apply the brake to bring it to a full stop. However, as can be seen from Figure 2-10, it is limited to the field of view of the camera and it does not detect cyclists located in the blind spot.

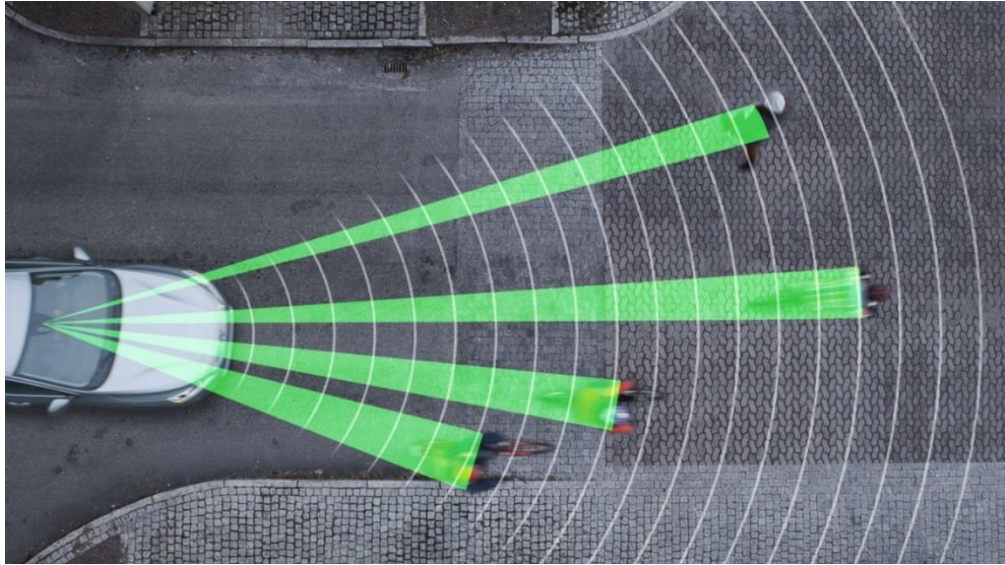


Figure 2-10: Volvo's pedestrian and cyclist detection system [48].

Moreover, the recent development of autonomous-vehicle (AV) technology, which is capable of sensing its environment and navigating without the input from a human driver, typically employs LiDAR (Light Detection and Ranging) sensors, cameras to detect its surroundings, and utilises an inertial measurement unit (IMU) together with the global positioning system for navigation. However, there are many technological challenges and potential disadvantages of AVs. In the scope of this research project, the challenges include artificial intelligence (AI), which is not able to function accurately in chaotic urban environments; the sensing and navigation system, which is susceptible to different types of weather conditions; and the accurate recognition and tracking of different types of obstacles [49] [50] [51] [52] [53]. The recent fatal accident of a pedestrian with a bicycle caused by an AV in Tempe, Arizona [54] demonstrates the potential limitation and challenges of this new technology. However, the research proposed in this thesis could, in theory, support and improve the detection accuracy, and will act as an added layer of safety where the autonomous technology may fail to recognise or detect cyclists. Chapter 3 gives further detail about this research.

Other systems such as infrared and ultrasonic detection systems, with or without RADAR and a camera, have also been developed and installed on trucks to increase the safety of cyclists by providing audible warnings to the driver when an object is close to the vehicle. Some of the sensing system providers, who offer

solutions for detecting objects on the near side of vehicles, include, Backwatch [55], Brigade Electronics [56] and Fusion Processing [57].

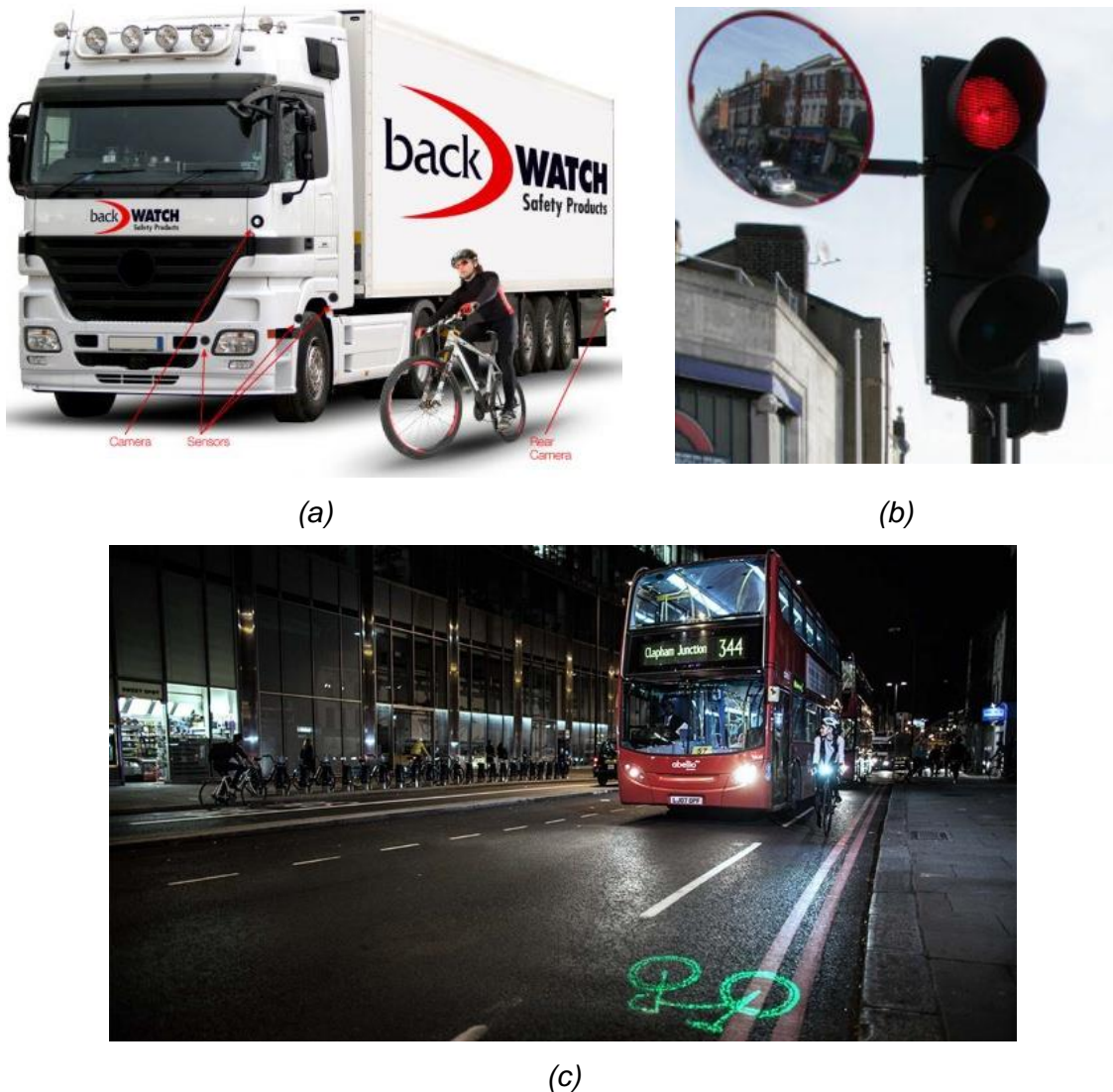


Figure 2-11: (a) Backwatch's blind spot detection system [55]; (b) Trixi traffic light mirrors (right) [41]; (c) Blaze Laserlights [58]

As illustrated in Figure 2-11 (a), the warning is purely based on the detected distance between the sensor and the object. As a result, they are found to be somewhat overly sensitive and distract the drivers unnecessarily by false alerts and found to be inaccurate in many cases, especially in urban traffic scenarios where the driver has to contend with the heavy mental burden of looking out for hazards. Therefore, these additional warnings can be distracting and counterproductive.

Additionally, passive measures such as the installation of blind-spot mirrors at junctions, have been implemented by some authorities to prevent blind spot

collisions, but their actual effectiveness in preventing accidents remains questionable [59]. On the other hand, quantitative assessment [60] and the literature review [61] of the safety impacts of intelligent transport systems do show that fatalities and injuries of vulnerable road users, including cyclists, can be reduced with existing technologies. However, the ultimate aim of this research project is to develop a more reliable and cost-effective system that would ultimately remove the potential hazards for cyclists when they are in the vicinity of vehicles and allow them to ride more safely.

2.6 Conclusions

From the literature review of the accident statistics presented in this chapter, it is clear that the pedal cycle casualties are a growing hazard seen in many cities around the world. In particular, London has seen a dramatic increase in the number of cyclists who are seriously injured as a result of collisions involving another vehicle. It is also clear from the review that although left turning manoeuvres by a large vehicle across the path of a cyclist have the highest rate of fatalities, it is not the only type of conflict for cyclists. For example, the vehicle turning right across the path of a cyclist is ranked first with 243 seriously injured casualties and two fatalities in Figure 2-5. As a result, a number of conflict scenarios exist in an urban region and the main two contributory factors are found to be the blind spots around large vehicles and careless driving as discussed in Section 2.4. Around 75 % of fatal or serious cyclist accidents take place in cities.

Many research and collaborative projects have attempted to design and develop an efficient and low-cost system to confront the issue but their results have not been taken up due to limitations in methodology and technology. Industrial research has also been conducted to detect cyclists with sensors mounted on the vehicle but most of the solutions are limited to a single field of view and they do not offer a reliable warning to the driver. In fact, most of the off-the-shelf blind spots detection systems available to drivers are found to be not very effective or intelligent. These systems are rather creating additional distractions for drivers in some traffic situations in which they may fail to spot a hazard while distracted by the safety system. Thus, this research considers each type of conflict carefully and explores a low-cost solution using existing technologies and methodologies in Chapter 3.

Chapter 3: Formulation of Cyclist 360° Alert

3.1 Introduction

In this chapter, an innovative ITS concept is formalised from the analysis of the bicycle-vehicle related collisions in Chapter 2 so that future accidents can be prevented. Section 3.2 presents the overall system architecture with key design requirements for “Cyclist 360° Alert”, a term devised to denote this new concept. Section 3.3 investigates the current localisation techniques by reviewing the measurement methods, measurement parameters and positioning techniques used in localisation systems. Section 3.4 studies how the current localisation systems work and what are the limitations of the currently available positioning systems based on wireless communication technologies (WCT) found in smart devices and common communication infrastructures found in urban areas. Section 3.5 presents a summary of localisation systems with their positioning accuracies and briefly discusses why a single positioning system alone cannot be utilised to fulfil the design requirements. Section 3.6 proposes a novel methodology to improve localisation accuracy with multi-level sensor fusion that could be employed for the Cyclist 360° Alert system. Section 3.7 discusses an implementation strategy of the overall system while Section 3.8 summarises the findings from this chapter.

3.2 Overall System Architecture & Design Requirements

It is established from the review of the accident data and studies in chapter 2 that one of the major causes of bicycle-vehicle related collisions is that drivers are unable or fail to spot cyclists from their driving position. Therefore, this research study proposes a technological solution named the “Cyclist 360° Alert”, and Figure 1-5 and Figure 3-1 illustrate one way of implementing the overall concept of the system. Given that the ultimate aims are: (1) to provide the ability to monitor the obscured regions; and (2) to provide the ability to take preventive action if a collision scenario is detected based on predicted trajectories of the vehicles. An illustration of the proposed concept is demonstrated in Figure 1-5 (b), where the four cyclists in the blind spot regions are now clearly visible to the driver on the display unit and in

Figure 1-5 (c), where a collision is avoided by using a prediction model which generates a warning message on the display unit with sounds. Furthermore, the system can be adapted to different driving styles and can be developed to notify drivers with three levels of warnings: Normal – no immediate threats, Warning – a threat maybe approaching and Alert – a threat is imminent. The three levels of warnings are illustrated in Figure 3-1 (Green and Amber warnings) and Figure 1-5 (c) (Red Alert warning).

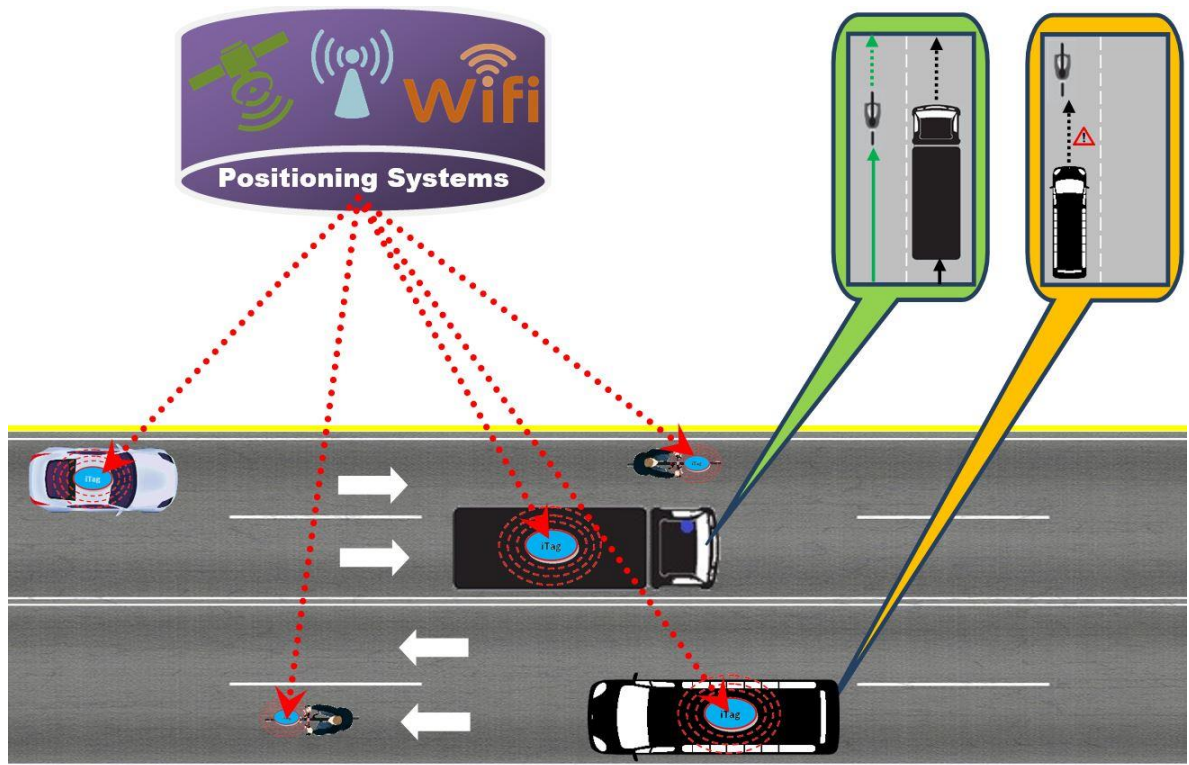


Figure 3-1: Overall system architecture of the Cyclist 360° Alert system.

The overall concept requires bicycles and vehicles to be equipped with an integrated wireless communication tag (iTag). This will incorporate a Dedicated Short-Range Communication (DSRC) system that can be used as a tracking device. The real-time signals transmitted from positioning systems such as Global Positioning System will be received by each Cycle-iTag (C-iTag) and Vehicle-iTag (V-iTag) installed on the bicycles and vehicles respectively. C-iTag will compute its current position based on a localisation method and transmit the data via cycle-to-vehicle (C2V) message transmission system. The V-iTag will also compute its current position using the C-iTag approach and employ a suitable trajectory prediction model to predict the future positions and trajectories of the cyclist and the vehicle

based on the available information. An in-vehicle display unit will be employed to give the driver a graphical representation of the cyclists' position in relation to the vehicle and to give appropriate warnings if a conflict scenario is detected by a collision prediction and warning system. The system will be developed further to brake automatically if the driver does not respond or fails to detect a hazard. The system will be integrated with additional features, such as trajectory or path modelling and non-visual interfaces (e.g. auditory and haptic feedback), so as to facilitate more effective warnings to both drivers and cyclists.

The overall system will form the Internet of Things (IoT) where cyclists and vehicles will collectively exchange data to present an augmented graphical representation of cyclists' positions in relation to vehicles' positions on roads. As a result, drivers will be able to observe the cyclists even if they are obscured by other vehicles, objects or in the blind spots regions in slow-moving traffic. The system has to work in all environmental conditions such as poor weather and dark light conditions. Hence, it has to be based on non-line-of-sight communication technologies.

Another important requirement is that the cost of the overall system has to be low so that it is affordable to be installed on bicycles and vehicles. As a result, this study proposes to develop the overall Cyclist 360° Alert system architecture based on sensors commonly found on smart devices such as smartphones and tablets and ubiquitous communication technologies found in urban areas such as Wi-Fi. A smartphone has all the capability of processing information similar to a computer but also has a number of additional modules including Wi-Fi, Bluetooth, GPS receiver and Inertial Measurement Unit (IMU) with Motion Processing Unit (MPU). According to the Ofcom Communications Market Report [62], in 2016, about 71 % of adults now own a smartphone. Hence, an app will be developed at a later stage of the project to implement the system architecture on smart devices to make the overall system as cost-effective and simple to use as possible.

Section 2.4 shows that to design an accurate collision prediction warning system, which does not give false alarms to distract the drivers unnecessarily, it is important to accurately locate the vehicles and bicycles so that future positions can be predicted more precisely. This is because any inaccuracy in the localisation of vehicles and bicycles will have implications and this is one of the major challenges

for any reliable collision avoidance and warning system. Therefore, it is important to first define the tolerable error in the positioning system as there is no error-free system currently in existence. From the Handbook [22] the minimum dynamic width required by cyclists in motion should be at least 1 m and it is greater on hills and curves. Therefore, in this study, a cyclist is considered as a point of mass and the minimum clearance around it should be at least 0.5 m radius from its actual position on the road. Thus, the tolerable positional error to satisfy the requirement of the localisation accuracy for the Cyclist 360° Alert system could be as much as ± 0.5 m.

Consequently, from the overall system architecture, the major challenge is to find a reliable positioning system or method to fulfil the ± 0.5 m localisation accuracy with technologies found in smart devices. Moreover, bicycles are significantly smaller in comparison to large vehicles, their movements are erratic, and they are able to move more freely than the vehicles. As a result, no single system currently exists to fulfil the requirements, and this may be due to the challenges stated above. This research study develops a novel method which could be utilised in Cyclist 360° Alert system by reviewing the existing localisation techniques and localisation sensor technologies in Sections 3.3 and 3.4 respectively.

3.3 Review of Localisation Techniques

The transmission of radio waves in the “real” environment is subject to many issues such as multipath, absorption, diffraction and reflection as described in [63]; the signal cannot be measured precisely. Therefore, there are many localisation algorithms which have been proposed by Farid et al. [64] and in general, they can be categorised as distance and angle estimations for coordinate localisation systems. Also available are other techniques such as proximity estimation. Because of the nature of the information provided, the exact location coordinates cannot be determined with these techniques. Hence, they are outside the scope of this project. The position estimation can be performed either directly on the signals travelling between nodes or by a two-step approach in which certain parameters are extracted from the signals first, and then the position is estimated based on those signal parameters. The two-step approach is less complex than the direct approach and the former approach offers similar performance for sufficiently high signal-to-noise ratios (SNRs) and signal bandwidths. Most practical systems employ the two-

step approach, which will be employed for this project as well. There are mainly two basic positioning techniques for an accurate localisation: lateration and angulation. There are three main measurement parameters: signal strength, propagation-time and received angle, which are used to measure the signals. Hybrid approaches that use combinations of measurement techniques are also possible with the positioning techniques. Figure 3-2 illustrates an overview of measurement techniques with the positioning estimation techniques, where the bottom level of the hierarchy shows the five different measurement methods.

3.3.1 Measurement Methods:

A review of each measurement methods is summarised below:

- **Received Signal Strength (RSS)** is a measurement method that provides information about the distance between a transmitter and a receiver based on the attenuation of a propagation path. The idea behind this method is that if the relation between distance and power loss is known, the RSS measurement at the receiver can be used to estimate the distance between the receiver and the transmitter. However, in order to apply this method successfully the transmission power has to be known beforehand. The total attenuation of signal propagation through the path then can be computed by subtracting the received power from the transmitted power. In general, the attenuation of a signal can be found from the theory that the intensity of received signal strength in electromagnetic waves is inversely proportional to the square of the distance from the source. Thus, this can be employed to estimate the distance between the sender and receiver.

- **Time of Arrival (TOA)**, often also known as Time of Flight (TOF), is a measurement method that provides information regarding distance by estimating the time of flight of a signal that travels from a transmitter to a receiver. In other words, this method employs the delay time between the transmission of a signal from one point to another. Synchronisation is required in order to prevent ambiguity in TOA estimation. It is generally assumed that all electromagnetic waves travel at the speed of light. Although this speed is only true in the case of a vacuum and the speed is different for all other material when they pass through, the principle can be applied to compute the distance between transmitter and

receiver by a simple multiplication of the TOF with the speed of light. There are two approaches to implementing this method. One of them is to use a transmitter to send a signal to many receivers, where all the receivers measure the TOF and transmit this information to a central system which computes the distance. The other approach is to use many transmitters to send signals to a single receiver. The receiver measures the TOFs of all the signals and computes comparison in the receiver system. However, there might be technical issues with this approach as all transmitters must be synchronised in order for them to transmit signals among certain time segments, and if the signal propagation time is exactly equal to the duration of time segment then signals might be lost owing to multiple signals being received concurrently.

- **Time Difference of Arrival (TDOA)** is an enhancement of the above method to avoid synchronisation difficulty and packet loss issues. In order to implement TDOA, a transmitter is required to transmit two dissimilar signals with different propagation speeds. When the two signals are received at the receiver, the difference of arrival times between two signals can be measured. Using the difference of arrival times, time of flight (TOF) of a signal can be found, and it is exactly equal to the propagation time of a signal.

- **Roundtrip-time of Flight (RTOF)** is a method for finding the distance between transmitter and receiver from the length of time it took for a signal to travel back and forth to the transmitter. In other words, the transmitter transmits a signal to a receiver which then transmits an acknowledgement signal back to the source. Thus, this time delay consists of the propagation times between two points of a signal and it can be divided in half and multiplied with the speed of light to compute the distance between them.

- **Angle of Arrival (AOA)** is a measurement method that provides information regarding the direction of the receiving signal; the angle of arrival of a received signal between the transmitter and receiver can be determined using this method. Generally, antenna arrays are employed to measure the AOA of a signal. The angle information is determined at the antenna arrays by employing TDOA at individual elements but this TDOA measurement is completed by measuring the

difference in received phase at each element in the antenna array and the delay of arrival at each element is measured directly and converted to an AOA measurement.

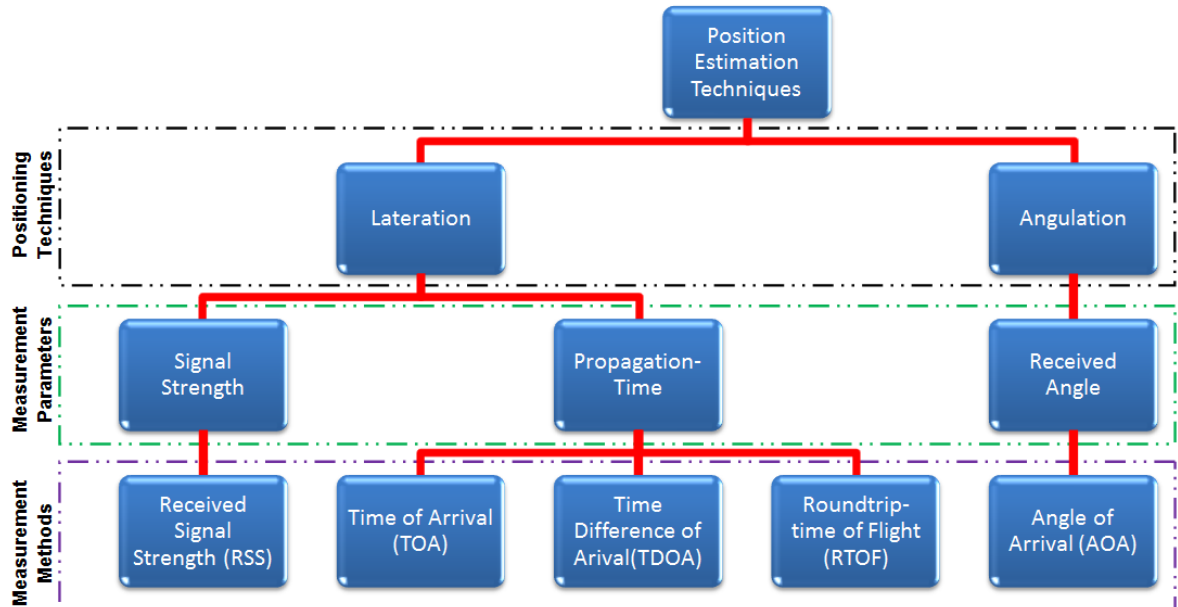


Figure 3-2: Classification of localisation techniques.

3.3.2 Positioning Techniques

As with the two-step approach stated previously, a measurement method alone cannot be employed to determine the precise coordinates or location of an object as the measurement only provides information about the distance or angle to it. Therefore, positioning techniques are used for localisation of an object and they can be divided into two categories: fingerprinting (mapping) and geometric or statistical techniques. A fingerprinting technique involves a database that contains signal measurements at known positions that had been surveyed beforehand. On the other hand, a geometric technique employs only the measurement parameters. Due to the nature of this project where the environmental characteristics would vary from place to place, only the latter technique will be explored and in this technique, there are mainly two basic approaches: triangulation and trilateration. These two approaches are discussed below:

- **Triangulation** estimation is a trigonometric approach which determines an unknown location of an object based on knowing two absolute angles to it from at least two known stations set at either end of a fixed baseline, and a distance

between them. Figure 3-3 illustrates the idea of triangulation, where S_1 and S_2 are the reference stations, T is the object with the unknown location, d_T is the distance between the object and the fixed baseline, and d_s is the distance between the stations. In this approach, the distance between the stations must be known in advance in order to compute the position of the target object T . Based on the basic triangulation with the trigonometric relationships illustrated below, Equation (3.5) can be used to determine the position of an object on a single axis. A similar procedure can be followed to determine the other axis with another baseline at the horizontal plane.

With reference to Figure 3-3, the formula can be developed as follows:

$$d_s = \frac{d_T}{\tan(\alpha)} + \frac{d_T}{\tan(\beta)} \quad (3.1)$$

Using trigonometric identity, the above equation can be written as:

$$\frac{d_s}{d_T} = \left(\frac{\cos(\alpha)}{\sin(\alpha)} + \frac{\cos(\beta)}{\sin(\beta)} \right) = \frac{\cos(\alpha) \cdot \sin(\beta) + \sin(\alpha) \cdot \cos(\beta)}{\sin(\alpha) \cdot \sin(\beta)} \quad (3.2)$$

Thus, using the trigonometric identity: $\sin(\alpha + \beta) = \sin(\alpha) \cdot \cos(\beta) + \cos(\alpha) \cdot \sin(\beta)$, the above equation can be simplified as below:

$$d_T = d_s \cdot \frac{\sin(\alpha) \cdot \sin(\beta)}{\sin(\alpha + \beta)} \quad (3.3)$$

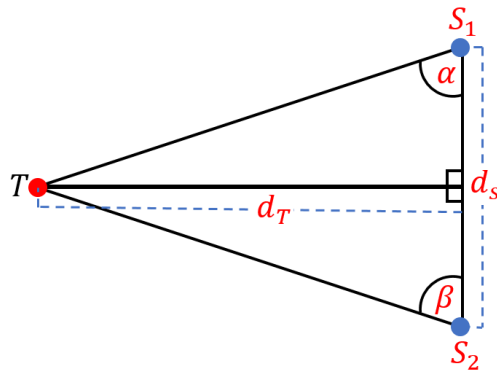


Figure 3-3: Triangulation approach.

- **Trilateration** estimation is an approach used to find the unknown location of an object by measurement of distances from several reference stations. In contrast with triangulation, trilateration does not involve the measurement of angles. In other words, instead of measuring the angles from reference stations to the target object, trilateration employs the distances between the reference stations and the

unknown location and these distances are considered as the radii of as many circles as the reference stations with centres at every one of them. Therefore, the unknown location lies at the intersection of all the circles. In this method, a minimum of three reference stations are required with the distances to the target object T_1 and coordinates of the three stations to determine the coordinates of the unknown location in two-dimensional space. The diagram below illustrates the idea of trilateration.

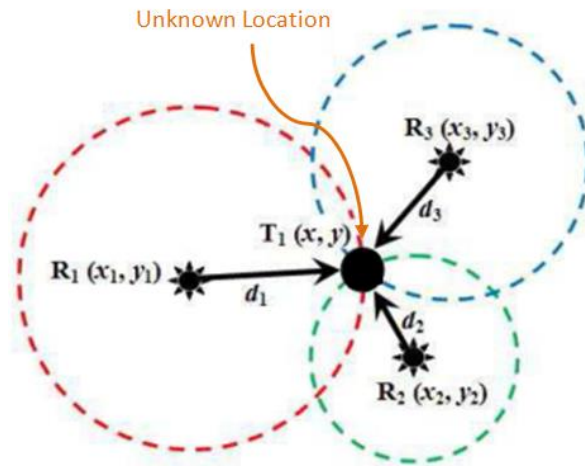


Figure 3-4: Trilateration approach – Intersection of circles.

The Pythagorean Theorem can be used to determine the intersection of the three circles and formulate the following three equations:

$$d_1^2 = (x_1 - x)^2 + (y_1 - y)^2 \quad (3.4)$$

$$d_2^2 = (x_2 - x)^2 + (y_2 - y)^2 \quad (3.5)$$

$$d_3^2 = (x_3 - x)^2 + (y_3 - y)^2 \quad (3.6)$$

The above equations can be rearranged to solve for x and y for the unknown location of the object as follows:

$$x = \frac{\alpha(y_3 - y_2) + \beta(x_1 - x_3) + \gamma(y_2 - y_1)}{2(x_1(y_3 - y_2) + x_2(y_1 - y_3) + x_3(y_2 - y_1))} \quad (3.7)$$

$$y = \frac{\alpha(x_3 - x_2) + \beta(y_1 - y_3) + \gamma(x_2 - x_1)}{2(y_1(x_3 - x_2) + y_2(x_1 - x_3) + y_3(x_2 - x_1))} \quad (3.8)$$

Where,

$$\alpha = (x_1^2 + y_1^2 - d_1^2), \beta = (x_2^2 + y_2^2 - d_2^2), \gamma = (x_3^2 + y_3^2 - d_3^2) \quad (3.9)$$

3.4 Review of Common Localisation Technologies

To localise an object uniquely, a localisation system requires transmitters and at least one receiver. The following subsections review positioning systems based on satellite technologies that are available globally, and also review two other communication technologies widely found in urban areas and in smartphones which can be employed to localise smart devices. An extensive study was also conducted on other technologies such as Radio-frequency identification (RFID), Ultra-wideband and Bluetooth that could be used as measurement methods for localisation systems. However, since these technologies are not commonly available in local infrastructures or have restrictions on the range or have restrictions their use, they are not included in the chapter.

3.4.1 Global Navigation Satellite System (GNSS)

3.4.1.1 General System Overview

There are four kinds of satellite-based navigation systems currently in existence and these are the Global Positioning System (GPS), “Globalnaya navigatsionnaya sputnikovaya sistema” (GLONASS), Galileo and COMPASS. However, only two of the systems are in operation: the GPS and GLONASS, and they are operated and maintained by the US Department of Defence and the Russian Aerospace Defence Forces respectively. The Galileo is currently being built by the European Union (EU) and European Space Agency (ESA). Similarly, the COMPASS is also under construction by China. In the scope of this thesis, only the GPS technology is reviewed as it is widely used in the EU, but the primary principle of all satellite-based navigation systems remains the same.

The GPS is a satellite-based navigation system that consists of a network of a minimum of twenty-four satellites orbiting around the earth where at least six satellites are always visible to a receiver on the ground from almost everywhere on the Earth's surface [65]. Figure 3-5 (left) illustrates a GPS satellite constellation that covers the complete earth's surface. The operation of GPS depends on a very accurate time reference, which is provided by atomic clocks on board the satellites. A GPS receiver device on or near the surface of the earth at any moment of time can be used to obtain the current location and time information. The complete

system is designed to operate in all weather conditions, but the receiver device must have access to at least four satellites with unobstructed line-of-sight (LOS) to them. Although the system was originally intended for military applications, the system can be used by anyone with a GPS receiver without any subscription fees or setup charges. The messages are transmitted on two separate carrier frequencies that are common to all satellites in the network: 1.57542 GHz (L1 signal) and 1.2276 GHz (L2 signal). The messages are also encoded using two different encodings: one for the public that enables low-resolution navigation and the other for U.S. military use, that is encrypted. Although the signal travels at the speed of light, it still takes some measurable time to arrive at the ground receiver. Thus, this principle can be used to determine the receiver's location.

3.4.1.2 GPS Localisation Method

GPS satellites orbit the earth roughly every 12 hours at an approximate height above the sea level of 20,000 km. The atomic clocks in each satellite continuously generate and broadcast a unique coded signal. Concurrently, the receiver on the ground generates the same coded signal for each satellite and the receiver compares the received code with the one being generated. The time difference between the two codes indicates the TOF between the satellite and the receiver. Thus, this information is translated into a distance between the satellite and the receiver using the speed of light as portrayed in Equation (3.10). Each distance to the satellite from the receiver is the radius of a sphere where the receiver is assumed to be on the surface and the satellite is at the centre of the sphere. However, for simplicity, the diagram in Figure 3-5(b) illustrates circles instead of spheres and each radius represents the distance to the satellite. As can be seen from the diagram, only three satellites are needed to reduce the possible position of the device to a single region where three circles intersect each other, similar to the trilateration approach discussed in Section 3.3.2.

$$\text{Range to satellite } (d) = \text{signal travel time } (t) \times \text{speed of light } (c) \quad (3.10)$$

Since each satellite generates a unique coded signal, and this enables distances or pseudo-ranges to several satellites to be computed simultaneously. Nevertheless, to precisely determine the TOF, the receiver must also have a very accurate time

reference but, in general, the receiver cannot house an atomic clock as it would be impracticable and very expensive. Therefore, the fourth satellite is used to adjust the internal clock of the receiver unit. The receiver on the ground scans and then locks onto signals from a number of GPS satellites. The receiver also knows the position coordinates of each of the GPS satellites. Hence, if the distances to at least four satellites are known, the position of the receiver can be computed.

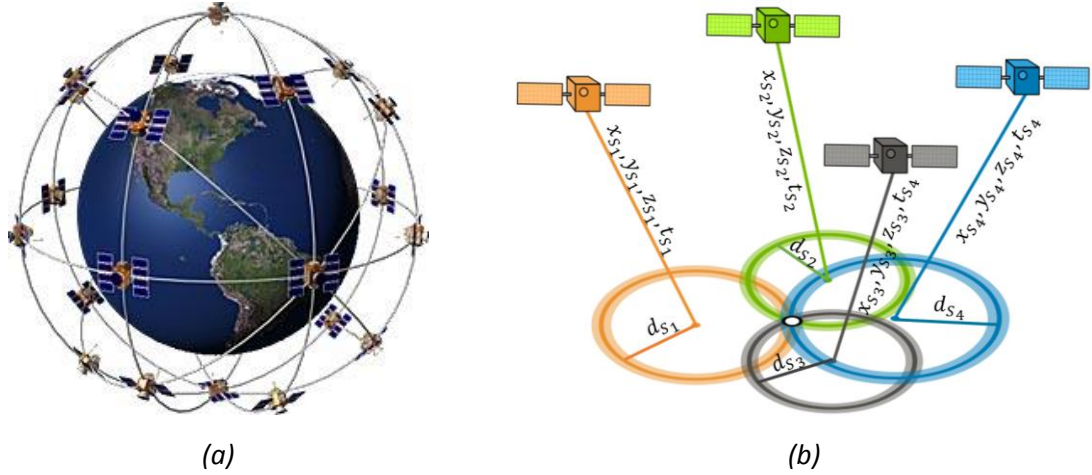


Figure 3-5: (a) Satellite Constellation and (b) Intersection of the spheres.

To simplify the problem, from the description above, it can be assumed that each GPS satellite transmits messages that include the time the message was transmitted and the satellite position at the time of message transmission to the receiver on the ground. As a result, the position of the receiver can be estimated by solving the following four sets of equations simultaneously and rearranging them to find the unknown coordinates like the trilateration method described Section 3.3.2.

$$d_{s_1} = c(t_{s_1} - R_{t_1} + C_t) = \sqrt{(x_{s_1} - x_r)^2 + (y_{s_1} - y_r)^2 + (z_{s_1} - z_r)^2} \quad (3.11)$$

$$d_{s_2} = c(t_{s_2} - R_{t_2} + C_t) = \sqrt{(x_{s_2} - x_r)^2 + (y_{s_2} - y_r)^2 + (z_{s_2} - z_r)^2} \quad (3.12)$$

$$d_{s_3} = c(t_{s_3} - R_{t_3} + C_t) = \sqrt{(x_{s_3} - x_r)^2 + (y_{s_3} - y_r)^2 + (z_{s_3} - z_r)^2} \quad (3.13)$$

$$d_{s_4} = c(t_{s_4} - R_{t_4} + C_t) = \sqrt{(x_{s_4} - x_r)^2 + (y_{s_4} - y_r)^2 + (z_{s_4} - z_r)^2} \quad (3.14)$$

where:

- $d_{s_1}, d_{s_2}, d_{s_3}$ & d_{s_4} are the associated distances for each of the satellites
- c is the speed of light (3×10^8 m/s)

- $t_{s_1}, t_{s_2}, t_{s_3}$ & t_{s_4} are the associated message transmitted time for each of the satellites
- $R_{t_1}, R_{t_2}, R_{t_3}$ & R_{t_4} are the associated message received time
- C_t is the unknown time correction for the GPS receiver's clock
- $x_{s_1}, y_{s_1}, z_{s_1}$ etc are the coordinates of the associated GPS satellites
- x_r, y_r, z_r are the unknown coordinates of the receiver

Some more advanced methods described in [66] [67] can also be employed to improve the positioning accuracy but these methods can only produce approximations of the actual position, and they cannot filter all the errors such as multipath and frame losses.

3.4.1.3 Error Associated with GPS

The position information obtained by the GPS receiver is far from perfect mainly due to timing errors. Although signals travel at the speed of light in vacuum, when they pass through the earth's ionosphere and troposphere they are slowed down and bent. Thus, they take considerably more time to reach the receiver. In other words, the signals do not arrive at the receiver in a straight path but in a zigzag formation. These cause an error in the computation of the true flight time of the signals travelling from the satellite to the receiver and it is known as the propagation delay. The signals' travel times are also increased by refraction and diffraction when they reflect from buildings, hills trees and water, and this is known as multipath. There are other internal delays such as those caused by impurities in the electrical components. As the distances to the satellites are computed using the speed of light, a time inaccuracy of 10 nanoseconds (ns) leads to position errors of 3 m. However, the time inaccuracies encountered in urban areas usually are much greater than 10 ns, so position errors can be very significant.

3.4.1.4 Differential Global Positioning System (DGPS)

A technique known as the Differential Global Positioning System (DGPS) can be used to compensate for some of the errors in measurement of time that are caused by propagation delay discussed above. In this system, GPS signals as well as differential signals from a base station are received. In Figure 3-6, the ground-based station receives the same GPS signals as the receivers but the procedure is reversed. The ground-based reference station knows its exact location at all times; it uses this information to determine the theoretical flight time for each of the

satellites visible to the ground-based station. This differential signal is then retransmitted with another carrier frequency to the roving receiver which then uses this information to correct the distances. This system can be expensive mainly due to the requirement of special hardware for the ground-based station and the roving receiver and it is impracticable for the scope of this project.

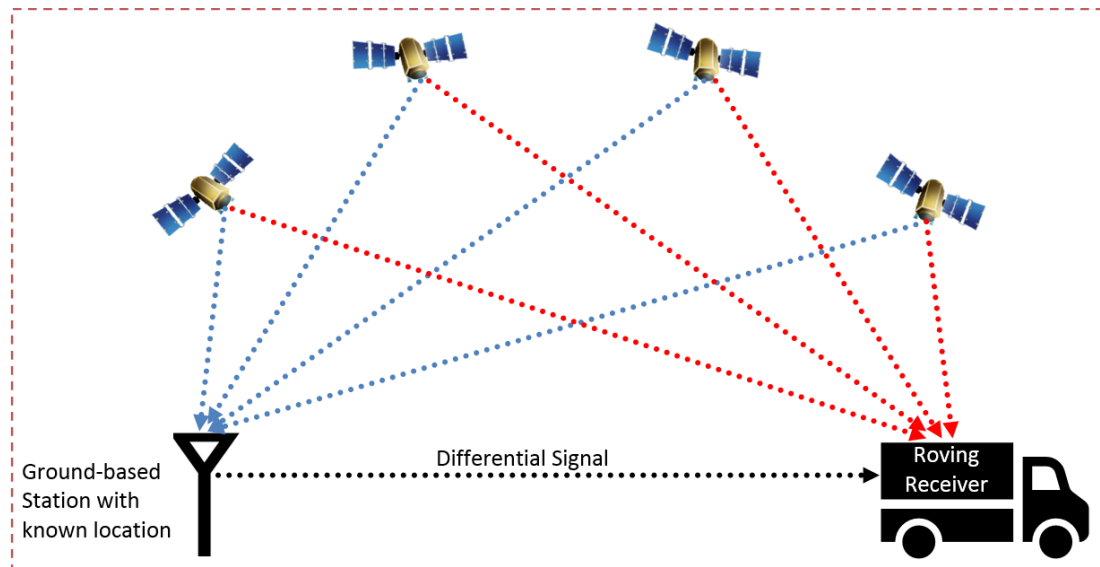


Figure 3-6: DGPS operation principal.

3.4.2 Wi-Fi Positioning System (WPS)

3.4.2.1 General System Overview

A wireless access point (WAP) is a networking hardware device that acts as a wireless node for transmitting and receiving information using Wireless Fidelity (Wi-Fi) protocols. This technology, with its Wi-Fi hotspots for public wireless, has grown rapidly in the early 21st century and it is widely available in urban areas. The Wi-Fi Alliance is a non-profit international association formed in 1999 to certify interoperability of Wireless Local Area Network (WLAN) products based on the Institute of Electrical and Electronics Engineers (IEEE) 802.11x wireless standards. The Wi-Fi is a popular technology that utilises radio waves to provide wireless high-speed network and Internet connections. Initially, the Wi-Fi 802.11b standard was only used for the radio frequency band 2.4 GHz to exchange data wirelessly at a maximum raw data of 11Mbps. However, the Wi-Fi Alliance has expanded the generic use of the Wi-Fi term to include any type of network or WLAN products which are based on 802.11 standards. In other words, it now includes all the

standards such as 5 GHz for 802.11a and 2.4GHz for 802.11g. As a result, it allows electronic devices to exchange data wirelessly using a radio frequency bands 2.4 GHz, 3.6 GHz or 5 GHz over a network.

As illustrated in Figure 3-7, the main use of the Wi-Fi technology is to share the Internet connection among all the compatible devices such as video game consoles, mobiles and computers which are capable of using this technology. These devices can not only use the internet but can also share resources or communicate with each other within the local area network (LAN) or wide area network (WAN). In other words, a Wi-Fi Access Point (WAP) creates a small network zone where devices can access Internet connection or share resources among themselves wirelessly. Therefore, by utilising WAP, the Wi-Fi device location within the Wi-Fi coverage can be positioned with a certain degree of accuracy and this method is widely employed in indoor positioning systems where GNSS is inadequate. Additionally, a coverage range for Wi-Fi APs varies depending on the environmental characteristics and the frequency band used. The range is also limited by local regulations and antenna type. For instance, in the EU the maximum equivalent isotropically radiated power (EIRP) that a Wi-Fi device can transmit is limited to 20 dBm (100 mW) for 2.4GHz [68].

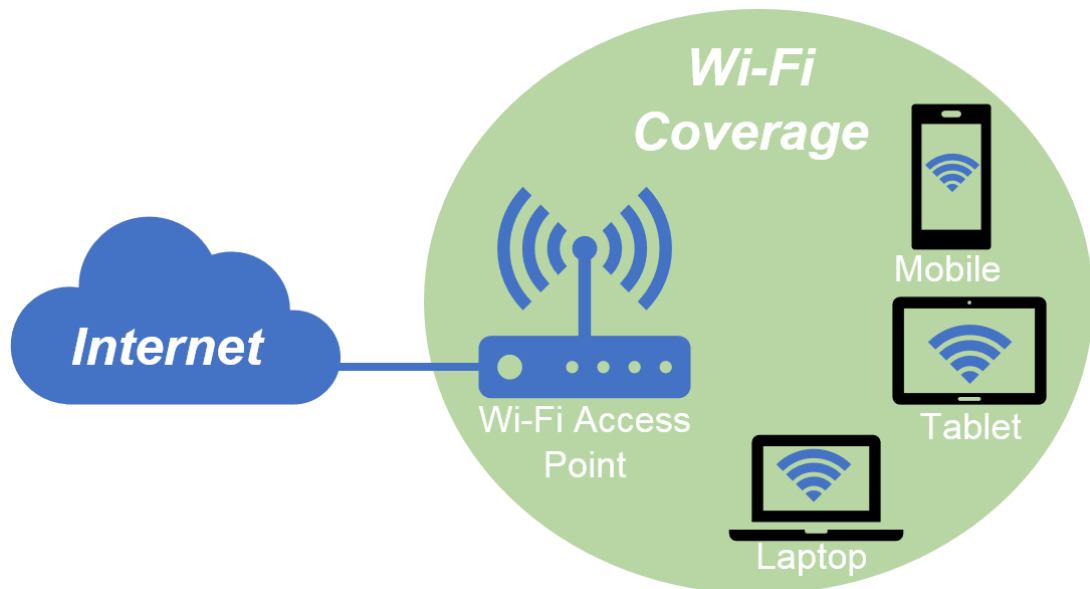


Figure 3-7: Wi-Fi network configuration.

3.4.2.2 RSS-Based Distance Approximation

At present, the three main measurement methods that can be used to compute the distance between a mobile device and the Wi-Fi AP are the RSS, AOA and TOF. However, as demonstrated in the literature [69] [70] [71], the most common and widespread localisation technique is based on RSS. This is because the IEEE 802.11 system incorporates an RSS indicator (RSSI) that measures the received power level and the measurements can be easily utilised to calculate the distance between the transmitter and receiver as demonstrated below.

There are mainly three types of RSS signal propagation models for wireless sensor networks (WSNs): Free Space Path Loss Model (FSPLM), log-distance path loss model and site-specific model based on ray tracing. Here, only the FSPLM is considered for the purpose of demonstration of the method. The FSPLM is the loss of signal strength that occurs from a line-of-sight path through free space, usually air, of an electromagnetic wave. Thus, this model assumes that reflection or diffraction that could be caused by a nearby obstacle or any other factors such as hardware imperfections do not occur.

As with all electromagnetic waves, the intensity of received signal strength is inversely proportional to the square of the distance from the source. Hence, the following equation is formed, and this can be utilised to find the model for mapping RSS measurements to distance estimates.

$$Intensity \propto \frac{1}{Distance (d)^2} \quad (3.15)$$

A line-of-sight free space path loss is proportional to the square of the distance between the transmitter and receiver and inversely proportional to the square of the signal wavelength. Thus, Equation (3.16) can be applied to compute the free space path loss (PL) of a signal, where λ is the wavelength, d is the distance between the transmitter and the receiver, f is the frequency of the radio signal and c is the speed of light.

$$PL = \left(\frac{4\pi d}{\lambda}\right)^2 = \left(\frac{4\pi d f}{c}\right)^2 \quad (3.16)$$

The power of a signal is usually measured in decibels (dB); thus, the above path attenuation can be represented in dB as follows:

$$PL_{dB} = 10 \log_{10} \left(\frac{4\pi df}{c} \right)^2 = 20 \log_{10} \left(\frac{4\pi df}{c} \right) \quad (3.17)$$

Thus, the simplified RSS localisation model using the path loss is given by the following formula, which can be found in the literature [72] [73] [74].

$$RSS = T_p - PL_{dB} \quad (3.18)$$

where, RSS is the received signal strength in [dBm] and T_p is the transmitter output signal strength in [dBm].

The above Equation (3.18) can be solved for d to compute the distance between a Wi-Fi AP and a mobile device within the Wi-Fi zone, and it is portrayed by the equation below.

$$d = \frac{c \times 10^{\left(\frac{T_p - RSS}{20}\right)}}{4\pi f} \quad (3.19)$$

3.4.2.3 WPS Localisation Method

Unlike GPS, Wi-Fi APs were not originally designed for positioning, hence, the receiver does not know the location of the APs. As a result, WPS requires a database with known geolocation of the Wi-Fi hotspots so that a mobile device can be localised with known distances to the Wi-Fi APs and by utilising the trilateration method discussed in Section 3.3.2.

A Wi-Fi AP periodically broadcasts its Service Set Identifiers (SSID), also known as the wireless network name, using a special 802.11 Media Access Control (MAC) management frame known as a beacon frame. As illustrated in Figure 3-8(a), from the frame, a mobile device can extract the header information which contains the unique address for the Wi-Fi AP. Thus, as shown in Figure 3-8(b), a mobile device capable of using Wi-Fi protocols can easily sense all the nearby Wi-Fi APs and gather the SSIDs to find the unique MAC addresses. Hence, the device can use the information to fetch the associated coordinates of all visible APs in a database where the APs are previously mapped using a survey. Then utilising the RSSI with a model such as the FSPLM, the relative distances to the APs can be found and then a mobile device can compute its position using the trilateration.

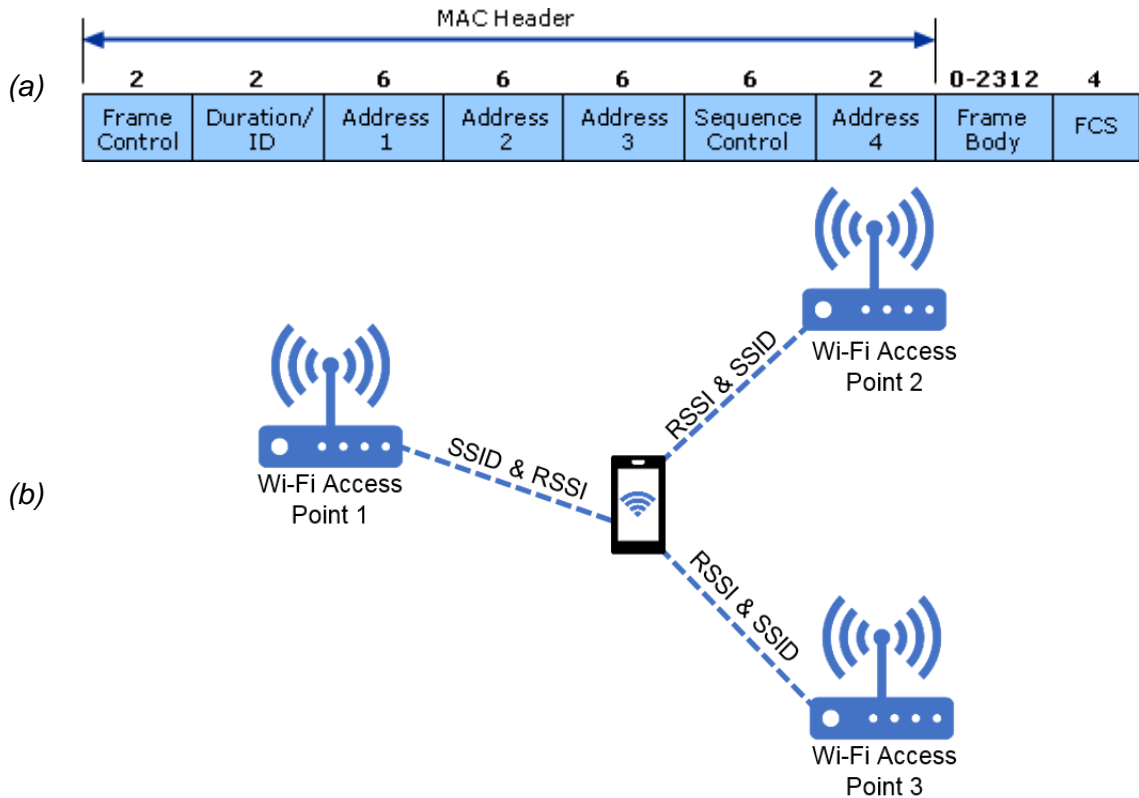


Figure 3-8: (a) 802.11 MAC frame format [75], (b) WPS operation principle.

3.4.2.4 Error Associated with WPS

Using the described methodology above, in theory, only three APs are required to compute the absolute coordinate of the device. However, in reality, it is impossible to compute the precise distances between visible nearby APs and a mobile device purely based on RSS. This is because, a radio signal is subject to many issues, given in Section 3.3, which may result in signal fluctuations and these can lead to increase in positional errors of the device.

Another type of error may occur from the method of a survey of the Wi-Fi APs, in order to assign them with geolocations and to add to a database. The mapping of the APs usually requires a device with both GPS and Wi-Fi. The location of the device is first determined by the GPS and then the device senses the neighbouring Wi-Fi APs' SSID together with RSS. This information is later used to assign approximate position coordinates of the APs based on RSS and then the coordinates are stored in a Wi-Fi hotspot database. Moreover, in some cases, coordinates from the GPS are assigned directly (without measurements of RSS) to the neighbouring Wi-Fi APs of the mapping device. Therefore, inaccuracies can also

occur from the initial mapping method applied to locate the APs and accuracy of WPS can fluctuate up to the coverage range of the WAP.

3.4.3 Cell Towers Positioning System (CTPS)

3.4.3.1 General System Overview

A cell tower is a mobile telephone system site where antennae and electronic communications are located and a typical setup of the system with further definitions is given in [76]. Especially in the context of urban areas, the location of a cell tower is often known as a base station (BS) which serves as a fixed point of wireless communication for mobile phones on a carrier network. A cellular network or mobile network is formed by distributing the base stations over regions called cells. Typically, a cell is arranged to use a set of radio frequencies different from those in neighbouring cells to avoid radio interference. An example of BS arrangement in an urban area is illustrated in Figure 3-9(a) where hexagons are used to show the division among the cells. Hence, combining the cells enables a large number of portable devices to communicate with the network and provides radio coverage over a large region such as a city.

Global System for Mobile Communications (GSM) is a wireless system standard for digital cellular technology [77] that describes the protocols used by mobile phones and allows them to connect the network by searching for cells near the phones. There are a number of different carrier frequencies used in the GSM networks such as 900 MHz, 1800 MHz and 1900 MHz. Each frequency is divided into timeslots to be used by an individual phone to communicate with the network during voice and data transfer. Moreover, there are currently five different cell sizes in a GSM network such as Macrocell, Microcell and Picocell, hence the coverage range of each BS varies depending on the cell type. Similar to Wi-Fi, mobile telecommunications technology has grown rapidly in the 21st century and it is continually evolving. Also, the technology is available throughout urban areas even where GPS signals may be out of reach or poor. There are a number of mobile technology standards for sending voice, multimedia data and signalling data between mobile phones and base stations which can be found in [78] but they are not discussed here as they are beyond the scope of this review.

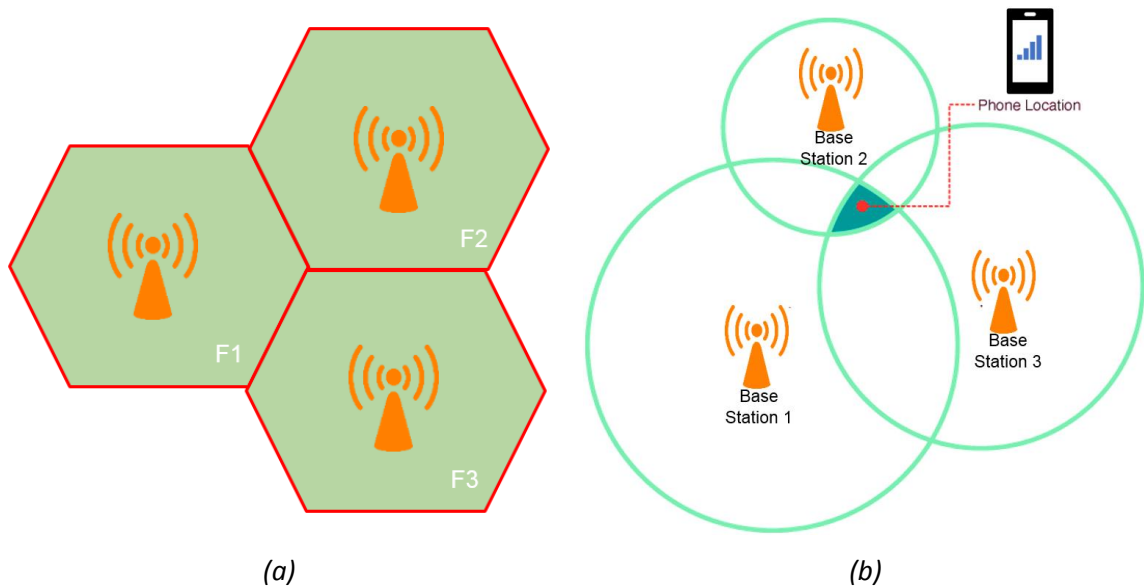


Figure 3-9: (a) Typical cells arrangement in a cellular network and (b) CTPS operation principle.

3.4.3.2 CTPS Localisation Method

In simple terms, a BS creates a radio coverage zone that most often allows greater range than the Wi-Fi AP discussed in the previous section, where mobile devices can connect and communicate with the network wirelessly. Furthermore, some of the BS incorporates a GPS receiver for timing such as in Code-Division Multiple Access (CDMA) method [79] where transmissions must be precisely synchronised. Thus, it is possible to accurately localise a mobile device but unlike GPS, base stations do not transmit very accurate timestamp messages. Instead from the BS broadcast messages, it is possible to extract the Mobile Country Code (MCC), Mobile Network Code (MNC), Location Area Code (LAC) and Cell ID (CID) using a simple app such as Netmonitor [80]. This information then can be used to search the coordinates of the cell tower in a database such as OpenCellid [81], which documents cell towers and Wi-Fi APs around the world along with their locations. Typically, in cities, a mobile network is fabricated with smaller cellular base station cells such Femtocell which has a typical range of 10m or less. This means a mobile device location can be approximated even with one cell within an accuracy of 10m or less. On the other hand, if the mobile device can sense the neighbouring cells and measure the RSS or RTOF, then the device position can be estimated with a greater accuracy using the described trilateration technique in Section 3.3.2 and Cell Phone Triangulation [82]. An operation principle of the cell tower positioning

system using three base stations and RSS is illustrated in Figure 3-9(b), which is similar to WPS.

3.4.3.3 Error Associated with CTPS

Since CTPS and WPS operate similarly, they also share similar errors described in Section 3.4.2.4. In other words, a survey is needed to record the cell tower coordinates with the parameters such as Cell ID and this survey is often conducted using a GPS receiver, which is not very accurate. However, in theory, the accuracy of CTPS can be improved as the base stations are normally located in fixed sites so the exact position of the stations can be assigned. On the other hand, errors associated with distances to the stations cannot be removed entirely due to measurement errors. It is also possible that a mobile device may not always see three base stations simultaneously which is required in order to confine the device location to a single position.

3.5 Summary of Localisation Technologies

A number of other wireless communication technologies such as ZigBee [83], Bluetooth [84] and Visible Light Communication [85] that can also be utilised as localisation systems were identified and reviewed as part of this study. Although some of these technologies are included in smartphones such as Bluetooth, they are not widely available in local infrastructure in urban areas. As a result, they cannot currently be used. In addition, a review of traffic monitoring infrastructures in London [86] found that some of the traffic sensing technologies can be used to detect cyclists but from this study, it can be concluded that existing traffic monitoring infrastructures are not capable of tracking an individual cyclist with a good positioning accuracy.

Moreover, from the review of the three common localisation technologies widely employed to localise smartphones, which are also summarised in Table 3.1 below, it has been found that although most of them such as GPS can be utilised to estimate the position, these technologies do not provide sufficiently high resolution and accuracy to locate a bicycle with the design requirement for this project. A technology, on the other hand, that could satisfy the technical requirement is Ultra-wideband (UWB) [87] [88]. An Ultra-wideband positioning system (UWBPS) can provide a maximum accuracy of 30 cm and there are a few commercial systems

available such as Dart UWB Technology [89] and Ubisense Series 7000 IP Sensors [90]. However, current legislation restricts Ultra-wideband to indoor use only [91], in order to prevent harmful interference with other radio wave communications.

Table 3.1: Summary of common localisation technologies including UWBPS.

Parameters:	GPS:	WPS:	CTPS:	UWBPS:
Coverage Range:	worldwide	Maximum 90-100m for each Wi-Fi AP	Macrocell: <35km Microcell: <2km Picocell: <200m Femtocell: <10m	<100m for each station
Approximate Accuracy:	5-10m possible but varies depending on the condition	1-2m possible but errors can increase	<10m Possible but differs depending on the cell type	30cm possible
Frequency Bands:	L1: 1575.42MHz	2.4GHz 3.6GHz 5Ghz	GSM 900 MHz GSM 1800 MHz GSM 1900 MHz UMTS 2100 MHz	3.1GHz to 10.6 GHz
Interference:	Signal interference, jamming and multipath	Interference at 2.4GHz (ISM) with other devices	Noise Other Mobiles	Bluetooth GSM
Bandwidth or Channel:	24MHz	20MHz (802.11n: 40MHz)	<30MHz	500 MHz
Sample or Data rate:	50bps	1Mbps 2Mbps 11Mbps 54Mbps	8 full channels per radio frequency: 270 kbps	110Mbps 480Mbps
Antenna type:	Requires Line-Of-Sight for better accuracy	Omi-directional	Omi-directional	Omi-directional
Measurement Method:	TOA	RSS, TDOA, TOA & RTOF	RSS & TDOA	TDOA, TOA & RTOF
Cost:	Low	Low	Low	High
Latency:	50-100ms	~1s	<1s	~50ms

As from the summary above, a single localisation technology alone cannot be utilised to track a bicycle with the positioning accuracy required for the Cyclist 360° Alert. Instead, a hybrid localisation system approach has to be adopted.

3.6 Proposed Approach for Cyclist 360° Alert System

A hybrid approach, where using two or three positioning data are fused together, needs to be adopted so that localisation accuracy and reliability can be improved. Figure 3-10 illustrates a method which can be integrated to Cyclist 360° Alert to estimate the exact position of cyclists or vehicles.

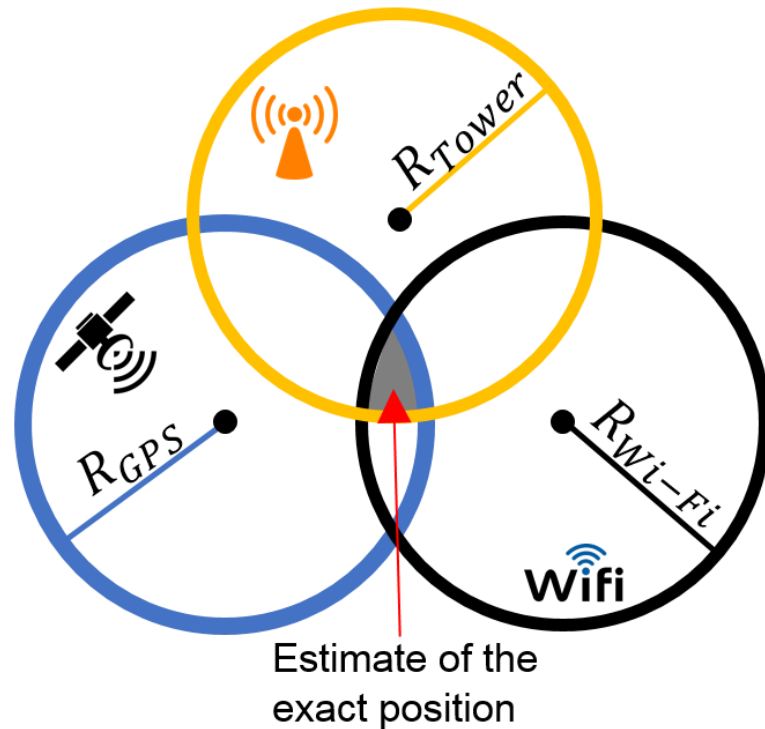


Figure 3-10: Hybrid localisation approach.

In the above diagram, the black dots represent the inaccurate position from GPS, WPS and CTPS, and each radius, R , to the circle represents the accuracy of the positioning system. Since the circles and radii are subject to measurement errors, the circles overlap in an area rather than intersecting at a single point. Therefore, trilateration method described in Section 3.3.2 cannot be applied directly, instead, an enhanced method is required. There are mainly two options available: one method is to compute the position using least squares algorithms described in [92], and the other method is to use circle intersections with clustering presented in [93]. Apart from this, a number of collective samples can be taken to minimise the measurement errors while objects are stationary so as to improve accuracy.

However, the above method is only appropriate to estimate the position when cyclists and vehicles are stationary or travelling very slowly. This is because when they are in motion, signals received by the smartphone from WAP and cell towers will fluctuate extensively. Moreover, extracting SSID or Cell ID and measuring RSS for Wi-Fi hotspots and cell towers take considerable computational time. As a result, localisation precision will be decreased even further. Moreover, the position data gathered from each of the three positioning systems will not be in synchronised form, causing a greater inaccuracy. Also, the measurement noise in an urban traffic

situation is likely to fluctuate even when the object is stationary, and this may cause the calculated position to jump from one location to another in a random manner.

Figure 3-11 proposes a novel method that can be employed to improve localisation accuracy for cyclists even when cyclists are in motion. This method utilises the relative position of the bicycle from its motion and fuses the data with GPS, WAP and CTPS when their measurements are available. The method assumes that no two-sensory system has exactly the same errors. For example, GPS measurements of the absolute position of the cyclist are noisy and measurements of a relative position from the object's motion are prone to drift. Therefore, fusing the measurements with an appropriate method can improve localisation accuracy that will be suitable for Cyclist 360° Alert system. The system block diagram illustrated in Figure 3-11 utilises existing local and global positioning systems to compute the absolute position of vehicles and bicycles by utilising a multi-level sensor fusion technique briefly described below:

- **Local Infrastructure:** Wi-Fi APs broadcast their SSIDs to iTags and they then extract unique MAC addresses of each WAPs and fetch WAPs' coordinates from a database. Simultaneously, the iTags measure RSS from each of the detected WAPs and convert the measurements into distances. The position is then estimated using suitable trilateration algorithms. A very similar approach is applied to estimate the position of the iTags using cell towers.
- **Global Infrastructure:** GPS broadcasts signals to iTags which then translate the data and computes iTags' current positions using the method described in Section 3.4.1.2.
- **On-board Sensor System:** Sensors measure various kinematic parameters to compute the relative position of the object with an update frequency higher than the above systems. This data is then fused along with the positioning data based on RSS and GPS signals to estimate the exact position.

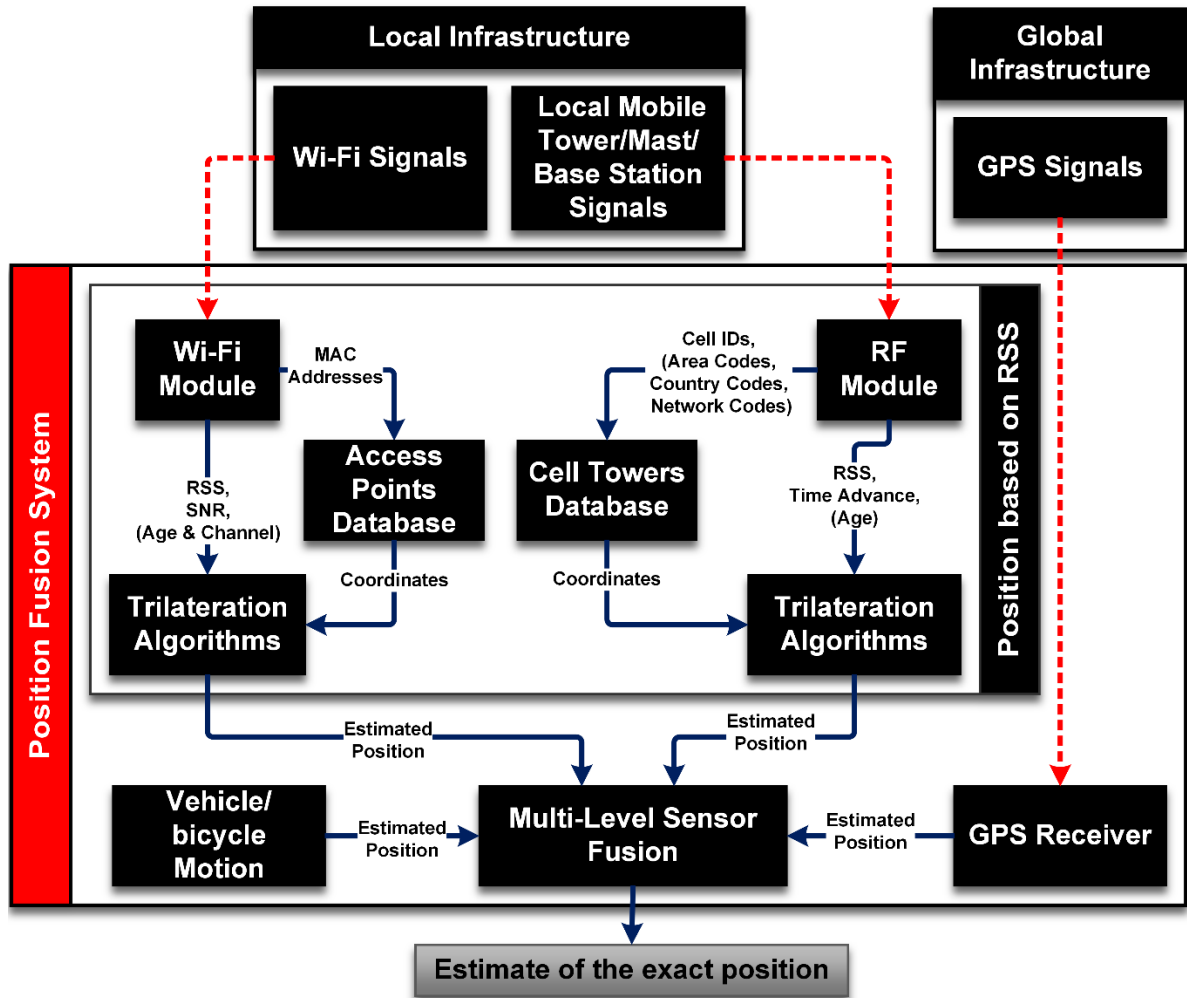


Figure 3-11: Block diagram of position fusion system.

Many researchers use the equation of motion to develop simple models where current position, heading direction, velocity and acceleration information are employed to predict future positions. These models assume that the heading direction, velocity and acceleration remain constant within a time horizon. A similar approach from the above 'Multi-Level Sensor Fusion' block can also be utilised to predict future positions but these simple prediction models generally do not provide a high accuracy and reliable forecast, especially in the context of urban driving conditions. Consequently, a more robust and dependable model is proposed in Figure 3-12 which is to be integrated with cyclist 360 Alert system. As can be seen from the block diagram below, the collision prediction and warning system (CPaWS) consists of digital maps, dynamic localisation, local road geometry, vehicle and cyclist path planning, driver inputs, cyclists and drivers' behaviour models. These models then combined to generate contextual outputs which can be translated into the multi-model user interface for cyclists and drivers so as to alert them more

effectively with different level of warnings.

One of the main systems that drive the CPaWS is the position fusion system illustrated in Figure 3-11. Thus, if the input to the system has an error greater than ± 0.5 m, the output from the system is most likely to follow the same trend. Therefore, it is important accurately to localise cyclists and vehicles so that detection of potential future collisions can be made more reliable to avoid false alerts being triggered by the system, which could be hazardous in under certain conditions where the driver may unnecessarily get distracted and may miss a potential hazard.

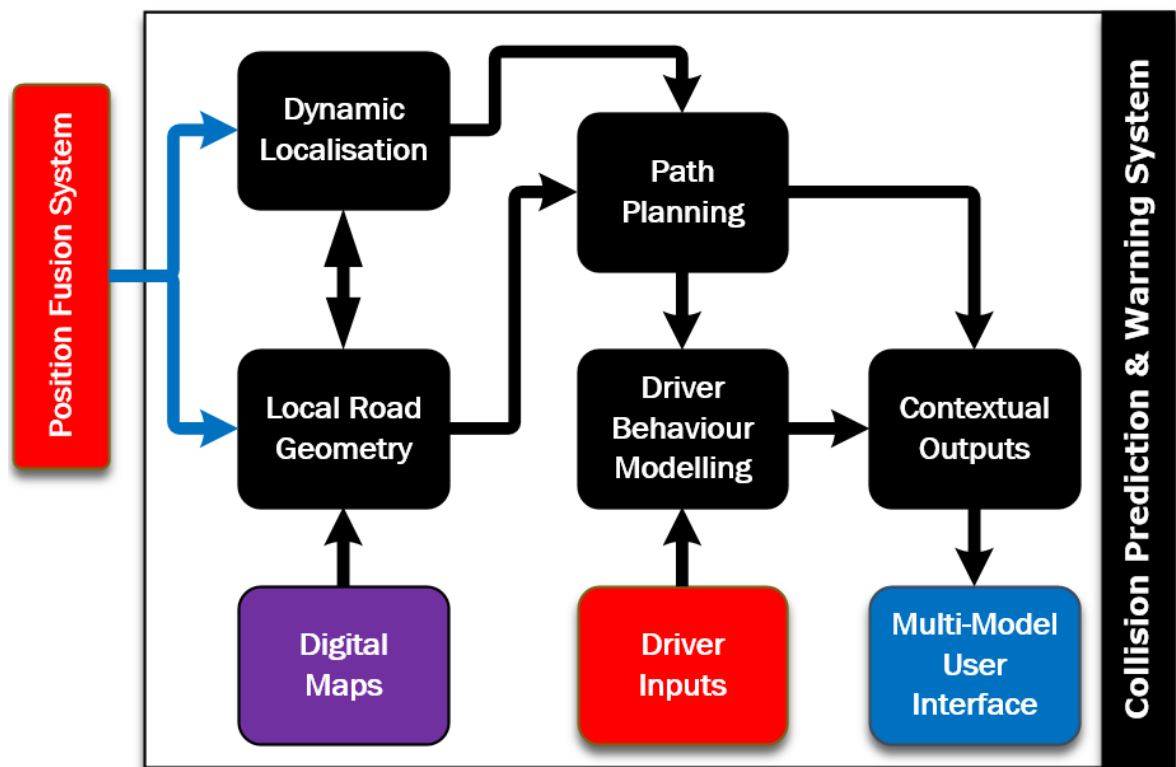


Figure 3-12: Collision prediction & warning system block diagram.

3.7 Implementation Strategy

As can be seen from the above block diagrams, the development of the entire Cyclist 360° Alert system is quite complex as it requires in-depth study to implement the complete system. Therefore, it was decided that the Cyclist 360° Alert system will be developed in phases and the following four phases have been identified in the earliest stage of this research project:

1. To develop methodologies, algorithms and a prototype iBike system that can be utilised for the position fusion system as illustrated in Figure 3-11.

2. To implement similar strategy developed in phase 1 for an instrumented vehicle and to develop a prototype communication interface C2V and V2C that will link both bicycle and vehicle. To develop an app for the driver's display unit and to implement it on smartphones.
3. To conduct an in-depth study of collision avoidance strategy and to develop the algorithms for CPaWS illustrated in Figure 3-12. Apart from this, from phase 2, cyclists and drivers' behaviour will be studied to further enhance CPaWS.
4. To develop "multi-modal" user interface includes haptic, audio and visual feedback for the drivers and the cyclists, to test the complete Cyclist 360° Alert system thoroughly, and to improve the reliability of the overall system.

It is understood that once the basic system architecture is formed many other systems will be derived from it. For instance, the system can be adapted to detect other vulnerable road users such as pedestrians, mopeds and motorcycles. The data from the Cyclist 360° Alert system can also be utilised for many other applications such as understanding the behaviour of cyclists, localisation services for emergency vehicles and environmental data collection. As a result, the system architecture design opens a promising path for further developments.

However, the four development phases identified above are not possible to implement within the time limit for this PhD. Consequently, the scope of this PhD research is to develop a prototype iBike system to improve localisation accuracy for cyclists who are very challenging to track with existing sensor technologies mainly due to their size and ability to move more freely than vehicles and, to the best of the author's knowledge, currently no system specifically to track cyclists in urban environments exists and this could be due to the challenges mentioned earlier.

3.8 Conclusions

This chapter presented the concept that was formulated as part of this research study to track cyclists and vehicles using low-cost sensor technologies found in smart devices and existing infrastructures. The overall concept proposes to employ smartphones, which are becoming widely available, to reduce the cost of the Cyclist 360° Alert system. The ultimate goal is to employ the methodologies formulated in this research studies to provide the ability to monitor the obscured regions and take

preventive action if a conflict is detected based on predicted trajectories of the vehicles.

This chapter also reviewed localisation techniques and technologies and found that although most of the localisation systems can be utilised to estimate the position of an object, these systems do not provide sufficiently high resolution and accuracy to locate a bicycle with the design requirement specified for the Cyclist 360° Alert concept. Consequently, a hybrid approach is proposed using GPS, WPS, CTPS and vehicle motions. The results of the position fusion system are then to be integrated with a collision prediction and warning system. Overall, this is an innovative concept to track cyclists and vehicles in complex traffic situations and to alert both cyclists and vehicles in advance with a high precision.

The development of the comprehensive concept is a complex task because it requires an in-depth study into a wide range of subject areas as well as novel methodologies. As a result, it was decided that the Cyclist 360° Alert system will be developed in phases. The first and the most important identified phase is to develop methodologies, algorithms and a prototype iBike system that can be utilised to enhance the accuracy for tracking cyclists using the proposed strategies. Thus, the rest of this report concentrates on the development of the iBike system because, as stated, cyclists are more difficult to track and if they can be tracked with a high precision, then similar strategies can be applied to other types of vehicles.

Chapter 4: Bicycle Positioning Models & Algorithms

4.1 Introduction

Pedal cycle localisation accuracy can be increased if the trajectory can be reconstructed based on its motion data with a high update frequency so that they can be fused with other localisation systems. Thus, this chapter presents the study undertaken to derive the necessary models to transform various measurements into a trajectory. In this chapter, Section 4.2 describes the unique modelling characteristics of a bicycle compared with other types of vehicles. In addition, this section also examines the unique steering mechanism of a bicycle and how one is able to negotiate a turn while in motion. Section 4.3 presents the geometrical relationships and accomplishes the model for the effective steering angle of a bicycle. This section also illustrates a two-step Dead-Reckoning technique and derives a kinematics model that can be utilised in conjunction with a Kalman filter. Section 4.4 briefly describes the standard mathematical equations for a Kalman filter and then derives the relevant parameters for two Kalman filters for positioning and yaw estimation. Section 4.5 briefly studies the geodetic system and illustrates a datum conversion software that can be employed for the prototype system. Finally, Section 4.6 reveals the overall design of the fusion algorithms based on the derived models and demonstrates how different trajectories are generated through the algorithms.

4.2 The Unique Characteristics of a Bicycle

Most people consider a bicycle to be a simple two-wheeled mechanical system but a detailed study reveals that it consists of many mechanical parts as illustrated in Figure 4-1 and that its dynamics are far more complicated than other wheeled vehicles or even an aeroplane. This is because a bicycle is a multibody system and this makes it difficult to model its dynamics as opposed to a rigid body. For example, the front wheel can be steered and tilted concurrently whereas the rear wheel cannot be turned directly but it follows the commands from the front wheel. Moreover, when a bicycle stands still its dynamics are analogous to an inverted pendulum: it

is a nonlinear, non-minimum phase system, and is therefore unstable when not controlled appropriately. Thus, it is not surprising that since the end of the 19th century many authors have been attempting to derive suitable equations to describe the motion of a bicycle system. In recent years, a number of experiments have been conducted to understand the dynamics of the bicycle. One such study was an investigation of fundamental characteristics of human riders using an instrumented bicycle [94], and another study focused on the stability of the bicycle [95]. Both of these studies show the unique behaviour patterns and fundamental elements associated with bicycle dynamics.

Furthermore, according to Cossalter [96] there are constantly some 15 forces that act on a bicycle when it is in motion on a semi-smoothed surface, and among them, 13 need to be controlled but only two (the steering and the speed) are actuated. In other words, a detailed model of a bicycle is complex, as the system has many degrees of freedom and there are not many studies that can adequately illustrate the full working principles of a bicycle.

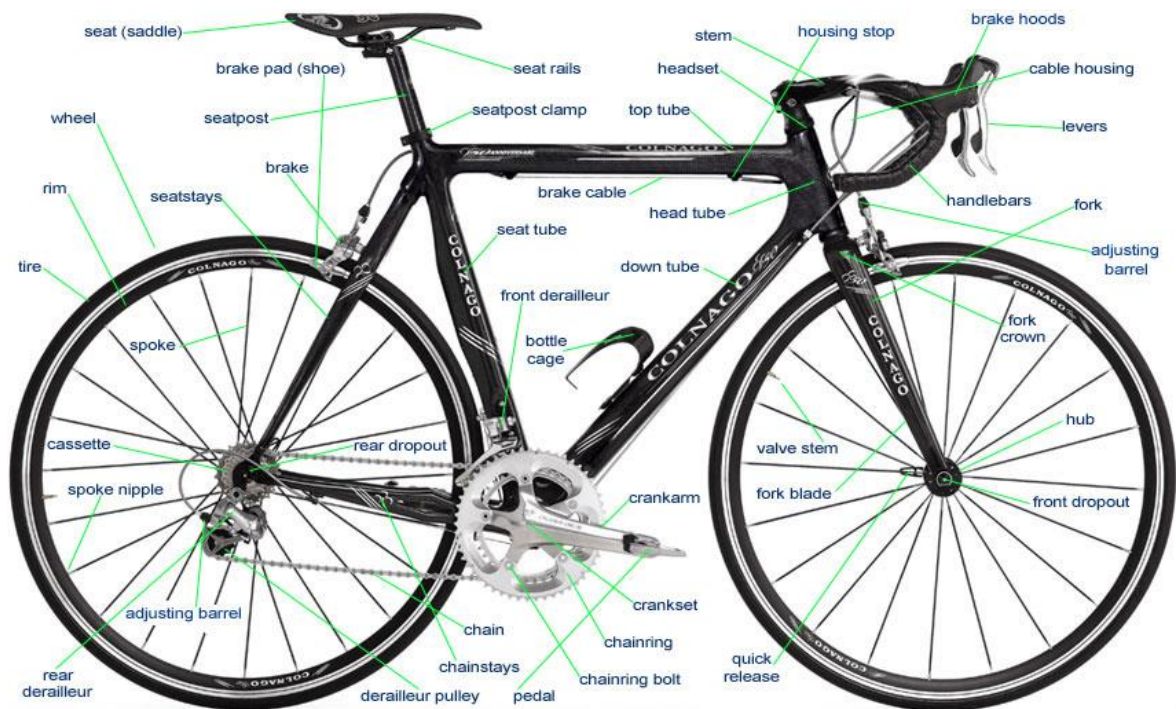


Figure 4-1: components of a modern bicycle [97].

Studies of bicycle physics found in [98] [99] [100] reveal that steering plays a major role in balancing a bicycle and that one cannot simply steer the handlebars to the desired direction while in motion. In order to keep the balance and to negotiate a

turn successfully, one must first lean into the direction of the turn. This is achieved by momentarily steering the handlebars in the opposite direction to make the bicycle unstable briefly so that it tilts inward toward the direction of the turn. This process is known as “countersteering”. Then, almost immediately afterwards the rider must turn the handlebars in the desired direction of the turn while at the same time the rider’s body must counteract the centrifugal force generated by the lean angle. In other words, the balancing of the bicycle is achieved by steering to the same side as the tilt. When the centrifugal force balances the gravitational force, the bicycle will be held at an equilibrium roll angle. A typical right turn of a bicycle in motion is illustrated in Figure 4-2. Therefore, the roll angle depends on the turning radius and speed, and the roll angle is critical when modelling the effective steering angle of the bicycle.

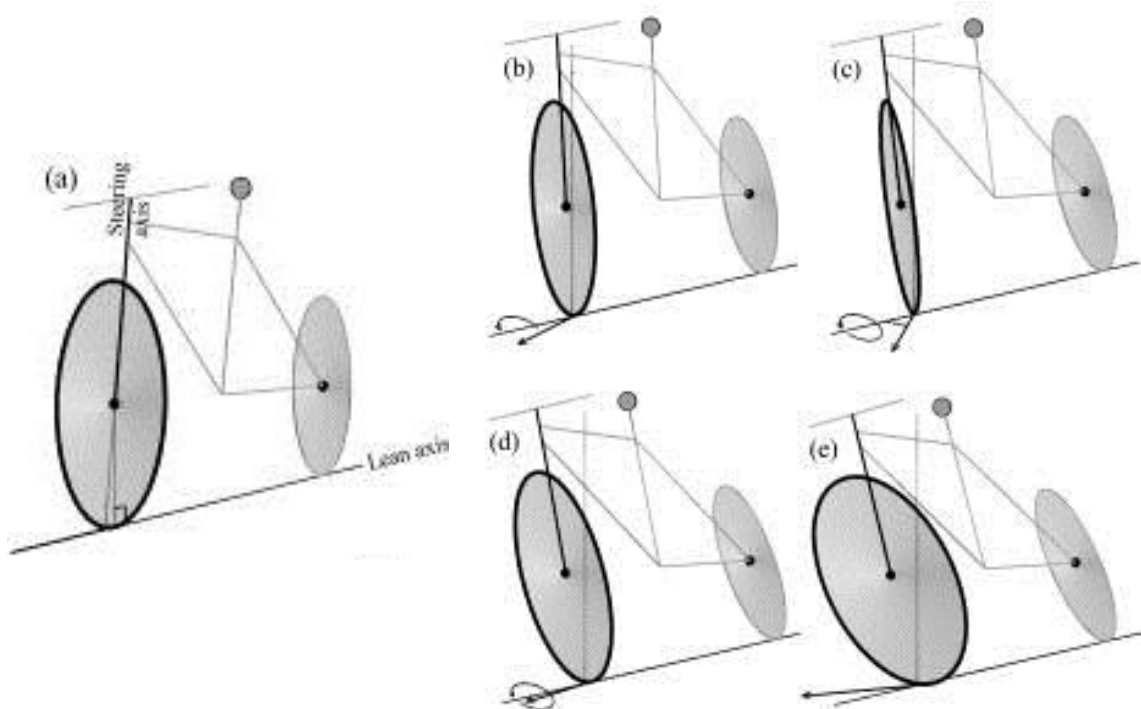


Figure 4-2: Illustration of a typical right turn with countersteering [101].

In the above diagram: (a) the steering and lean axis. (b) Initiating steering to the left when the desired direction is right. (c) bicycle turns to the left, the centrifugal force rolls the frame to the right. (d) The steering angle decreases. The roll angle continues to increase because the bicycle is still turning left. (e) Steering angle passes through zero and points toward the right.

A simplified linear model of a vehicle with two-degree of freedom, which considers lateral and yaw motions, is shown in Equation (4.1). These models are widely found in the literature [102], [103] and [104] related to control engineering.

$$\begin{bmatrix} \dot{v} \\ \dot{\psi} \end{bmatrix} = \begin{bmatrix} -\frac{C_f + C_r}{mu} & -u - \frac{C_f - C_r}{mu} \\ \frac{aC_f - bC_r}{I_z u} & -\frac{a^2 C_f - b^2 C_r}{I_z u} \end{bmatrix} \begin{bmatrix} v \\ \psi \end{bmatrix} + \begin{bmatrix} \frac{C_f}{m} \\ \frac{aC_f}{I_z} \end{bmatrix} \delta_f \quad (4.1)$$

where, v is the velocity, ψ is the yaw angle, m is the mass of the vehicle, I_z is the moment of inertia about the z-axis (refer to Figure 4-4), δ_f is the steering angle, C_f and C_r are the front and rear wheel cornering stiffness respectively. Coefficients a and b represent the distance from the front and rear axles respectively to the central of gravity and u is the vehicle speed.

These models have two main drawbacks. First, as can be seen from the equation above, the model neglects roll angle. Secondly, the measurements of the parameters such as the centre of gravity and rider's weight in the case of a bicycle system are difficult to measure accurately. Moreover, developing the sensing system for this model would be complex and expensive. Hence, this research develops an overall model to reconstruct the trajectory based on the kinematics and geometrical relationships of a bicycle.

4.3 Transformation of Bicycle Motions

A simple kinematic bicycle model is a common approximation approach used for robot car motion planning [105]. In this model, the left and right wheels of a vehicle are considered as a pair of single wheels as shown in Figure 4-3. Moreover, the equations of motion for the kinematic bicycle model of a vehicle are readily found in the literature [106] [107] [108]. However, as discussed in Section 4.2, the behaviour patterns of a bicycle and a robot are not the same and the kinematics bicycle model of a robot car neglects roll angle, which is an important parameter for modelling the effective steering angle of a bicycle (refer to Figure 4-4). Initial experimental data confirm this dependence, and this is also evident from other related studies, such as the ones investigating motorcycle dynamics [96]. As a result, it is desirable to incorporate the roll angle to improve the localisation accuracy.

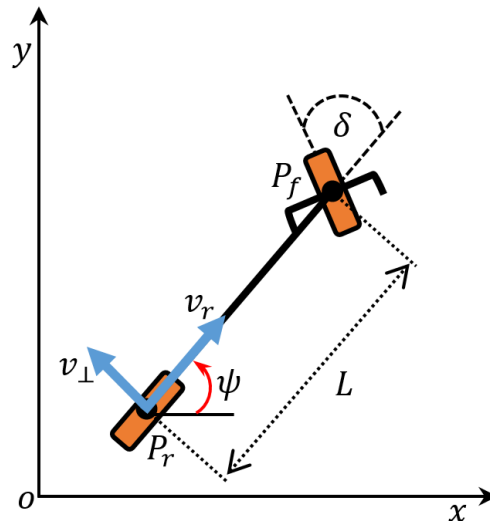


Figure 4-3: A simple kinematic bicycle model of a vehicle.

In the diagram above, x & y is the global coordinate frame, P_r and P_f are the rear wheel and front wheel positions in the global frame respectively, ψ is the yaw angle (or heading angle) of the vehicle in the global frame with respect to the x -axis, δ is the steering angle in the body frame, v_r and v_{\perp} are the respective velocity components of the rear wheel, and L is the length from the rear wheel axle to the front wheel axle.

The most prominent example of a model describing bicycle kinematics is the one described in [96] [109]. This relies on the coordinate system in Figure 4-4, as well as on the following assumptions:

- For the steering angle, left turning is the positive direction.
- For the roll angle, tilting right from the vertical is the positive direction.
- There is no lateral slippage between the wheels and the road plane.
- Both wheels are always in contact with the ground or road.
- Between two consecutive sample points, the steering angle remains unchanged
- The bicycle only has forward momentum i.e. it does not roll back or turn in the reverse direction

The kinematics (or the effective steering angle) of a bicycle depends on both the handlebar steering angle and the roll (or tilt) angle. This can be obtained through a geometric relationship of the steering mechanism in Figure 4-4 and can be also found in research paper [110].

$$\tan(\beta) = \frac{\tan(\delta) \cdot \sin(\eta)}{\cos(\phi)} \quad (4.2)$$

The instantaneous effective steering angle can be also expressed as portrayed below:

$$\tan(\beta) = \frac{W}{R} \quad (4.3)$$

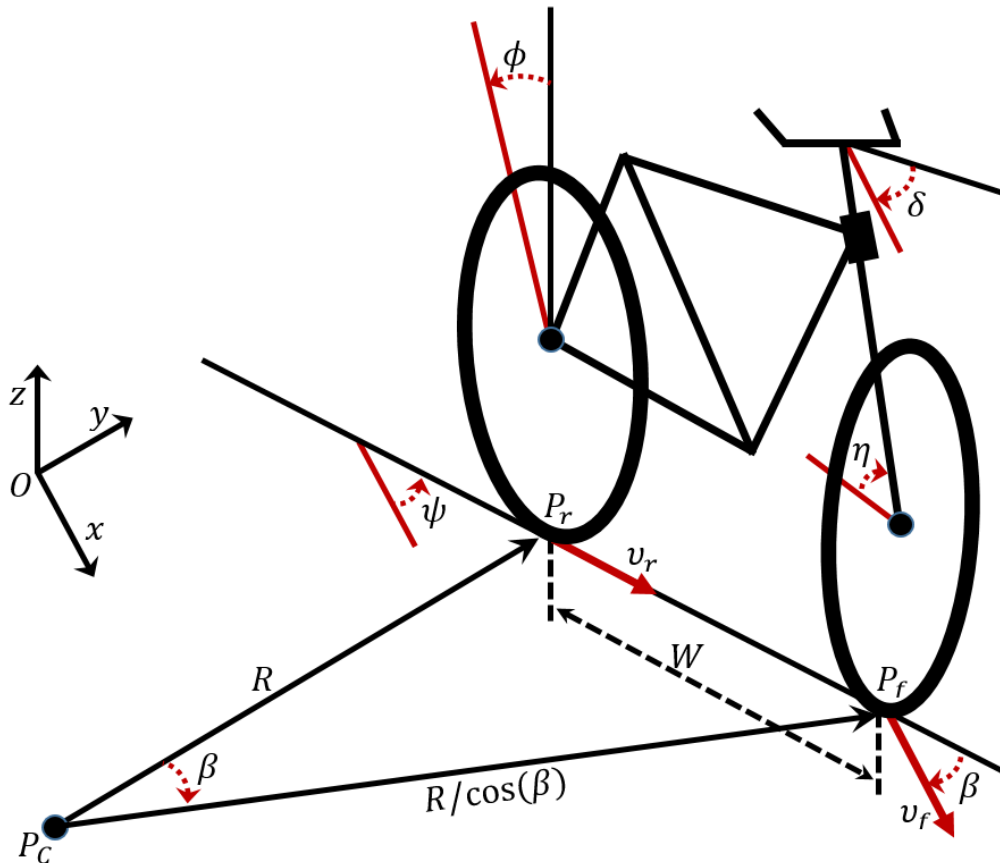


Figure 4-4: Turning geometry of a bicycle.

In the diagram above, x , y and z are global coordinate system, W is the bicycle wheelbase, R is the turning radius, η is the castor angle, ϕ is the rear wheel/frame roll angle, ψ is the frame yaw angle reference to x -axis, δ is the steering angle, β is the effective steering angle, P_f is the front wheel ground contact point, P_r is the rear wheel ground contact point, v_r is the rear wheel longitudinal velocity, v_f is the front wheel longitudinal velocity, and P_C is the instantaneous centre of rotation.

From the illustration in Figure 4-5, it is also clear that a bicycle produces two trails: one from the front wheel and other from the rear wheel. However, from the analysis of bicycle geometry in [111], the front wheel mechanism is much more complex than the rear wheel, as the front wheel can be steered and tilted simultaneously.

Therefore, to reconstruct the bicycle trajectory based on the simple kinematic model, only the rear wheel path is traced using the technique outlined in the next section.

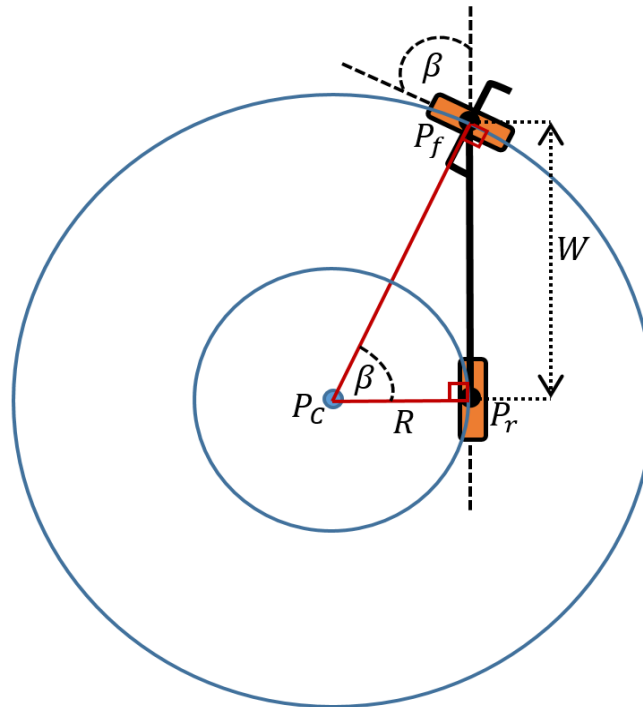


Figure 4-5: Top view of geometric bicycle model.

In the diagram above, P_c is the instantaneous centre of rotation traced by the front and rear wheel with a constant β , P_f and P_r are the front and rear wheels coordinates respectively.

4.3.1 Bicycle ground-path trajectory based on a two-step approach

A number of path tracking techniques and algorithms exist. These include Fuzzy-Logic based techniques [112] [113], the Pure-Pursuit based approach [114] and the Vector-Pursuit method [115]. However, one of the most common path tracking techniques employed in robotics is known as geometric path tracking, founded on a process called Dead-Reckoning (DR) [116] [117], which is more suitable for this research into accurate localisation of cyclists. This method estimates one's current position based upon a previously determined or known position and advances that position based on speed and yaw angle. While traditional methods of DR are no longer considered primary means of navigation, modern inertial navigation systems, such as U-blox's 3D automotive DR chip [118], which also depend upon DR, are very widely used for vehicles, as GPS is not accurate or adequate in places such as in tunnels and in multi-storey car parks. Hence, the method is to be utilised to

transform the motion parameters' values into a trajectory. The DR algorithm assumes the following two conditions:

- That the initial yaw angle with respect to the x-axis is known.
- That the initial coordinates with respect to a global coordinate system (x,y) are known.

The above two initial settings can be obtained from the technique discussed in Section 3.6, where a hybrid localisation system can be utilised to estimate two initial positions. Thus, they can be employed to find the initial coordinates and heading of the bicycle.

Figure 4-6 illustrates the geometrical relationship between a previous position at time $k - 1$ and a current position at time k .

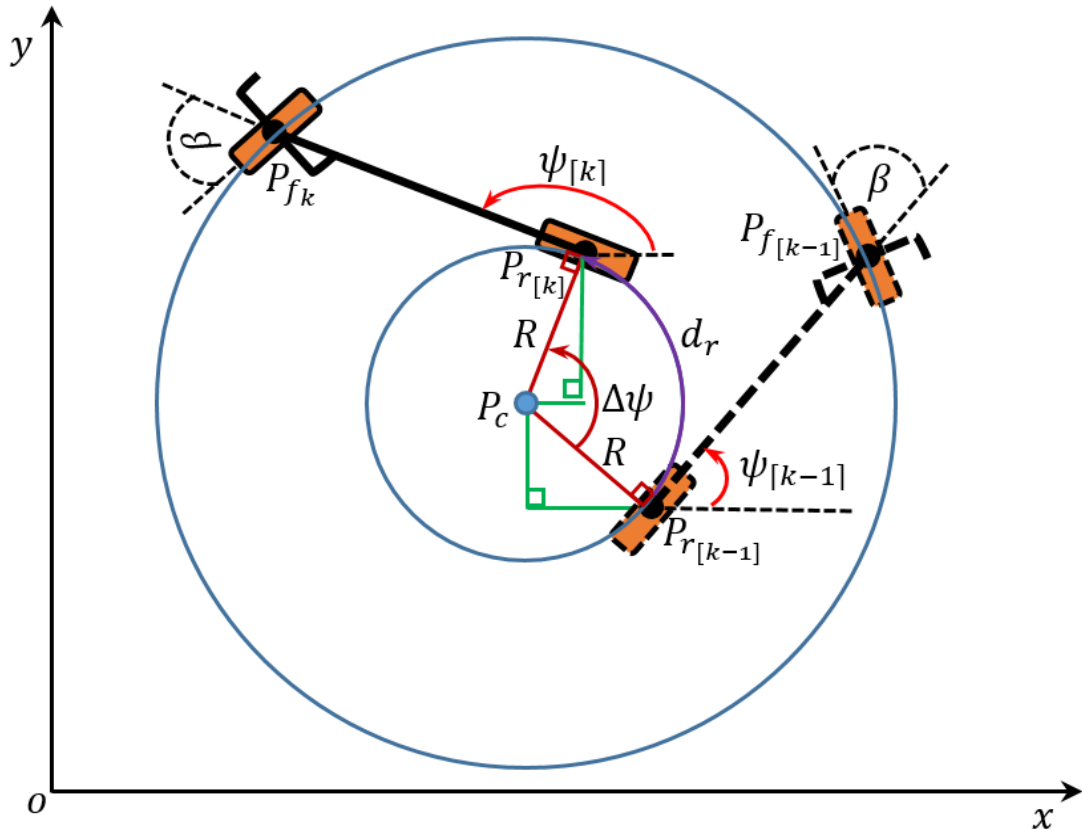


Figure 4-6: Geometric relationship from the previous location to current location (exaggerated for the purpose of demonstration of the method). In this diagram: $P_{r[k]}$ and $P_{f[k]}$ are the rear wheel and front wheel positions in the global frame respectively, the subscript k is associated with time, (x, y) is the global coordinate frame and O is the origin. The parameters without the subscript k are assumed to remain constant for a single time frame.

It is assumed that between the two consecutive sample times the effective steering angle of the bicycle remains constant. Thus, Equation (4.4) can be expressed as Equation (4.5):

$$\Delta\psi = \psi_{[k]} - \psi_{[k-1]} \quad (4.4)$$

$$\Delta\psi = \frac{d_r}{R} \quad (4.5)$$

where $\Delta\psi$ is the instantaneous central angle in radians, and d_r is the length of the arc from points $P_{r[k-1]}$ to $P_{r[k]}$ in metres.

The instantaneous turning angle portrayed by Equation (4.6) can be determined from Equation (4.3) to make R the subject and substituting the results in Equation (4.5).

$$\Delta\psi = \frac{d_r \cdot \tan(\beta)}{W} \quad (4.6)$$

The simplest form of the DR algorithm follows a two-step procedure where depending on the instantaneous turning angle, $\Delta\psi$, the trajectory can be computed as follows:

1. For an instantaneous turning angle of less than a certain tolerance angle, it can be simply approximated as a straight line given by Equations (4.7)-(4.8). For more accurate prediction in the next iteration, Equation (4.9) is used to update and temperately store the current yaw angle.

$$x_{[k]} = x_{[k-1]} + d_r \cdot \cos(\psi_{[k-1]}) \quad (4.7)$$

$$y_{[k]} = y_{[k-1]} + d_r \cdot \sin(\psi_{[k-1]}) \quad (4.8)$$

$$\psi_{[k]} = (\psi_{[k-1]} + \Delta\psi) \bmod 2\pi \quad (4.9)$$

2. For an instantaneous turning angle of more than the tolerance angle, the trajectory can be approximated with a two-step method – firstly by computing the coordinates of P_c from $P_{r[k-1]}$ with Equations (4.10) and (4.11), and secondly by updating the yaw angle using Equation (4.9), the current position $P_{r[k]}$ from P_c can be found using Equations (4.12) and (4.13).

$$P_{C_x} = x_{[k-1]} - R \cdot \sin(\psi_{[k-1]}) \quad (4.10)$$

$$P_{C_y} = y_{[k-1]} + R \cdot \cos(\psi_{[k-1]}) \quad (4.11)$$

$$x_{[k]} = P_{C_x} + R \cdot \sin(\psi_{[k]}) \quad (4.12)$$

$$y_{[k]} = P_{C_y} - R \cdot \cos(\psi_{[k]}) \quad (4.13)$$

The above two-step approximation method of transforming the ψ and d_r into a current position based upon a previously position is further illustrated in Figure 4-7.

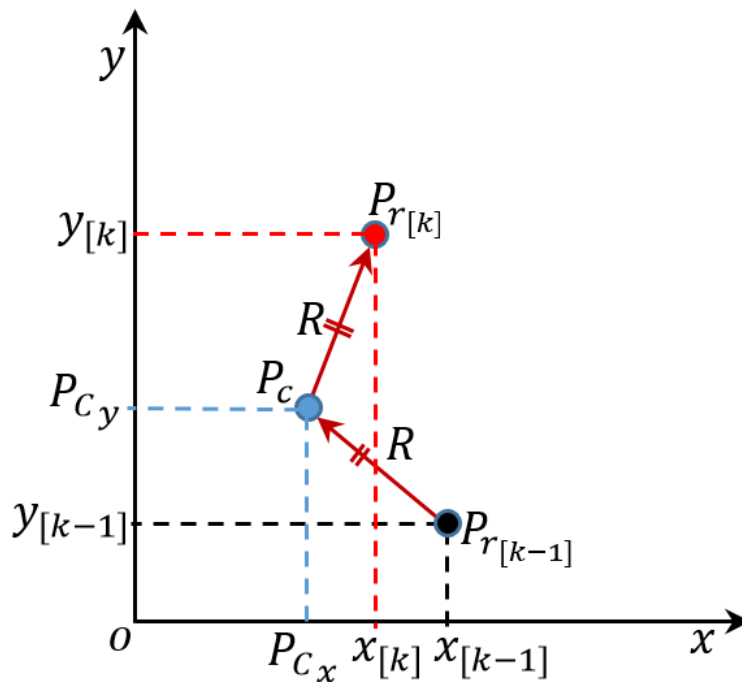


Figure 4-7: Approximation with a two-step DR method.

4.3.2 Simplified Positioning Model

The DR algorithm described in the previous section is computationally inefficient and is rather unsuitable from the perspective of a fusion algorithm and the use of a Kalman filter later on. Therefore, an alternative approximation positioning model is developed in this section.

Based on the geometry of Figure 4-8 below, the length of arc, d_r , can be found as:

$$d_r = R(2\alpha) \quad (4.14)$$

where R is the turning radius and α is the half of the central angle in radian.

As a result, the instantaneous turning angle, $\Delta\psi$, can be portrayed through the equation below:

$$\Delta\psi = 2\alpha = \frac{d_r \tan(\beta)}{W} \quad (4.15)$$

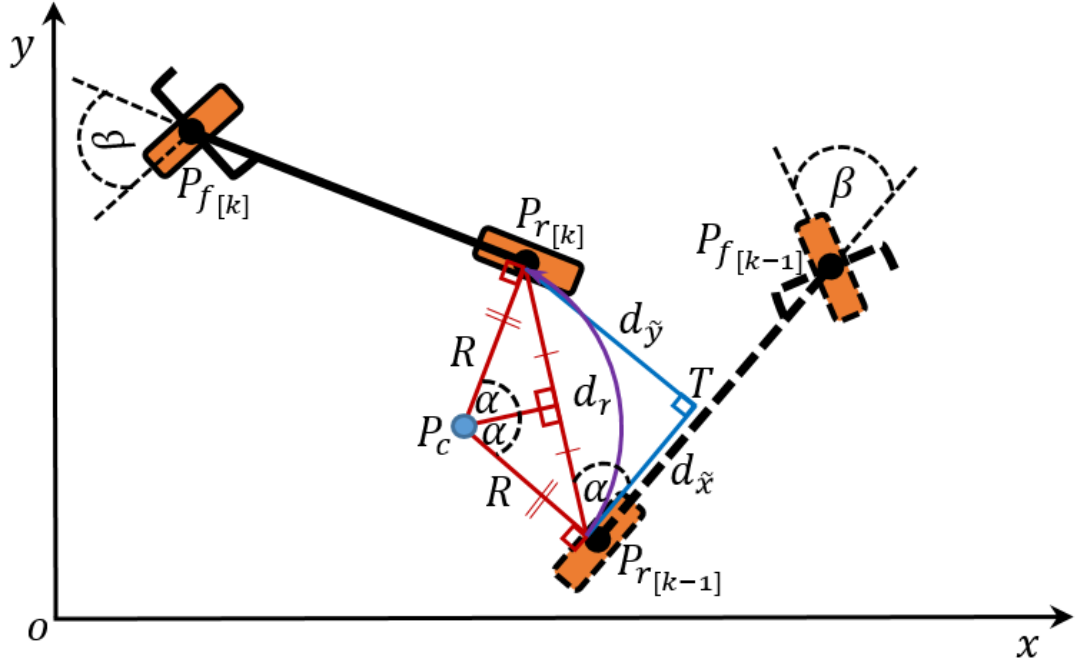


Figure 4-8: Bicycle geometric relationship with body and global coordinates system.

With reference to the diagram above, the length of the chord between points $P_{r[k-1]}$ and $P_{r[k]}$ can be found through the equation below:

$$L_{chord} = 2R\sin(\alpha) \quad (4.16)$$

The angle between a chord and a tangent is the half of the arc belonging to the chord as shown in the above diagram. Hence, based on the geometry of Figure 4-6 and Figure 4-8, the position of the rear frame between time t_{k-1} and t_k is given in body fixed coordinates by:

$$d\tilde{x} = L_{chord} \cos(\alpha) = 2R\sin(\alpha)\cos(\alpha) \quad (4.17)$$

$$d\tilde{y} = L_{chord} \sin(\alpha) = 2R\sin(\alpha)\sin(\alpha) \quad (4.18)$$

Using the double angle standard trigonometric formulas $\sin(2\alpha) = 2\sin(\alpha)\cos(\alpha)$ and $\cos(2\alpha) = 1 - 2\sin^2(\alpha)$, the above two equations can be simplified as:

$$d\tilde{x} = R\sin(2\alpha) \quad (4.19)$$

$$d\tilde{y} = R - R\cos(2\alpha) \quad (4.20)$$

Using the established relationship in Equation (4.15), the above equations can now be rewritten using the $\Delta\psi$ as follows:

$$d\tilde{x} = R\sin(\Delta\psi) \quad (4.21)$$

$$d\tilde{y} = R - R\cos(\Delta\psi) \quad (4.22)$$

The rotation of vector L_{chord} illustrated in Figure 4-9, in the clockwise angle is the same as rotating the body axis in the counter-clockwise angle [119]. Hence, the rotational matrix \mathbf{R} shown below can be used to translate the vector to the global coordinate system (x,y) from the body frame.

$$\mathbf{R}(\psi_{[k-1]}) = \begin{bmatrix} \cos(\psi_{[k-1]}) & -\sin(\psi_{[k-1]}) \\ \sin(\psi_{[k-1]}) & \cos(\psi_{[k-1]}) \end{bmatrix} \quad (4.23)$$

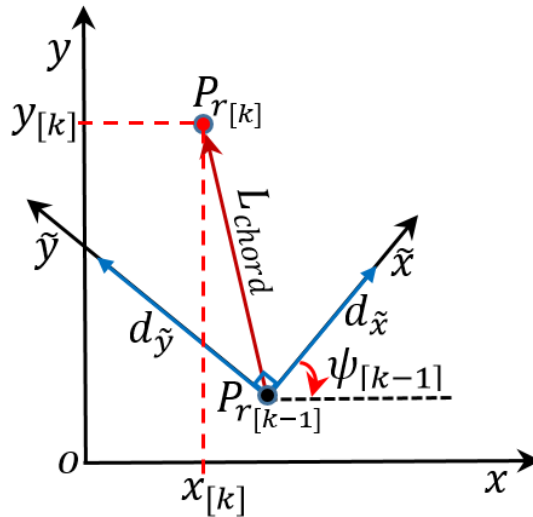


Figure 4-9: Approximation with simplified positioning model

As a result, the kinematics model for the position of the bicycle in the global coordinate system is then portrayed by:

$$\begin{bmatrix} x_{[k]} \\ y_{[k]} \end{bmatrix} = \begin{bmatrix} x_{[k-1]} \\ y_{[k-1]} \end{bmatrix} + \begin{bmatrix} \cos(\psi_{[k-1]}) & -\sin(\psi_{[k-1]}) \\ \sin(\psi_{[k-1]}) & \cos(\psi_{[k-1]}) \end{bmatrix} \begin{bmatrix} d\tilde{x}_{[k-1]} \\ d\tilde{y}_{[k-1]} \end{bmatrix} \quad (4.24)$$

where subscripts $k - 1$ in $d\tilde{x}$ and $d\tilde{y}$ denote the computation of Equations (4.21) and (4.22) between time $k - 1$ and k .

Thus, the proposed model bypasses the estimation of the instantaneous centre of rotation of the two-step DR algorithm. Hence, the model can be readily used in the

fusion algorithm as a position Kalman filter. It should be noted that since the DR process depends on the accumulation of previous positions, calculated solely from bicycle's data acquisition is prone to drift and is only suitable for a short time horizon. However, fusing this data with GNSS and localisation systems based on ubiquitous wireless communications, widely found in urban areas, can lead to improved overall accuracy. Thus, the next section looks at the proposed fusion technique.

4.4 Sensor Data Fusion

4.4.1 Standard Kalman Filter Equations

A Kalman filter is an optimal state estimation algorithm that utilises a series of measurements observed over time and outputs approximations of unknown variables that tend to be more precise than those based on a single measurement alone. In other words, a Kalman filter is a feedback control system that keeps track of the estimated state of the system and also the uncertainty of the estimate. Although the filter was designed over 50 years ago, it is still one of the most vital and common data fusion algorithms in use today. The Kalman filter is based on a recursive algorithm, which is theoretically more suitable for the fusion of noisy sensor data. The algorithm works in a two-stage process: (1) it produces estimations of the current state variables along with their uncertainties; (2) then it updates the estimations by utilising a weighted average. The discrete Kalman filter described in [120], [121] and [122] is based on a linear time-varying state space representation as followings:

$$\mathbf{X}_{[k]} = \mathbf{F}_{[k-1]}\mathbf{X}_{[k-1]} + \mathbf{B}_{[k-1]}\mathbf{u}_{[k-1]} + \mathbf{w}_{[k-1]} \quad (4.25)$$

$$\mathbf{Z}_{[k-1]} = \mathbf{H}_{[k-1]}\mathbf{X}_{[k-1]} + \mathbf{v}_{[k-1]} \quad (4.26)$$

where $\mathbf{X}_{[k]}$ is the state vector at time k , $\mathbf{F}_{[k]}$ is the state transition matrix at time k , $\mathbf{B}_{[k]}$ is the control input matrix, $\mathbf{u}_{[k]}$ is the vector containing any control inputs, $\mathbf{w}_{[k]}$ is the Gaussian process noise with covariance matrix $\mathbf{R}_{[k]}$, $\mathbf{Z}_{[k]}$ is the vector of measurements, $\mathbf{H}_{[k]}$ is the output matrix and $\mathbf{v}_{[k]}$ is the Gaussian measurement noise with covariance matrix $\mathbf{Q}_{[k]}$.

For the estimation of states at time k , the Kalman filter algorithm is performed by two steps known as “prediction” and “update” and they are described mathematically below:

1. Prediction:

$$\hat{\mathbf{X}}_{[k|k-1]} = \mathbf{F}_{[k-1]} \hat{\mathbf{X}}_{[k-1|k-1]} + \mathbf{B}_{[k-1]} \mathbf{u}_{[k-1]} \quad (4.27)$$

$$\mathbf{P}_{[k|k-1]} = \mathbf{F}_{[k-1]} \mathbf{P}_{[k-1|k-1]} \mathbf{F}_{[k-1]}^T + \mathbf{Q}_{[k-1]} \quad (4.28)$$

2. Update:

$$\mathbf{K}_{[k]} = \mathbf{P}_{[k|k-1]} \mathbf{H}_{[k-1]}^T (\mathbf{H}_{[k-1]} \mathbf{P}_{[k|k-1]} \mathbf{H}_{[k-1]}^T + \mathbf{R}_{[k-1]})^{-1} \quad (4.29)$$

$$\hat{\mathbf{X}}_{[k|k]} = \hat{\mathbf{X}}_{[k|k-1]} + \mathbf{K}_{[k]} (\mathbf{Z}_{[k]} - \mathbf{H}_{[k]} \hat{\mathbf{X}}_{[k|k-1]}) \quad (4.30)$$

$$\mathbf{P}_{[k|k]} = \mathbf{P}_{[k|k-1]} - \mathbf{K}_{[k]} \mathbf{H}_{[k]} \mathbf{P}_{[k|k-1]} \quad (4.31)$$

where $\mathbf{K}_{[k]}$ is the optimal Kalman gain, $\mathbf{P}_{[k|k-1]}$ is the covariance matrix (confidence) before data fusion, $\mathbf{P}_{[k|k]}$ is the covariance matrix (confidence) following data fusion, $\hat{\mathbf{X}}_{[k|k-1]}$ is the state vector before data fusion, and $\hat{\mathbf{X}}_{[k|k]}$ is the state vector following data fusion.

4.4.2 Yaw Angle Kalman Filter

The yaw angle has been identified as an important parameter to compute the relative position and its mathematical significance can be seen in Section 4.3. However, sensor data in the real world can be noisy, and in the case of a bicycle some of the kinematic parameters, such as the roll angle, cannot be determined accurately due to the physical structure of the vehicle. One way to improve the accuracy is to employ multiple sensors to measure the same parameter with alternative approaches. To apply this method successfully, the data from the multiple sensors must be fused with an appropriate technique. For this reason, as illustrated in Figure 4-10, a Kalman filter algorithm is designed and the development of the mathematical models to fulfil the standard Kalman filter equations stated earlier is described next.

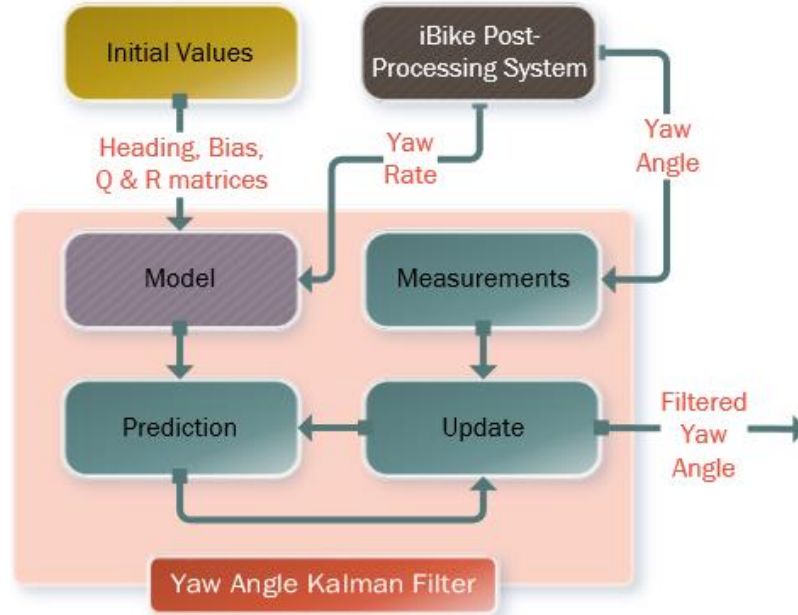


Figure 4-10: Design of the yaw angle Kalman filter.

The relationship between the yaw angle (ψ) and the yaw rate ($\omega = \dot{\psi}$) at time scan k and $k - 1$ can be expressed as shown below:

$$\psi_{[k]} = \psi_{[k-1]} + (\omega_{[k-1]} \cdot \Delta t) \quad (4.32)$$

where Δt is the time interval between two samples. From the above equation, the yaw rate can be then expressed as:

$$\omega_{[k-1]} = \frac{\psi_{[k]} - \psi_{[k-1]}}{\Delta t} \quad (4.33)$$

However, the measurement of the yaw rates using an electronic gyroscope also incorporates bias, ω_{bias} , as well as measurement noise w_{ω} . Hence, at time instant $k - 1$ the measured yaw rate can be expressed as:

$$\omega_{[k-1]} = \omega_{m[k-1]} - \omega_{bias[k-1]} - w_{\omega[k-1]} \quad (4.34)$$

where $\omega_{m[k-1]}$ is the measured yaw rate and acts as a known input to the yaw model.

The yaw rate bias, which can be measured from experimental data, is normally considered to be unchanged, and therefore, the ω_{bias} at time $k - 1$ is:

$$\omega_{bias[k]} = \omega_{bias[k-1]} \quad (4.35)$$

Therefore, the yaw angle (ψ) at time k can be expressed as:

$$\therefore \psi_{[k]} = \psi_{[k-1]} + (\omega_{m[k-1]} - \omega_{bias[k-1]} - w_{\omega[k-1]}) \cdot \Delta t \quad (4.36)$$

Using $\psi_{[k]}$ and $\omega_{bias[k]}$ as states, and $\psi_{[k]}$ as an output and $\omega_{m[k]}$ as an input, Equations (4.35) and (4.36) give rise to the following yaw angle model:

$$\mathbf{X}_{[k]} = \begin{bmatrix} \psi_{[k]} \\ \omega_{bias[k]} \end{bmatrix} = \begin{bmatrix} 1 & -\Delta t \\ 0 & 1 \end{bmatrix} \begin{bmatrix} \psi_{[k-1]} \\ \omega_{bias[k-1]} \end{bmatrix} + \begin{bmatrix} \Delta t \\ 0 \end{bmatrix} \omega_{m[k-1]} + \mathbf{w}_{[k-1]} \quad (4.37)$$

$$\mathbf{Z}_{[k-1]} = [1 \quad 0] \begin{bmatrix} \psi_{[k-1]} \\ \omega_{bias[k-1]} \end{bmatrix} + v_{[k-1]} \quad (4.38)$$

Therefore, from the expressions above, the relevant parameters for the Kalman filter algorithm can be set as:

$$\mathbf{X}_{[k]} = \begin{bmatrix} \psi_{[k]} \\ \omega_{bias[k]} \end{bmatrix}, \mathbf{u}_{[k]} = \omega_{m[k]}, \mathbf{Z}_{[k]} = \psi_{[k]} + v_{[k]} \quad (4.39)$$

$$\mathbf{F} = \begin{bmatrix} 1 & -\Delta t \\ 0 & 1 \end{bmatrix}, \mathbf{B} = \begin{bmatrix} \Delta t \\ 0 \end{bmatrix}, \mathbf{H} = [1 \quad 0] \quad (4.40)$$

Moreover, the covariance matrices $\mathbf{Q}_{[k]}$ and $\mathbf{R}_{[k]}$ are assumed constant of the following form:

$$\mathbf{Q}_{[k]} = \begin{bmatrix} \sigma_{\omega}^2 & 0 \\ 0 & 0 \end{bmatrix}, \mathbf{R}_{[k]} = \sigma_{\psi}^2 \quad (4.41)$$

where the values σ_{ω}^2 and σ_{ψ}^2 can be approximated through field experiments using the well-known expression of variance of a random variable $\tilde{\alpha}$ from N observations:

$$\sigma_{\tilde{\alpha}}^2 = \frac{1}{(N-1)} \sum_{i=1}^N |\tilde{\alpha}_i - \mu_{\tilde{\alpha}}|^2 \quad (4.42)$$

with,

$$\mu_{\tilde{\alpha}} = \frac{1}{N} \sum_{i=1}^N \tilde{\alpha}_i \quad (4.43)$$

4.4.3 Multi-System Yaw Angle Fusion

The accuracy of the yaw angle can be further improved by fusing the orientation information of the bicycle from the identified positioning systems in Section 3.4. Hence, Figure 4-11 shows an algorithm design that can be utilised to enhance the overall system accuracy from multiple systems. The derived Kalman filter models in the previous section are exploited in the additional system with the similar implementation strategy as shown in Figure 4-10. Here, the only differences are the initial values of the covariance matrices and the bias which is assumed to be zero. In addition, the heading angle from GPS measurement is referred from the y-axis (north) but Equation (4.44) can be used to transform the angle so that the angle is referenced from the x-axis (east), which is the reference system used in this study as with the yaw angle Kalman filter in Section 4.4.2.

$$\psi_{GPS[k]} = \frac{\pi[(90 - \psi_{GPS[k]}) \bmod 360]}{180} \quad (4.44)$$

The two Kalman filters can be operated in parallel so that the outputs from them are always synchronised. In addition, both Kalman filters in Figure 4-11 can be driven by the yaw rate which is assumed to have a higher update rate than the measurements from GPS. The outputs from each of the Kalman filters can then be combined using Equation (4.45) in which weighting factors, Wt_{GPS} and Wt_{iBike} , whose sum never exceeds one, are incorporated. The weightings make it possible to tune the fusion algorithm and to select an appropriate level of combination of the data from two systems.

$$\psi_{fused[k]} = Wt_{GPS}[\psi_{GPS[k]}] + Wt_{iBike}[\psi_m[k]] \quad (4.45)$$

The actual value of the weighting factors can be determined experimentally from the field data and using the equation below:

$$Wt_{[i]} = 1 - \frac{\mu_{\tilde{\alpha}[i]}}{\sum_{i=1}^N \mu_{\tilde{\alpha}[i]}} \quad (4.46)$$

where, the subscript $[i]$ denotes the index for the system (GPS or iBike) and $\mu_{\tilde{\alpha}}$ represents the mean positional error of the system with respect to a known location.

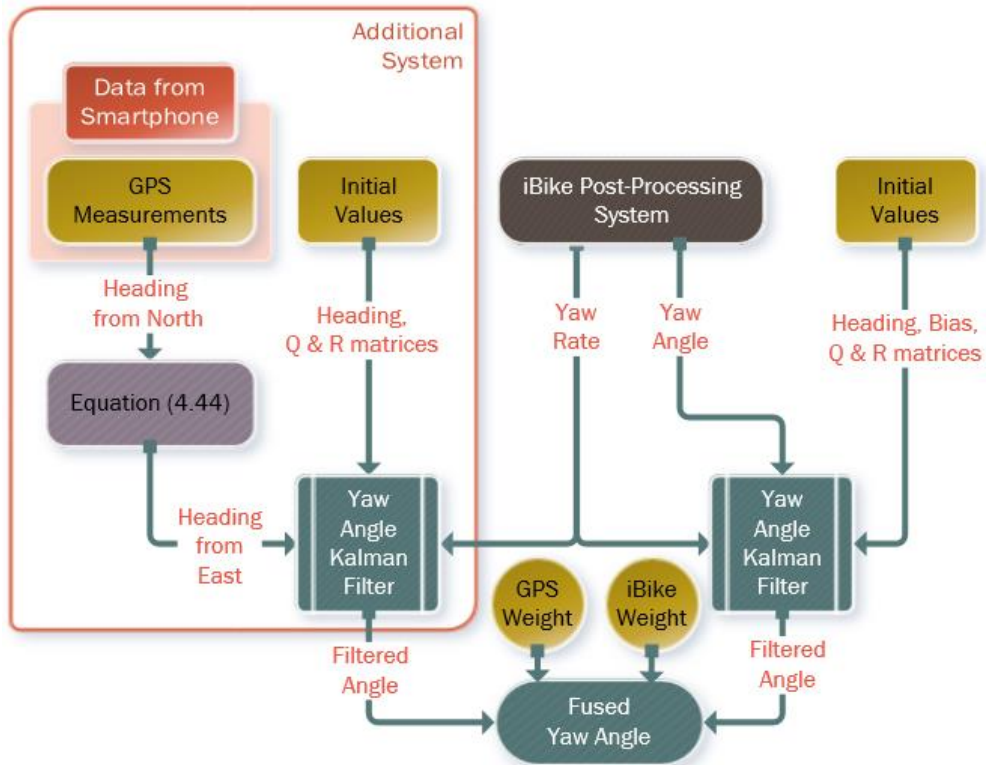


Figure 4-11: Design of the multi-system yaw angle fusion.

GPS measurements, on the other hand, do not give the heading angle directly, instead, it is computed from two measured positions i.e. current and previous positions. Nevertheless, if the accepted measurements are far apart as shown in Figure 4-12, the accuracy of the heading angle will be compromised. Therefore, an alternative method is devised for establishing the accurate yaw angle based on the measured positions.

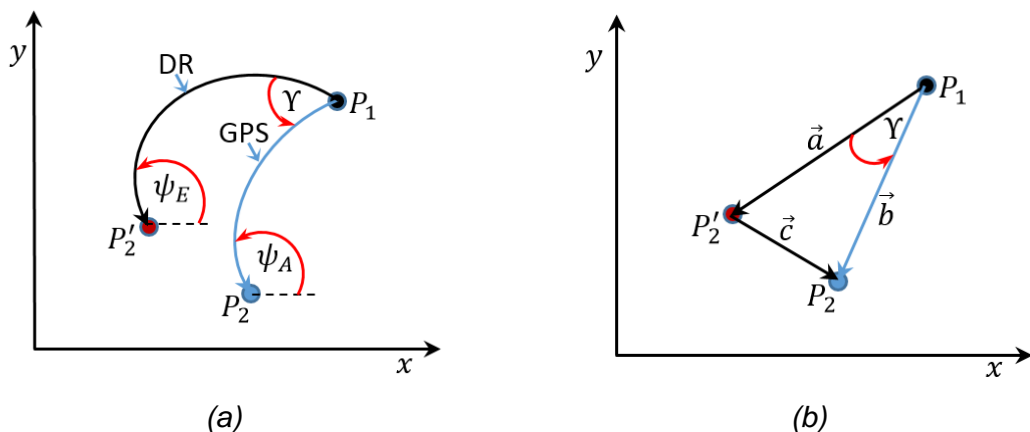


Figure 4-12: (a) Modelled trajectories based on DR algorithm and GPS; (b) Equivalent representation of the points with vector quantities.

In the above diagrams, P_1 is an accurate known position, P_2' is the position established using the DR algorithm based on P_1 after some time, P_2 is an accepted measured position using

GPS at the time of P'_2 , ψ_E is the estimated known yaw angle, ψ_A is the accurate unknown yaw angle, γ is the unknown angle between the two trajectories, and \vec{a} , \vec{b} , \vec{c} are the associated vectors for the points shown in the diagram on the right.

Based on Figure 4-12, the accurate yaw angle can be found from the relationship portrayed below:

$$\psi_A = \psi_E \mp \gamma \quad (4.47)$$

where, the unknown γ can be found using the cosine formula as presented below:

$$\cos(\gamma) = \frac{|\vec{a}|^2 + |\vec{b}|^2 - |\vec{c}|^2}{2|\vec{a}||\vec{b}|} \quad (4.48)$$

where, the vectors can be found from the global coordinates of the points as shown below:

$$\vec{a} = \begin{bmatrix} x' \\ y' \\ 0 \end{bmatrix} = \begin{bmatrix} x'_2 - x_1 \\ y'_2 - y_1 \\ 0 \end{bmatrix}, \vec{b} = \begin{bmatrix} x \\ y \\ 0 \end{bmatrix} = \begin{bmatrix} x_2 - x_1 \\ y_2 - y_1 \\ 0 \end{bmatrix}, \vec{c} = \begin{bmatrix} x'' \\ y'' \\ 0 \end{bmatrix} = \begin{bmatrix} x'_2 - x_2 \\ y'_2 - y_2 \\ 0 \end{bmatrix} \quad (4.49)$$

However, the challenge is to decide on the sign of the angle γ as the measured GPS position P_2 in the real world could lie on the left or right of the point P'_2 . To resolve this issue, cross product of the vectors \vec{a} and \vec{b} can be employed to determine the sign as demonstrated below:

$$\vec{a} \times \vec{b} = \begin{bmatrix} \vec{i} & \vec{j} & \vec{k} \\ x' & y' & 0 \\ x & y & 0 \end{bmatrix} = 0\vec{i} + 0\vec{j} + [x'y - xy']\vec{k} \quad (4.50)$$

Thus, if the k -coordinate of the cross product is a positive value then the sign of the angle γ should be also positive and vice versa; i.e.

$$\gamma > 0 \text{ if } x'y - xy' > 0 \text{ or } \gamma < 0 \text{ if } x'y - xy' < 0 \quad (4.51)$$

4.4.4 Position Kalman Filter

Since new positions are calculated solely from previous positions, the errors of the process are cumulative over time, and this is one of the major disadvantages of the DR algorithm stated earlier. One of the reasons for this is to do with inaccurate

measurements. For instance, the travelled distance or the length of the arc illustrated in Figure 4-8 in Section 4.3.2 cannot be measured precisely due to the fluctuation of the tyre pressure and the measurement of the diameter. One of the ways to improve this is through data fusion. It is assumed that no two systems will have the same type of error. Consequently, using sensor fusion, the overall position accuracy can be improved.

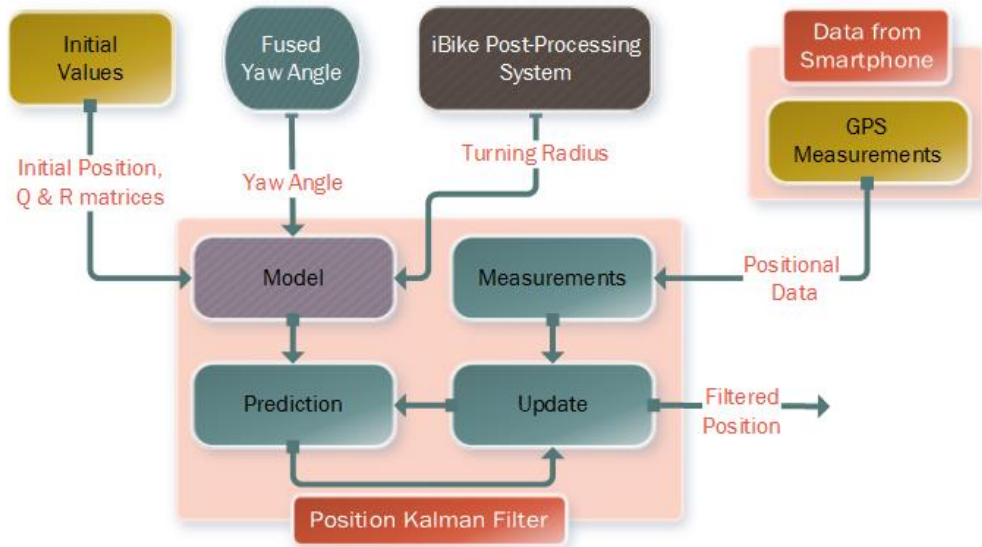


Figure 4-13: Design of the position Kalman filter.

Figure 4-13 above illustrates the design of the position fusion Kalman filter. In this design, the yaw angle is gathered from the design shown in Figure 4-11, the turning radius R is acquired through Equation (4.3) and the GPS data are aggregated via the smartphone. The derivation of the mathematical models to fulfil the standard Kalman filter equations outlined in Section 4.4.1 is described next.

The position Kalman filter can be derived from the simplified positioning model in Section 4.3.2 through Equations (4.21), (4.22) and (4.24). Assuming the global position coordinates $x_{[k]}$, $y_{[k]}$ as states, and also as outputs, and $d\tilde{x}_{[k]}$, $d\tilde{y}_{[k]}$ as inputs, Equation (4.24) gives rise to the following position model:

$$\mathbf{X}_{[k]} = \begin{bmatrix} x_{[k]} \\ y_{[k]} \end{bmatrix} = \begin{bmatrix} 1 & 0 \\ 0 & 1 \end{bmatrix} \begin{bmatrix} x_{[k-1]} \\ y_{[k-1]} \end{bmatrix} + \begin{bmatrix} \cos(\psi_{[k-1]}) & -\sin(\psi_{[k-1]}) \\ \sin(\psi_{[k-1]}) & \cos(\psi_{[k-1]}) \end{bmatrix} \begin{bmatrix} d\tilde{x}_{[k-1]} \\ d\tilde{y}_{[k-1]} \end{bmatrix} + \mathbf{w}_{[k-1]} \quad (4.52)$$

$$\mathbf{Z}_{[k-1]} = \mathbf{X}_{[k-1]} + \mathbf{v}_{[k-1]} \quad (4.53)$$

Therefore, from the expressions above, the relevant parameters for the Kalman filter algorithms can be set as:

$$\mathbf{X}_{[k]} = \begin{bmatrix} x_{[k]} \\ y_{[k]} \end{bmatrix}, \mathbf{u}_{[k]} = \begin{bmatrix} d\tilde{x}_{[k]} \\ d\tilde{y}_{[k]} \end{bmatrix}, \mathbf{Z}_{[k]} = \mathbf{X}_{[k]} \quad (4.54)$$

$$\mathbf{F} = \begin{bmatrix} 1 & 0 \\ 0 & 1 \end{bmatrix}, \mathbf{B}_{[k]} = \begin{bmatrix} \cos(\psi_{[k]}) & -\sin(\psi_{[k]}) \\ \sin(\psi_{[k]}) & \cos(\psi_{[k]}) \end{bmatrix}, \mathbf{H} = \begin{bmatrix} 1 & 0 \\ 0 & 1 \end{bmatrix} \quad (4.55)$$

In addition, the covariance matrices $\mathbf{Q}_{[k]}$ and $\mathbf{R}_{[k]}$ are assumed again in this case constant of the following form:

$$\mathbf{Q}_{[k]} = \begin{bmatrix} \sigma_{sys}^2 & 0 \\ 0 & \sigma_{sys}^2 \end{bmatrix} \quad (4.56)$$

$$\mathbf{R}_{[k]} = \begin{bmatrix} \sigma_{pos}^2 & 0 \\ 0 & \sigma_{pos}^2 \end{bmatrix} \quad (4.57)$$

The value σ_{sys}^2 can be derived experimentally from the filtered yaw angle and distance measurements. The value σ_{pos}^2 can be approximated experimentally from a number of observations of absolute measurements for a known location.

4.4.5 Multi-System Position Fusion

The position accuracy can be improved by integrating multiple positioning systems and fusing their data with the bicycle motion data. Thus, Figure 4-14 illustrates the design of the multi-system position fusion where additional positioning systems are incorporated into the design demonstrated in Figure 4-13. In other words, the Kalman filter model derived in the previous section can also be employed to fuse the data from Wi-Fi and cell tower localisation systems. However, the covariance matrix $\mathbf{R}_{[k]}$ will be different as the additional systems are considered to have different kinds of error than the GPS. In addition, as found from the review in Section 3.4, Wi-Fi hotspots and cell towers are usually mapped using GPS and their position errors in some cases could be larger than GPS. As a result, the value σ_{pos}^2 can be determined experimentally from a set of observations for several known locations and signals from Wi-Fi and cell tower systems.

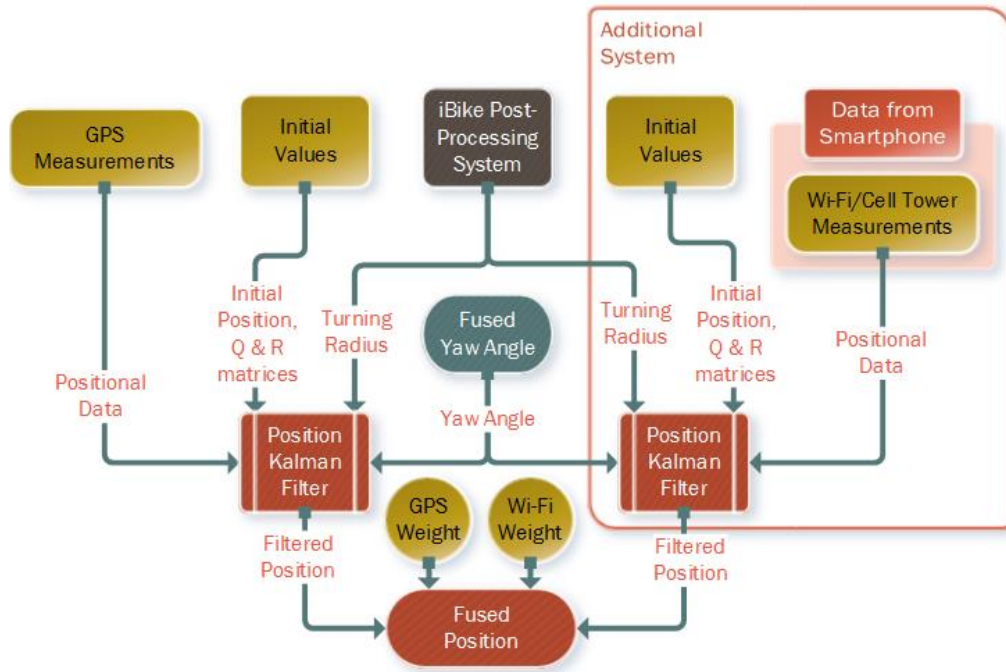


Figure 4-14: Design of the multi-system position fusion.

The outputs from each Kalman filter can be merged using Equation (4.58) in which weighting factors, Wt_{GPS} , Wt_{WPS} and Wt_{CTPS} are incorporated and they can be used to select an appropriate fusion level of the positioning data. Again, the weighting factors can be determined experimentally from the field trials and using Equation (4.46).

$$\mathbf{X}_{fused[k]} = Wt_{GPS}[\mathbf{X}_{[k]}] + Wt_{WPS}[\mathbf{X}_{[k]}] + Wt_{CTPS}[\mathbf{X}_{[k]}] \quad (4.58)$$

4.5 Datum Conversions

The subject of geodesy, on which all mapping and navigation are based, seems extraordinarily complex as modelling the real-world surface of the Earth is difficult due its shape and motion. Thus, only approximate models (with several assumptions) exist to transform coordinates from one coordinate system to another. Nevertheless, for validation of trajectories data that will be gathered through the instrumented bicycle, it was decided to use the Ordnance Survey National Grid (OSNG) reference system [123], a system of geographic grid references used in Great Britain. The Ordnance Survey grid is suitable because distances between the points are straightforward to calculate by applying Pythagoras' theorem. The National Grid is different from using latitude and longitude, the most common way of stating terrestrial position, to define a unique point with two sets of angles. The

National Grid is based on the Ordnance Survey of Great Britain 1936 (OSGB36) datum. The Terrestrial Reference System (TRS) for GPS is known as the World Geodetic System 1984 (WGS84) [124]. The longitude and latitude positions on OSGB36 are the same as for WGS84 at point 49°N 2°W (the ‘true origin’ of the OSGB). The OSNG uses a simple 2D Cartesian system, in which the two axes are known as eastings and northings, and this is the coordinate system employed in this study.

The most common geodetic transformation between OSGB36 and WGS84 is called the Helmert datum transformation [125], [126]. The conversion procedures and algorithms can be obtained from the guide to coordinate systems in Great Britain [127]. However, for the purpose of a prototype system, the data from the positioning systems will not be fused in real-time. Hence, the Grid InQuestII software [128], developed by Ordnance Survey, can be used to convert between the datums during post-processing stage. A screenshot of the software is shown below.

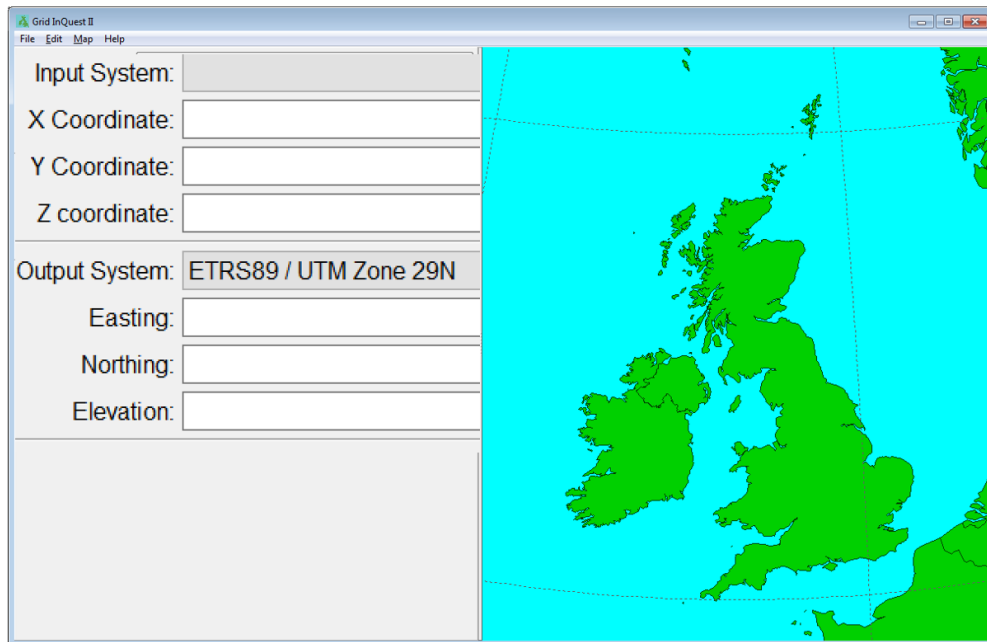


Figure 4-15: Datum conversion software [128].

Moreover, Equation (4.24) can be easily represented in latitude (lat) and longitude (lon) if the initial values are also in the same format. The following equations can be used to carry out the conversion.

$$lat_{[k]} = lat_{[k-1]} + \frac{180(y_{[k]})}{\pi(R_E)} \quad (4.59)$$

$$lon_{[k]} = lon_{[k-1]} + \left(\frac{180^2(x_{[k]})}{\pi^2(R_E) \cos(lat_{[k]})} \right) \quad (4.60)$$

where R_E is the radius of the Earth (6378137m) and $x_{[k]}$ and $y_{[k]}$ are as follows:

$$x_{[k]} = d\tilde{x}_{[k-1]} \cdot \cos(\psi_{[k-1]}) + d\tilde{y}_{[k-1]} \cdot (-\sin(\psi_{[k-1]})) \quad (4.61)$$

$$y_{[k]} = d\tilde{x}_{[k-1]} \cdot \sin(\psi_{[k-1]}) + d\tilde{y}_{[k-1]} \cdot \cos(\psi_{[k-1]}) \quad (4.62)$$

where $d\tilde{x}$ and $d\tilde{y}$ can be found using Equations (4.21) and (4.22).

4.6 Design of the Post-Processing Algorithms

From the study of bicycle geometry and the derivation of the models in this chapter, Figure 4-16 illustrates the design of the overall algorithms, together with the data flow.

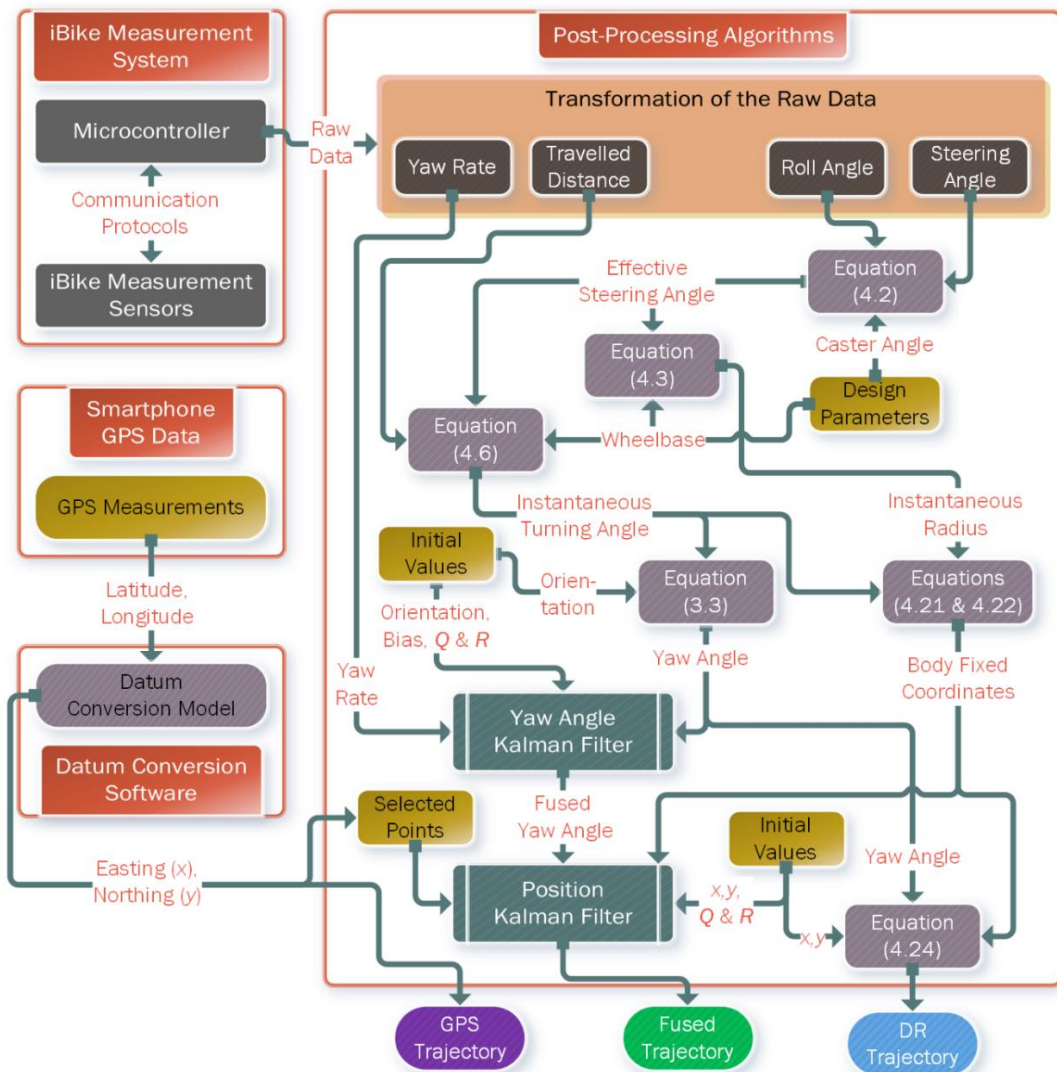


Figure 4-16: Design of the overall algorithms.

The design in Figure 4-16 above is to be utilised to transform bicycle motion measurements into relative positions and to fuse the positions with localisation systems discussed in Section 3.6. The overall design is vastly simplified for illustration purposes and it only shows one yaw angle and one position Kalman filters from Sections 4.4.2 and 4.4.4 respectively. As can be seen from the diagram, the algorithms take the input raw data from several measurement sensors and the data then transformed into two essential parameters: the yaw angle and the turning radius of the rear wheel. These two input parameters are required for the simplified model outlined in Section 4.3.2. The algorithms then output a trajectory based on the DR technique described and also produce a fused trajectory based on the Kalman filter models, which also take the positioning data collected via a smartphone. Finally, outputs also show the GPS trajectory so that the DR and the fused trajectories can be compared. Therefore, the goal is to generate three trajectories based on the measurements and to compare them with a ground truth path so that the algorithms can be validated.

In summary, the four critical kinematics measurement parameters of steering angle (δ), roll angle (ϕ), yaw rate ($\dot{\psi} = \omega$) and travelled distance (d_r), along with two crucial bicycle design parameters of wheelbase (W) and caster angle (η) are required to successfully implement the models. Inherently, this means that roll rate ($\dot{\phi}$), and real wheel diameter (\mathcal{D}) are also required. However, in general, sensor acquired data do not directly provide the required measurement parameters. This part of data acquisition and processing of the raw data in the case of the iBike is explained in Chapter 5 – the development of the prototype system.

4.7 Conclusions

From the analysis of the bicycle's unique characteristics, it is understood that it is an underactuated system; it has fewer control variables than the degrees of freedom. However, under normal conditions a bicycle's motion is controlled through three essential parameters: steering angle, tilt angle and speed. Thus, kinematics and a turning geometry of a bicycle were studied to formulate a geometric relationship of the steering mechanism. Then a path tracking technique commonly employed in robotics known as Dead-Reckoning algorithm was identified and the relevant models for the algorithm were established.

Supported by the initial set of experiment results, it was found that the model can be further enhanced. Hence, a new simplified model is derived by assuming that the effective steering angle of a bicycle never equals zero and the turning radius is much greater than the instantaneous arc distance, which can be approximated as a straight line. This led to the design of the optimal state estimation algorithm, the Kalman filter, to fuse GPS and other localisation systems data with the measurements of the bicycle's motion parameters. In summary, from the bicycle geometrical relationship and analysis, it is determined that five kinematics measurements and three design parameters are required along with the measurements from GPS, Wi-Fi hotspots and cell towers.

Chapter 5: Development of iBike Prototype System

5.1 Introduction

The development of the complete Cyclist 360° Alert system consists of several phases. The present study relates to the first phase, whose objective is to develop a prototype instrumented bicycle to collect real-world data using the methodology derived in Chapter 4 in order to apply the proposed algorithms using the field data. Therefore, this chapter presents the development of the instrumented bicycle together with the software system. Specifically, Section 5.2 presents the chosen measurement sensors and explains how the raw data from the sensors are converted to the required kinematic measurements outlined in the previous chapter. Section 5.3 outlines each separate system acting as a standalone system instrumented on the bicycle, and illustrates the architecture design that combines the data from each system to form one collective dataset. Section 5.4 demonstrates the final prototype system of the instrumented bicycle and provides the outputs data field of the overall system. Section 5.5 firstly outlines the formulation of the overall system architecture and then discusses the development and implementation of the data acquisition and post-processing software via the database structure. Finally, Section 5.6 concludes this chapter with a summary of the implementation of the prototype system.

5.2 iBike Measurement Sensors

The objective is to instrument a bicycle with sensors to capture its five kinematic parameters of steering angle (δ), roll angle (ϕ), roll rate ($\dot{\phi}$), yaw rate ($\dot{\psi} = \omega$), travelled distance (d_r). Therefore, the following four sensors are identified:

- Hall Effect – to measure the revolution of the wheel.
- Absolute Encoder – to measure the steering angle.
- Gyroscope – to measure the yaw and roll rates.
- Accelerometer – to measure the roll angle.

Thus, the following subsections briefly discuss the actual off-the-shelf selected sensors for this project, and demonstrate how the raw data from each sensor is transformed to obtain the necessary kinematics measurements of the bicycle for the design of the algorithms in Section 4.6. In addition, the operating principle of each of the sensors can be found in Appendix A.

5.2.1 Hall Effect

5.2.1.1 Selected Sensor

There are two basic types of digital Hall Effect sensors; bipolar and unipolar. Bipolar sensors require a positive magnetic field (South Pole) to operate them and a negative field (North Pole) to release them and these bipolar sensors are known as Hall Effect latches. On the other hand, unipolar sensors require only a single magnetic south pole to both operate and release them as they move in and out of the magnetic field and these sensors are known as Hall Effect switches. A wide range of off-the-shelf Hall Effect sensors are available and they all have unique features that distinguish them. The Cherry GS100502 [129] sensor is chosen for this project. This is a geartooth speed sensor and it is designed for use in applications where ferrous edge detection or near zero speed sensing is required. These sensors employ the Hall element to sense the variation in flux found in the airgap between a magnet and passing ferrous gearteeth. Thus, this type of Hall Effect sensor operates differently from a normal Hall Effect sensor. In other words, the Hall Effect geartooth sensor produces magnetic fields and when a ferrous material passes near the device, it disturbs the magnetic flux; hence the sensor detects this signal and generates an output voltage signal accordingly. The picture in Figure 5-1 shows the actual sensor that is used for the instrumentation of the bicycle.



Figure 5-1: Hall Effect geartooth sensor [130].

The chosen Hall Effect geartooth sensor has the following key features:

- Housing Material: Aluminium
- IP rating: IP68
- Length: 65mm
- Operating Voltage Range: 5-24V
- Maximum Supply Current: 6mA
- Output Type: 3-wire sink
- Operating Temperature Range: -40 to 125 °C
- Output Rise Time: 5 μ S
- Output Fall Time: 5 μ S

Figure 5-2 illustrates the circuit diagram of this device, which is used to configure the sensor to a microcontroller so that generated pulses from the sensor can be detected accurately with a timestamp.

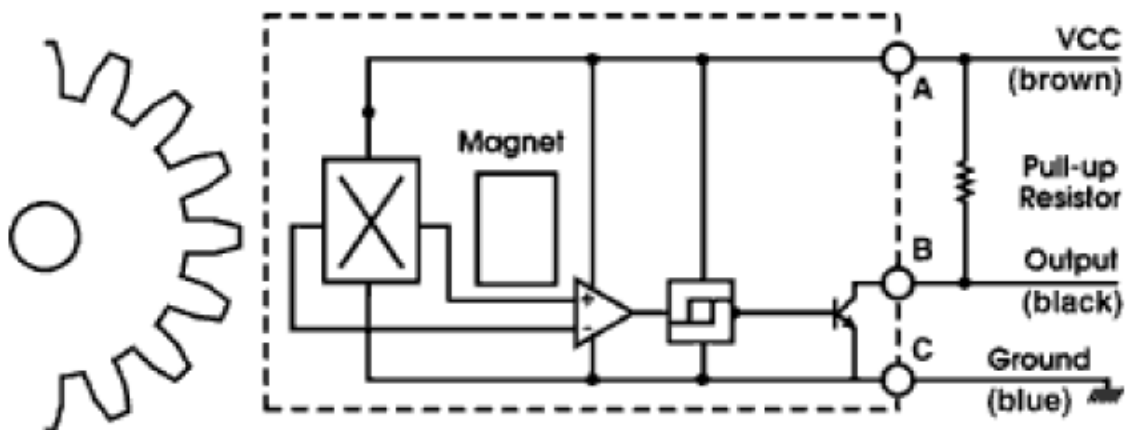


Figure 5-2: Hall Effect - Open Collector Sinking Block Diagram [129].

An initial test with the chosen sensor and the spokes on the bicycle has shown that the material used for the production of the spokes is not ferromagnetic. Thus, the sensor cannot detect the spokes very well. Consequently, as illustrated in Figure 5-3, 18 additional spoke magnets were attached to the wheel to fulfil the requirement stated in Section 4.3.2, where the assumption is that the arc distance, d_r , is very small compared to turning radius R .



Figure 5-3: Installation of spoke magnets

5.2.1.2 Transformation of the Raw Data to Travelled Distances

A microcontroller can be used to detect the pulses and to time their presence with millisecond accuracy. However, to translate the pulses into a travelled distance from point A to B, a mathematical model is required. As a result, Equations (5.1) and (5.2) are derived to convert the detected pulses into d_r . Thus, once the distance and time measurement between two points are known, the speed can be computed as portrayed by Equation (5.3).

$$\text{Arc Length } (L_{arc}) = \frac{\pi \cdot \mathcal{D}}{\text{Number of spoke magnets}} \quad (5.1)$$

$$d_{r[k]} = L_{arc} \cdot (\text{Count}_{[k]} - \text{Count}_{[k-1]}) \quad (5.2)$$

$$\text{Speed}_{[k]} = \frac{d_{r[k]}}{\text{Time}_{[k]} - \text{Time}_{[k-1]}} \left[\frac{m}{s} \right] \quad (5.3)$$

Figure 5-4 illustrates the concept and overall algorithm design that were used to convert the raw measurements to travelled distances.

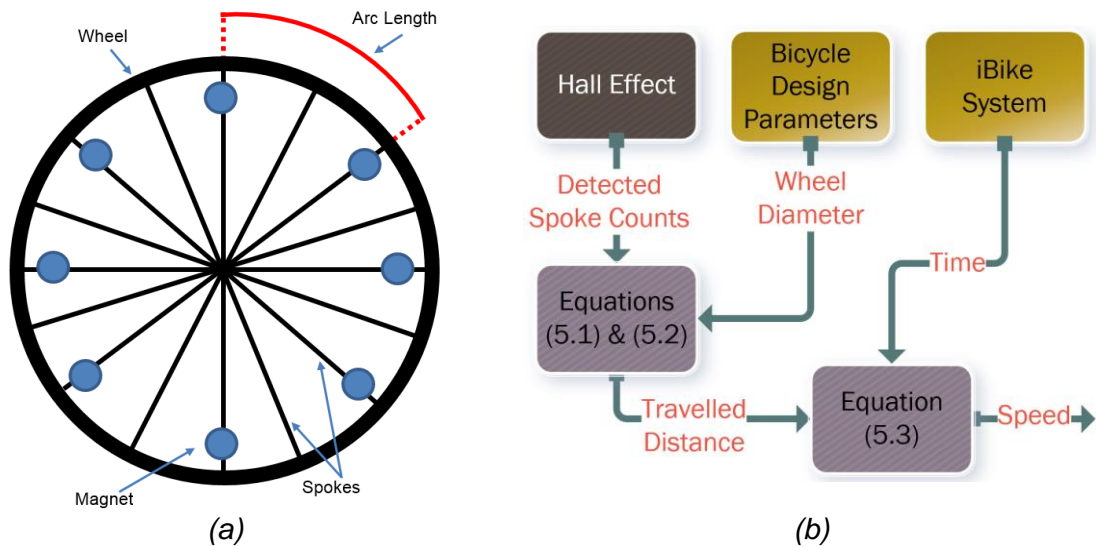


Figure 5-4: (a) Spoke magnets arrangement, (b) pulses to distance algorithm design.

5.2.2 Absolute Encoder

5.2.2.1 Selected Sensor

For this project, an absolute optical encoder is employed to measure the steering angle (δ) as this type of sensor maintains its position information even when the power is turned off and eliminates the need for a zero cycle. The A2K optical encoder [131], manufactured by US Digital, is chosen for the instrumentation. This A2K is a 12-bit absolute rotary position sensor kit that reports a shaft angle within a single 360-degree rotation of a shaft. The interface of the A2K utilises the US Digital Serial Encoder Interface (SEI) [132] bus, but the chosen A2K also has the option of analogue outputs. In other words, the A2K can provide an analogue voltage proportional to the angular position with a 12-bit resolution. The internal microcontroller in this device takes a sample of the disk every seven microseconds and stores the position in a memory. It responds immediately to a "report position request" by sending this value that is always the most current position. The A2K has the following key features [133]:

- Operating Temperature: -25 to 70 °C
- Maximum Acceleration: 100000 rad/sec²
- Supply Voltage: 5.5 to 16V
- Maximum Supply Current (Active): 18.5mA
- Maximum Full-Scale Analogue Voltage: 4.11V
- Angle Tracking Speed (Single-turn mode): 3600rpm

- Position Update Rate: 7ms

The picture in Figure 5-5 shows the chosen A2K optical encoder. As can be seen, the kit needs to be assembled onto an existing shaft and bearing so that an absolute steering angle based on a shaft can be obtained. A detailed configuration of the A2K kit on the bicycle steering hub is illustrated in Appendix A.

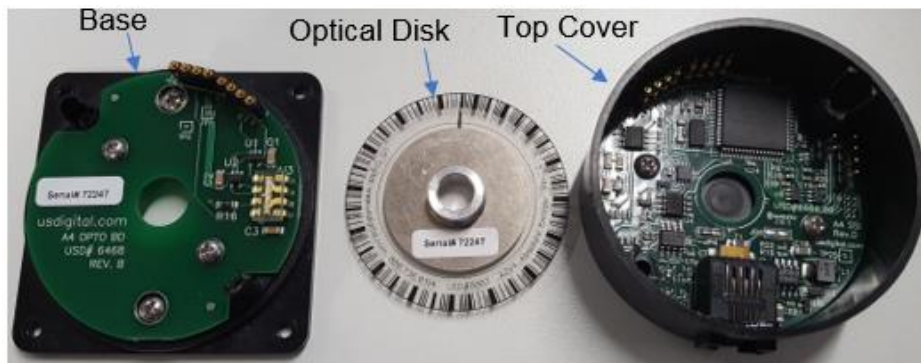


Figure 5-5: US digital A2K absolute encoder.

5.2.2.2 Transformation of the Raw Data to Bicycle Steering Angle

The following equation is used to convert the analogue value from the encoder into a steering angle.

$$\delta_{[k]} = \frac{ADC_{value}(Zero_{RefValue} - A2K_{value[k]}) \cdot \pi}{180} [rad] \quad (5.4)$$

where ADC_{value} is the analogue to digital converter value, $Zero_{RefValue}$ is the value of the encoder when the bicycle's handlebar is orthogonal to the rear main frame, which is obtained through an experiment result illustrated in Appendix C, and $A2K_{value[k]}$ is the value from the sensor.

Figure 5-6 below further illustrates the design of the algorithm to convert the raw data into the bicycle steering angle.

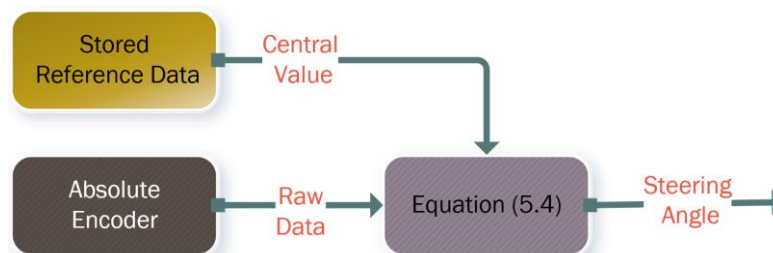


Figure 5-6: Raw value into steering angle algorithm design.

5.2.3 Gyroscope

5.2.3.1 Selected Gyroscope

MEMS gyroscope L3G4200D is chosen to be used in this project. The L3G4200D is a low-cost and low-power three-axis angular rate sensor which is able to provide stability and sensitivity over temperature and time. The device also includes a sensing element and an IC interface capable of providing the measured angular rate to the external world through a digital interface. The device has two types of digital interface; Inter-Integrated Circuit (IIC) and Serial Peripheral Interface (SPI). The IIC communication protocol is chosen to integrate the sensor with the rest of the iBike components. This type of protocol allows multiple devices to be connected to two-bidirectional communication lines where a microcontroller can act as the master and all the other devices on the lines act as the slaves. In other words, this type of protocol allows a straightforward connection and method to communicate with the device to read the raw data.

The chosen gyroscope has the following key features [134] which made it an appropriate sensor to be used for the iBike system:

- Three selectable full scales: 250 or 500 or 2000 degrees per second (dps)
- 16 bit-rate value data output
- Integrated low- and high-pass filters with user-selectable bandwidth
- Ultra-stable over temperature and time
- Wide supply voltage: 2.4 V to 3.6 V
- Embedded power-down and sleep mode
- Embedded temperature sensor
- Embedded first in, first out (FIFO) data buffer
- High shock survivability
- Extended operating temperature range (-40 °C to +85 °C)

Figure 5-7 shows the pinouts and the direction of the sensing axis, which is crucial to design the circuit and the firmware for the microcontroller to be used so that data can be interpreted correctly.

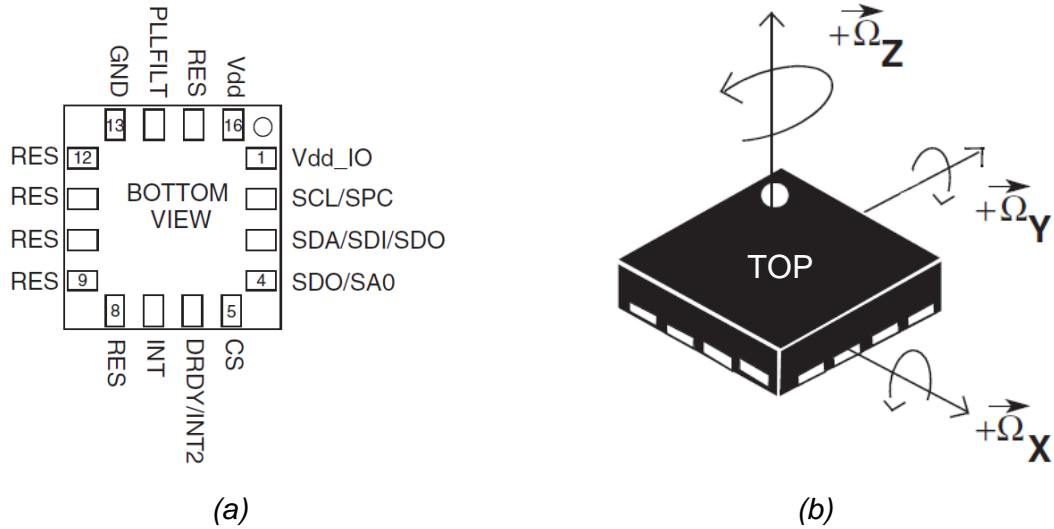


Figure 5-7: (a) L3G4200D pinout description and (b) direction of the detectable angular rates [134].

5.2.3.2 Transformation of the Raw Data to Bicycle Angular Rates

The MEMS Gyroscope measures in its body axis and in order to translate the measurements into the bicycle axis, the following two standard matrices, which are widely used to determine orientation of an aircraft [135], can be used, where p, q, r are the rates in the body axis and $\dot{\phi}, \dot{\theta}, \dot{\psi}$ are non-orthogonal Euler-angle rates.

$$\begin{bmatrix} p \\ q \\ r \end{bmatrix} = \begin{bmatrix} 1 & 0 & -\sin(\theta) \\ 0 & \cos(\phi) & \sin(\phi) \cos(\theta) \\ 0 & -\sin(\phi) & \cos(\phi) \cos(\theta) \end{bmatrix} \begin{bmatrix} \dot{\phi} \\ \dot{\theta} \\ \dot{\psi} \end{bmatrix} \quad (5.5)$$

$$\begin{bmatrix} \dot{\phi} \\ \dot{\theta} \\ \dot{\psi} \end{bmatrix} = \begin{bmatrix} 1 & \sin(\phi) \tan(\theta) & \cos(\phi) \tan(\theta) \\ 0 & \cos(\phi) & -\sin(\phi) \\ 0 & \sin(\phi) \sec(\theta) & \cos(\phi) \sec(\theta) \end{bmatrix} \begin{bmatrix} p \\ q \\ r \end{bmatrix} \quad (5.6)$$

Assuming a flat surface and a negligible pitch angle for the bicycle, i.e. $\theta \cong 0$, the above matrices can be simplified as follows:

$$p = \dot{\phi} \quad (5.7)$$

$$q = \dot{\psi} \sin(\phi) \quad (5.8)$$

$$r = \dot{\psi} \cos(\phi) \quad (5.9)$$

$$\dot{\phi} = p \quad (5.10)$$

$$\dot{\theta} = q \cos(\phi) - r \sin(\phi) \quad (5.11)$$

$$\dot{\psi} = q \sin(\phi) + r \cos(\phi) \quad (5.12)$$

However, if $\theta \cong 0$ then the rate, $\dot{\theta}$, must also be approximately equal to zero. Therefore, Equation (5.12) can be simplified as follows:

$$\dot{\theta} = q \cos(\phi) - r \sin(\phi) = 0 \quad (5.13)$$

$$\therefore q = \frac{r \sin(\phi)}{\cos(\phi)} \quad (5.14)$$

Substituting q in Equation (5.14):

$$\dot{\psi} = \frac{r \sin(\phi) \sin(\phi)}{\cos(\phi)} + r \cos(\phi) \quad (5.15)$$

The above equation can be simplified as follows:

$$\dot{\psi} = r \left(\frac{\cos^2(\phi) + \sin^2(\phi)}{\cos(\phi)} \right) \quad (5.16)$$

$$\dot{\psi} = \frac{r}{\cos(\phi)} \quad (5.17)$$

Consequently, the relationship of the gyroscope's roll rates stated in Equation (5.10) are directly proportional to the roll rates in bicycle axis, and from Equation (5.17) the bicycle yaw rates can be found by dividing the gyroscope's yaw rates with the cosine of the roll angle in the bicycle axis. The latter equation also relates to Equation (4.2) where the roll angle is used to compute the effective steering angle.

The measurement of the angular rates using a MEMS gyroscope also incorporates bias, ω_{bias} , and measurement noise. For this reason, MEMS sensors require careful calibration before the signals can be converted to angles. The true calibration procedure can be quite complex as demonstrated in [136] but, very briefly, it involves prior knowledge of the MEMS sensors' behaviour, and this is commonly found through experiments since noise presented in the signals can vary from one sensor to another. Environment parameters such as temperature also affect the sensor's outputs. In this study, an experiment is conducted with a test rig and the calibration is based on the adjustment of the sensor's outputs with respect to the preliminary defined sensitivity and the measured offset. Equation (5.18) illustrates the mathematical relationship of the calibration of the raw data.

$$Gc_{[k]} = \frac{(\mu_{Gyro} Gr_{[k]} - Gf) \cdot \pi}{180} \text{ [rad/s]} \quad (5.18)$$

Where, $Gc_{[k]}$ is the calibrated raw value of the gyroscope at time k , μ_{Gyro} is the sensitivity of the gyroscope based on the datasheet [137], $Gr_{[k]}$ is the extracted raw data from the gyroscope at time k and Gf is the measured offset value found using an experiment conducted through the aid of a test rig which was developed to obtain initial sets of data from the sensors and to test the measurement accuracy of angles in static and dynamic conditions. Further details of the developed test rig are given in Appendix B.

The following Trapezoidal integration method from [138] is employed to compute the angles based on each respective axis of the gyroscope from the calibrated data $Gc_{[k]}$:

$$(t_{[k]} - t_{[k-1]}) [Gc_{[k-1]} + 0.5(Gc_{[k]} - Gc_{[k-1]})] \quad (5.19)$$

where, $t_{[k]}$ and $t_{[k-1]}$ are the previous and current integration time respectively.

Figure 5-8 below demonstrates the data flow from the sensor and the iBike system, which are used to translate the raw data into angles.

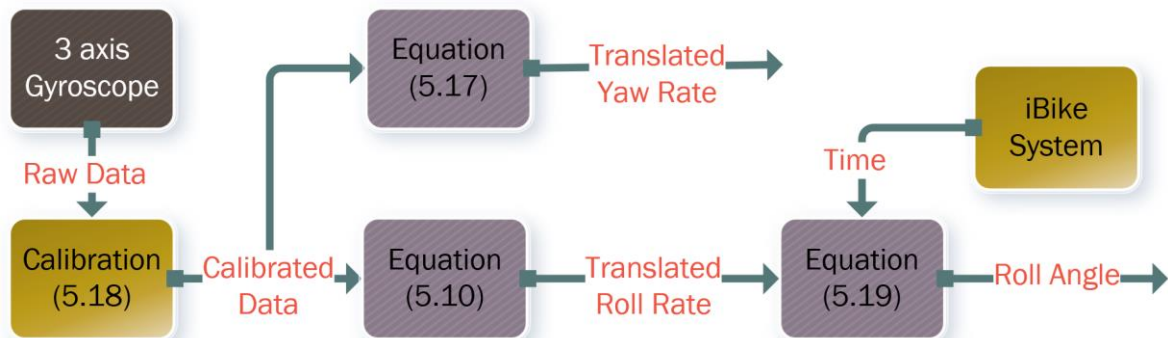


Figure 5-8: Raw value to angles algorithm design.

5.2.4 Accelerometer

5.2.4.1 Selected Accelerometer

The MEMS gyroscope sensors often provide very accurate angular rates momentarily in dynamic situations, whereas the MEMS accelerometer sensors

provide accurate acceleration data mostly in static situations. As a result, often these sensors' data are fused to obtain more accurate measurements. Furthermore, the bicycle's roll angle cannot be measured directly with an encoder as it requires a relative reference point. For these reasons, the ADXL345 digital accelerometer, manufactured by Analog Devices [139], is chosen to be used for this project. The ADXL345 is a small, low-cost, low-power, 3-axis accelerometer which offers a high resolution. Like the L3G4200D gyroscope discussed previously, the output data is also formatted as a 16-bit two's complement and is accessible through either an SPI (3- or 4-wire) or IIC digital interface. The IIC protocol is chosen so that both the gyroscope and accelerometer can be connected to the same communication lines. The ADXL345 accelerometer has the following key features, which meet the specification for this project.

- Ultra low power: 40 μA in measurement mode and 0.1 μA in standby mode at $V_S = 2.5\text{ V}$ (typical)
- Power consumption scales automatically with bandwidth
- User-selectable resolution: 10 to 13-bit resolution at $\pm 16\text{ g}$
- Measurement accuracy of inclination changes: 1° or less
- Temperature range: -55°C to $+105^\circ\text{C}$

Figure 5-9 illustrates the pinout and the axes of acceleration sensitivity of the selected accelerometer. This information is vital for the circuit design and the correct interpretation of the raw data.

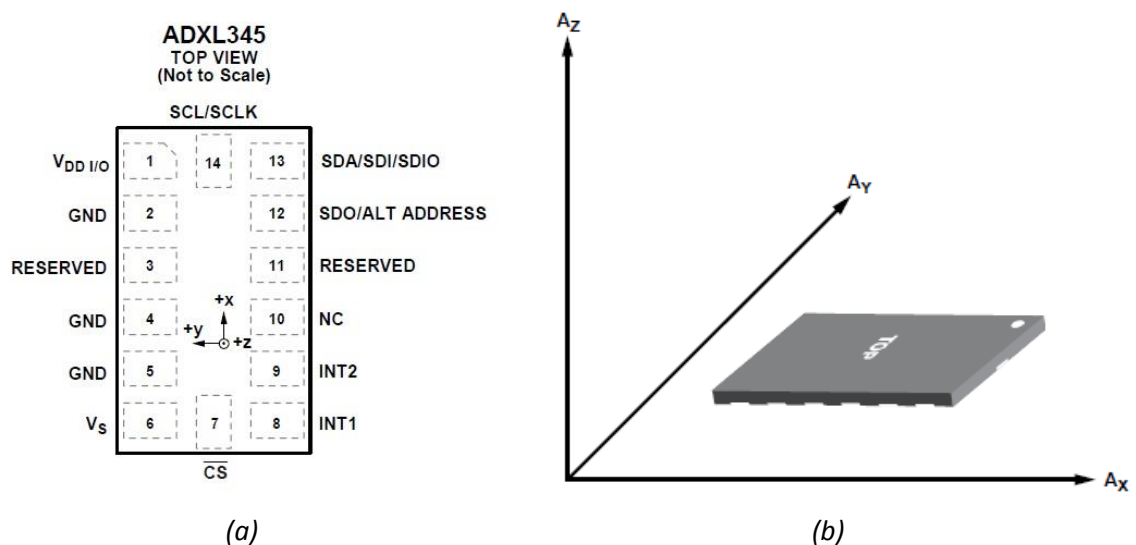


Figure 5-9: (a) ADXL345 pinout configuration and axes of acceleration sensitivity [139].

Figure 5-10 below demonstrates the outputs response of a typical electronic accelerometer. As can be seen from the diagrams, each axis responds to the force of the gravity differently and this makes it possible to determine an object's orientation in a three-dimensional space. Similarly, the orientation of the bicycle can be determined accurately but the accelerometer must be placed with respect to the bicycle axes defined in Figure 4-4. The following values will vary according to the angle of the bicycle.

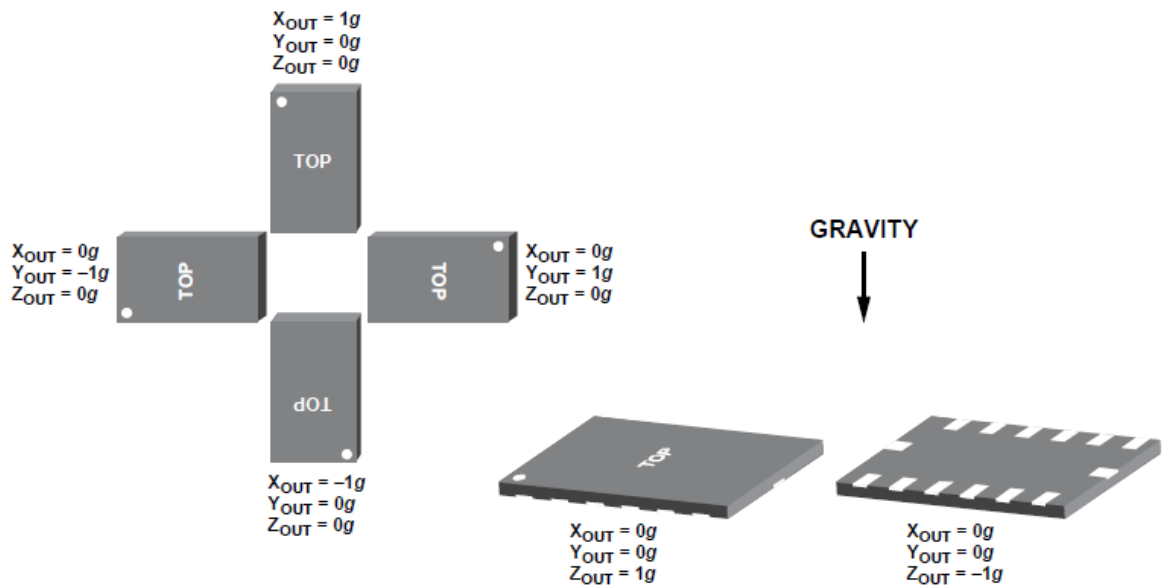


Figure 5-10: Accelerometer output response versus its orientation to gravity [139].

5.2.4.2 Transformation of the Raw Data to Bicycle Roll Angle

The measurements from the MEMS Accelerometer also contain noise but it can be minimised with a careful calibration. Thus, as with the gyroscope, the calibration of the data from the accelerometer is based on a prior knowledge of the measurement offset. The corresponding mathematical equation is portrayed below.

$$Ac_{[k]} = \mu_{Acc}Ar_{[k]} - Af \quad (5.20)$$

where, $Ac_{[k]}$ is the calibrated raw value of the accelerometer at time k , μ_{Acc} is the scale factor from the datasheet [139] based the configuration of the sensor, $Ar_{[k]}$ is the extracted raw data from the accelerometer at time k and Af is the measured offset value found using an experiment with the test rig discussed in Appendix B. The above formula is applied to all three axes of the accelerometer's raw data.

Given that the accelerometer can provide accurate measurements in static conditions, and if the only measured acceleration is due to gravity, the following equation found in the application note [140] can be employed to compute the roll angle of the sensor.

$$\phi_{Ac[k]} = \tan^{-1} \left(\frac{\sqrt{Ac_X^2[k] + Ac_Y^2[k]}}{Ac_Z[k]} \right) [rad] \quad (5.21)$$

where, $Ac_X[k]$, $Ac_Y[k]$ and $Ac_Z[k]$ are the calibrated raw value of the accelerometer at time k for each respective axis. The above formula assumes that the reference position is taken with the X-axis and Y-axis in the plane of the horizon (0g field) and the Z-axis orthogonal to the horizon (1g field). It is also assumed that the reference system correlates to the bicycle axis. In other words, it is assumed that when the bike is perpendicular to the ground, the roll angle based on Equation (5.21) above is zero.

Since neither the accelerometer nor the gyroscope provides very accurate rotational measurements alone, the implementation of a sensor fusion algorithm can compensate for the errors as both sensors have a different type of error. A complementary filter can be utilised to fuse the accelerometer and gyroscope angles through a simple algorithm found in the literature [141] and [142]. Figure 5-11 represents a complementary filter algorithm design, which was also incorporated in Figure 4-16. As can be seen from the diagram below, in order to optimise the results, the accelerometer and gyroscope signals have to be filtered through a low-pass and high-pass filters respectively. The equations for the filters are as follows:

- Digital low-pass filter:

$$\phi_{A[k]} = \vartheta \cdot \phi_{Ac[k]} + (1 - \vartheta)\phi_{A[k-1]} \quad (5.22)$$

where the smoothing factor $0 \leq \vartheta \leq 1$ can be approximated as follows:

$$\vartheta = \frac{\Delta T}{\tau + \Delta T} \quad (5.23)$$

where, τ is the time constant of the relative duration of the signal that the filter will act on and ΔT is the sample period. However, τ is difficult to

determine theoretically so the test rig presented in Appendix B was used to approximate the smoothing factor experimentally.

➤ Digital high-pass filter:

$$\phi_G[k] = \vartheta \cdot \phi_G[k-1] + \vartheta(\phi_{Gc}[k] - \phi_{Gc}[k-1]) \quad (5.24)$$

Again, the smoothing factor $0 \leq \vartheta \leq 1$ can be found experimentally or can be approximated as follows, if τ is known.

$$\vartheta = \frac{\tau}{\tau + \Delta T} \quad (5.25)$$

The output fused angle can then be obtained as follows:

$$\phi_{fused}[k] = Wt_{Gyro} \cdot \phi_G[k] + (1 - Wt_{Gyro})\phi_A[k] \quad (5.26)$$

where, $\phi_{fused}[k]$ is the fused roll angle at time k , $\phi_G[k]$ is the output from the high pass filter at time k , $\phi_A[k]$ is the output from the low pass filter at time k and Wt_{Gyro} is the weighted factor for the gyroscope and it is adjusted experimentally. The factor makes it possible intelligently to adjust the coefficient depending on the scenario. For instance, if the bicycle is observed to be stationary then the weighted factor will be reduced, thus placing more importance on the measurements of the accelerometer.

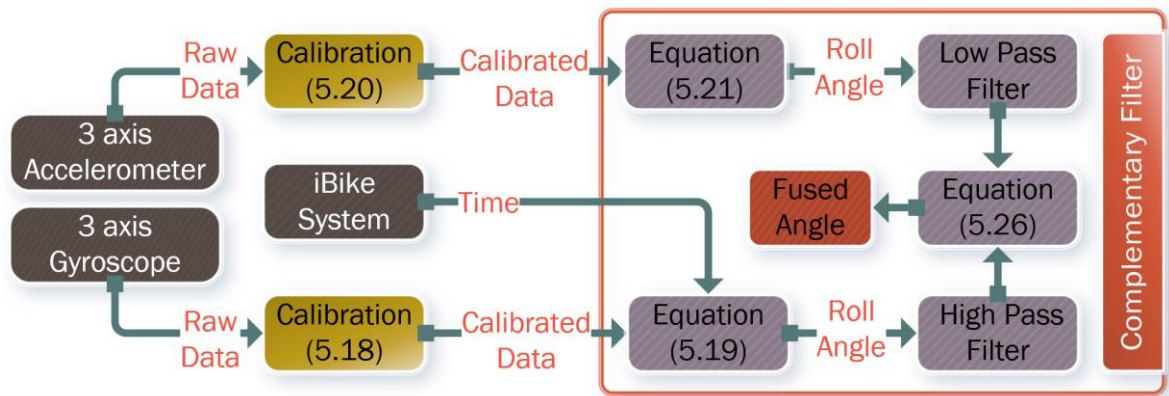


Figure 5-11: Design of the complementary filter.

5.3 Individual Subsystems

The following subsections describe each individual system, designed to operate independently of each other, on the bicycle. These subsections also illustrate with

diagrams how the data from each system are then gathered as one collective set of data by a data acquisition system.

5.3.1 iBike Measurement System

A microcontroller is required first to take sample measurements of the iBike sensors shown in the previous Section 5.2. Secondly, it is required to store the data on a memory card or to transmit the data to a laptop in real-time. For these applications, an Arduino board is an appropriate choice as it simplifies the hardware and software requirements for the development of a prototype system with the addition to the open-source libraries that can be used for the embedded system.

5.3.1.1 Selected Boards

Arduino Mega 2560 is chosen to be utilised for this project as it meets the required technical specifications. The Mega, based on the ATmega2560, is a microcontroller board which also incorporates a 16 MHz crystal oscillator, a USB connection, a power jack, an ICSP header and a reset button [143]. The board has 54 digital input and output pins and 16 analogue input pins. In addition, some of the digital and analogue pins have specialised functions which include four hardware serial ports and six hardware interrupts. The board also supports both the SPI and IIC communications. A summary of the key technical features is listed below:

- Operating Voltage: 5 V
- Input Voltage (recommended): 7-12 V
- DC Current per I/O Pin: 40 mA
- DC Current for 3.3V Pin: 50 mA
- Flash Memory: 256 KB of which 8 KB used by boot loader
- Static Random Access Memory (SRAM): 8 KB
- Electrically Erasable Programmable Read-Only Memory (EEPROM): 4 KB

Figure 5-12 below illustrates the Arduino Mega board with annotated features.

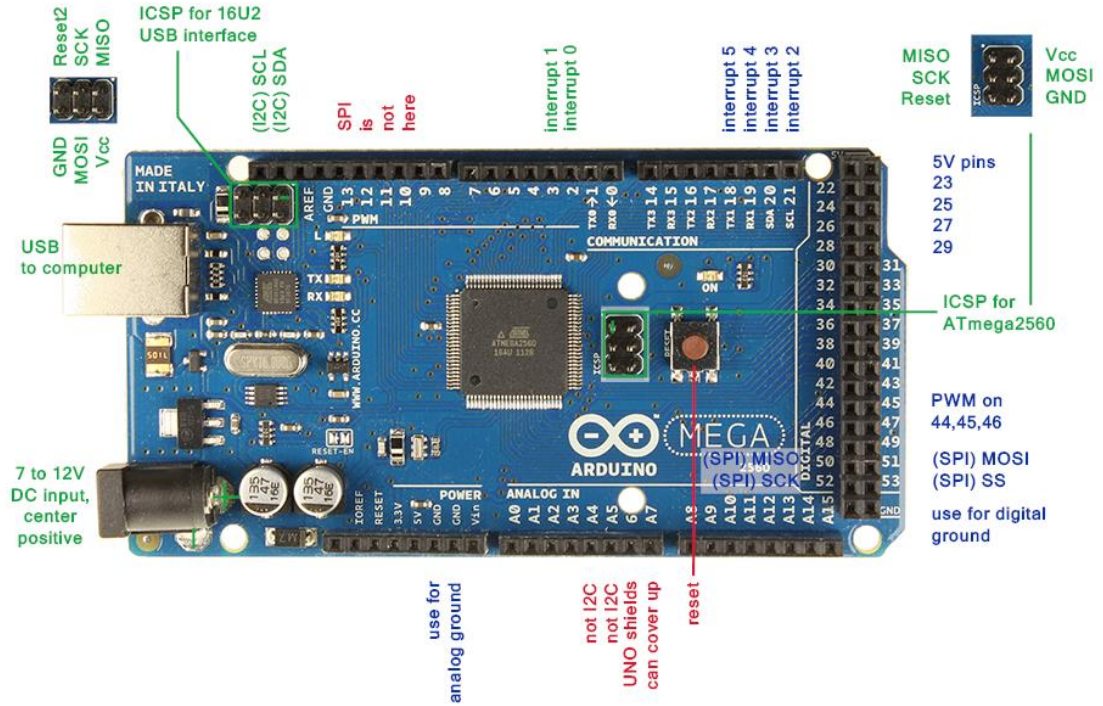


Figure 5-12: Arduino Mega 2560 R3 Front [144].

Given the ultimate goal of developing a portable version of the iBike system, it was, therefore, decided to incorporate an Arduino Mini board in the design so as to enable future development and testing of a portable system. The Arduino Mini is a small microcontroller board originally based on the ATmega168, but now supplied with the ATmega328. The Mini has 14 digital input and output pins and 8 analogue input pins with a 16 MHz crystal oscillator and a reset button. The board also supports serial and IIC communications. However, unlike the Arduino Mega board, the Mini requires an external serial adapter to upload the firmware or the sketch. The new Mini (revision 05) has a new package for the ATmega328, which enables all components to be on the top of the board [145]. Figure 5-13 below illustrates the Arduino mini with pin annotation.

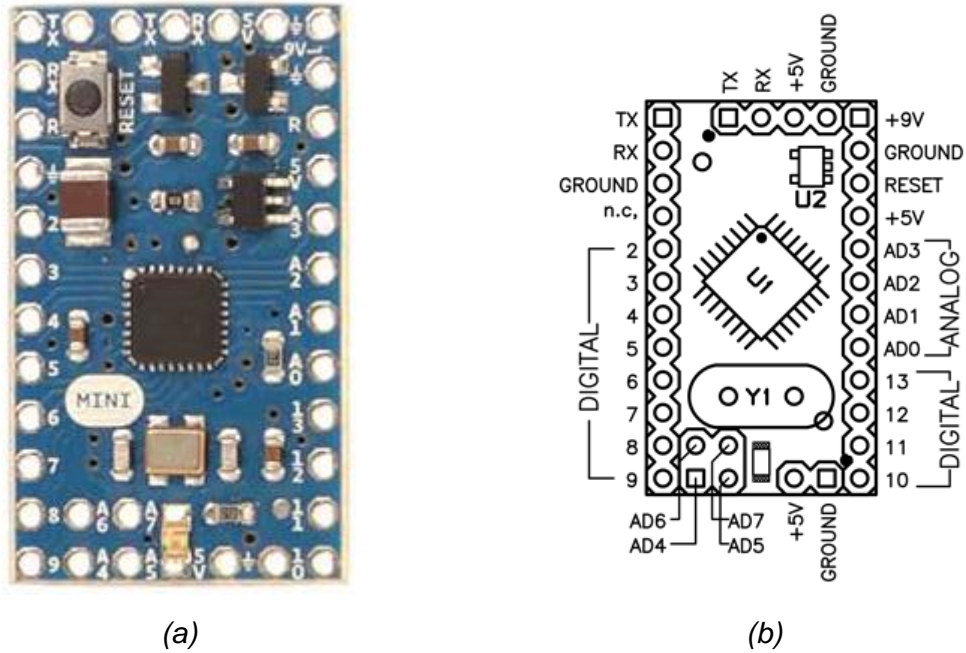


Figure 5-13: (a) Arduino Mini front without headers; (b) pin annotation of a typical board.

5.3.1.2 Hardware Implementation

The objective is to develop an embedded system that will manipulate the raw data using the communication protocols of the selected sensors, and to store the data on a memory card or transmit the data to a laptop in real-time. Consequently, Figure 5-14 illustrates the iBike measurement system architecture which employs the Arduino Mega 2560 board for the data acquisition with the selected measurement sensors. This figure also shows the relevant communications and functions which are used to interface with the sensors. In particular, the push switch, which is used to start and stop the data acquisition, and Hall Effect sensor are connected to external interrupts, while the A2K absolute encoder is connected to an analogue input pin on the Arduino board so that the analogue to digital converter (ADC) within the microcontroller can be utilised to translate the steering angle of the sensor.

The kinematics of a bicycle discussed in Chapter 4 is somewhat complicated due to the fact that a bicycle is able to steer and roll at the same time, and this makes the geometry of the steering handlebar fairly complex. However, in order to establish experimentally the optimum sensor configuration for reliable information, the measurement system also integrates an IMU module. This module incorporates the chosen ADXL345 accelerometer and L3G4200D gyroscope as well as a digital magnetometer and a pressure sensor.

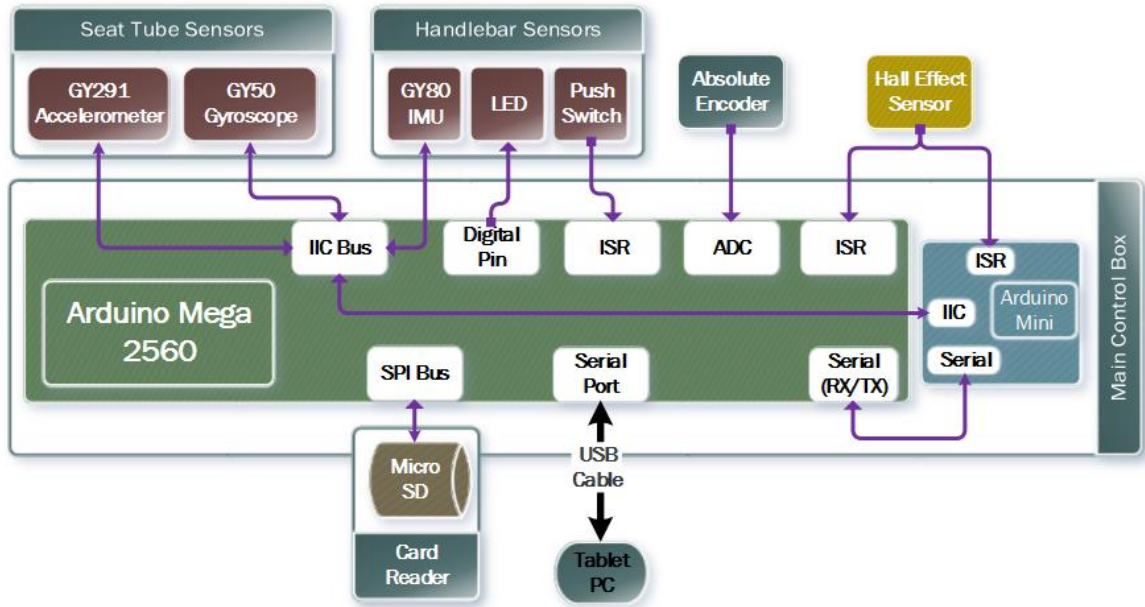


Figure 5-14: iBike measurement system architecture.

As can be seen from the architecture in Figure 5-14 above, the iBike measurement system employs GY291, GY50 and GY80 breakout boards along with a push switch, the A2K encoder and Hall Effect sensors as the inputs. The system also utilises LEDs (light-emitting diodes) and a breakout board for the SD (Secure Digital) card reader as the outputs from the system. The off-the-shelf breakout boards are used to simplify the implementation, since the scope of the project is to instrument a bicycle rather than the electronics themselves.

The main control box, which houses the Arduino Mega, Arduino Mini and SD card reader along with various electronic components, forms the communication link with the sensors via cables. Moreover, to provide electrical connections and mechanical supports for the Arduino and the breakout boards, three separate printed circuit boards (PCBs) are developed. PCB development and manufacturing consists of several stages, and three of the main processes for the seat tube sensors PCB are outlined below.

- 1) Schematic design – Figure 5-15 illustrates the schematic circuit diagram of the seat tube sensors. This design was developed using OrCAD Capture software [146]. Since the GY50 module also incorporates the same sensors, the default addresses are the same for the gyroscopes and accelerometers, which act as the slaves using the IIC protocols, and this was a problem as the two gyroscopes or the accelerometers would try to respond

simultaneously. The issue is resolved by studying the datasheets carefully. It is found that the serial data output (SDO) pin can be used to modify the least significant bit (LSB) of the slave address (SAD) associated with the L3G4200D and ADXL345 devices. Consequently, the SDO pin of the GY50 is connected to ground and the SDO pin of GY291 is connected to 3.3V as shown below. In addition, a LED is added to the schematic to indicate the power status of the system.

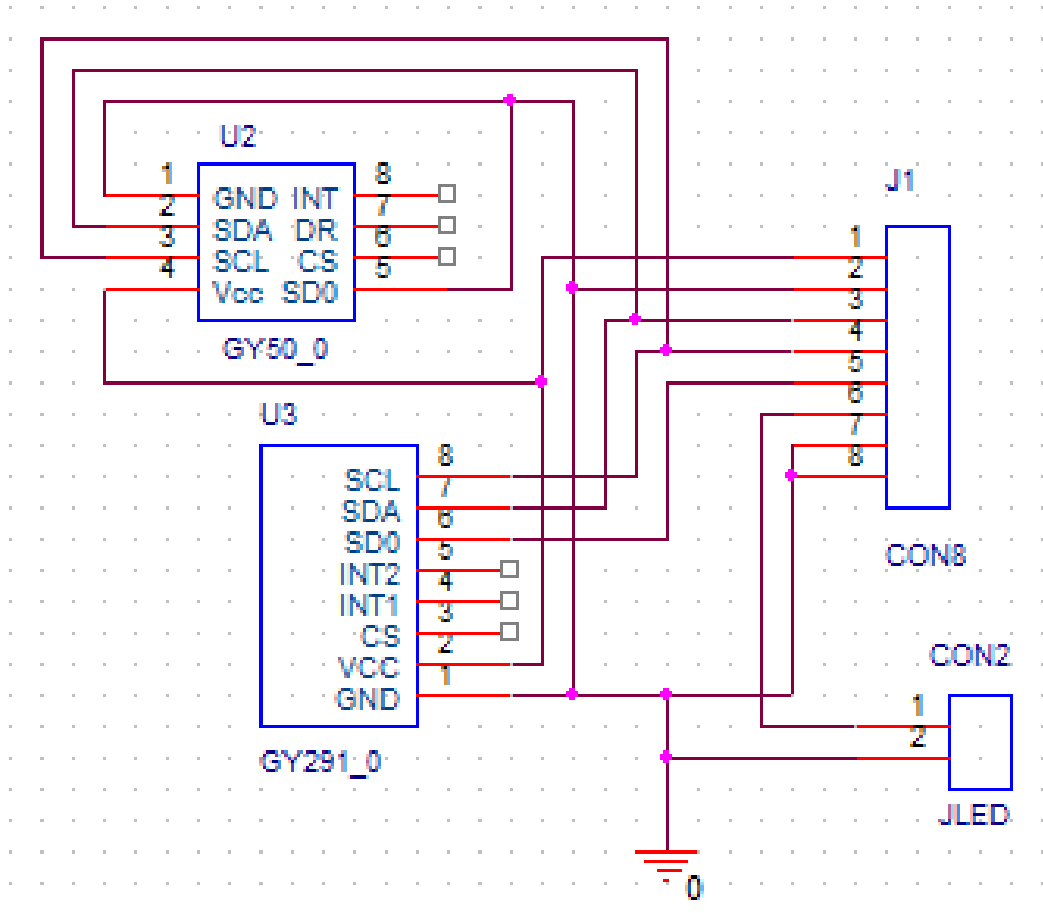


Figure 5-15: Schematic circuit diagram of the seat tube sensors.

- 2) PCB design – Figure 5-16 represents the design of the top and bottom layers wire routing of the above schematic. The PCB routing was developed using OrCAD PCB Designer software [147], which allows the art files and drilling information to be exported for the actual manufacturing of the PCB.

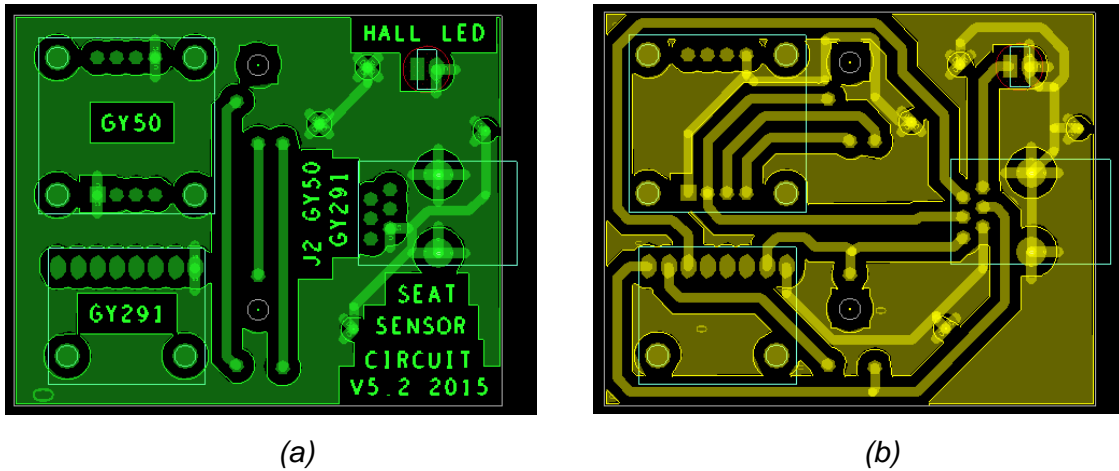


Figure 5-16: (a) Design of the top layer routing and (b) the bottom layer routing of the seat tube sensors PCB.

- 3) Manufacturing and Soldering – Figure 5-17(a) shows the actual PCB of the seat tube sensors. The printer used for the manufacturing only routed the tracks and made the drilling holes. The vias and connectors had to be manually soldered to complete the circuits and to hold the components respectively. As illustrated in (b) and (c), the header pins on the breakout boards also required soldering before mounting the boards on the developed PCB with screws to hold them securely.

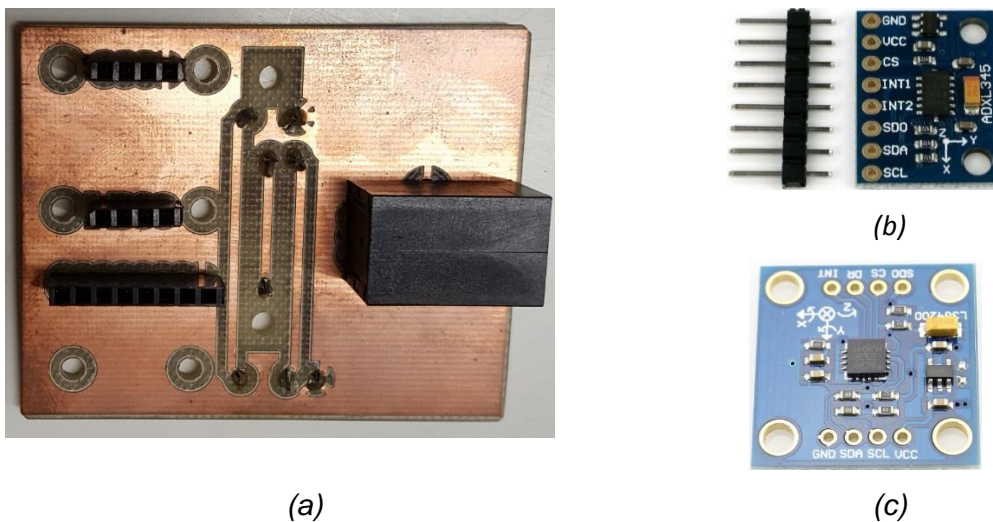


Figure 5-17: (a) Developed PCB; (b) GY291 breakout board with header pins; (c) GY50 breakout board.

Finally, to house and to install the above PCB with the sensors on to the body of the bicycle, a bespoke 3D part was designed using the Autodesk Inventor 3D Computer-

Aided Design (CAD) software [148], and then printed with a 3D printer. The developed design and the installation of the parts on the bicycle are shown below.

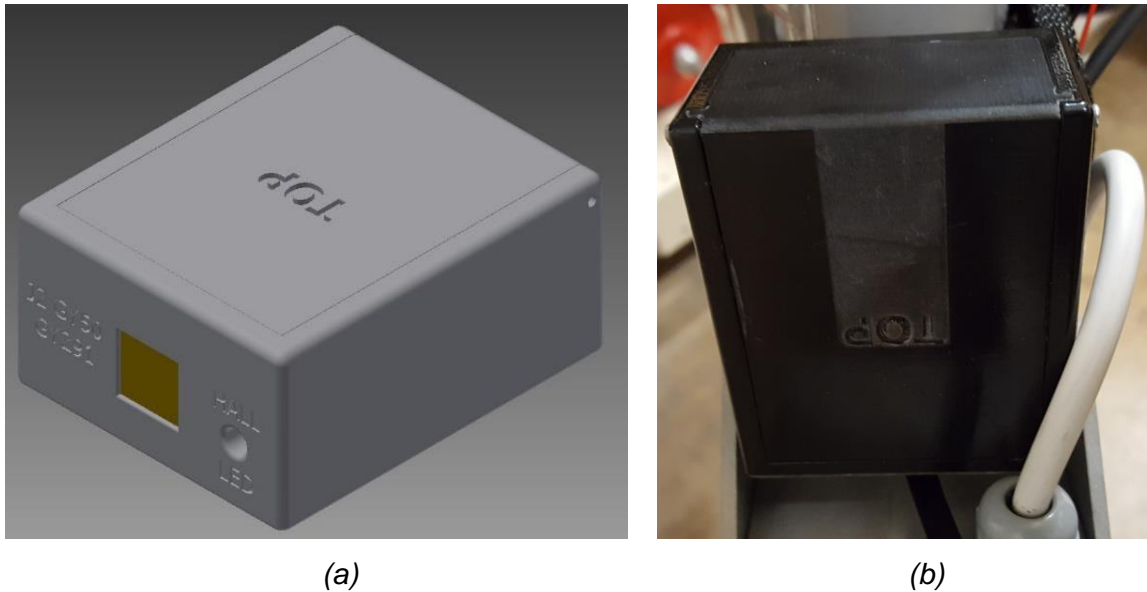


Figure 5-18: (a) the CAD design of the housing and (b) the 3D printed part installed on the bicycle.

The design and implementation of the main control box and the handlebar sensors PCBs are shown in Appendix A along with 3D parts that were developed and printed to house the PCBs and to attach the boxes to the frame of the bike.

5.3.1.3 Firmware Implementation

A firmware is required for the Arduino boards in order to provide the control and data manipulation of the sensors. For the design of the firmware, a detailed study of the datasheets of the sensors was conducted to establish the relevant control registers and protocols for them. Hence, using this information, the flowchart in Figure 5-19 was developed as the main program within the firmware. As can be seen from the design, the program consists of many variables, subroutines and instructions, but for the purpose of simplicity, not all the steps are included here. For instance, the special block of code associated with the interrupt service routine (ISR) for the push switch and the Hall Effect sensor is not illustrated here.

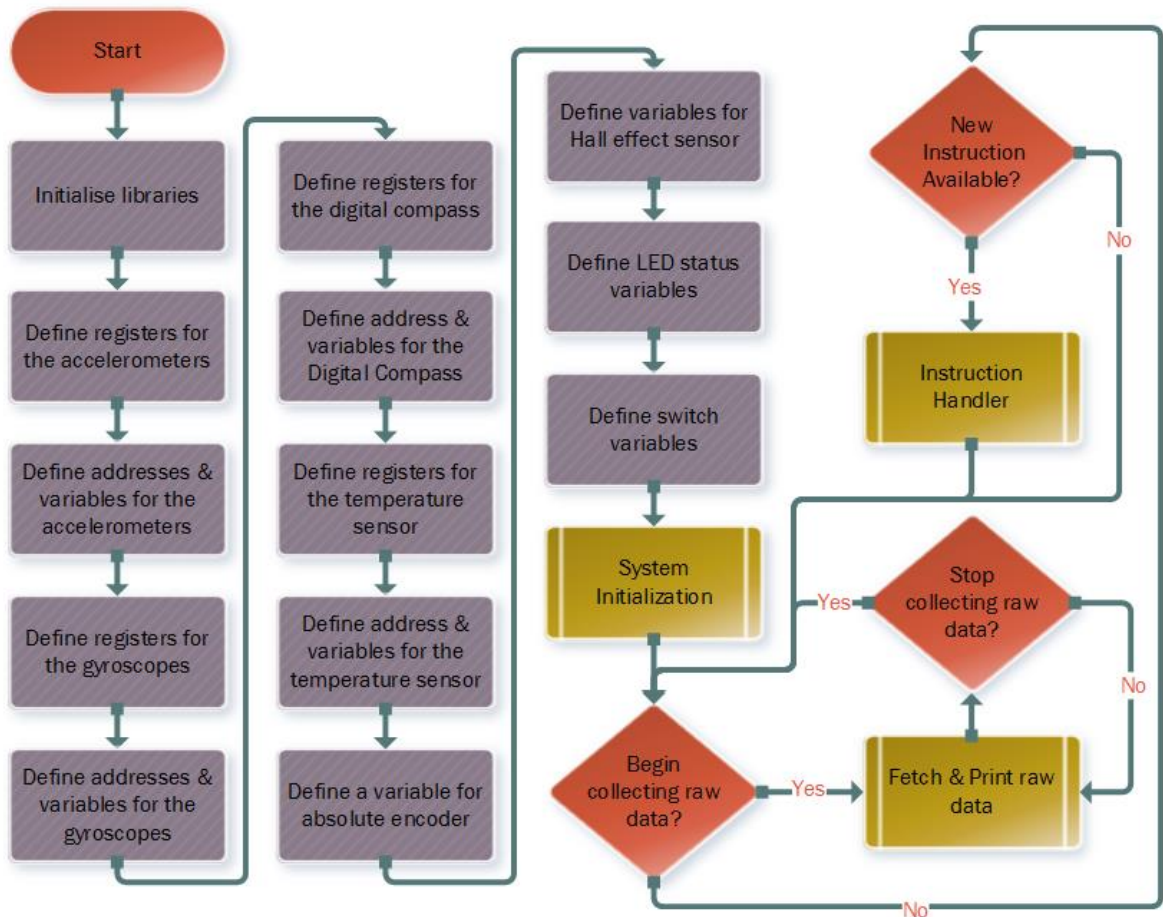


Figure 5-19: Flowchart design of the main program within the firmware

The Arduino comes with a simple Integrated Development Environment (IDE) [149] and open-source libraries [150] for various communication interfaces. Thus, to implement the above design, the Arduino's IDE is employed with the libraries illustrated in Figure 5-20 below together with the Arduino's language reference [151].

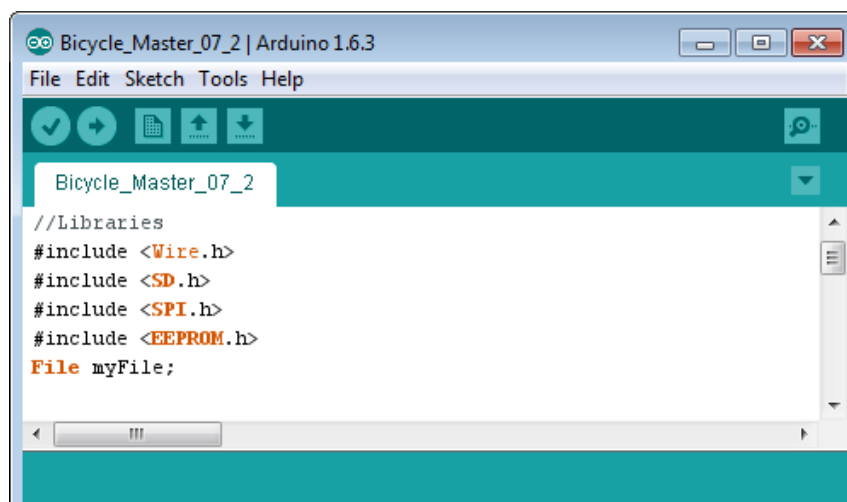


Figure 5-20: Screenshot of the Arduino's IDE.

As illustrated in Figure 5-19, the firmware supports instructions from the user, and five of the essential commands, which allow changing the default settings of the firmware, are shown below. The values of the associated variables are stored in the EEPROM and loaded during the system initialization process.

Table 5.1: Five essential commands of the iBike measurement system.

Command	Performed Action	Associated Variable	Additional Notes
#PM	Writes the data to the memory card	char Print = 'M'; EEPROM Address 0	the value stored in relevant the EEPROM
#PS	Writes the data to the serial port of each sample	char Print = 'S'; EEPROM Address 0	the value stored in relevant the EEPROM
#DD11	Updates EEPROM DateDay to 11	byte DateDay = 06; EEPROM Address 1	The value stored in relevant the EEPROM
#DM03	Updates EEPROM Datemonth to 03	byte DateMonth = 05; EEPROM Address 2	The value stored in relevant the EEPROM
#DY2017	Updates EEPROM DateYear to 2017	int DateYear = 2017; EEPROM Address 3	value stored in relevant the EEPROM

5.3.2 Smartphone

The task of extracting raw data from the local and global infrastructures and implementing the necessary procedures to transform the data into position information is a project on its own and it is beyond the scope of this study. In addition, a number of open-source databases are already in existence, which can provide the position information based on Cell IDs, Wi-Fi MAC addresses and RSS. For instance, Google uses publicly broadcast Wi-Fi data from wireless access points, cell towers and GPS to improve the positioning. Thus, Google's Application Programming Interface (API) of the geolocation cloud-based server [152] can be used to obtain the position based on the signals from the local infrastructure.

Consequently, for this study, it was decided to utilise a smartphone during a survey to collect signals from Wi-Fi hotspots and cell towers and to convert the raw data into position information as well as to collect and to process the data from the GNSS. Thus, the position based on the local and global infrastructure can then be fused

with the relative position of the bicycle using the Kalman filter design illustrated in Sections 4.4.2 - 4.4.4.5. Accordingly, a Samsung Galaxy S6 edge [153] is employed with Google maps [154] and GPS logger [155] apps, which are illustrated below. The Google maps app is used to collect stationary position data of the bicycle based on GPS, Wi-Fi hotspots and base stations, whereas the GPS logger app is used to collect GPS data while the bicycle is in motion.

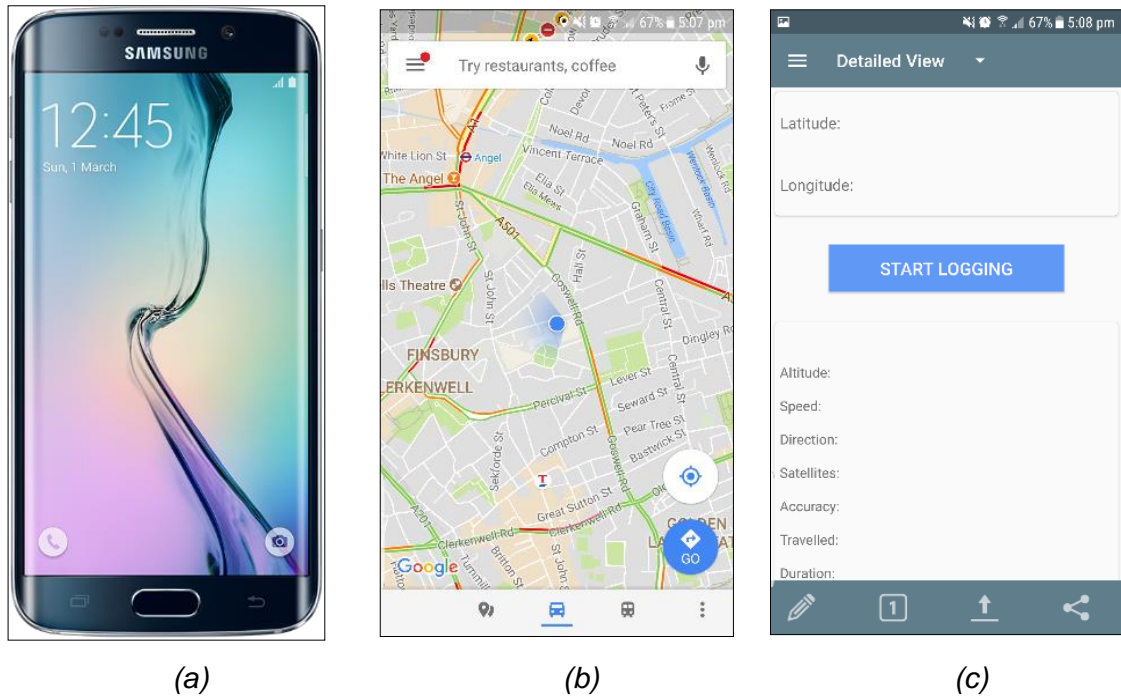


Figure 5-21: (a) Samsung S6 edge; (b) screenshot of Google maps app; (c) screenshot of GPS logger app.

Figure 5-22 shows the architecture design of the overall data collection process using the smartphone. As can be seen, the idea is to use the inbuilt radio frequency (RF), Wi-Fi, and GPS receiver modules to collect the nearby Wi-Fi and base station signals as well as GPS data. Hence, the data from the signals are then manipulated by the processor in order to extract the MAC addresses and Cell IDs and to measure the strength of each of the signals. This information is then transferred to the cloud server (via 3G mobile network) which has a database of the access points and cell towers and has the capability to compute the position based on the information and return the result back to the smartphone. The processor then locally stores or displays the result. These tasks are handled by the Google maps app as well as fusing this result based on the GPS data.

Separately, the GPS logger app handles the task of collecting and processing the GPS data which are then stored locally on the smartphone. The data from the local storage is then manually transferred to a PC where the data is pre-processed to remove any unwanted data. This process also includes converting the position data from latitudes and longitudes to eastings and northings. The pre-processed data are then permanently stored in a database via the data acquisition software so that during the fusion process the GPS data can be used as illustrated in Section 4.6 to compute the fused trajectory. Further details of the data acquisition system and the relational database structure are given in Section 5.5.

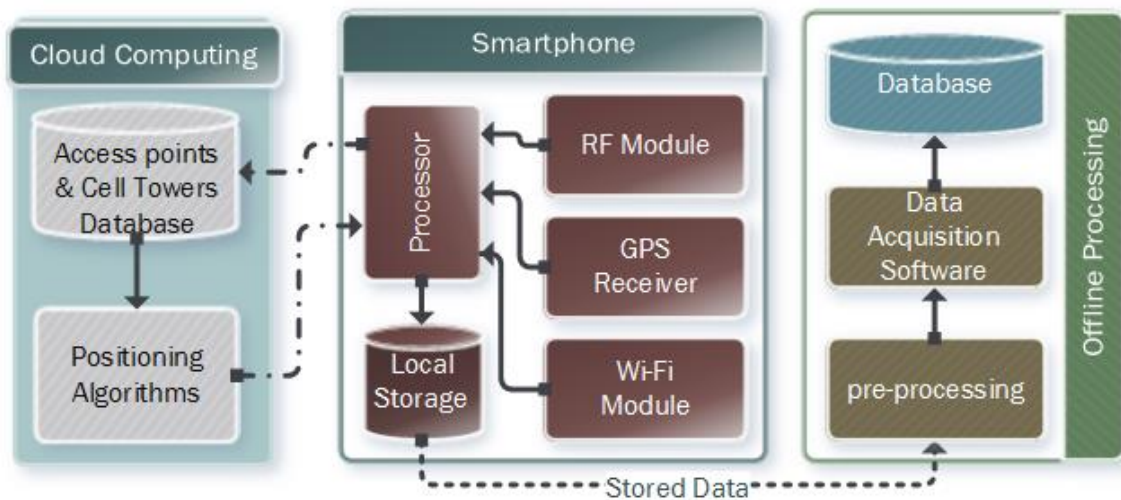


Figure 5-22: the architecture of data storage system from a smartphone.

5.3.3 Off-the-shelf INS

To validate the developed methodology in Chapter 4 and to compare the overall results of the measurement system with an off-the-shelf enhanced positioning system, it was decided to equip the bicycle with an Inertial Navigation System (INS). In theory, the INS can achieve accurate positioning, but it is specifically designed for four-wheeled vehicles and is therefore very expensive when used for tracking bicycles. Nevertheless, the Spatial INS [156], which is available as a commercial product, is selected to validate the overall iBike system. The Spatial system comprises an external GNSS antenna and a small cube which houses a high accuracy MEMS IMU and a Central Processing Unit (CPU). Furthermore, as illustrated in Figure 5-23, the Spatial has general purpose input-output (GPIO) pins that support a wide range of external peripherals, including an odometer-based input

for ground vehicles, so as to improve the accuracy. A summary of the essential technical features is listed below:

- Position Accuracy: 2 m (Horizontal) and 3 m (Vertical)
- Operating Voltage: 5-36 V
- Power Consumption: 100 mA (at 5 V)
- Operating Temperature: -40°C to $+85^{\circ}\text{C}$
- Update Rate: 1000Hz (data output) and 10 Hz (GNSS)
- Communication Interface: RS232
- Protocol: AN Packet Protocol
- GPIO Voltage Level: 5-20 V

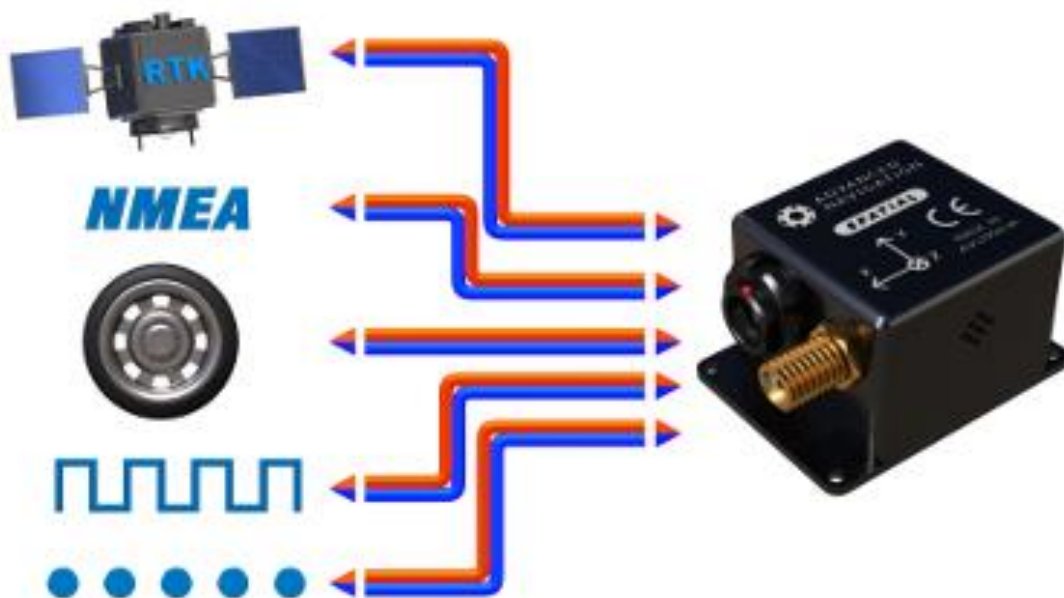


Figure 5-23: Spatial INS Cube [156].

It was further decided to feed the signals from the chosen Hall Effect sensor into the Spatial so as to improve the positioning accuracy of the system. This task required a thorough study of the Spatial reference manual [157] and required the device to be configured with Spatial Manager software. Table 5.2 below provides the pinout of the device and this information was used to construct the necessary electrical connection with the Hall Effect sensor. The implementation required the use of a VGA female adapter breakout board and an 8 pin DIN connector plug. An illustration of the overall electrical diagram is given in Appendix A.

Table 5.2: Spatial breakout cable connector pinout.

Pin	Colour	Function	Primary	Auxiliary	GPIO	Power
1	Black	Ground	5	5	5	
2	Brown	Power				Tip
3	White	GPIO 1			2	
4	Green	GPIO 2			3	
5	Red	Primary RS232 Tx	2			
6	Orange	Primary RS232 Rx	3			
7	Yellow	Auxiliary RS232 Tx		2		
8	Blue	Auxiliary RS232 Rx		3		
9	Pink	Ground				Ring

Unlike the smartphone, the data from the Spatial system cannot be stored locally as it does not have an internal storage. Moreover, as the purpose of the INS is to validate the overall methodology, the data from the iBike measurement system and the Spatial system must both be stored in a synchronised manner so that the exact corresponding sample points can be compared. Figure 5-24 illustrates the architecture design of the data acquisition and storage system utilised in this study. As stated previously, the signal from the Hall Effect sensor that feeds the iBike measurement system is also used as the odometer input to the Spatial INS. The real-time processed data from the INS is acquired by a Tablet PC where bespoke data acquisition software collects the data and stores them in the database structure. The real-time data acquisition system and the developed data acquisition software are presented in Section 5.5.

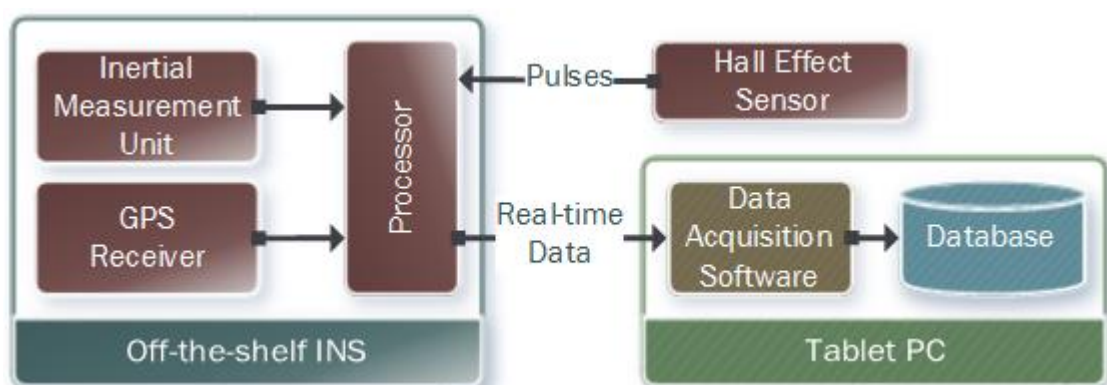


Figure 5-24: The data collection and storage system for the INS.

5.3.4 Tablet PC

A tablet PC is required so that it can be mounted on the bicycle easily. The purpose is to employ the tablet PC to acquire and synchronise the data from the iBike measurement system and the Spatial INS, and to store the data in real-time in a database structure for post-processing. For this reason, as shown below, a Microsoft Surface Pro tablet PC is used and the full specification of the PC can be obtained from Microsoft [158]. The idea is to configure the iBike system to output real-time data via the serial port and to connect both external systems to the tablet PC with USB cables. The data acquisition software is then used to communicate with the device interface to gather the data as well as to detect the point when the user presses the push switch on the handlebar sensors so that the software knows when to start and stop acquiring data from the INS. This method ensures that all sample data from the external systems are synchronised correctly. Finally, the coordinated data from each system are then stored in a database structure.

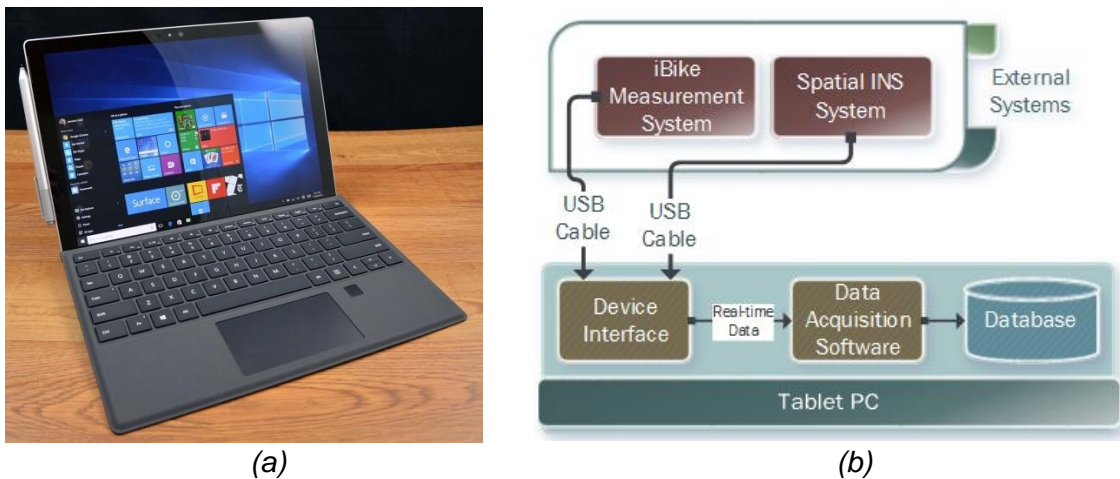


Figure 5-25: (a) Surface Pro Tablet PC; (b) the real-time data acquisition system.

5.3.5 Camera

To validate the trajectories visually based on GPS, INS and iBike measurement data of the bicycle, it also was decided to install a small camera. Hence, a GoPro Hero camera was chosen, as these cameras are very compact and can be easily mounted on the bike, and the cameras also feature a wide-angle lens, water resistance case, and they record in high-definition. The full specification of the camera model used in this project can be obtained from CNET [159].

Figure 5-26 (b) illustrates the camera's data acquisition system. The idea is to capture the motion path of the bike and store the video locally during the experiment. After the experiment, the footages are transferred to a PC where the acquisition software can be used to link each video to a unique journey ID and store these footages in a relational database structure.

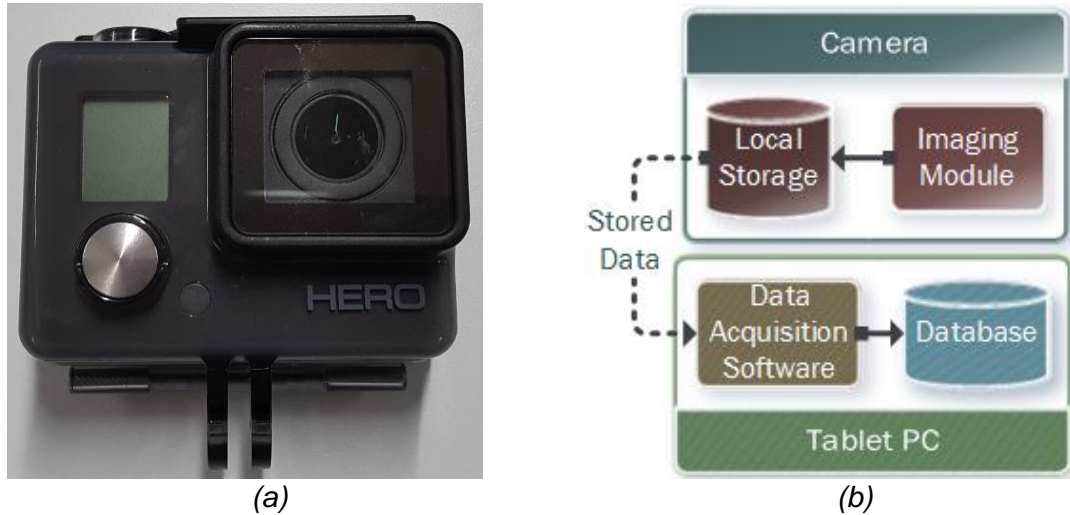


Figure 5-26: (a) GoPro Camera; (b) data acquisition system.

5.4 The Instrumented Bicycle

There are very few instrumented bicycles found in literature as in [94] and [160], where they were utilised for the investigation of human and bicycle dynamics and the assessment of cycle path surface quality respectively. However, these bikes are designed for a specific purpose and they cannot directly be employed for this project. Consequently, for this study, it was decided to instrument one of the 'Barclays Cycle Hire' bicycles (now sponsored by Santander). This is because there are currently 11,500 of these bicycles in use in London [161] and similar bikes are also used in other cities around the world. As a result, these bicycles can be seen as the model bikes for many cities. Figure 5-27 illustrates the evolved prototype of the instrumented bicycle with the sensor configuration. This bike (with ID: 23067) is supplied by TfL for this research study and it is instrumented with the measurement sensors and the individual subsystems discussed in Sections 5.2 and 5.3 respectively. Specifically, the Spatial INS and smartphone holder are installed directly above the rear wheel contact point since this is the point traced in the model

algorithms in Chapter 4. The GoPro camera is also mounted to record the position of the rear wheel while the bicycle is in motion.

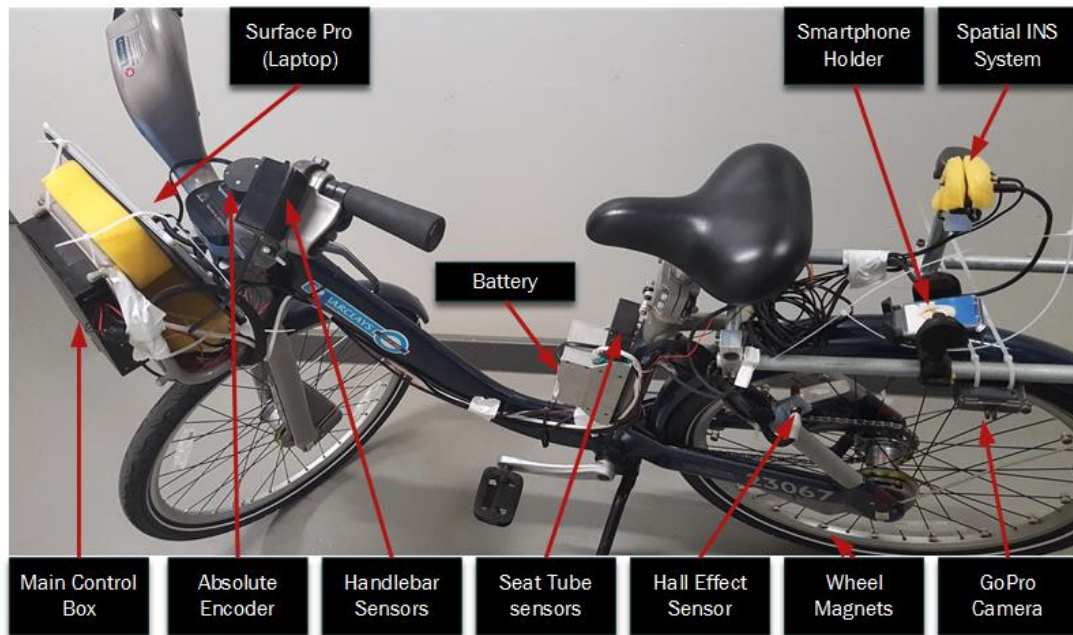


Figure 5-27: The Prototype Instrumented Bicycle (iBike).

In summary, the overall system of the iBike incorporates the four subsystems discussed previously and Figure 5-28 represents the output data from each of the subsystems installed on the bike. As can be seen, each set of samples consists of many fields and during a survey, the iBike generates thousands of samples which all need to be stored in a synchronised manner. As a result, the data management is also considered to be a critical task as part of the development of the prototype system. A number of existing high-quality traffic datasets have been investigated such as the NGSIM [162] to support the development of algorithms for vehicle or driver behaviour modelling at microscopic levels. However, to the best of the author's knowledge, there is no single dataset in existence for cyclists' trajectories or modelling studies. For these reasons, a relational database structure is constructed to store and manage the data in a synchronised form and to make it possible to retrieve each set of data with a unique ID for future studies. Further detail on the design and development of the structure is given in Section 5.5.3.

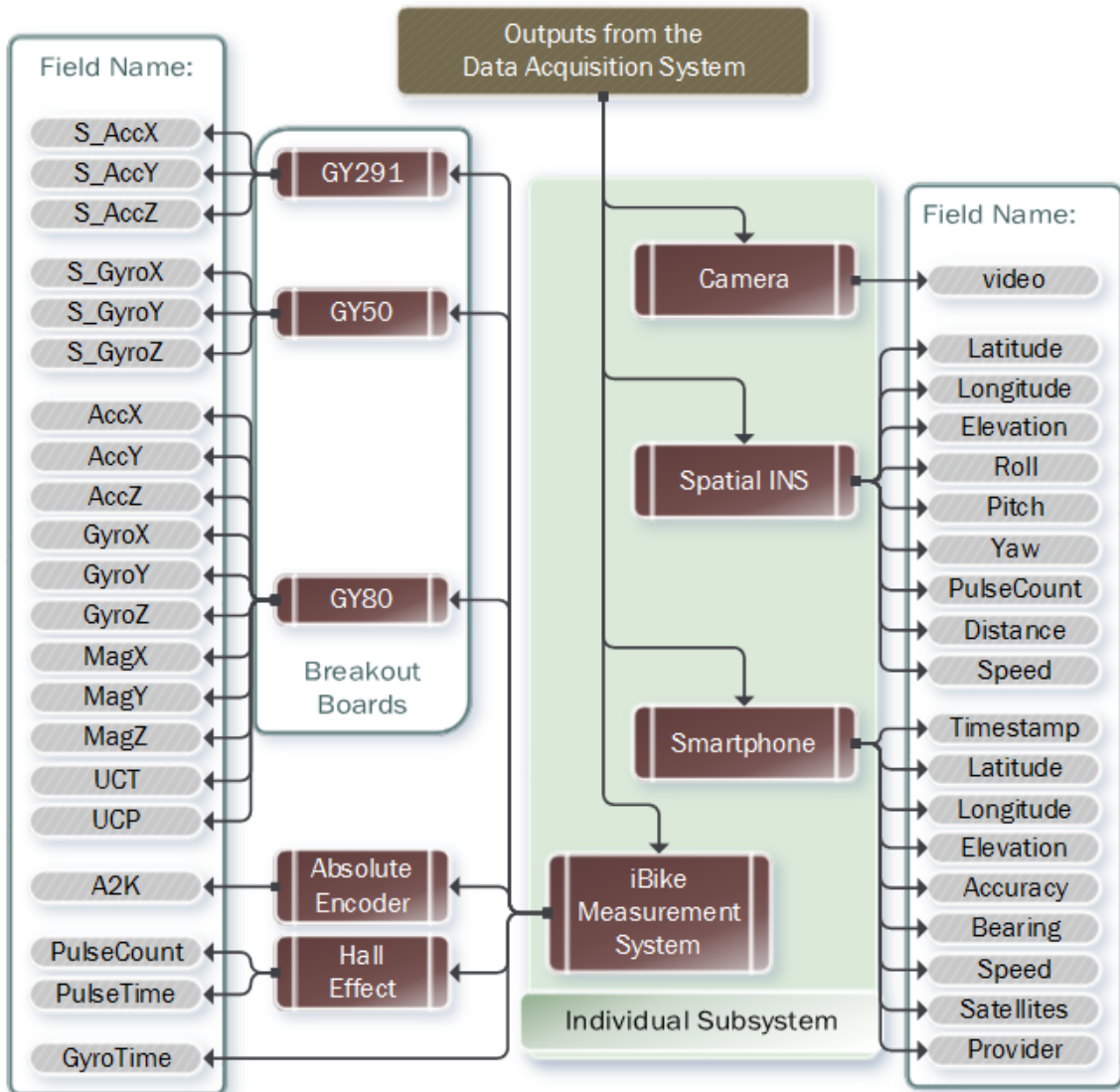


Figure 5-28: Outputs data field of the overall system.

5.5 Development of Software and Database

5.5.1 Overall System Architecture

Figure 5-29 illustrates the overall architecture of the data manipulation and data processing systems. As can be seen, the overall system utilises the measurements from the iBike sensors and smartphone to serve as the input data. This is so that the developed algorithms presented in Chapter 4 can be implemented and applied to the input data from field experiments. The system also utilises two types of validation systems: an INS and a camera. The data from all four individual systems are then mapped via the data acquisition system and stored in a relational database structure for further processes. The GPS and INS data from the smartphone and Spatial respectively are then retrieved from the database and processed with a

piece of third-party software in order to convert the positioning data from WGS84 (Latitude and Longitude) to OSGB36 (Eastings and Northings). On the other hand, the iBike measurement data is processed using bespoke software developed in MATLAB to output the trajectories based on the DR and fused algorithms. Further details of the data acquisition system, relational database and data post-processing system are given in the following subsections.

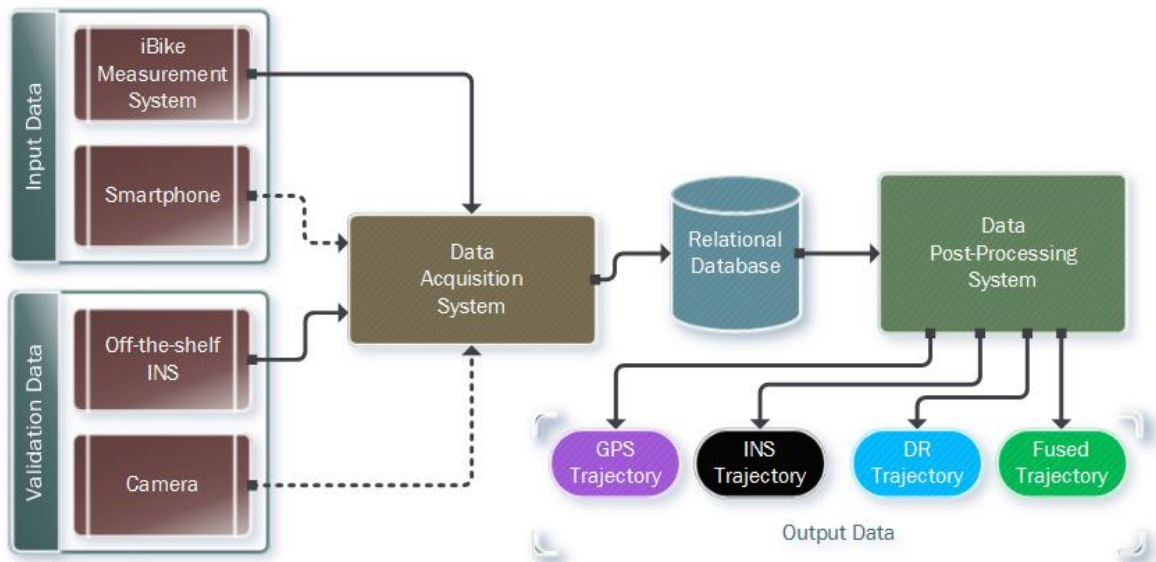


Figure 5-29: The overall system architecture.

5.5.2 Data Acquisition System

A piece of software was developed for the data acquisition system using the IDE of Microsoft Visual Studio since it enables a simple integration of the Spatial's software development kit (SDK) and communication protocols of the iBike measurement system. The Visual Studio also incorporates extensive libraries and has an easy communication interface for a wide range of database management systems (DBMS). The developed software comprises two tabs: one tab is dedicated for the real-time data acquisition of the iBike measurement system and Spatial INS system synchronously, and the other tab is for mapping the data from the smartphone, the camera and management of the data.

The annotation in Figure 5-30 illustrates the 'Acquisition' tab which consists of five separate panels. The first panel is used to initiate the communication between the data acquisition and iBike measurement systems. This panel also allows the user to send commands listed in Table 5.1 in order to configure the latter system

remotely. The second panel allows the user to establish the communication between the data acquisition system and the Spatial INS. The third panel enables the user to select from a dropdown list the route ID, the iBike ID and the rider ID, and the initial coordinates either in WGS84 or in OSGB36 with the heading angle can then be entered in the appropriate text boxes. The data collected by the developed software can be saved either in a database or in a file with comma-separated values (CSV). Finally, the software makes it possible to write additional comments for each survey, which can be viewed later for the post-processing stage, and to record the data simply by clicking the “Start Recording” button which automatically generates a unique journey ID for the survey. In this way, each set of data can be uniquely identified at a later stage.

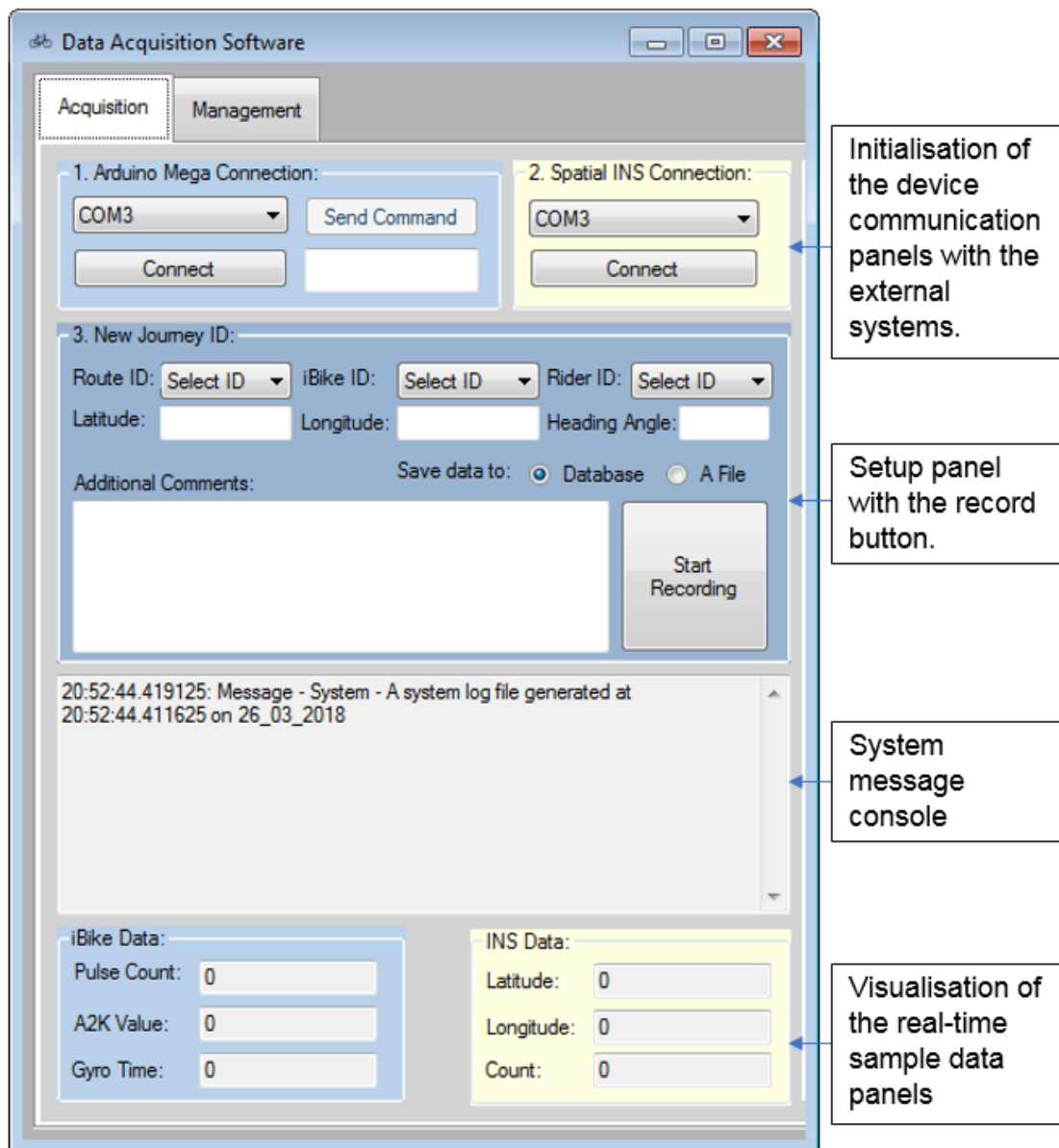


Figure 5-30: The data acquisition tab of the developed software.

Figure 5-31 illustrates the 'Management' tab of the developed software and it too consists of several panels. The 'Route Details' and 'Control Points' panels are used to manage or add a new survey route to the system with the ground truth points. The 'iBike Parameters' panel is used to manage or add a new bicycle with sensor configuration and the design parameters, whereas the 'Rider Details' is used to manage or add a new cyclist to the database. The 'Data Visualisation' is utilised to manage and view the data for each system. This panel also makes it possible to upload and map the smartphone's GPS data and the GoPro's videos to the associated journey. The overall functionality of the interface varies dynamically depending on the availability of the data in the database and the selection of the IDs.

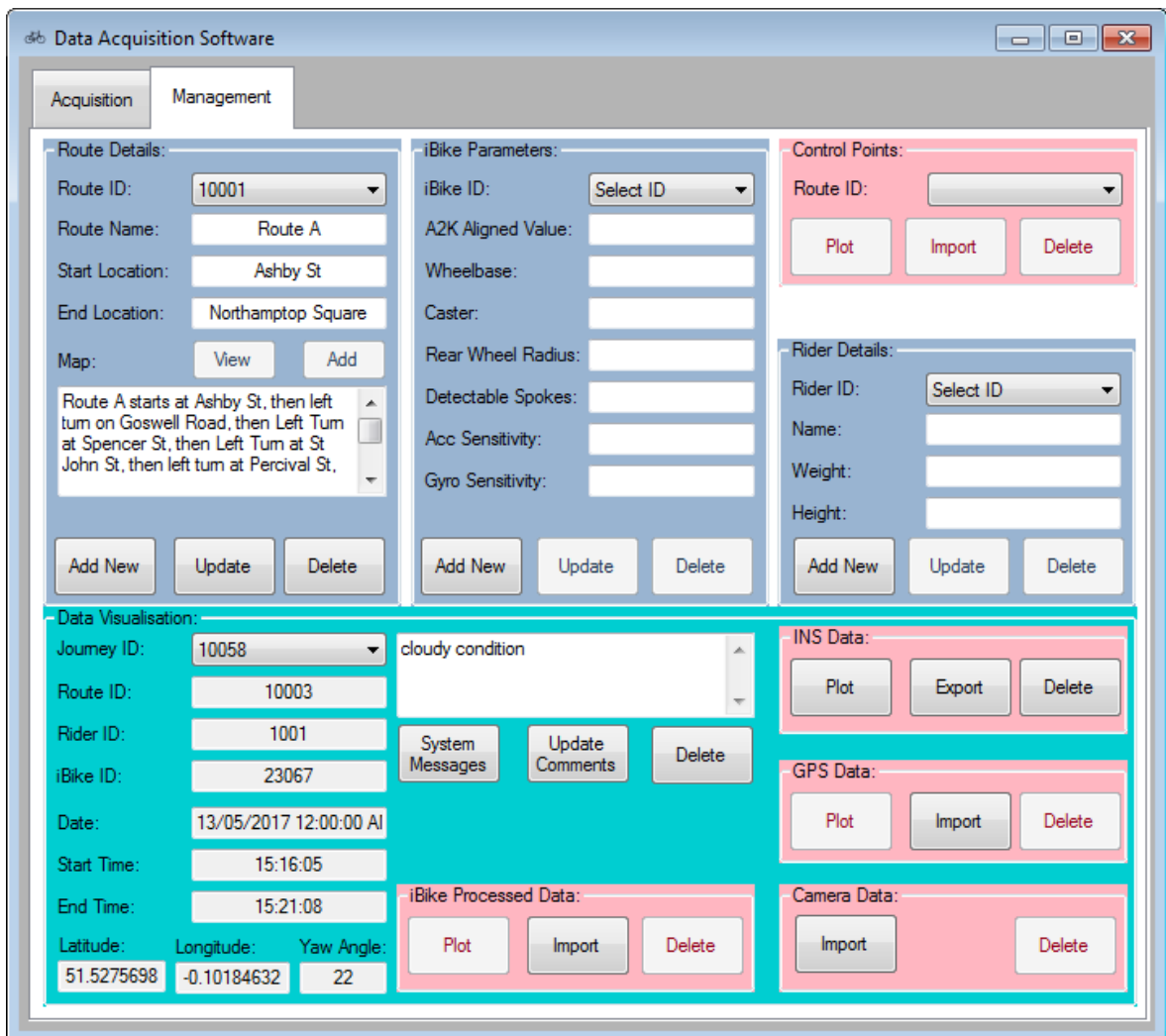


Figure 5-31: The data management tab of the developed software.

5.5.3 Relational Database

Figure 5-32 shows the design of the entity relationship diagram of the database structure, which was formalised as part of this study. The diagram illustrates the eleven identified tables to store the necessary information and it also demonstrates how each table relates to each other table with a one-to-many relationship. In this design, the “Journey Details” is the central table which assigns a unique key for each set of data such that the ‘Rider Details’, ‘Route Details’, ‘iBike Parameters’ as well as the raw and processed data from each of the system on-board the instrumented bicycle illustrated in Section 5.4 are all linked with this unique key. In other words, the unique key links all the data and facilitates the manipulation of the entire set of data for each set of experiments.

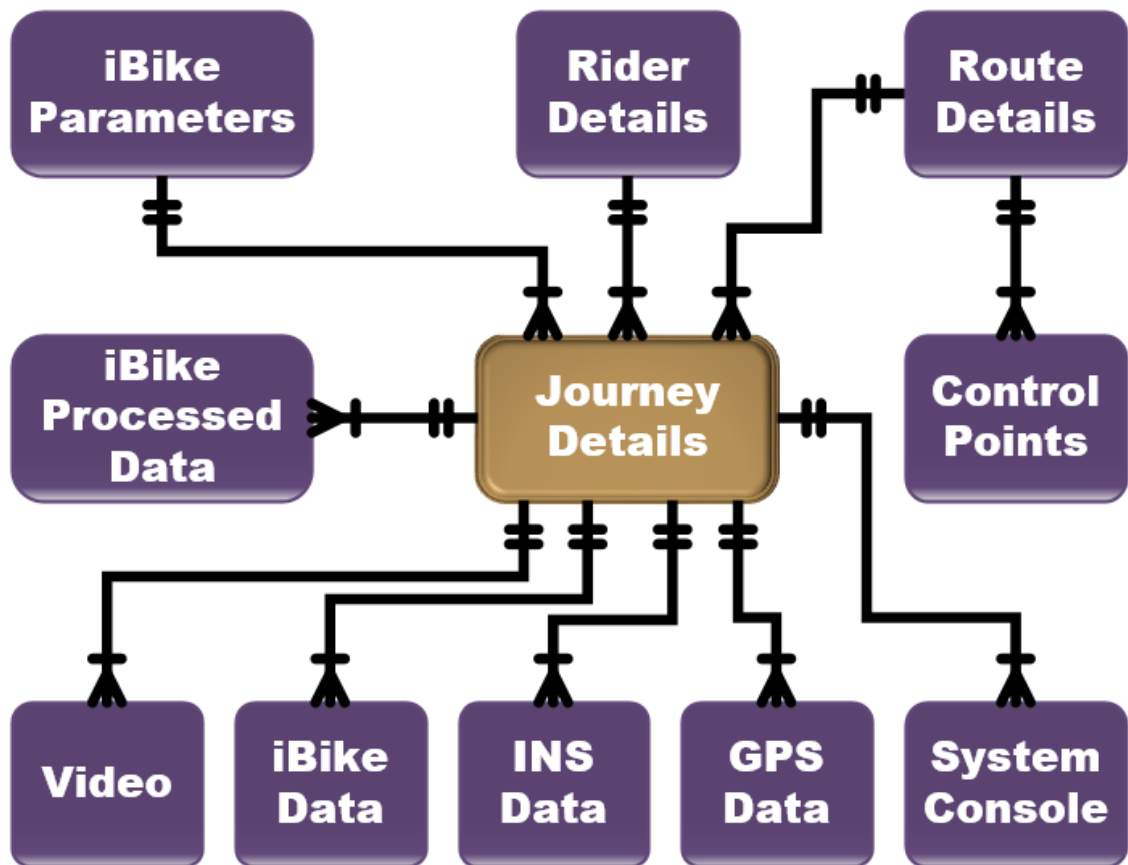


Figure 5-32: Entity relationship diagram of the iBike database.

Table 5.3 illustrates the file-level structure and storage requirement for the Journey table. It presents the necessary fields of the table with the primary and foreign keys as well as the data type, data format and example data. This design acts as the basis for the implementation of the database structure since it defines the essential

properties of the data fields. In addition, it also provides the approximation of the memory requirements for each individual field. A similar design was also created for each of the identified tables in Figure 5-32 above.

Table 5.3: Design of the file structure and storage of the Journey Details table.

Journey Details					
Field Name (Key Type)	Data Type	Format	Example Data	Comment	Size (bytes)
Journey ID (Primary)	Big Integer	Must be at least 5 digits long	10023	Table entity-unique	4
Route ID (Foreign Key)	Integer	-	10001	ID from Route Details	3
iBike ID (Foreign Key)	Integer	-	23067	ID from iBike Parameters	3
Rider ID (Foreign Key)	Integer	-	1001	ID from Rider Details	3
Date	Date	DD/MM/YYYY	11/07/2015	Current date	8
Start Time	Time	hh:mm:ss.nnnn	13:21:54.0793	Inspection start time	12
End Time	Time	hh:mm:ss.nnnn	13:21:54.0793	Inspection end time	12
Start Latitude	Double	-	51.23353535°	Starting position	6
Start Longitude	Double	-	-0.1013558°	Starting position	500
Start Orientation	Double	-	20°	Starting Orientation	100
Operator Comments	Medium Text	-	-	General comments	1024
Total Size:					1,669

MySQL community server is an open-source Relational Database Management System (RDBMS) that offers a high performance, data security and on-demand scalability. Thus, the RDBMS is chosen to implement the database structure shown in Figure 5-32 since it is an extensively-used open-source database and provides flexible and simple solutions compatible with the Visual Studio IDE. Specifically, MySQL Workbench [163] was employed to implement the database structure and Figure 5-33 shows the screenshot of the interface which is used to create all the tables.

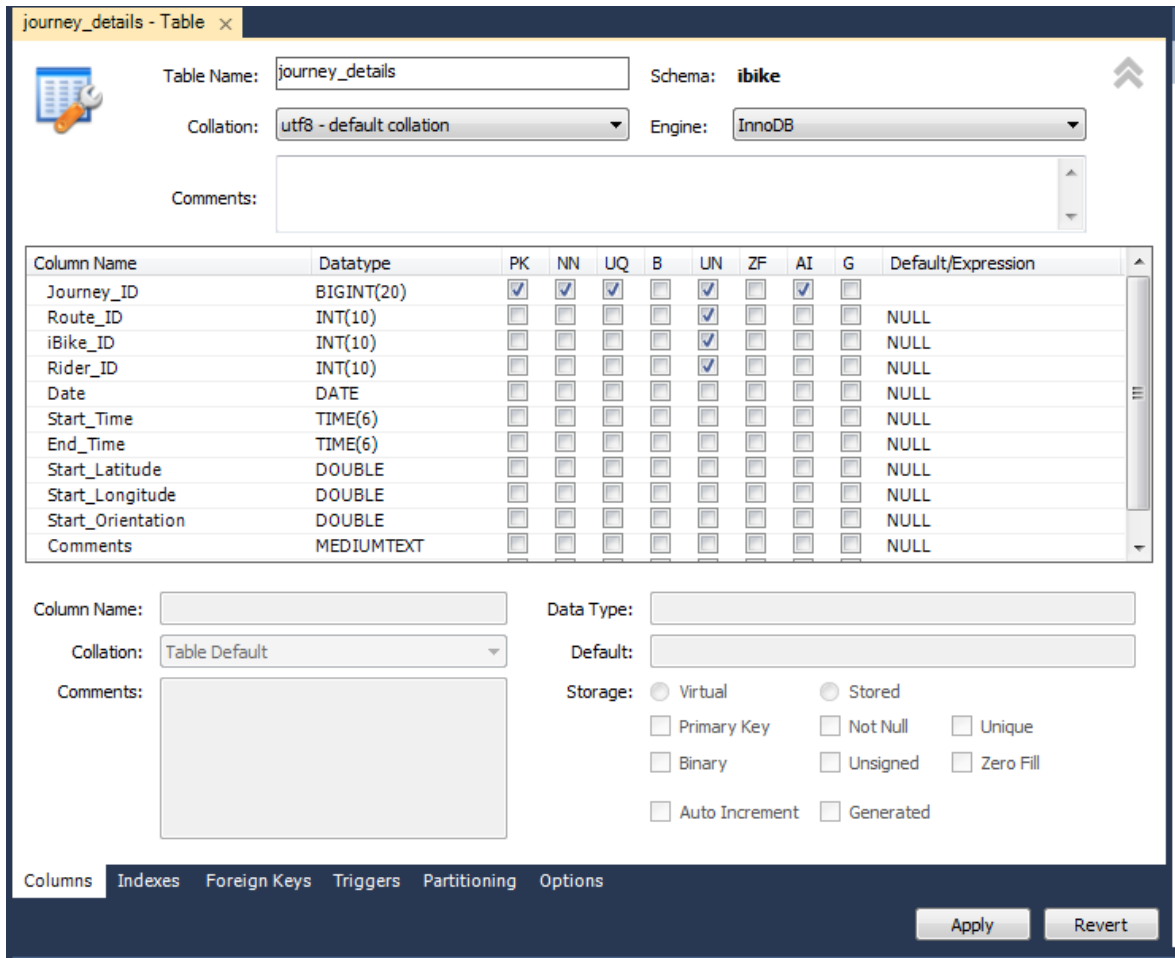


Figure 5-33: Implementation of the Journey Details table using MySQL Workbench.

Figure 5-34 illustrates the enhanced entity-relationship (EER) model of the implemented database. As can be seen from the diagram, there are 11 relational tables in the database, each of which has a one-to-many relationship to each of the others.

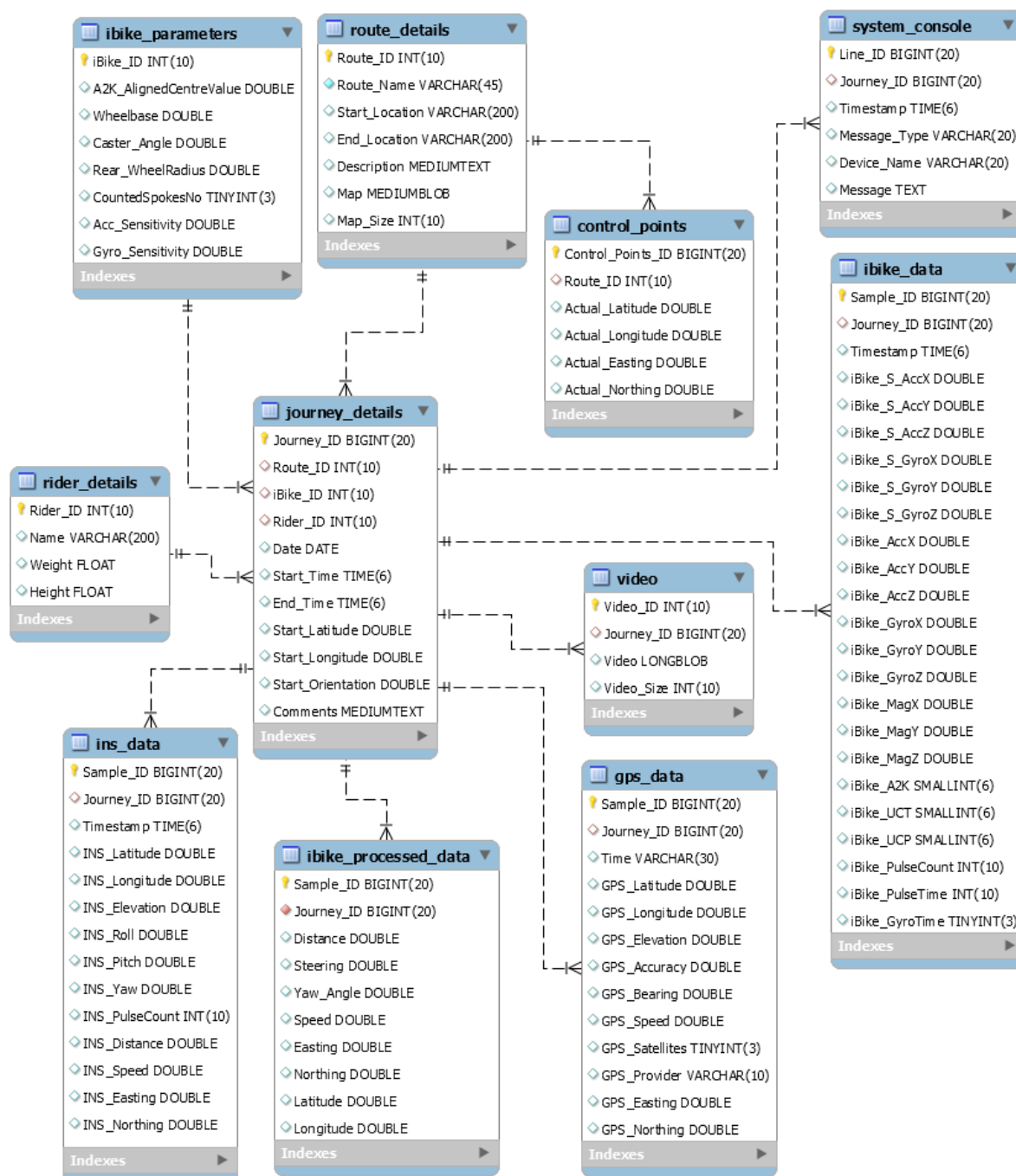
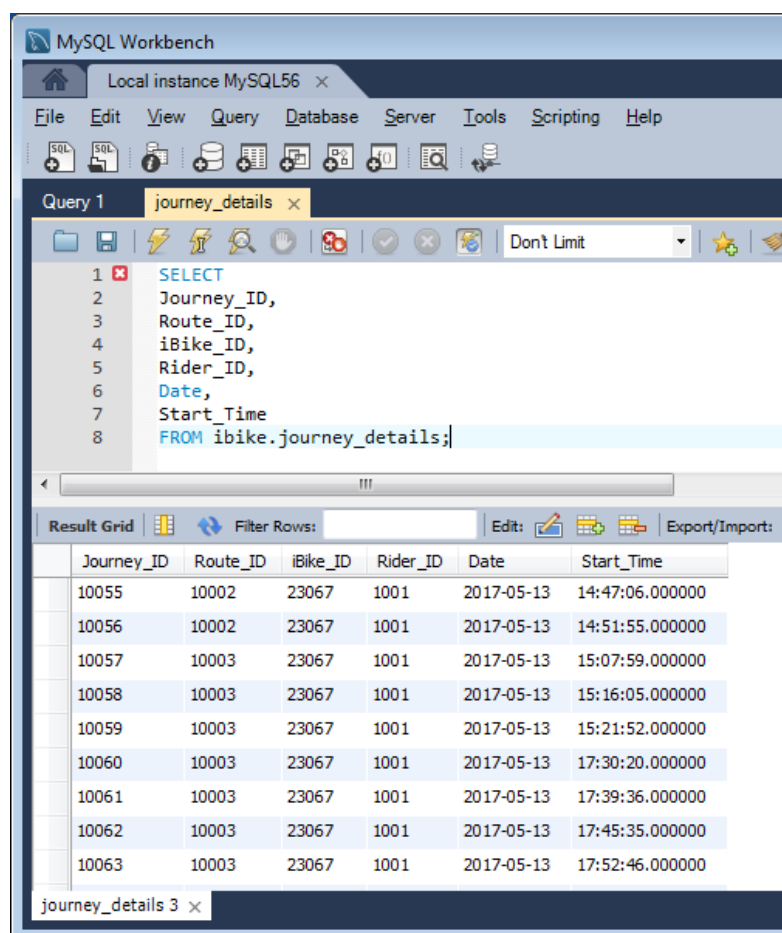


Figure 5-34: EER model of the database structure.

Figure 5-35 represents the Journey Details table with sets of data that were logged during surveys. It shows the Journey ID, Route ID, iBike ID, Rider ID, Date and Start Time of each of the surveys. The information contained in this table can be used to fetch all other data related to each survey that are stored in Rider Details, Route Details, iBike Parameter, iBike Data, INS Data, GPS Data and Video tables for further processing.



The screenshot shows the MySQL Workbench interface. The query editor contains the following SQL code:

```

1 SELECT
2 Journey_ID,
3 Route_ID,
4 iBike_ID,
5 Rider_ID,
6 Date,
7 Start_Time
8 FROM ibike.journey_details;

```

The results are displayed in a table with the following columns: Journey_ID, Route_ID, iBike_ID, Rider_ID, Date, and Start_Time. The data rows are as follows:

Journey_ID	Route_ID	iBike_ID	Rider_ID	Date	Start_Time
10055	10002	23067	1001	2017-05-13	14:47:06.000000
10056	10002	23067	1001	2017-05-13	14:51:55.000000
10057	10003	23067	1001	2017-05-13	15:07:59.000000
10058	10003	23067	1001	2017-05-13	15:16:05.000000
10059	10003	23067	1001	2017-05-13	15:21:52.000000
10060	10003	23067	1001	2017-05-13	17:30:20.000000
10061	10003	23067	1001	2017-05-13	17:39:36.000000
10062	10003	23067	1001	2017-05-13	17:45:35.000000
10063	10003	23067	1001	2017-05-13	17:52:46.000000

Figure 5-35: Sample dataset of the journey table.

5.5.4 Data Post-Processing System

The following subsections report on the processing of the data once they are collected. Each section discusses the different stages of the data processing in detail with illustrations. The final section also presents the developed post-processing software to process and fuse sensors' data based on the design of the algorithms presented in Section 4.6.

5.5.4.1 Smartphone Data

The Samsung Galaxy S6 smartphone together with the GPS logger app presented in Section 5.3.2 is used to collect the GPS positions of the iBike during an experiment while it is in motion. The app stores a number of fields which are not all required for the purpose of this study, and some of the fields are not always populated by the app. As a result, after the extraction of the data from the smartphone's local storage, the data is first pre-processed using Microsoft Excel. The pre-process involves the removal of some of the column data such as

horizontal, vertical and position ‘dilution of precision’ (DOP) fields. It also involves filtering data where satellites’ value is zero and renaming the file to match the field names of the ‘GPS Data’ table of the iBike database shown in Figure 5-34. The latitude and longitude of the processed GPS data are then uploaded to the datum conversion software illustrated in Figure 4-15. The outputs data from the software includes eastings and northings of input latitudes and longitudes, which are then stored with the pre-processed data to the iBike database. Figure 5-36 below shows the different stages in the processing and storing of the GPS data, while Appendix C illustrates screenshots with sample data of the software used for the data process.

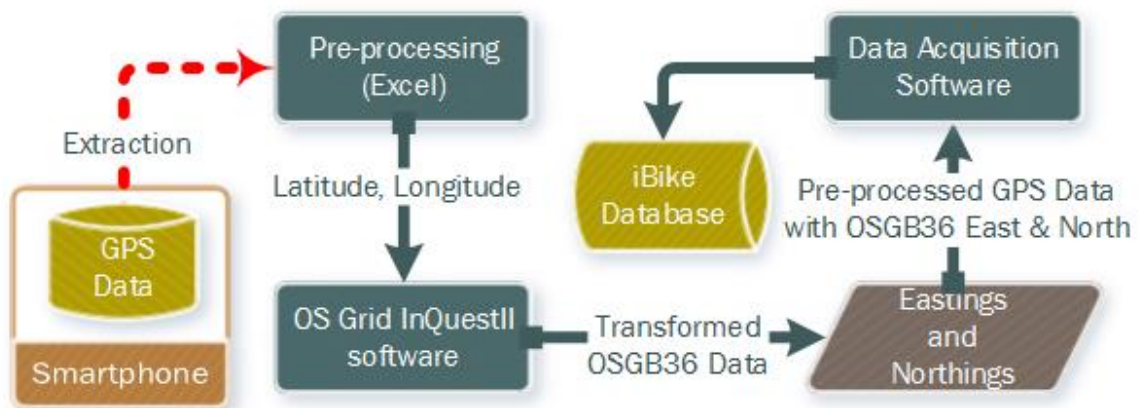


Figure 5-36: Process and storage of the smartphone GPS data.

5.5.4.2 Spatial INS Data

The Spatial INS presented in Section 5.3.3 is employed to collect the enhanced GPS data along with other parameters of the iBike during field experiments. The INS data is stored directly in the database by the data acquisition software shown in Figure 5-30. However, given that this study utilises the UK Ordnance Survey (eastings and northings) coordinate system, the enhanced GPS positional data need to be transformed into eastings and northings. For this reason, the data from INS Data table of the iBike database structure is first extracted using the Journey ID, and the fetched data is then uploaded to the datum conversion software, which processes the data and generates an output file. This file is then uploaded back to the database via the data acquisition software shown in Figure 5-31. The complete process described above is illustrated in Figure 5-37 below, while Appendix C illustrates the screenshots with a sample data set along with the software and processed data from it.

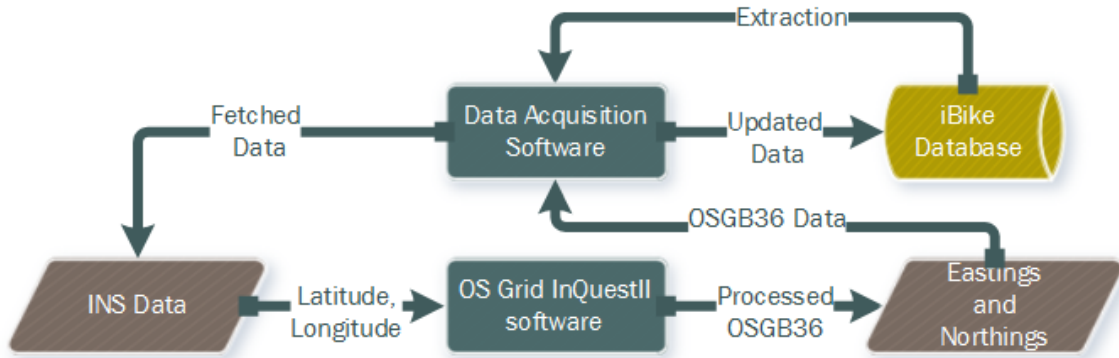


Figure 5-37: Process and storage of the Spatial INS data.

5.5.4.3 iBike Measurement System Data

An application was created in MATLAB with graphical user interfaces (GUI) [164] to process the raw measurement data from the iBike sensors, to implement the design of the post-processing algorithms shown in Section 4.6 and to analyse the processed data. Figure 5-38 below illustrates the developed application that incorporates many MATLAB scripts.

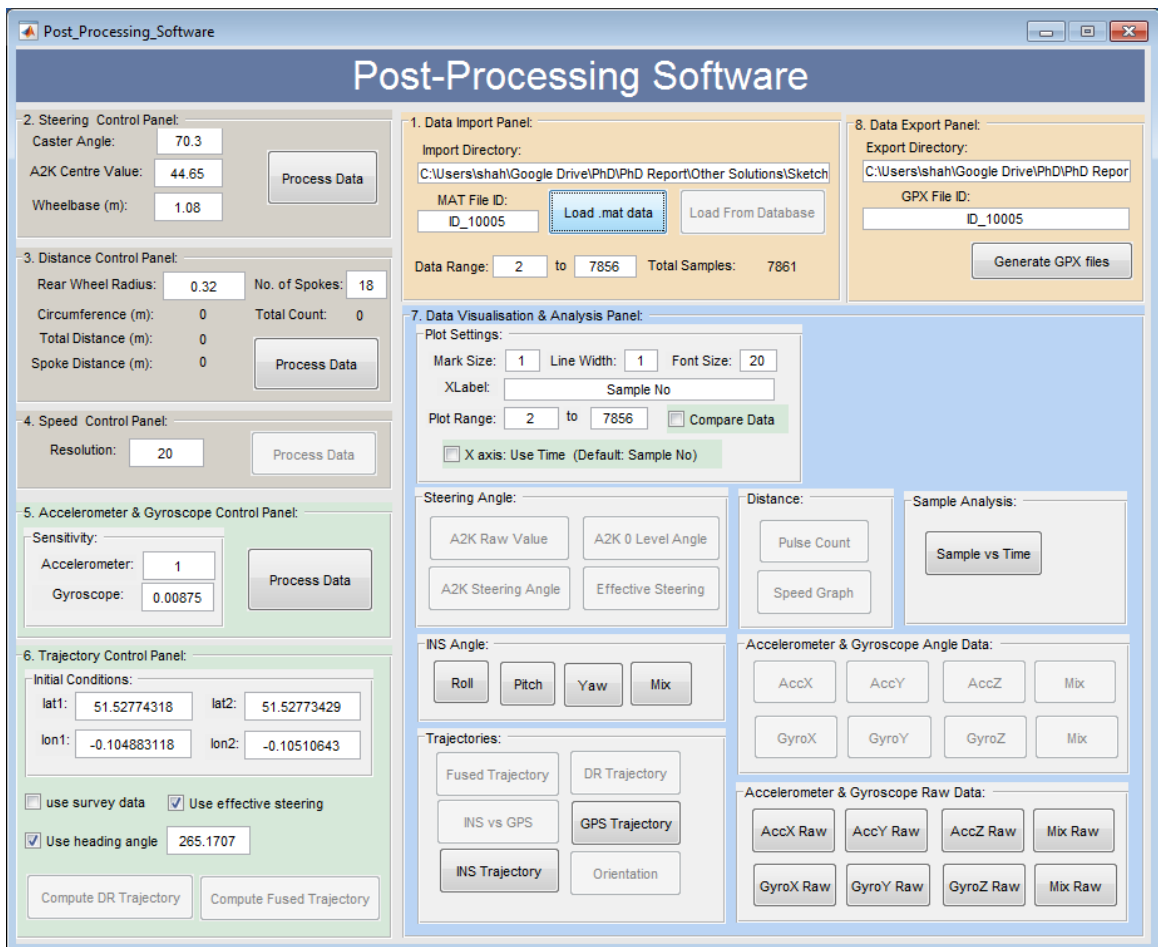


Figure 5-38: MATLAB Post-processing GUI.

The functionalities of the above application vary according to the availability of the raw and processed data within the program, and the overall interface consists of several panels. The first panel serves to import the data for a specific Journey ID on the MATLAB environment, whereas panels 2-6 are used to process the data. The seventh panel is used to visualise and analyse the processed data at different stages of the post-processing algorithms, and the eighth panel can be utilised to generate a GPS Exchange Format (GPX) file of the iBike position data, which can then be visualised on the actual map using a website interface such as GPS Visualizer [165] and GPX Editor [166].

Moreover, for optimisation purposes, currently, data processing also involves extracting the data from the database manually for a specific Journey ID and then converting them to MAT file format [167] and storing the MAT files to a file structure so that the application can import the data successfully. This process can be simplified by using the Database Toolbox [168] and adopting the application. Nevertheless, this Toolbox was not available at the time of the development under the university's MATLAB Toolboxes licence. Thus, this feature was not implemented. The feature can be easily adapted to load the data from the database using the Journey ID in order to extract the necessary data as shown in Figure 5-39 for the post-processing algorithms in the application. The processing of the data would remain the same as before, but the processed data can be stored directly to the database using the post-processing software rather than the 'Management' tab of the data acquisition software illustrated in Figure 5-31.

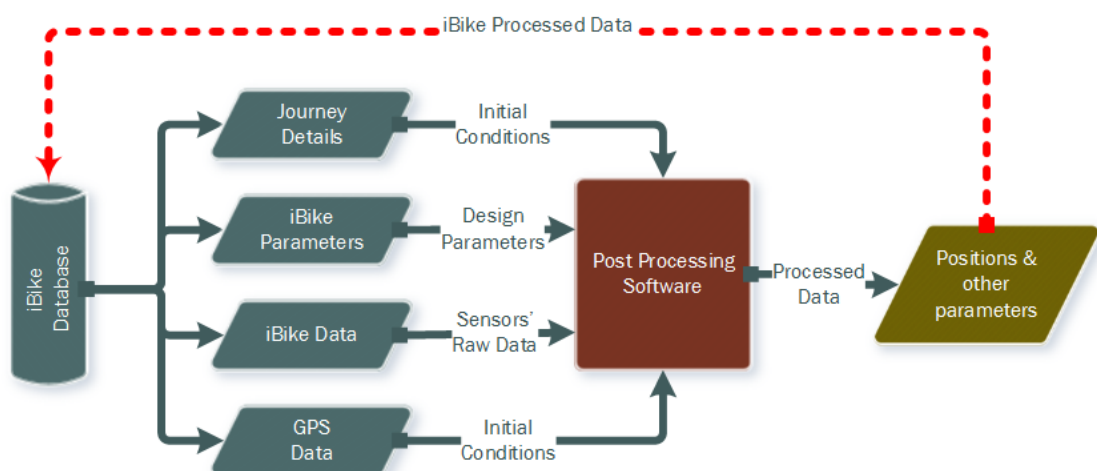


Figure 5-39: Process and storage of the iBike measurement data via the post-processing software.

5.6 Conclusions

This chapter focused on the development of the iBike prototype system and outlined the construction of the complete system, while the full details of the hardware and software implementation are given in the Appendix.

In summary, Section 5.2 presented the selected sensors to capture the necessary measurement data in order to fulfil the design requirements of the algorithms in Section 4.6. However, as stated, the sensors themselves do not output the required information for the implementation of the entire algorithms. Thus, a thorough study of the documentations and investigation into the behaviours of the selected sensors was carried out so as to transform the raw data. Accordingly, models were created to convert the raw data of the sensors into the five kinematic parameters of the bicycle which are the steering angle (δ), roll angle (ϕ), roll rate ($\dot{\phi}$), yaw rate ($\dot{\psi}$) and travelled distance (d_r). Moreover, as stated previously, the MEMS gyroscope provides very accurate instantaneous angular rates, but it was observed from an initial experiment through the Trapezoidal integration method that the computed roll angles drift over a period of time. Two main causes were identified for this issue: the accumulation of the integration error and the presence of random measurements noise in the raw data. Therefore, to minimise the drift and improve the accuracy of the roll angles, a MEMS accelerometer was utilised with the development of an intelligent fusion method to combine the data from both the gyroscope and accelerometer.

Section 5.3 described the implementation of the iBike measurement system with the selection of the appropriate hardware and software systems. This section also presented the chosen smartphone with the system architecture design, which was used to collect GPS data as well as the stationary positions of the bicycle based on Wi-Fi APs, Cell towers and GPS. Finally, this section also illustrates the off-the-shelf systems installed on the bicycle, for the purpose of validating the overall iBike system and the methodology, with the data acquisition architecture.

Section 5.4 demonstrated the actual instrumented 'Barclays Hire Cycle' bicycle used for this study as it is the most popular type of bicycle used in many world cities. This section also illustrated the outputs data field of the overall system. Section 5.5

concerned the pieces of software which were developed to acquire and process the data according to the design of the post-processing algorithms. This section also represented the different stages of the development of the state-of-the-art relational-database structure for cyclist trajectories and the measurement data. Finally, this section presented a unique key which can be used to fetch and process each set of data.

In conclusion, the objective of this chapter was to present the research and development work undertaken in order to construct the first prototype system and to present the instrumented bicycle which is formulated as part this study. In addition, two pieces of bespoke software and a relational database structure were developed in order to fetch, store and process the data.

Chapter 6: Validation of the Developed System

6.1 Introduction

The validation of the complete iBike measurement system in Chapter 5 with the methodology in Chapter 4 was a challenging task. This is because there is no error-free positioning system which can give the absolute position of the bicycle while it is in motion and which can serve as the ground truth. Although the Spatial INS is installed on the bike to compare the trajectories, it cannot be employed to serve as the ground truth data since the outputs of the Spatial INS system also contain error. As a result, a new method had to be found to validate the overall iBike system. Hence, the idea was to employ a line-of-sight positioning system to track the bicycle and to produce a trajectory based on the bike's motion.

One of the first trials was conducted in an indoor environment using the Ultrasound Cricket Indoor Location System [169] developed by MIT, and according to specification [170] the system can deliver a distance-ranging and positioning precision of 1 to 3 cm. Although the setup of this experiment was complex, since the beacons had to be mounted on the ceiling and at precise measured locations, the outcomes of this experiment were inconclusive as the Cricket system could not track the bicycle very well. This was partly due to the limit of the beacons' range and the number of beacons which were available at the time of the experiment. The overall setup of the experiment with the Cricket system is illustrated in Appendix C.

Consequently, a total station (TS), a topographical surveying instrument capable of tracking objects with an accuracy of 20 mm or less, was employed for the validation and this chapter reports on results of three separate experiments conducted using the instrument. Specifically, Section 6.2 presents the setup of an initial field experiment with a TS as well as the results obtained from the trial. Section 6.3 describes the field experiment that was conducted to validate the derived models and the design of the algorithms in Chapter 4. This section also provides the probability of the accuracy of the fused and non-fused bicycle trajectories. Section

6.4 evaluates and compares the accuracy of fused trajectories based on the developed system with the Spatial INS and GPS on its own. Section 6.5 draws conclusions on the applicability of specific sensor configurations, both in terms of sensors' accuracy and reliability with respect to the measurements of motion, and the ability to track cyclists based on the data gathered from the sensors.

6.2 Initial Experiment with Total Station

This section reports on the first set of initial measurement data that were obtained through riding the bicycle in Northampton Square (in front of the university's campus) while it was also tracked by a TS. As a result, the computed trajectory based on the measurements of the iBike system can be compared and the accuracy of the system can be determined with respect to the points based on the TS. Further details about the TS system and the initial experimental setup together with results are given in the following sections.

6.2.1 Experimental Setup

A TS is a very precise electronic and optical measurement instrument utilised in modern surveying and building construction. The TS incorporates an electronic theodolite and distance measurement unit as well as an on-board computer to collect data and perform computations. Thus, the instrument (with reference to itself) can be employed to accurately calculate the position, according to surveying principles [171], of a particular point or a 360-degree reflector by measuring the angle and distance to it. Although the instrument is designed to calculate stationary positions, it can be also used to track and record the angles and distances of a slow-moving object with the reflector mounted on it, whilst keeping a line of sight.

Accordingly, for the purpose of tracking and recording the trajectory of the iBike while it was being ridden, a Leica TPS1105 TS was employed. According to the user manual [172], the chosen station has a range of up to 2500m and a distance measurement accuracy of 20mm or less for a fast-tracking mode. The 360-degree reflector was mounted on the bicycle to enable the tracking of its trajectory. However, to keep in line of sight to the TS, the reflector had to be mounted on a pole at a height of approximately 2m from the ground to ensure that it was above the cyclist's head so that it could be tracked from any direction within 360 degrees,

without any interference from the cyclist's body. The sensor configuration with the reflector on the bicycle is shown in Figure 6-1. In addition, the box containing seat tube sensors was installed on top of the encoder so as to study the best sensor configuration for the accelerometer and gyroscope on the bicycle. Moreover, the Arduino Mega in the main control box was configured to acquire the raw data from the sensors at 22Hz and to store the raw data in a memory card for post-processing.

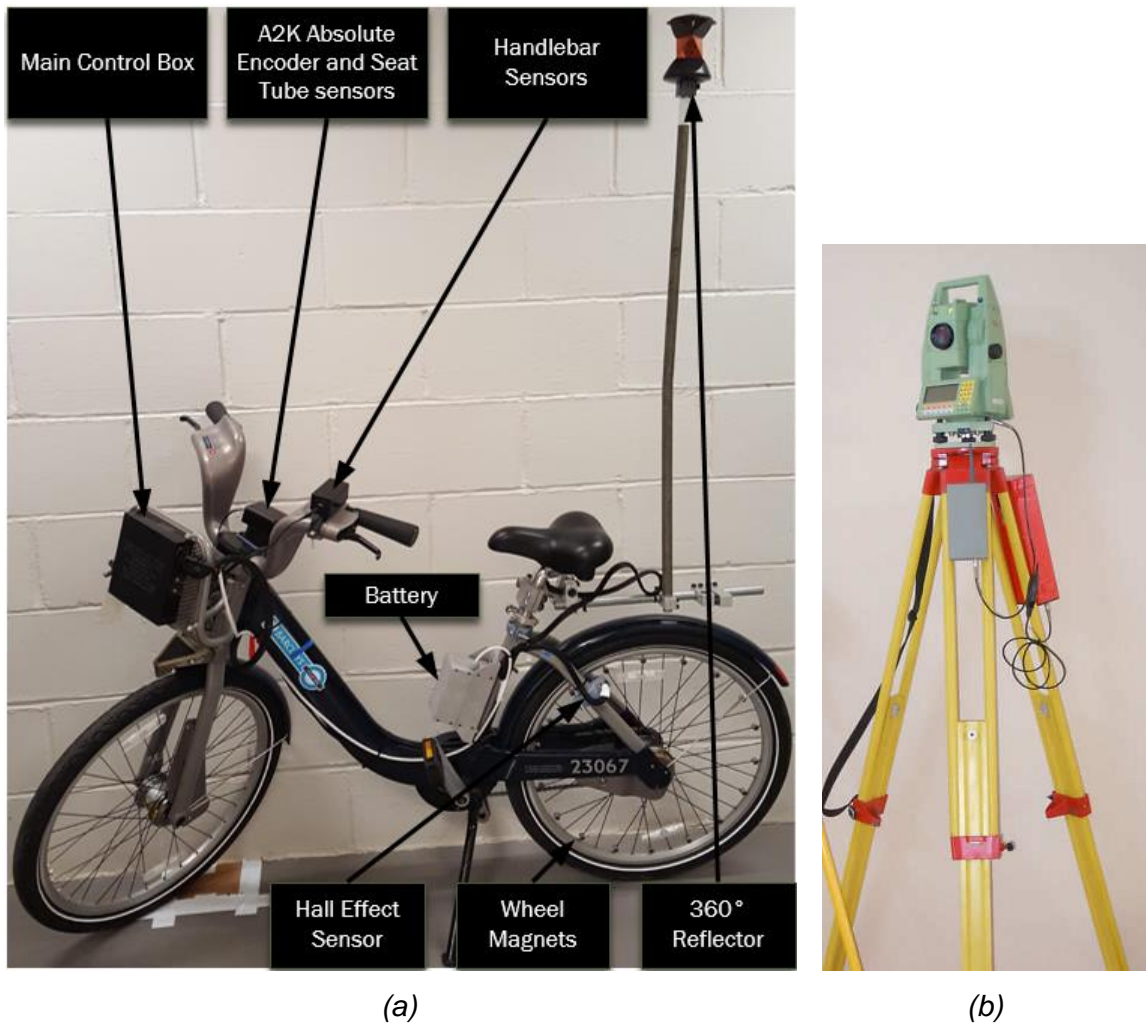


Figure 6-1: (a) Instrumented bicycle with the reflector; (b) total station instrument.

Figure 6-2 below illustrates the experiment setup on a map, where the location of the TS and the bicycle path are also represented. The road on which the experiment took place was approximately 4m wide and the bicycle was ridden for 96.24 m. The positions of the bicycle between the start point and end point of the route, as measured by the TS instrument, were recorded manually by an operator, while the raw data from the sensors on board the bicycle were recorded automatically by the iBike measurement system.

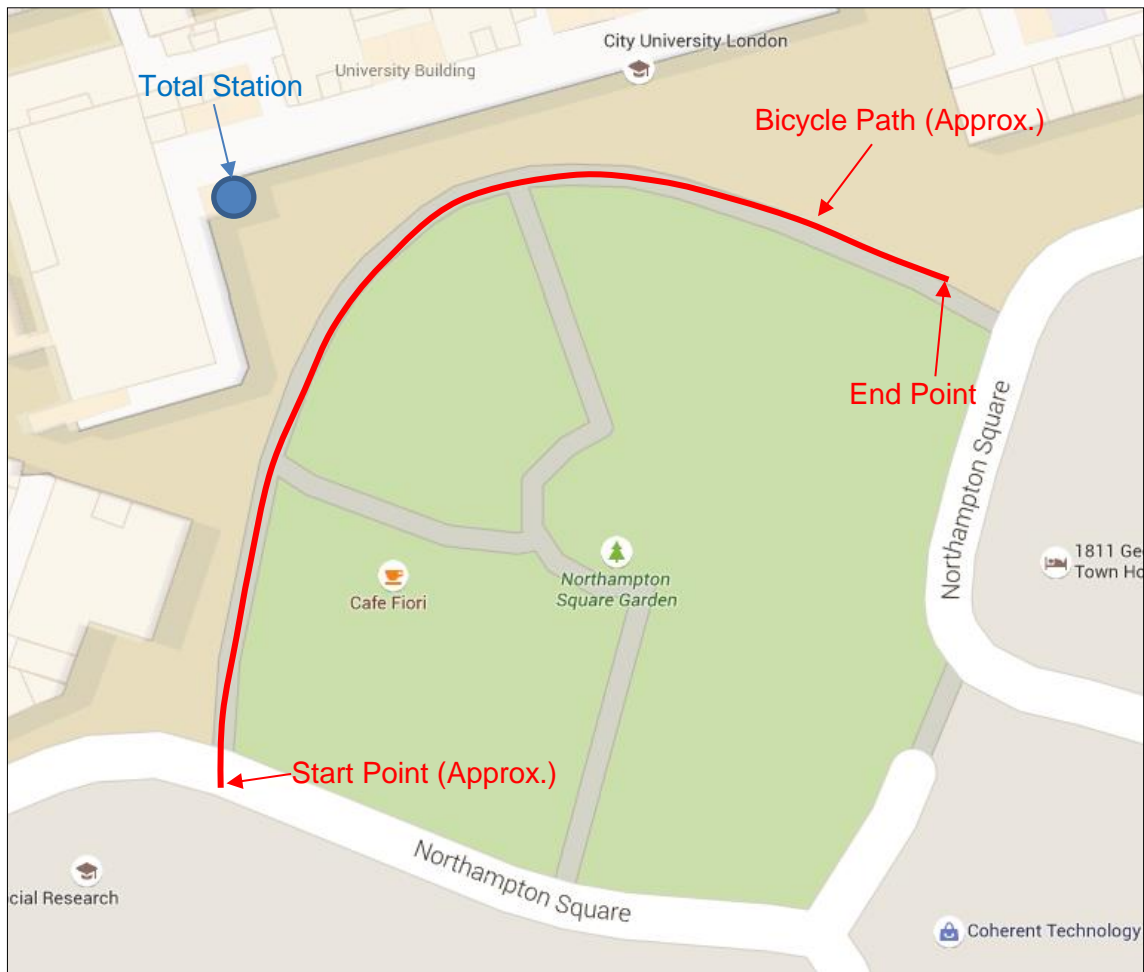


Figure 6-2: Initial experimental setup map.

6.2.2 Data Processing and Results

Following the experiment, the data from the TS were post-processed using a command line interface (CLI) program, which was developed by Stirling [173], in order to convert the measurements from the instrument into positions. On the other hand, the raw data from the sensors were first converted into angles and speeds or distances, from which the trajectory was reconstructed based on the dead-reckoning technique presented in Section 4.3.1 and the post-processing software illustrated in Figure 5-38.

The graph in Figure 6-3 illustrates the recorded positions of the bicycle during the experiment, in which the TS recorded a total of 36 points, while the iBike collected 1774 measurement samples. In the graph, the blue solid line represents the reconstructed trajectory based on the samples, while the red dashed line with circles represents the positions of the bicycle with reference to the TS marked in Figure 6-2

above. The starting point marked as a red star in the graph below was measured prior to the experiment with the TS instrument.

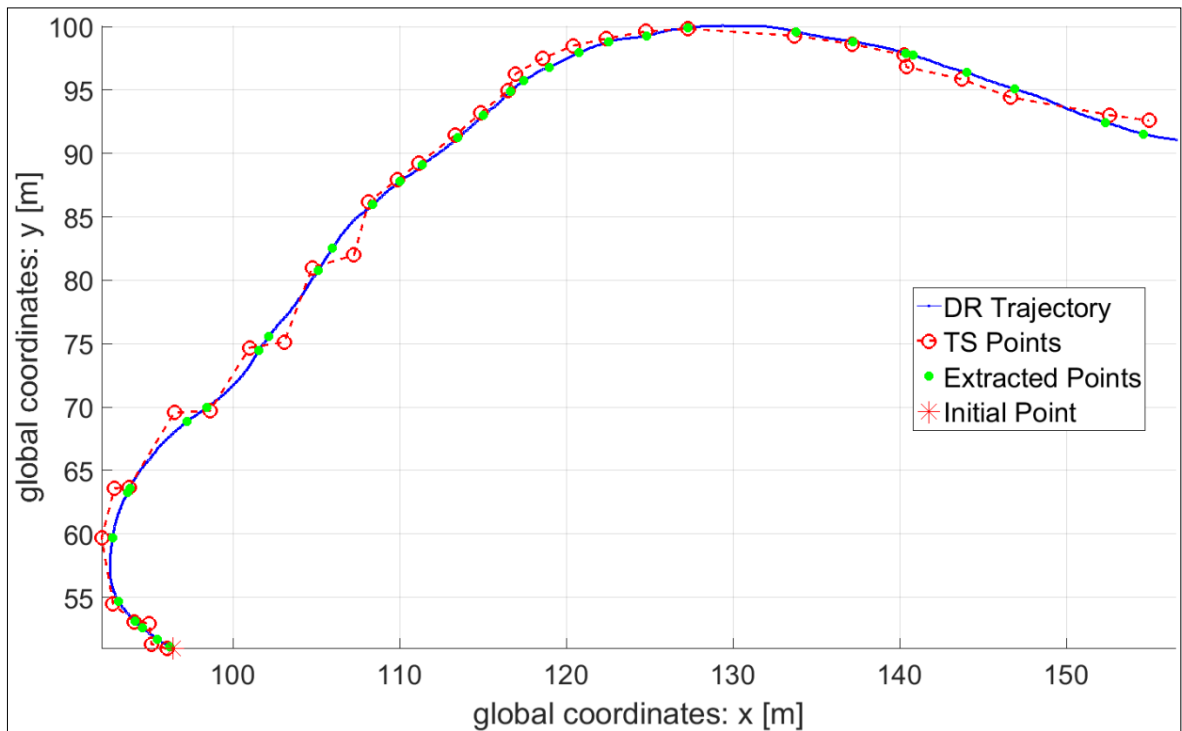


Figure 6-3: A comparison of DR trajectory and TS points.

As can be seen from the above graph, the trajectory based on the iBike measurement sensors is smoother than TS points, and illustrates better the natural behaviour of the bicycle such as course changes that it would follow while being ridden. Some points based on the TS instrument appear not to capture the behaviour of the bicycle changing course and direction. This could be due to the resolution of the data (points) from the TS, since it is designed to compute stationary positions or track a very slow-moving object. On the other hand, the measurements from the instrument are also inconsistent and these could be due to the non-consideration of the rolling effect of the bicycle. Indeed, with the reflector mounted at 2 m from the ground, a 15-degree roll can result in a discrepancy of up to 0.5 m in the position computed by the TS, whereas the DR trajectory refers to the position of the contact point of the bicycle's rear wheel on the ground. As a result, the inherent 0.5 m positional error from the ground truth system needs to be subtracted from the absolute displacement between the reconstructed trajectory and the measured TS points. This point is further illustrated in Figure 6-4.

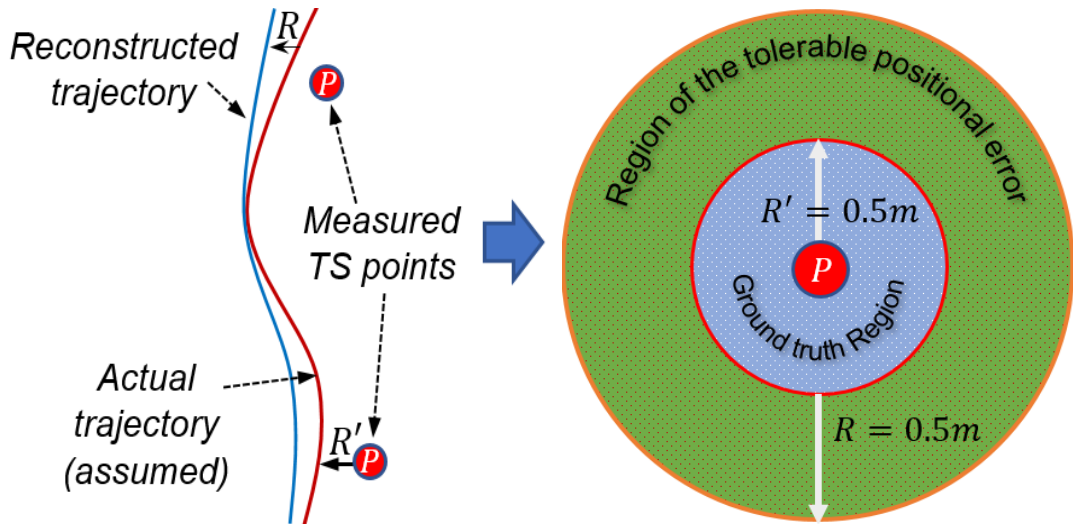


Figure 6-4: The maximum tolerable positional error from the actual location

In the above diagrams, P is the measured location of the bicycle, R' represents the assumed maximum average error from the ground truth system such that the actual trajectory (red line) or the absolute location of the bicycle will always fall within the region of the ground truth error, R represents the tolerable positional error of the reconstructed trajectory (blue line) with respect to the actual trajectory of the bicycle.

The 'Filtered Positional Error' (FPE) is the computed discrepancy between the reconstructed trajectory and the presumed actual trajectory. Where any errors fall within the 'ground truth region' are considered to be zero, or negligible. All other errors which fall outside this region are calculated as the absolute displacement minus the 0.5 m error from the ground truth region.

To compute the differences between two trajectories illustrated in Figure 6-3 and to calculate the accuracy of the DR algorithm, the closest neighbouring points to the TS points (marked as red circles) were extracted from the DR trajectory using the k-nearest neighbours algorithm, which is available through MATLAB's "knnsearch" function [174]. The results of the knnsearch function are marked as green dots on the DR trajectory in Figure 6-3. Moreover, to calculate the displacement between the TS points and the extracted points, the following equation was used:

$$\text{Absolute Displacement} = \sqrt{(TS_x - DR_x)^2 + (TS_y - DR_y)^2} \quad (6.1)$$

where TS_x and TS_y are the coordinates of the TS point and DR_x and DR_y are the coordinates of the position based on the DR.

Accordingly, FPE was computed at each of the extracted points and was compared with each point recorded with the TS. Figure 6-5 shows the histogram of the results along with the mean error. The histogram shows a right-skewed distribution, which implies that there is a minimum error and it is largely concentrated within the lower bound of the data.

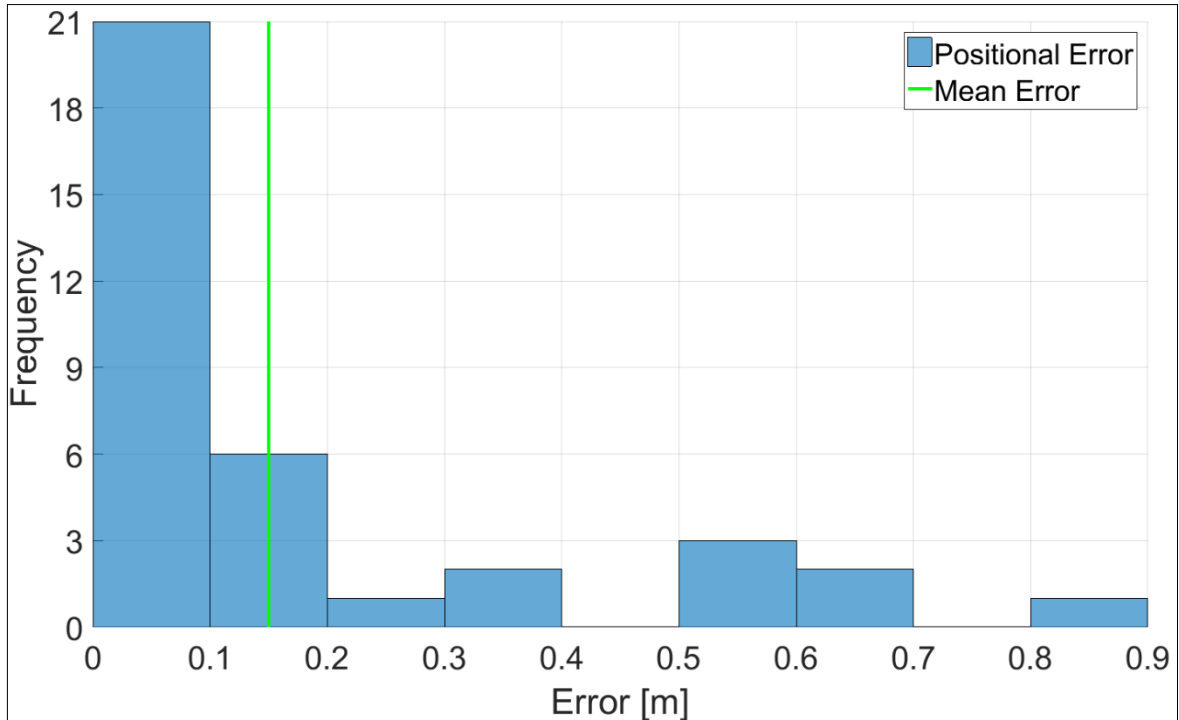


Figure 6-5: Histogram and the mean error for the extrapolated points of the DR trajectory

Furthermore, as can be seen from above histogram, the mean error is within the target accuracy, but 6 of the 36 extracted points fall above the acceptable accuracy for the localisation of cyclists. Nevertheless, the initial results were encouraging as the iBike measurement system appeared to have captured satisfactorily the essential kinematic parameters according to the design and implementation of the sensor configuration. A number of similar trials with the same experimental setup were conducted and the results contributed to the fine-tuning of the algorithms.

6.3 Fusion with Survey Points

The experimental results presented in the previous section was the initial testing of an earlier version of the iBike system, and this section concentrates on the experimental results obtained when the system was more advanced with the fusion algorithms. In other words, the limitation of the system found from the initial

experiment led to the more in-depth study of the bicycle kinematics and the geometrical relationships in order to formulate the sensor fusion algorithms. Thus, this section reports on the results from a field experiment to demonstrate and evaluate the proposed sensor fusion methodology discussed in Chapter 4. In this experiment, known survey points are randomly selected and assumed as the positions based on GNSS, Wi-Fi and GSM.

6.3.1 Experimental Setup

To implement the fusion algorithms described in Section 4.4, the instrumented bicycle underwent some modifications, so as to accommodate the new sensor configuration requirements. Figure 6-6 illustrates the instrumented bicycle with the new sensor configurations. One of the key differences is the placement of the seat tube sensors, which incorporates a gyroscope and accelerometer measuring the angular rates and accelerations of the rear frame respectively. In addition, the tablet PC is included to store the data in a database for future studies and the GoPro camera is installed to record the rear wheel path. Finally, the Arduino board is programmed to transfer the data fetched from the sensor at 66 Hz to the laptop.



Figure 6-6: The new iBike configuration.

An issue identified in the original experiment was that the bicycle was not continuously trackable in real-time by the TS in real-world traffic conditions, as the instrument requires a line of sight to the 360-degree reflector that was mounted on

the bicycle. In order to overcome this, an alternative method was devised for establishing the ground truth of the experiment, against which the computed trajectory from the presented sensor configuration would be validated. Specifically, a route was selected around City, University of London's campus and was then mapped using topographical surveying techniques, and specifically a Leica TCRA1103plus TS. Figure 6-7(a) illustrates the technique which was employed to map certain road features of the selected route with the TS. However, since the route presented many obstacles such as buildings and trees, a number of control stations were set up to survey the entire route and they are illustrated in Figure 6-7(b). The green markers 1 to 3 were surveyed based on the nearest OS control point stations; INT294, INT284, INT199, INT291 and INT283 which are situated in Canary Wharf Tower, Telecom Tower, St Paul's Cathedral, Crystal Palace North Mask and Big Ben respectively [175]. The red markers 4 to 10 were established as a subset based on the green markers.

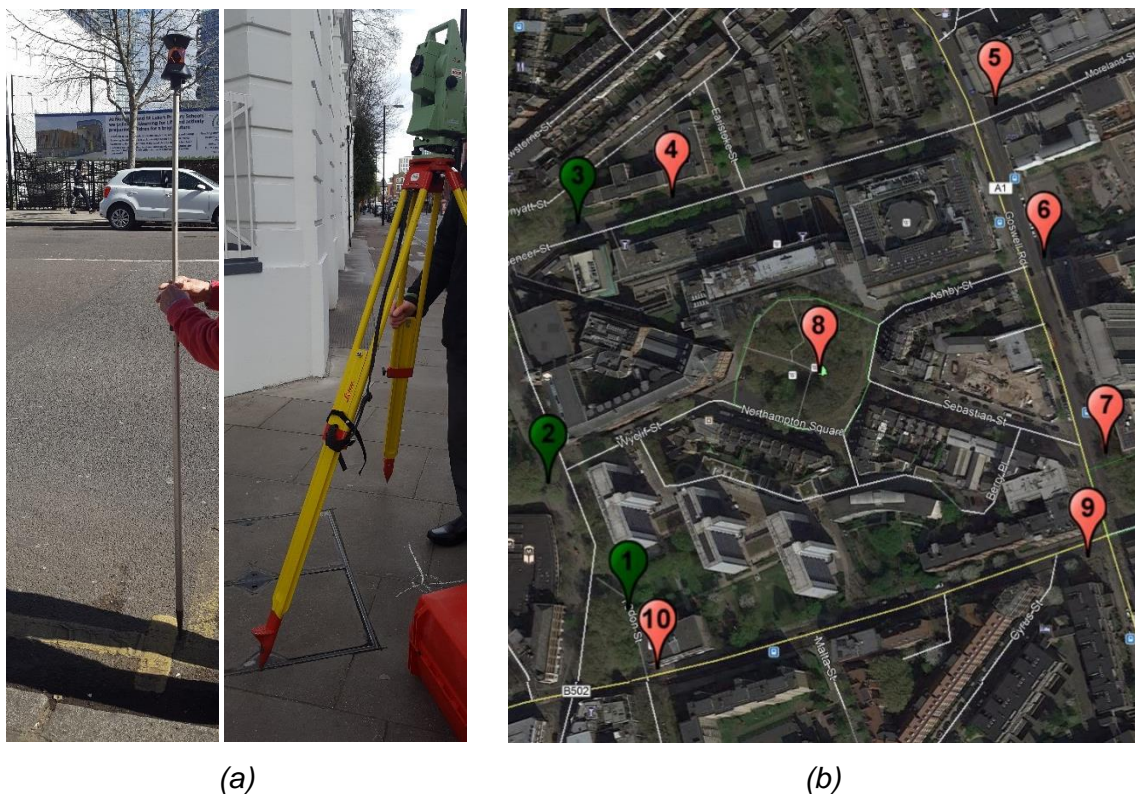


Figure 6-7: (a) Topographical surveying techniques; (b) location of the control stations of the survey

Figure 6-8(a) illustrates the route used for this trial, which was surveyed prior to the actual experiment with the iBike, and, as illustrated in Figure 6-8(b), the precise

coordinates of a number of points were measured and recorded using the UK Ordnance Survey (Eastings and Northings) coordinate system. During the actual experiment, the instrumented bicycle was ridden directly over (or as close as possible to) the surveyed points. As a result, approximate coordinates of the bicycle at the surveyed locations were available and this enabled the accuracy of the overall system with the proposed algorithms to be approximated. The overall survey route consisted of 93 survey points and the length of the route was approximately 1050 m from start to end.

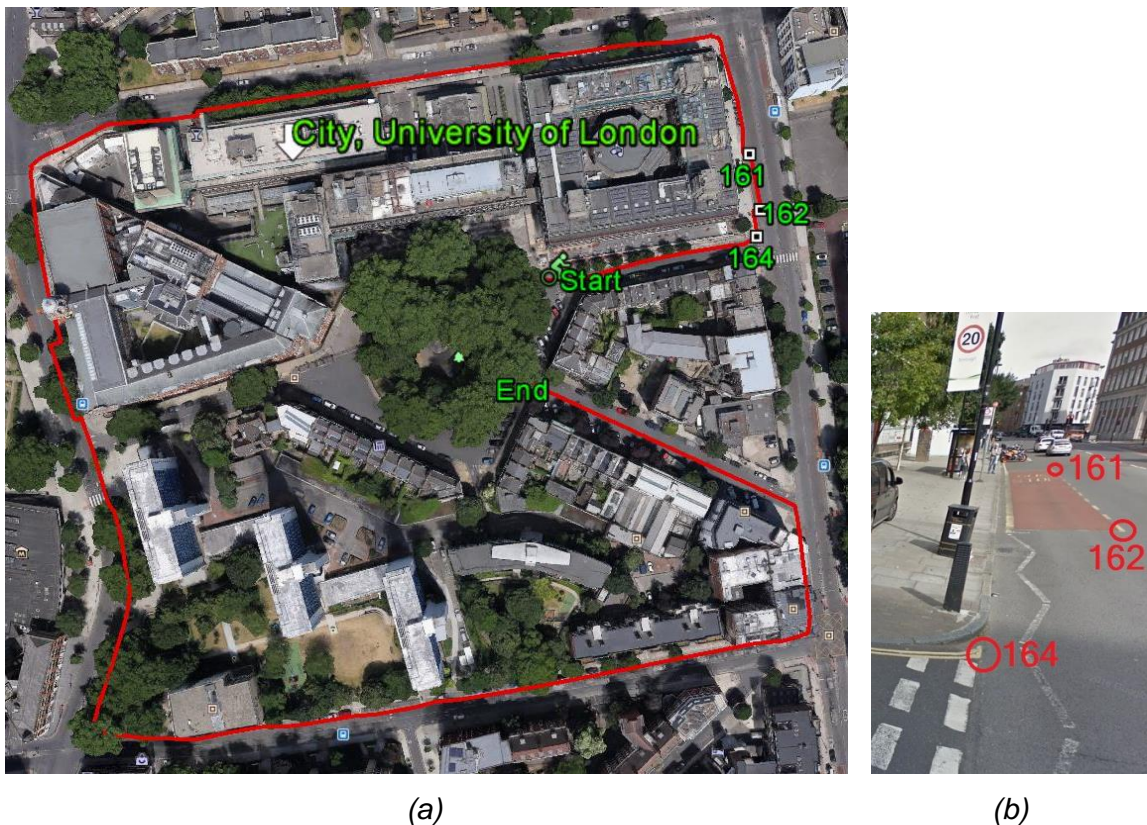


Figure 6-8: (a) Satellite view of the experimental route; (b) illustration of three surveyed points along the route.

As presented above, for practical reasons pertaining to the cyclist's vision and skill, as well as to the surrounding traffic conditions and due to the surveying techniques utilised, the bike could often not be ridden exactly over the survey points. This meant that there was very likely an inherent error in the measurement relating purely to external factors rather than to the iBike system itself. Therefore, the ground truth data are assumed to be within ± 0.5 m from the actual position of the bicycle and this assumption is made from the analysis of the video footage obtained via the GoPro camera. Hence, as in the previous experiment with the TS, the inherent 0.5 m

positional error from the ground truth system needs to be subtracted from the absolute displacement between the reconstructed and the presumed actual trajectories of the bicycle (refer to Figure 6-4) so as to calculate the FPE.

6.3.2 Data Processing and Results

Following the experiment, the acquired raw data from the iBike measurement sensors were utilised to transform bicycle motion measurements into relative positions and to fuse the positions with the known survey points discussed in the previous section. In summary, the data processing involved the reconstruction of the trajectory based on the DR technique and the fusion of the acquired data with the yaw angle and position Kalman filters. For the latter filter, the known survey points were randomly selected and were assumed as the positions based on GPS, Wi-Fi APs and GSM. The random selection process was employed to simulate the positions measured by the systems mentioned above, as some of the measurements from these systems would be subject to a large position error and they could not be fused with the sensor data.

The results obtained from a single journey along the surveyed route are illustrated in Figure 6-9, where the blue line represents the computed path from the iBike sensor data and the DR model and the green line represents the fused trajectory based on the Kalman filters. The red hollow circles represent the survey points established prior to the experiment, while the black dots represent the randomly selected survey points used in the position Kalman filter. Finally, the red star denotes the initial position used in the algorithm illustrated in Figure 4-16. Moreover, it can be seen from this figure that the reconstructed trajectory based on the iBike data with the DR technique alone is prone to drift; however, the fused trajectory, based on the Kalman filters and a random selection of survey points, clearly indicates an improvement on the overall results. Additionally, to examine the accuracy of the overall methodology, the k-nearest neighbours algorithm mentioned previously was applied to the generated trajectories together with the survey points. This process aided the extraction of the points which are correlated with the survey points, and allowed the error at each survey point to be computed for the DR and fused trajectories.

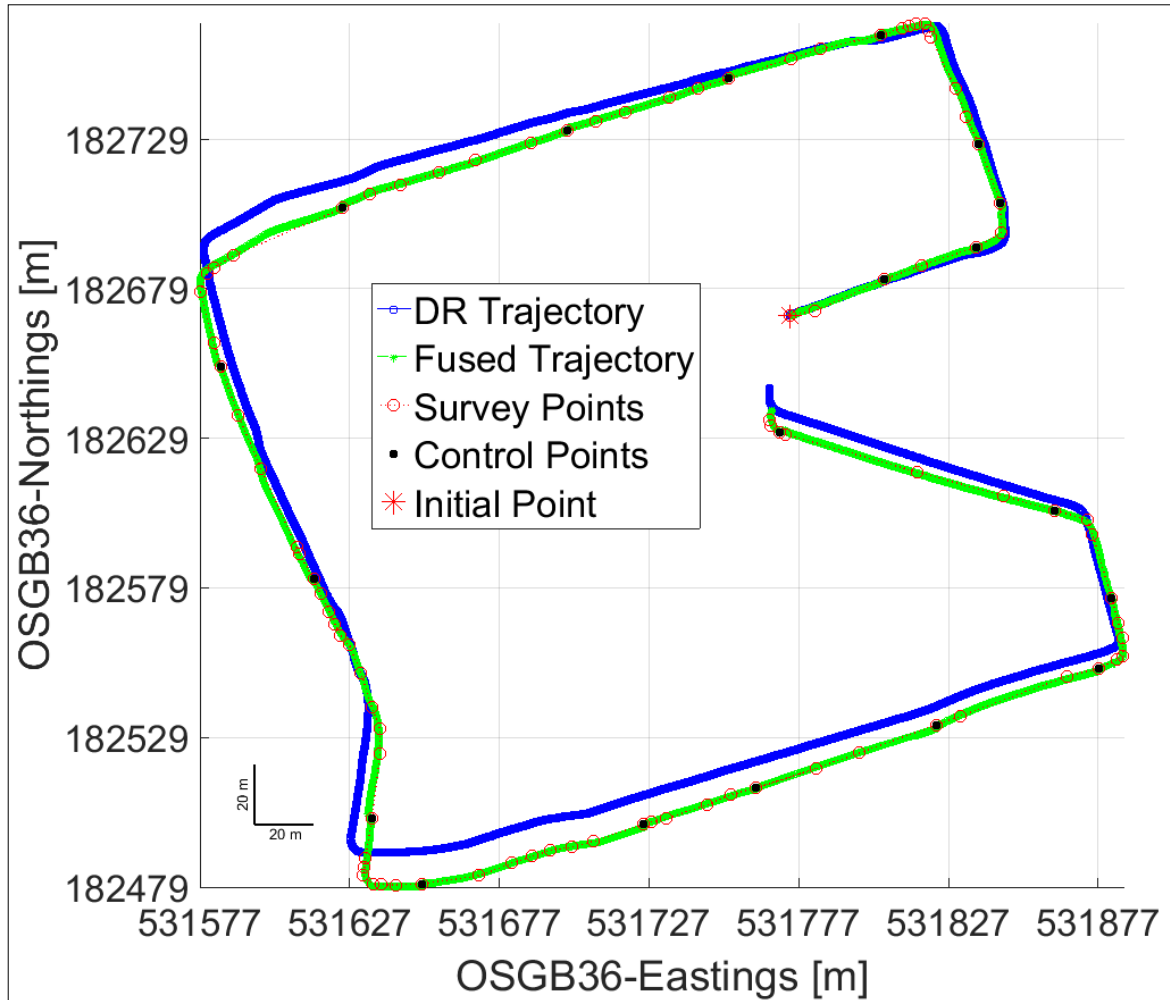


Figure 6-9: Comparison of the trajectories

Table 6.1 presents the mean, standard derivation and maximum of the FPE, while Figure 6-10 presents the comparison of the Cumulative Distribution Function (CDF) of the FPE of computed trajectories based on the DR and fused algorithms.

Table 6.1: Mean, standard deviation and maximum values of the DR and fused

Algorithms:	Mean (m):	Std. Dev. (m):	Maximum (m):
DR	4.16	3.31	10.83
Fused	0.13	0.28	1.47

As can be clearly seen from the graph in Figure 6-10, the proposed sensor fusion technique in Chapter 4 enhances the results; in fact, with a 90% probability a position can be estimated with less than 0.5 m error. On the other hand, the DR error accumulates continuously, and it can be used to estimate a position with less than 0.5 m error only with a 10% probability. Additionally, it should be noted here that for practical reasons pertaining to the cyclist's vision and skill, as well as to the

surrounding traffic conditions, the bike could often not be ridden exactly over the survey points. Thus, the actual positional error could be even lower than what is reported here.

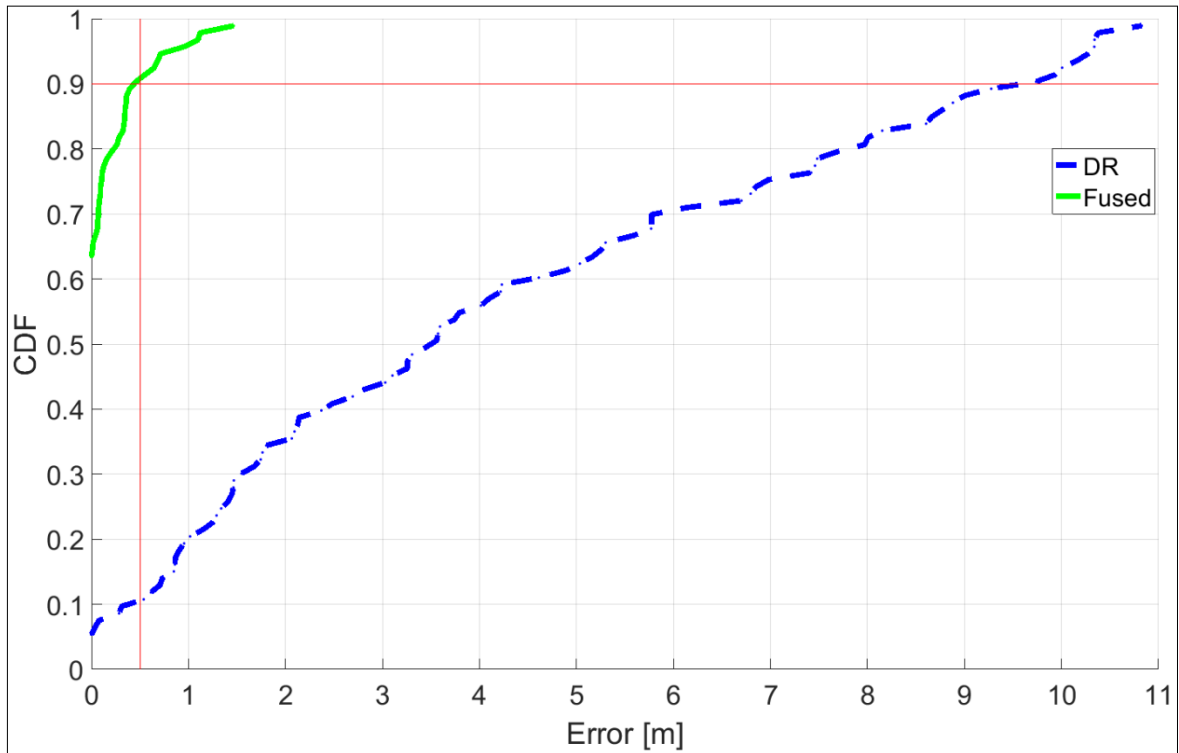


Figure 6-10: Comparison of the DR and Fused positional error

6.4 Fusion with GPS, WiFi and Cell Towers

It was observed that tracing the planned route was made difficult because of traffic variations on repeated journeys over the longer route presented in the previous section. Patterns covering the survey points could not be discerned. Therefore, for purposes of validation and to compare the accuracy with the readily available positioning systems of the overall iBike system together with the proposed sensor fusion algorithms, a quieter route was selected and surveyed using the same topographical survey principles reported in the previous section. The quieter route allowed the experiment to be repeated several times with the same setup. Thus, this section reports on the field results obtained from the Spatial INS, smartphone GPS and the fused trajectories based on the iBike acquisition data and methodology presented in Chapters 4 and 5. This section also then evaluates the accuracy of each system based on the survey points and presents the statistical analysis of the overall results.

6.4.1 Experimental Setup

For this experiment the instrumented bicycle illustrated in Figure 5-27, which incorporates the smartphone and the Spatial INS together with the sensor configuration presented in Figure 6-6, was used. As stated previously, the smartphone together with the app called GPSLogger was utilised to gather the GNSS data while the bicycle was in motion. In addition, the Spatial INS was used to collect enhanced position data with the aid of the tablet PC and bespoke data acquisition software illustrated in Figure 5-30. The selected survey route consists of Myddelton St, Gloucester Way and Whiskin St as illustrated in Figure 6-11(a) and comprises 39 survey points, of which two are presented in Figure 6-11(b) below.

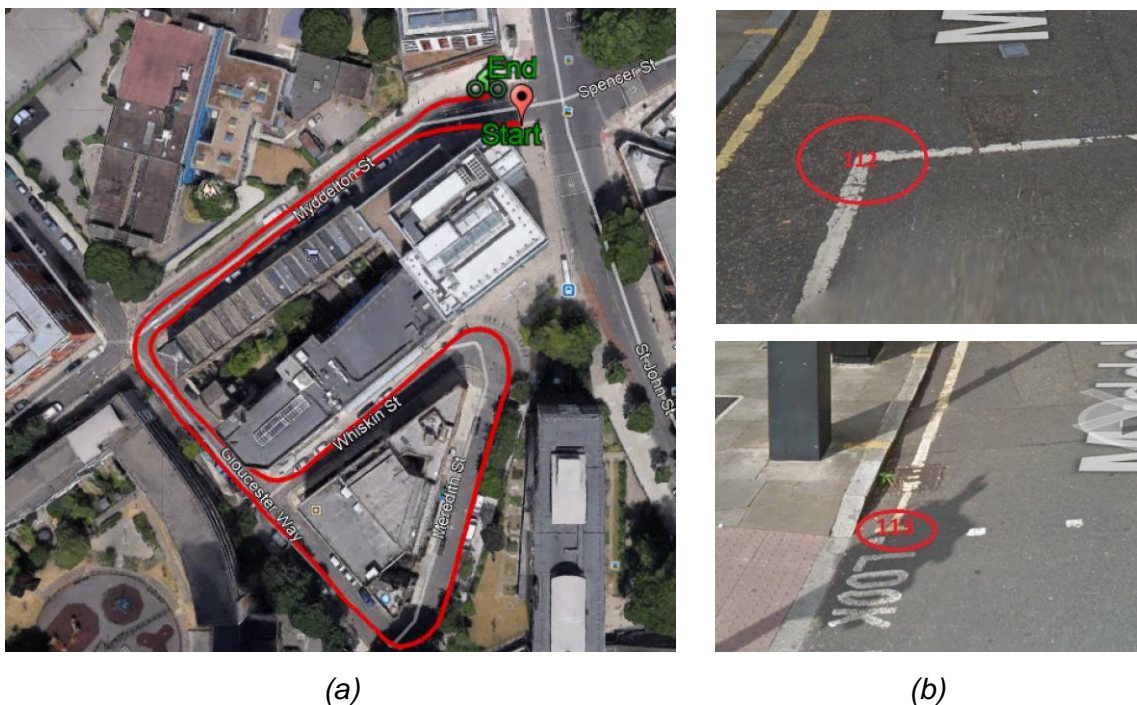


Figure 6-11: (a) OS map of the experimental route; (b) The first two control points along the survey route

6.4.2 Data processing and Results

Following the experiment setup, several trials were conducted and the graph in Figure 6-12 illustrates the Spatial INS trajectory obtained from a single trial along the surveyed route shown in Figure 6-11(a) above. In the graph below, the black line represents the INS trajectory, while the red hollow circles with the dotted line represent the survey points. It is clear from the graph that the Spatial INS could locate the initial and final few positions, but the Spatial INS could not track the

bicycle throughout the route with a high accuracy and could not maintain the positioning of the bicycle while it was in motion.

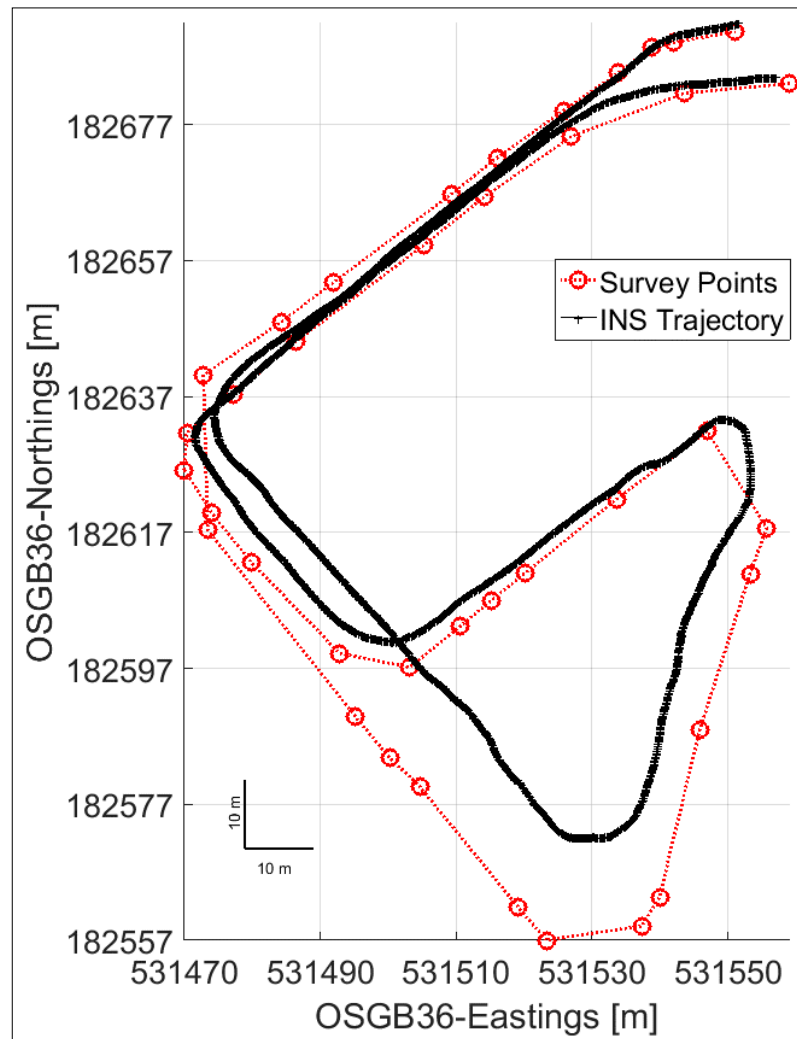


Figure 6-12: Survey points versus Spatial INS trajectory

Figure 6-13 represents the GPS trajectory of the bicycle motion along the survey route of the trial, where the pink line with the dots represents the GPS points established using the smartphone, and the red hollow circles with the dotted line represent the survey points. As expected, GPS alone does not provide a high accuracy throughout the route but some of the measured positions do correspond to the survey points. Thus, this information can be fused with the developed position Kalman filter discussed in Section 4.4.4 which was designed to enhance the positioning accuracy of the bicycle's motion with the acquired data from the onboard sensors. Thus, to select the appropriate GPS points for the fusion algorithms, error values were first computed for each of the sample points from the GPS with respect to the current position data based on the DR algorithm. For this step, it was assumed

that the accuracy of the DR position data is within the acceptable range for a given time horizon.

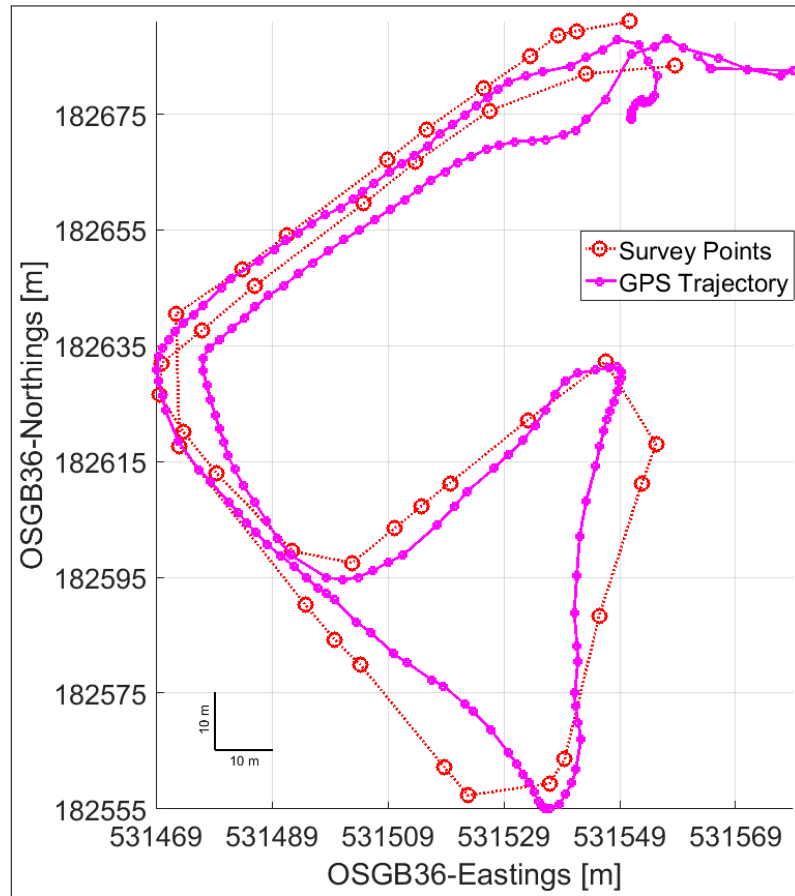


Figure 6-13: Survey points versus GPS trajectory

The graph below illustrates the error values and the points which were below the threshold and were selected for the position Kalman filter in the fusion algorithms.

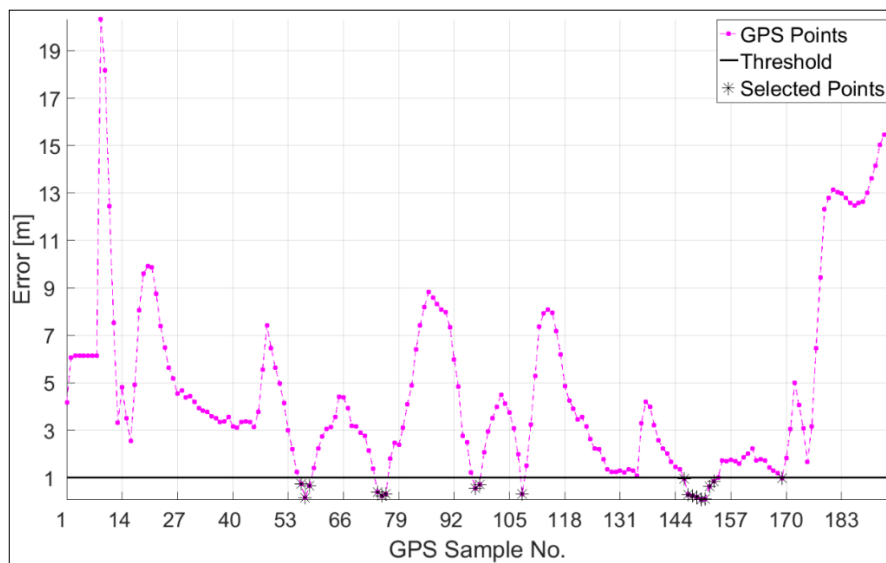


Figure 6-14: Selection of GPS points below the threshold limit

The graph in Figure 6-15 represents the fused trajectory consisting of the positions based on the GPS, RSS of Wi-Fi APs and mobile phone base stations, as well as relative positions found through the acquired data from the measurement sensors of the iBike. In the graph, the black dots denote the stationary positions of the bicycle, which were established using the Google Maps app, the pink dots represent the GPS positions, which were computed by the GPSLogger app when the bicycle was in motion, the green line represents the fused trajectory based on the fusion algorithms. The black and pink dots were used in the position Kalman filter as the measurements. Moreover, the red hollow circles represent the survey points established prior to the experiment, while the red star denotes the initial position used in the algorithms.

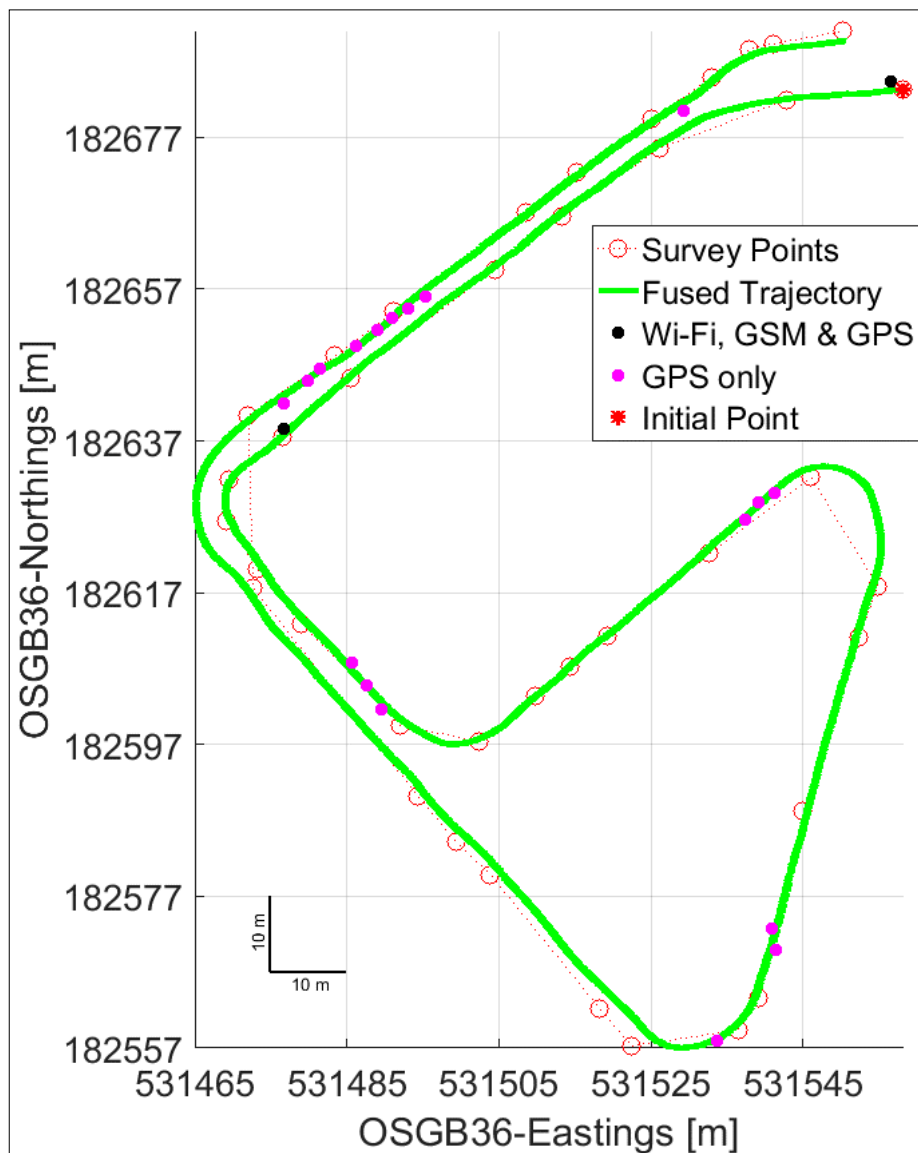


Figure 6-15: Survey points versus Fused trajectory

In summary, the graphs in Figure 6-12, Figure 6-13 and Figure 6-15 above demonstrate the trajectories of each of the systems of a single experiment along the survey path. These graphs show that each trajectory differs from all the others. The fused trajectory is more consistent with the survey path whereas the GPS and INS have a large discrepancy. Nevertheless, a process was devised to compute the error of each system against the ground truth survey points. This process involved extracting the data for each trial from the database, and extrapolating the timestamps which were associated with the survey points around the route using the k-nearest neighbours algorithm, where fused and survey points were used as the inputs to the function and the outputs were the extracted timestamps. Figure 6-16 presents the process described above.

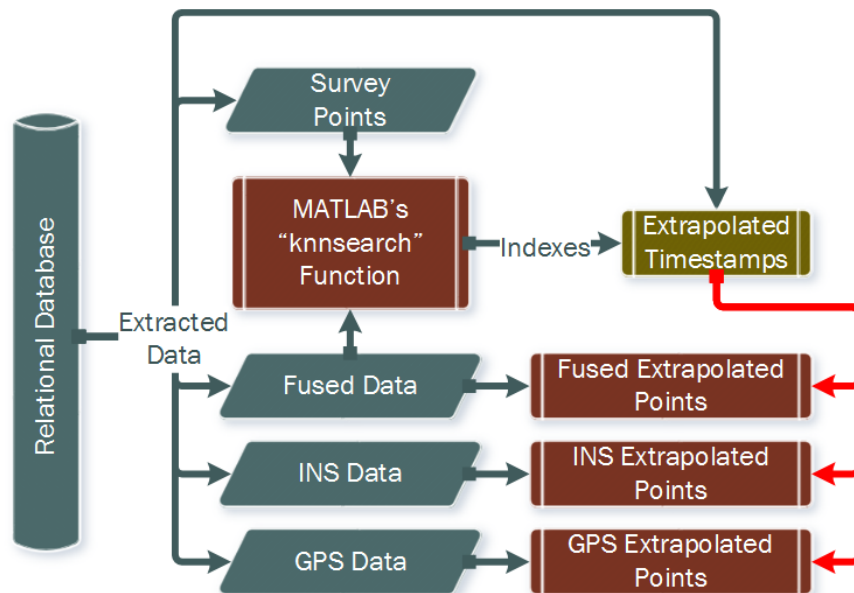


Figure 6-16: The process of data extraction and extrapolation

Thus, using the above process the extrapolated points of each of the trajectories presented in Figure 6-12, Figure 6-13, and Figure 6-15 are illustrated below. In this graph, the red hollow circles represent the survey points, and the black crosses, the pink squares and the green stars represent the extrapolated points of the Spatial INS, smartphone GPS and fused data respectively.

Following the extrapolation of the points, error values were then computed for each of the systems with respect to the 39 survey points and the same process was repeated for several trials. Thus, the next section reports on the analysis of the results of the experiments.

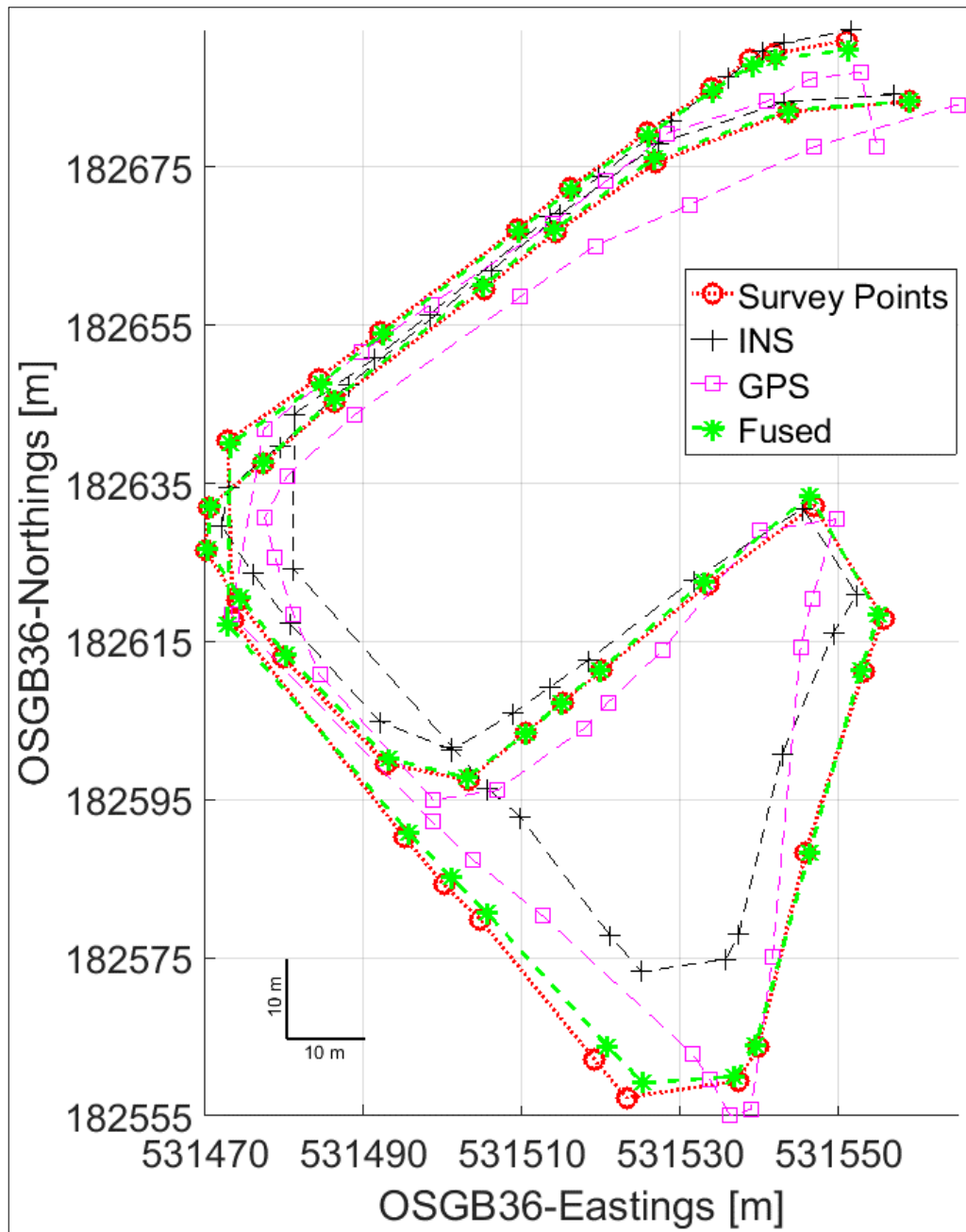


Figure 6-17: Survey points versus extrapolated points

6.4.3 Statistical Analysis of the Results

Following the data processing and extrapolation of the points, FPE values were then computed for each of the systems. The same process was repeated for several experiments, where Table 6.2 summarises and compares these experiments along the selected route. This table presents the average error, standard deviation, maximum and number of samples for each of the systems along with the trial number. Additionally, sample datasets of the raw (unfiltered) errors and positions of each system are included in Appendix C.

Table 6.2: Comparison of FPE of each system with 9 separate trials around the route

System:	Average (m):	Std. Dev. (m):	Maximum (m):	No. of Samples:	Trial No:
Fused	0.18	0.27	0.96	7435	1
INS	4.57	3.36	12.77	201	
GPS	11.33	4.42	21.41	7435	
Fused	0.09	0.25	1.03	6867	2
INS	6.78	4.45	14.96	172	
GPS	10.04	6.67	33.29	6867	
Fused	0.19	0.43	1.75	7148	3
INS	12.72	11.19	31.93	175	
GPS	9.11	5.98	30.55	7148	
Fused	0.35	0.63	2.66	7353	4
INS	11.77	7.87	31.70	177	
GPS	8.13	3.69	15.37	7353	
Fused	0.13	0.24	0.94	7430	5
INS	8.29	3.56	16.09	189	
GPS	11.67	10.49	41.80	7430	
Fused	0.45	0.82	3.56	7090	6
INS	18.75	15.62	44.73	181	
GPS	8.34	5.58	24.05	7090	
Fused	0.36	0.69	2.84	7631	7
INS	7.03	4.39	15.71	199	
GPS	8.28	4.63	22.16	7631	
Fused	0.24	0.49	2.28	7734	8
INS	5.43	4.77	15.53	194	
GPS	6.30	3.00	13.51	7734	
Fused	0.20	0.35	1.49	7039	9
INS	19.31	15.07	42.97	169	
GPS	7.28	6.81	31.11	7039	
Fused	0.24	0.38	1.80	7303	Average Results
INS	10.52	5.95	20.28	184	
GPS	8.94	4.09	20.89	7303	

Figure 6-18 illustrates the comparison of the average errors formulated from the above table, and, as can be seen, it is clear from the computed results that the average error of the fused trajectories is significantly lower than the Spatial INS and GPS by itself. On the other hand, the Spatial system achieved slightly better results than using the GPS alone in trial 1, 2, 5, 7 and 8, and these were the expected results in some respects, as the Spatial INS incorporates a high accuracy MEMS IMU with a better GPS receiver. However, in trial 3,4,6 and 9, the Spatial system

performed poorly in contrast with the GPS and this is an unexpected result given that the device is designed to enhance the positions based on the GPS signals. Then again, it also demonstrates the challenge of tracking a bicycle with a high precision in an urban area even with an expensive system. Nevertheless, in this experimental setup, the average FPE of all nine trials for the iBike system with the fusion algorithms is within the target localisation accuracy for the Cyclist 360° Alert system and this is an achievement obtained through this research work.

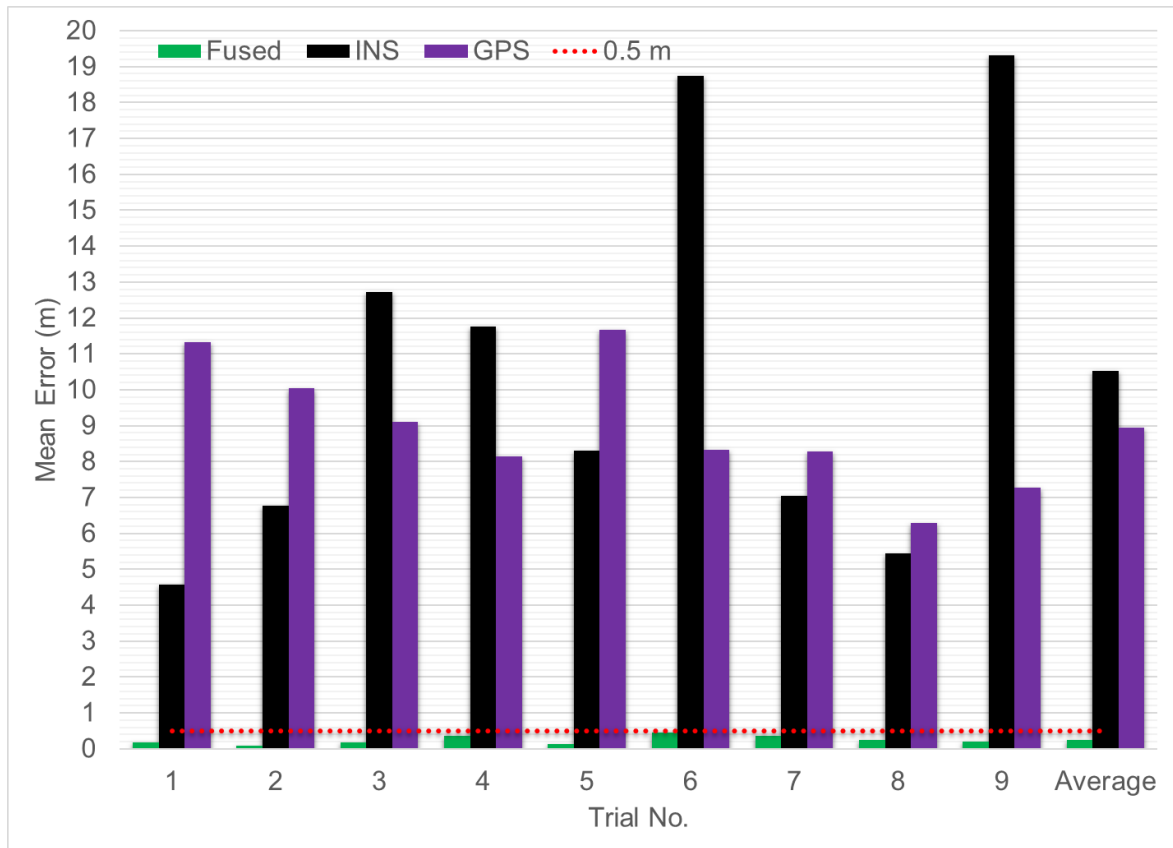


Figure 6-18: Comparison of mean error for each trial with the respected system

The statistical significance tests were also undertaken for the obtained results so as to assess the quality of the overall results and determine whether the differences in errors of the iBike system with the fusion algorithms are statistically significant. Thus, a t-test at 2% significance level was conducted for each trial with the following hypothesis:

- The null hypothesis is $H_0: \mu_0 = 0.5m$.
- The alternative hypothesis is $H_1: \mu_0 < 0.5m$.

The following well-known equation was used to obtain the t-test statistic value for each trial:

$$t = \frac{\bar{x} - \mu_0}{s/\sqrt{n}} \quad (6.2)$$

where \bar{x} is the sample mean, μ_0 is the specified mean value, s is the standard deviation of the sample, n is the sample size.

The sample mean and standard deviation of the sample for each fused trajectory is given in Table 6.2 and the sample size for each case is 39, which is equal to the survey points of the route. Based on these, the t-test value and the decision on the hypothesis for each trial are given in the following table, where the p-value, which represents the probability of the observing sample results using the t distribution, was calculated using the Excel T.DIST function.

Table 6.3: The t-test results of the trials with the decision

Trial No.:	t:	p-value (T.DIST):	Decision on the Hypothesis:
1	-7.61	1.88E-09	Reject Null and Accept Alternative Hypothesis
2	-10.27	8.20E-13	Reject Null and Accept Alternative Hypothesis
3	-4.58	2.43E-05	Reject Null and Accept Alternative Hypothesis
4	-1.47	7.45E-02	Fail to Reject Null Hypothesis
5	-9.66	4.48E-12	Reject Null and Accept Alternative Hypothesis
6	-0.35	3.63E-01	Fail to Reject Null Hypothesis
7	-1.30	1.00E-01	Fail to Reject Null Hypothesis
8	-3.33	9.64E-04	Reject Null and Accept Alternative Hypothesis
9	-5.40	1.87E-06	Reject Null and Accept Alternative Hypothesis
Average	-4.27	6.35E-05	Reject Null and Accept Alternative Hypothesis

As can be seen from the above table, trials 1,2,3,5,8,9 and the average results do provide sufficient evidence to conclude that the mean FPE of trials differs from 0.5 m at the 2% significance level, while trials 4 and 7 are statistically significant at the 10% level and trial 6 is significant at the 40% level. As a result, the latter trial has a lower confidence level compared to the all other trials, but the mean error is within the tolerable positional error of the reconstructed trajectory defined in Figure 6-4.

One of the reasons for the discrepancy of the results could be due to the quality of the accepted GPS data used for the fusion algorithms. In other words, if there was unexpected level of noise or errors on the sensors' data, the DR algorithm would incorporate any error into the trajectory, and by coincidence if the measured GPS positions also falls within its threshold, then the fused trajectory would follow the GPS, even though it is not accurate, rather the actual path. Though these occurrences are very low, they are highlighted in the field trial results.

Furthermore, the cumulative distribution of the average FPE for each of the respective systems are presented in Figure 6-19, while Appendix C shows the unfiltered cumulative distribution of each of the trials and systems. The graph below clearly indicates the improvements made through this research work and demonstrates that, on average with an 80% probability, the iBike system together with the fusion algorithms can be used to estimate a position with less than 0.5 m error, compared to an 11.6 m error from the GPS and a 16.2 m error from the Spatial INS under the same circumstances. Further comparisons are made in Table 6.4. Therefore, it can be concluded that the iBike achieves better positioning than the GPS and INS, and the overall results are encouraging for the future developments in this field of study.

Table 6.4: Comparisons of the probability of the positional error for each of the respective systems.

Probability:	Fused (m):	INS (m):	GPS (m):
90%:	0.63	18.25	14.87
50%:	0.09	12.90	7.55
30%:	0.60	5.03	6.29
10%:	0.03	3.58	5.46

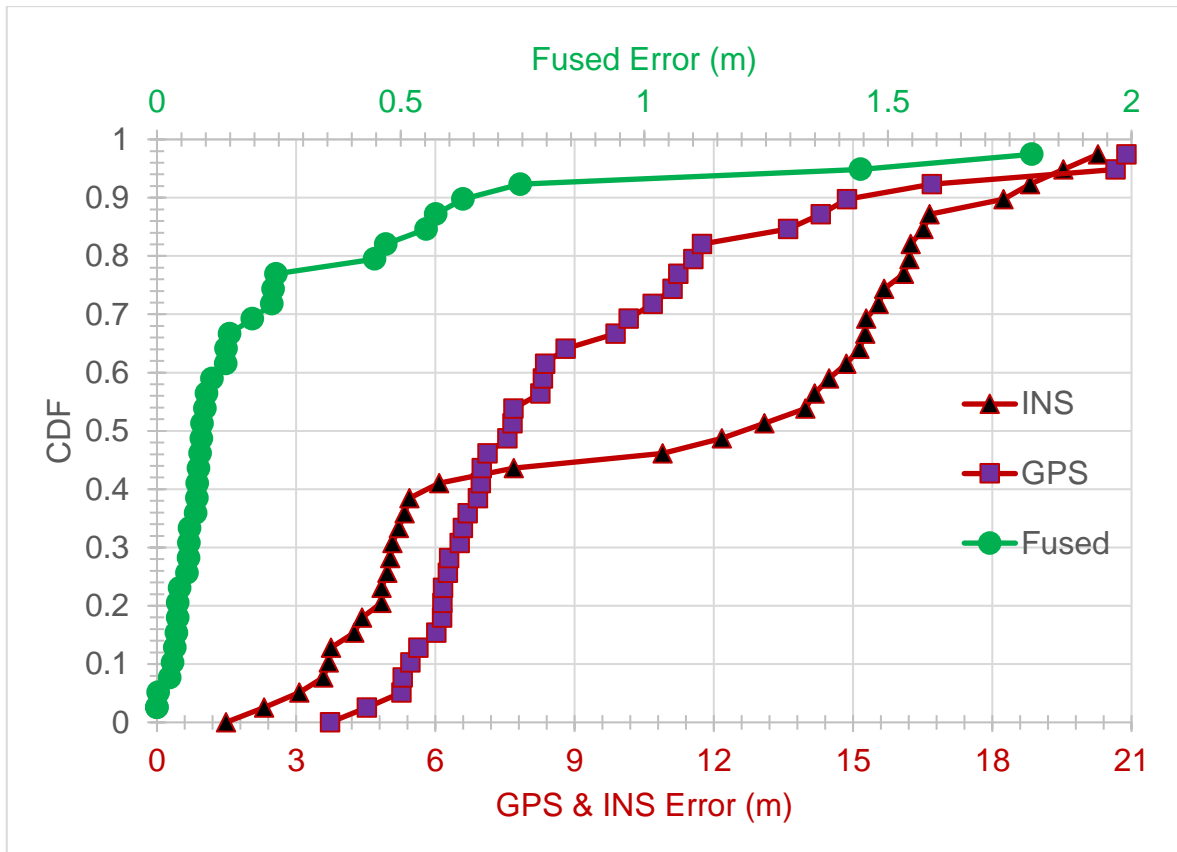


Figure 6-19: Comparison of fused, GPS and INS average positional error

6.5 Conclusions

This chapter concentrated on the testing and validating the developed iBike system with the proposed methodologies and focused on the evaluation of the accuracy of the overall system. Moreover, the chapter presented results from the field experiments which utilised the prototype iBike system in urban traffic conditions to gather real-world data while the bicycle was in motion. The collected data then post-processed using the developed software reported in Chapter 5.

In summary, Section 6.2 reported on the very first experiment of the iBike system with the TS in an outdoor environment. The idea of this experiment was to acquire the raw sensors data of the iBike while it was in motion and concurrently tracked by the TS. This trajectory was then compared with the positions of the motion of the bicycle established using the TS. Accordingly, error values were computed at each tracked position and were compared with the extracted point from the DR trajectory at the same location. This result was encouraging and led to further improvements.

Section 6.3 described the field experiment that was conducted to validate the developed fusion algorithms which incorporate the two Kalman filters designed in Section 4.4. The results from the field trials supported the proposed methodologies and showed that it is possible to achieve a higher accuracy using the developed algorithms.

Section 6.4 then evaluated and compared the accuracy of the fused trajectories, which were based on the data from the onboard measurement sensors as well as selected positioning data translated from the local and global infrastructures, with the Spatial INS and using GPS alone. The overall results led to the conclusion that the fused trajectories were smoother, and they resembled natural behaviour that a bicycle would follow while being ridden under normal circumstances, obeying the highway codes. On the other hand, the trajectories established employing the Spatial INS and the smartphone's GPS receiver did not always illustrate the same behaviour throughout the experiments, let alone the accuracy. Consequently, the field results confirmed that the innovative sensor fusion algorithms together with the iBike developed in this study, certainly, enhances the positioning accuracy and reliability.

Furthermore, taking into account the error introduced by the ground truth technology, the experimental results suggest that the design requirement of 0.5 m localisation accuracy for the Cyclist 360° Alert system is met with an 80% probability. Until further and more extensive tests are carried out to minimise that error, however, this result should be treated with some caution mainly due to the limitation of the method utilised to validate the system with the ground truth technology. Moreover, since the ultimate aim is to utilise the developed methodologies in a safety-critical application, the error which falls above 0.5 m for the fused trajectory will be addressed in future work.

Chapter 7: Conclusions and Future Work

7.1 Summary of the Chapter Findings

Bicycle-related collisions with motorised traffic at low speeds in urban areas are a growing problem in modern society and many stakeholders seek to find solutions. This thesis presented the first stage of the development of the timely Cyclist 360° Alert system, which aims at addressing the problem. The overall concept of the system is to provide the ability to monitor the obscured regions and take preventive action if a potential conflict scenario is detected. The concept was formulated from the review of the accident data in Chapter 2. The review found that one of the main causes of accidents between cyclists and vehicles is that the driver cannot spot the cyclist in some traffic conflict scenarios, especially in intersections and junctions, due to their small size and their erratic movement as well as the blind spots which the drivers of the vehicles cannot see from their driving positions. It was also clear from the review that although left-turning manoeuvres by a large vehicle across the path of a cyclist have the highest rate of fatalities, they were not the only type of conflict for cyclists.

A review of the existing ITS solutions found that a few detection systems are available to alert drivers to dangerous situations. However, due to the poor accuracy of the warning systems and detection of the cyclists, drivers may distrust and shut down the systems. The main reason for the poor accuracy of the systems is the errors in the position measurements. If the input position has an error greater than ± 0.5 m, the output prediction from the system is most likely to follow the same trend. Therefore, it is important to accurately localise cyclists and vehicles so that prediction of potential future collisions can be made with more confidence and that positive alerts being triggered by the warning system can be improved. However, accurate tracking and estimating one's position in a critical time-horizon are important unresolved challenges, especially for bicycles.

Moreover, a desk evaluation of the existing localisation technologies in Chapter 3 found that although most of the widely available localisation systems can be utilised to estimate the position of an object, these systems do not provide sufficiently high resolution and accuracy to locate and track a bicycle in real-time, mainly due to its small size and erratic movements. On the other hand, some systems able to meet the design requirements do exist, but they are either subject to restrictions or are too costly. Therefore, a hybrid approach was proposed using the GPS, WPS, CTPS and bicycle motions. Here, the objective was to develop innovative multi-level sensor fusion methodologies that relied on low-cost sensors, such as the ones commonly found in smart devices, to monitor the bicycle's motion, and to interact with ubiquitous communication technologies on the local and global infrastructures (such as Wi-Fi access points, mobile base stations and GPS). As a result, using an appropriate sensor fusion technique, the sensor data could then be combined to reconstruct the trajectory path of the bicycle to meet the desired localisation accuracy in a cost-effective way for the cyclists.

Consequently, through the study of bicycle kinematics and geometrical relationships illustrated in Chapter 4, sensor fusion algorithms with two Kalman filters, one for the direction and one for the position, were developed to improve the positioning accuracy for cyclists. The study also helped to identify the five critical kinematics measurement parameters of steering angle, roll angle, roll rate, yaw rate and travelled distance, along with three crucial bicycle design parameters of wheelbase, caster angle and rear wheel diameter, which were required successfully to implement the models.

Accordingly, as presented in Chapter 5, a 'Barclays Cycle Hire' bicycle (now sponsored by Santander) was instrumented with the MEMS gyroscopes, MEMS accelerometers, and absolute encoder and Hall Effect proximity sensors to measure the identified kinematics parameters stated above. Moreover, a data acquisition system was developed to acquire the sensors' data and the data from the smartphone, Spatial INS and camera, which were equipped on the bicycle as part of the prototype system. In addition, a state-of-the-art relational database with multiple tables using MySQL was developed to structurally store the raw and processed data collected via the iBike system. Two pieces of bespoke software

were also engineered for the acquisition and the post-processing of the data with the established methodologies.

Following the development of the prototype iBike system, Chapter 6 presented several field experiments which were conducted with the bicycle in urban areas in real-life traffic conditions so as to validate the iBike measurement system and to acquire real-world data to evaluate the accuracy of the developed methodology in Chapter 4 with the readily available positioning systems. Accordingly, the acquired measurement data from the sensors were transformed with the techniques discussed in Section 5.2 and then post-processed with the algorithm design presented in Section 4.6. The overall results of the field experiments led to the conclusion that the fused trajectories were smoother, and they resembled natural behaviour that a bicycle would follow while being ridden.

Moreover, taking into account the error introduced by the ground truth technology, the experimental results also demonstrated that, on average with an 80% probability, the developed methodology in this thesis can be utilised to estimate a position with less than 0.5 m error, compared to an 11.6 m error from the GPS and a 16.2 m error from the Spatial INS under the same circumstances. The error from the GPS was an expected result, as highlighted in the literature review in Chapter 3. However, the large error for the Spatial INS was an unexpected result given that the device is designed to enhance the positions based on the GPS signals. In contrast with the results from the iBike system, the Spatial INS performed poorly, and this could be due to the technique used to fuse the data. The iBike fusion algorithm is more sophisticated and enhanced to rely on both the onboard measurements (for a given time horizon) and GPS, WPS and CTPS whenever their data fall below the threshold. In comparison, the Spatial INS heavily relies on the GPS and it probably does not apply the above technique. Consequently, the real-world data from the field experiments clearly demonstrate the appropriateness of the developed system together with the algorithms designed in this thesis.

7.2 Summary of Contributions

The contributions of the research work are summarised below:

- **An Innovative Concept for Tracking Cyclists** – Traffic safety at or near intersections has always been a major concern due to the complex driving scenarios, and real-time tracking of cyclists in these environments is a major engineering challenge, especially as cyclists are able to move more freely and occupy a small region of space. They are also somewhat unpredictable. Localisation of cyclists is made even more difficult with the requirement of a high level of accuracy, so that false alerts to the driver, which could be dangerous in some traffic situations, could be avoided. Nevertheless, an innovative concept named “Cyclist 360° Alert” was formalised from the understanding of the main causes of bicycle-vehicle related collisions, and from the main drawbacks of the existing ITS solutions reviewed in Chapter 2. Furthermore, in the review of the existing positioning systems methodologies in Chapter 3, it was found that no single localisation system currently exists to fulfil the requirement of the formulated concept. Hence, a novel approach was proposed to fuse multi-sensor data to improve the localisation accuracy based on existing technologies and sensors widely found on smart devices and in urban areas.
- **Sensor Fusion Algorithms for Pedal Cycles** – A study was conducted to understand the characteristics of bicycle behaviour, specifically the turning behaviour while it is in motion, in order to develop a methodology to fuse multiple sensor data and output position information in terms of Eastings and Northings (Ordinary Survey coordinate system). Then from bicycle kinematics, a simplified positioning model was developed to reconstruct the bicycle’s trajectory using a dead-reckoning technique. The model was then further developed and utilised in a Kalman filter fusion algorithm to improve the localisation accuracy, compared to existing systems. The full design of the mapping algorithm with design models are presented in Chapter 4.
- **Instrumentation and Validation of an Instrumented Bicycle** – A number of kinematics measurement parameters and bicycle design parameters were defined from the design of the sensor fusion algorithms. Then an overall system architecture presented in Chapter 5 was formulated and developed to support the

proposed algorithms. Based on the design, a Santander Bicycle Hire cycle was instrumented with various low-cost sensors which are capable of taking real-time measurements of the specified kinematics parameters. The sensor data was fetched and either stored locally or transmitted to an onboard tablet PC for processing. The raw data was then post-processed to reconstruct the bicycle's trajectories using the derived models proposed through mapping algorithms and then fused with other positioning systems using the Kalman filters.

Validation of the completed system was a difficult task partly because there is no system which can truly give the actual trajectory of the bicycle and can serve as the ground truth for a journey. Thus, a pioneering method was proposed and used to validate the iBike measurement system as well as other positioning systems. A number of field trials were conducted with the iBike and results are promising.

- **A State-of-the-art Database of Cyclist Trajectories** – Although a number of datasets currently exist for vehicles, to the best of the author's knowledge, there is no single dataset for cyclists' trajectories or modelling studies. Therefore, this research study designed and developed a state-of-the-art relational database with multiple tables using MySQL to structurally store the raw and processed data collected via the iBike system from field experiments. In other words, the database contains organised data from multiple systems installed on the instrumented bicycle. These systems include the iBike measurement system, Global Positioning System, Spatial Inertial Navigation System and data from a camera. The database was designed with a unique set of keys so that data can be assessed effortlessly and can be used to conduct further road safety analysis studies, for example on the behaviour of cyclists.

7.3 Reflection on Overall Work

Reflecting on the work conducted for this thesis, the actual development of the iBike system was a complex process and involved many technical challenges which had to be resolved. A number of new skills were essential in order to develop the measurement system for the iBike. In particular, several new pieces of software had to be learned so as to implement the necessary circuits and electrical systems and to develop CAD models to house the electronics. However, one of the main challenges, in carrying out the experiments, was the establishment of the ground

truth position data, since there is no single existing system which can give the actual trajectory of the bicycle while it is in motion and which can serve as the ground truth. With reference to Sections 6.3 and 6.4, an alternative method was devised for establishing the ground truth of the experiments. As a result, approximate coordinates of the bicycle at the surveyed locations were available and this made possible an estimate of the accuracy of the overall system with the proposed algorithms. This method overcame the major challenge.

On the other hand, due to the limitation of the methodology utilised to validate the iBike system with the ground truth technology and the inherent positional error, the overall results should be treated with some caution until further tests are carried out. Another challenge was the amount of funding available for the project. With stronger financial support, an unmanned aerial vehicle could have been employed to track the bicycle from the air while it was being ridden. More time for modelling could have produced a non-linear approach for the fusion algorithm which would have resulted in better performance of the overall iBike system. However, the considerable time spent on the initial review of the localisation technologies proved to be highly valuable.

In summary, the results from the field trials with the instrumented bicycle demonstrated the appropriateness of the hybrid approach as the position accuracy indeed can be improved over what is currently offered by GPS alone. Moreover, the analysis of the validated results presented in this thesis demonstrated that the innovative sensor fusion algorithms together with the iBike developed in this study improves the accuracy of the localisation. As a result, the methodologies along with the iBike can be applied to track cyclists, can potentially be utilised with a collision warning algorithm to reduce the occurrence of false alerts and can be employed within the Cyclist 360° Alert system in order to improve cyclist safety.

Furthermore, the iBike concept alone has many applications, aside from being an enabler of the Cyclist 360° Alert system. For example, iBikes can be used to collect environmental data to monitor air quality or to identify common cycling paths in busy junctions, even going as far as triggering priority at traffic lights at certain times. The concept can also be employed to enhance anti-theft systems, as well as to assist emergency services in case of accidents by transmitting the precise location of the

bicycle involved. In an increasingly congested urban environment more and more people will be attracted to travelling by bicycle if they think cycling is a safe alternative mode, and the iBike concept could contribute to that vision by offering a portable version of the iBike system, such as a smartphone app and this is the ultimate aim of this project. Overall, the design of the iBike system is part of the IoT; thus, it can serve as a vital tool in the context of a smart city and ITS. For example, transport could be integrated with air pollution control and other sustainable systems in the smart city of the future.

7.4 Scope for Further Work

Besides the development of the entire Cyclist 360° Alert system and its work phases discussed in Section 3.7, there are several other ways in which the work presented in this thesis can be advanced. A few of these future advances in the context of the positioning accuracy of a bicycle are described in the following subsections.

7.4.1 Onboard Sensor Fusion and Hardware

Precise measurements of the identified kinematic parameters of the bicycle are some of the important factors that determine the accuracy of the overall system. In other words, if the input parameters to the algorithms have inaccuracies, the output position from the system is most likely to follow the same trend. Hence, it is crucial to obtain the measurements as precisely as possible.

As stated in Section 5.3.1, in this study, the GY80 breakout board, which consists of an L3G4200D Gyroscope, an HMC5883L magnetometer, an ADXL345 accelerometer and a BMP085 pressure sensor, was utilised. This relatively low-cost module is commonly found in various applications and similar kinds of MEMS sensors found in this module are also incorporated in smart devices such as mobile phones and tablet PCs. As can be seen in Figure 7-1, each of the subcomponents of the GY80 provides a specific kind of information about the object it is attached to, such as orientation from the gyroscope, north direction from the magnetometer, acceleration and gravity from the accelerometer, and elevation and temperature from the pressure sensor. Commonly, the fusion product of this information is then being used to obtain the information on the 3D rotation, travelling or heading direction and 3D translation. Consequently, the sensors data can also be used with

a suitable fusion algorithm to compensate for errors or noise in the sensors reading. For instance, the atmospheric temperature affects the gyroscope's output [176] and it can be corrected through the temperature readings. More importantly, since the direction or the yaw angle is a vital parameter to determine the position of the bicycle, the magnetometer data in future studies can be employed to deliver a more accurate and reliable orientation of the cyclist.

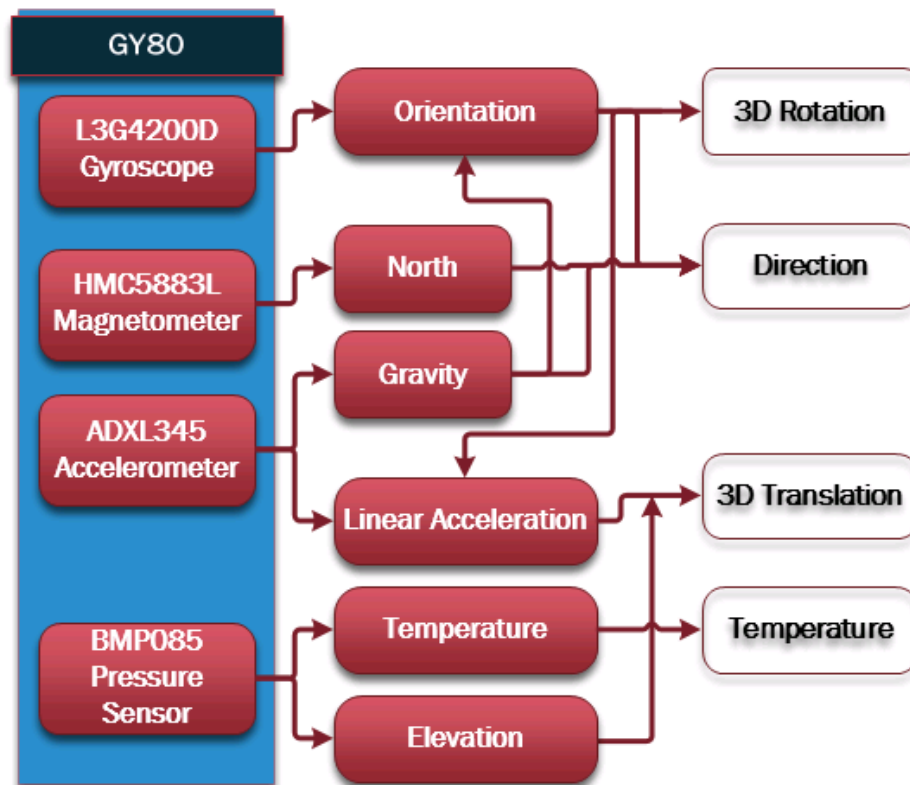


Figure 7-1: Sensor modules of GY80 with possible outputs from sensor fusion

Furthermore, more and more smart devices are also incorporated with an MPU that combines a 3-axis MEMS gyroscope, a 3-axis accelerometer and 3-axis compass on the same silicon die together with an onboard Digital Motion Processor (DMP) capable of processing complex 9-axis motion fusion algorithms [177]. The unit itself is a relatively low-cost module that can be utilised in the future version of the iBike system so as to improve the accuracy of the measurements of the kinematic parameters.

7.4.2 Collection and Processing of Wi-Fi and Cell Data

In this study, a smartphone and the Google Maps app were employed to determine the stationary positions of the bicycle based on Wi-Fi APs, cell towers and GPS.

However, even with the fusion of three separate systems, it was discovered that the position accuracy using the app does not always fall within the required accuracy, and this could be due to the methods which are utilised in the cloud to compute the positions. Thus, in future, an app could be developed to extract and collect the raw data from the infrastructures and apply improved RSS-based methods to enhance the positioning based on the Wi-Fi and cell towers signals. For instance, Yang et al. [178] presents an enhanced RSS-based model, which is established from Equation (3.18) but with more modelled parameters to increase the localisation accuracy of the receiver. Hence, similar models could be implemented with the extracted data from the Wi-Fi APs and cell towers and fused with GPS data using the developed fusion algorithms in this thesis.

7.4.3 GPS Weighting Factor with Artificial Neural network

The weighting factors which are used to combine the fused data from the output of the Kalman filters in Sections 4.4.3 and 4.4.5 are also important for a highly accurate localisation. Currently, these factors are determined from a sample set of experimental data where several sample positions for a known (surveyed) location were collected using the GPSlogger app and Google Maps app. The sample positions were compared with the surveyed location in order to determine the mean error for each system. This information was then utilised to determine the weighting factors with the Equation (4.46). However, this method can be optimised using artificial intelligence (AI) so as to integrate many other factors such as the estimation of noise from the sensors, weather conditions, approximate location using GPS, positional error and a number of visible satellites. The output weighting factor of the GPS from the AI can be then utilised for the combinations of the positioning data. The overall method could easily be implemented on the MATLAB with its user-friendly GUI for the development of the neural network and an illustration of such network is shown below.

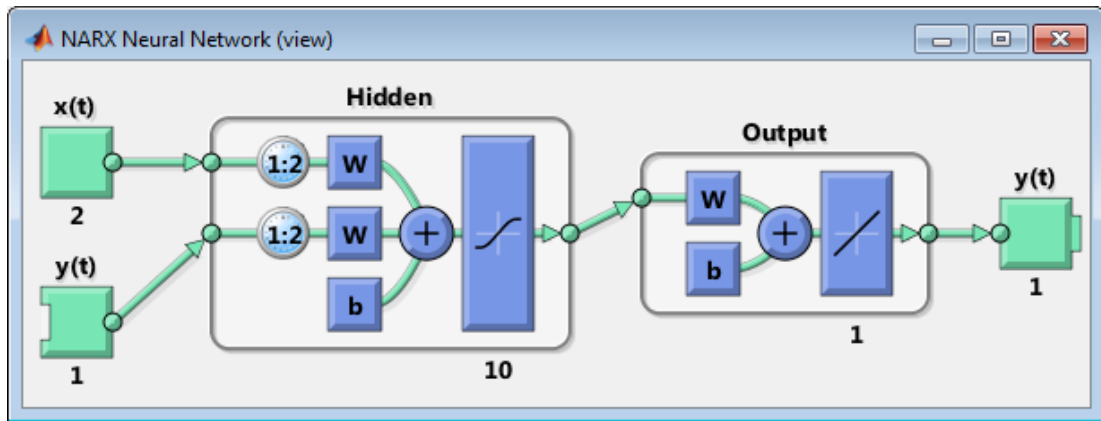


Figure 7-2: MATLAB's AI Neural Network [179]

7.4.4 Fusion of Local Sensors

Another characteristic that determines the accuracy of the position over a long distance is the fusion of the data generated by the local and global infrastructures. In this study, Wi-Fi APs, mobile phone base stations and satellites, on which localisation systems depend, were used with the addition of the two Kalman filters to enhance the positioning of the bicycle with its motion measurements. However, it was discovered that in a very few cases, if the motion measurements are not very accurate due to unexpected level of noise in the data, and if by coincidence the GPS measurements also fall within the threshold, then the fused trajectory tends to follow the GPS track, even though it is not accurate, rather the actual path (survey points), and such an occurrence is illustrated in Figure 7-3.

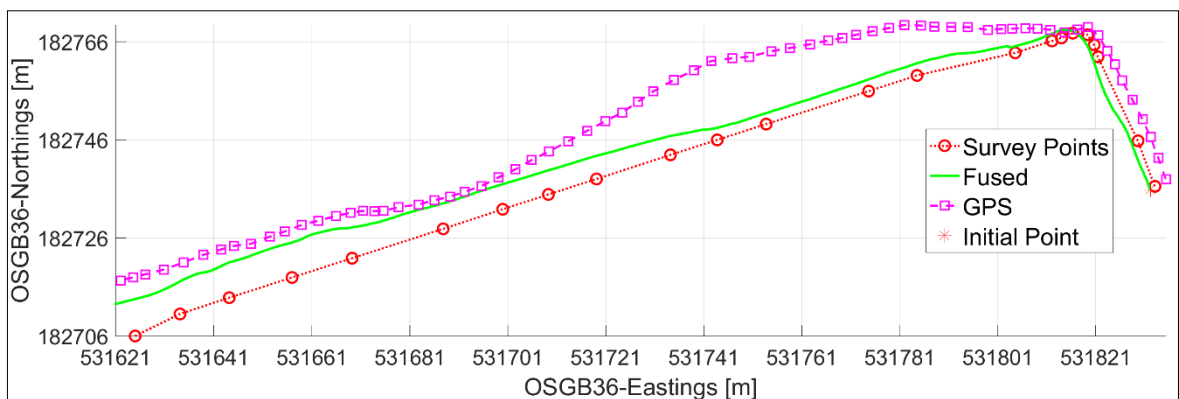


Figure 7-3: Survey points versus Fused trajectory with GPS data only

On the other hand, with respect to the developed fusion algorithms, the behaviour of the fused trajectory is as expected because it was designed to follow the path of GPS measurements whenever the data fall within the threshold. However, it is extremely difficult to precisely determine when the GPS measurements are within

the boundary or threshold of the actual path, so that generated data could be inaccurate. The precision could be improved with the integration of the AI mentioned in the previous section for the weight factors so that they could be reduced further in such conditions. Nevertheless, in order fully to resolve the issue, it is necessary to obtain the positioning data from a system which can be counted as a reliable source of information and two of the systems described below may fulfil the requirements.

Firstly, detection and movement of cyclists on the road with cameras and machine-learning techniques are areas of study that have recently gained importance in research on smart cities. For instance, Vivacity's traffic monitoring [180] and Aralia Systems [181] already have the capability of tracking and detecting objects with footage from cameras. Moreover, as per Aden's state-of-the-art review of traffic monitoring infrastructure in London [86], traffic monitoring cameras, especially the fixed cameras overlooking at the roads, can be employed to detect the position of the cyclists with high accuracy. Thus, this approach can be utilised to fuse the data acquired by the bicycle with that from the cameras where the weighting factors could be as high as one. In other words, more trust can be put on the positions based on the cameras than the GPS data.

Secondly, the recent development of smart parking sensors [182] can also be employed to detect the presence of the cyclists together with near-field communications where smart sensors can be assigned the precise location of their positions and transmit the information when the bicycle is ridden over it. Again, this information can be weighted as one and used with the fusion algorithms developed in this thesis. In other words, the smart parking sensors can be treated as the random control points used in Section 6.3, which made it possible to achieve 0.5 m or less positional error with 90% probability.

Publications Relating to this Research

➤ **The following papers have been published:**

Miah, S.; Milonidis, E.; Kaparias, I.; Karcanias, N., " A Novel Fusion Algorithm to Improve Localisation Accuracy of an Instrumented Bicycle," to be presented at the Transportation Research Board (TRB) 97th Annual Meeting, Washington, D.C., USA, January, 2018.

Miah, S.; Milonidis, E.; Kaparias, I.; Stirling, D.; Karcanias, N., " Cyclist 360° Alert: Validation of an Instrumented Bicycle Trajectory Reconstruction Mechanism Using Satellite and Inertial Navigation Systems," presented at the UTSG 49th Annual Conference, Dublin, Ireland, January, 2017.

Miah, S.; Kaparias, I.; Stirling, D.; Liatsis, P., "Development and Testing of a Prototype Instrumented Bicycle For The Prevention of Cyclist Accidents," presented at the Transportation Research Board (TRB) 95th Annual Meeting, Washington, D.C., USA, January, 2016.

Miah, S.; Kaparias, I.; Liatsis, P., " Cyclist 360° Alert: Evaluation of MEMS Sensors Accuracy Based on an Instrumented Bicycle for the Purpose of Tracking and Positioning," presented at the UTSG 48th Annual Conference, Bristol, UK, January, 2016.

Miah, S.; Kaparias, I.; Liatsis, P., "Evaluation of MEMS sensors accuracy for bicycle tracking and positioning," in Systems, Signals and Image Processing (IWSSIP), 22nd International Conference, London, UK, September, 2015

Miah, S.; Kaparias, I.; Liatsis, P., "Cyclist 360° Alert: Development and testing of a prototype instrumented bicycle model for the prevention of cyclist accidents," presented at the UTSG 47th Annual Conference, London, UK, January, 2015.

➤ **The following paper has been submitted:**

Miah, S.; Milonidis, E.; Kaparias, I.; Karcanias, N., " An Innovative Multi-Sensor Fusion Algorithm to Enhance Positioning Accuracy of an Instrumented Bicycle," submitted in IEEE Transactions on Intelligent Transportation Systems, submitted on 11-September-2017.

➤ **Part of this research has been contributed to the following EU funded projects:**

Road Pavements & Bridge deck Health monitoring/early warning using advanced inspection Technologies (RPBHealTec), Grant Agreement 606645 (2014-2016), [Online]. Available: <https://blogs.city.ac.uk/fp7-rpbhealtec/>. [Accessed 28 September 2017].

Composites Evaluation in aircraft industry through Triplex IR imaging system (CompETe), Grant Agreement 606636 (2014-2017), Online]. Available: <http://projectcompete.eu>. [Accessed 28 September 2017].

➤ **The following papers are to be submitted:**

Miah, S.; Milonidis, E.; Kaparias, I.; Karcianas, N., "Development of a Sensor Architecture for Accurate Positioning of an Instrumented Bicycle System", Journal of the International Measurement Confederation.

Miah, S.; Milonidis, E.; Kaparias, I.; Karcianas, N., " Validation of Trajectory Reconstruction of an Instrumented Bicycle", Journal of Intelligent Transportation Systems

References

- [1] Transport for London, "Travel in London Report 9," 2016. [Online]. Available: <http://content.tfl.gov.uk/travel-in-london-report-9.pdf>. [Accessed 1 May 2017].
- [2] D. V. Herlihy, *Bicycle: The History*, illustrated ed., New Haven: Yale University Press, 2006.
- [3] J. Woodcock, M. Tainio, J. Cheshire, O. O'Brien and A. Goodman, "Health effects of the London bicycle sharing system: health impact modelling study," *British Medical Journal*, vol. 348, no. 1, pp. 1-14, 12 February 2014.
- [4] J. Pucher and R. Buehler, "Health Benefits of Cycling," in *City Cycling*, London, MIT Press, 2012, pp. 31-55.
- [5] K. Teschke, C. C. Reynolds, F. J. Ries, B. Gouge and M. Winters, "Bicycling: Health Risk or Benefit?," *University of British Columbia Medical Journal*, vol. 3, no. 2, pp. 6-11, 2012.
- [6] F. Kuster, C. Laurence and R. Geffen, "Halving injury and fatality rates for cyclists by 2020," ECF , Brussels, 2010.
- [7] WHO, UN Habitat, "Global report on urban health: equitable, healthier cities for sustainable development," World Health Organization, Kobe, Japan, 2016.
- [8] State of Green, "PERSPECTIVE: SMART CITIES," [Online]. Available: <https://stateofgreen.com/en/infocus/perspective/smart-cities>. [Accessed 16 June 2017].
- [9] Department for Transport, "Reported road casualties in Great Britain: main results 2015," National Statistics, 30 June 2016. [Online]. Available: https://www.gov.uk/government/uploads/system/uploads/attachment_data/file/533293/rrcgb-main-results-2015.pdf. [Accessed 03 May 2017].
- [10] A. Nikitas, P. Wallgren and O. Rexfelt, "The paradox of public acceptance of bike sharing in Gothenburg," *Proceedings of the Institution of Civil Engineers - Engineering Sustainability*, vol. 169, no. 3, pp. 101 - 113, 2016.

-
- [11] D. Horton, P. Rosen and P. Cox, "Fear of Cycling," in *Cycling and Society*, Hampshire, Ashgate, 2012, pp. 133-151.
- [12] A. Thornton, L. Evans, K. Bunt, A. Simon, S. King and T. Webster, "Climate Change and Transport Choices," TNS BMRB, London, 2011.
- [13] A. Clarke, *Smart Cycling: Promoting Safety, Fun, Fitness, and the Environment*, Champaign: Human Kinetics, 2010.
- [14] M. R. Gray and M. Jiang, "Rational Recreations," *Once On A Tyme*, 29 December 2011. [Online]. Available: <https://onceonatyme.wordpress.com/2011/12/29/rational-recreations/>. [Accessed 1 May 2017].
- [15] National Museum of American History, "The Development of the Bicycle," [Online]. Available: http://amhistory.si.edu/onthemove/themes/story_69_2.html. [Accessed 01 May 2017].
- [16] Vélo Capital Partners, "Realizing Cycling's Potential through Innovation," 2012. [Online]. Available: <http://www.velocapitalpartners.com/index.php/page/permalink/title/key-developments>. [Accessed 22 June 2017].
- [17] European Commission, "European standard - EN15194," 2009. [Online]. Available: https://ec.europa.eu/energy/intelligent/projects/sites/iee-projects/files/projects/documents/presto_fact_sheet_legislation_en.pdf. [Accessed 16 June 2017].
- [18] Super pedestrian, "Copenhagen Wheel," [Online]. Available: <https://www.superpedestrian.com/>. [Accessed 16 June 2017].
- [19] N. Savage, "Cycling Through Data," *Communications of the ACM*, vol. 53, no. 9, pp. 16 -17, September 2010.
- [20] Design To Improve Life, "Copenhagen wheel finally on the streets," October 2013. [Online]. Available: <http://designtoimprovelife.dk/copenhagen-wheel-will-finally-be-available-to-everyone/>. [Accessed 16 September 2017].
- [21] Visit Copenhagen, "Copenhagen City Bike," [Online]. Available: <http://www.visitcopenhagen.com/copenhagen/copenhagen-city-bike-gdk495345>. [Accessed 27 February 2017].
- [22] G. French, J. Steer and N. Richardson, "Handbook for cycle-friendly design," Sustrans, Bristol, 2014.
-

-
- [23] A. Wong and N. Hounsell, "Using the iBus System to Provide Improved Public Transport Information and Applications for London," in *12th World Conference on Transport Research (WCTRS)*, Lisbon, Portugal, 2010.
- [24] The Royal Society for the Prevention of Accidents, "Cycling Accidents," RoSPA, Birmingham, 2012.
- [25] Department for Transport, "Reported Road Casualties in Great Britain: notes, definitions, symbols and conventions," [Online]. Available: https://www.gov.uk/government/uploads/system/uploads/attachment_data/file/462818/reported-road-casualties-gb-notes-definitions.pdf. [Accessed 08 March 2018].
- [26] European Commission, "Traffic Safety Basic Facts 2017 – Cyclists," European Commission, Directorate General for Transport, Brussels, 2017.
- [27] National Center for Statistics and Analysis, "Bicyclists and Other Cyclists: 2015 data," National Highway Traffic Safety Administration, Washington, DC, 2016.
- [28] H. Ward, S. Robertson, T. Lester and A. Peddler, "Reporting of Road Traffic Accidents in London: Matching Police STATS19 Data with Hospital Accident and Emergency Department Data," TRL, London, 2002.
- [29] A. S. Morgan, H. B. Dale, W. E. Lee and P. J. Edwards, "Deaths of cyclists in london: trends from 1992 to 2006," 2010.
- [30] Department for Transport, "Road accidents and safety tables index," [Online]. Available: <https://www.gov.uk/government/statistical-data-sets/road-accidents-and-safety-statistical-tables-index>. [Accessed 21 July 2017].
- [31] J. Knowles, S. Adams, R. Cuerden, T. Savill, S. Reid and M. Tight, "Collisions Involving Cyclists on Britain's Roads: Establishing the Causes," IHS, Berkshire, 2009.
- [32] BBC, "West Dulwich lorry-collision cyclist killed," 4 September 2013. [Online]. Available: <http://www.bbc.co.uk/news/uk-england-london-23959657>. [Accessed 16 October 2013].
- [33] Transport for London, "Road safety Fact Sheets," 2005-2014. [Online]. Available: <https://tfl.gov.uk/corporate/publications-and-reports/road-safety>. [Accessed 30 January 2017].
-

-
- [34] Ride On magazine, "Turning blind," 23 September 2013. [Online]. Available: <https://rideons.wordpress.com/2013/09/23/turning-blind/>. [Accessed 13 July 2017].
- [35] S. Cowland, "Factsheet - Pedal cyclist collisions and casualties in Greater London," September 2011. [Online]. Available: <http://content.tfl.gov.uk/pedal-cyclist-collisions-and-casualties-in-greater-london-sep-2011.pdf>. [Accessed 05 May 2017].
- [36] "Cyclist Safety Action Plan," Transport for London, London, 2014.
- [37] L. Watson and M. Cameron, "Bicycle and motor vehicle crash characteristics," Monash University Accident Research Centre, Victoria, 2006.
- [38] G. Sparkes, S. Cowland, J. Stordy and L. Matson, "Pedal cyclist collisions and casualties in Greater London," TfL, London, 2011.
- [39] C. Shooter and J. Reeve, "INTERSAFE-2 architecture and specification," *Intelligent Computer Communication and Processing*, pp. 379 - 386, 27-29 August 2009.
- [40] SWOV Institute for Road Safety Research, "Fact sheet: Blind spot crashes," SWOV, The Hague, the Netherlands, 2012.
- [41] A. Kambanis, "3 new initiatives that make cycling in London safe – will they work?," London Cyclist, 09 July 2010. [Online]. Available: <http://www.londoncyclist.co.uk/3-new-initiatives-that-make-cycling-in-london-safe-will-they-work/>.
- [42] C. Schoon, "Problematiek rechts afslaande vrachtauto's (Problems with right-handed lorries)," SWOV, Leidschendam, 2006.
- [43] UK Government Digital Service, "The Highway Code," [Online]. Available: <https://www.gov.uk/guidance/the-highway-code/rules-for-cyclists-59-to-82>. [Accessed 04 May 2017].
- [44] R. Aldred, "Cycling near misses: Their frequency, impact, and prevention," *Transportation Research Part A*, vol. 90, no. 1, p. 69–83, 2016.
- [45] WATCH-OVER, "Deliverables," 2008. [Online]. Available: <http://www.watchover-eu.org/deliverables.html>. [Accessed 24 November 2014].
-

-
- [46] CVIS, “CVIS Deliverables,” 2009. [Online]. Available: http://www.cvisproject.org/en/public_documents/. [Accessed 24 November 2014].
- [47] COOPERS, “Public Deliverables within COOPERS,” [Online]. Available: <http://www.coopers-ip.eu/index.php?id=150>. [Accessed 24 November 2014].
- [48] Volvo, “Volvo Car Group introduces world-first Cyclist Detection with full auto brake,” 27 March 2013. [Online]. Available: <https://www.media.volvocars.com/global/en-gb/media/pressreleases/48277>. [Accessed 01 May 2017].
- [49] L. Gomes, “Hidden Obstacles for Google’s Self-Driving Cars,” MIT Technology Review, 28 August 2014. [Online]. Available: <https://www.technologyreview.com/s/530276/hidden-obstacles-for-googles-self-driving-cars/>. [Accessed 17 February 2018].
- [50] F. Favarò, S. Eurich and N. Nader, “Autonomous vehicles' disengagements: Trends, triggers, and regulatory limitations,” *Accident Analysis and Prevention*, vol. 110, pp. 136 - 148, 2018.
- [51] N. Kalra and S. M. Paddock, “Driving to safety: How many miles of driving would it take to demonstrate autonomous vehicle reliability?,” *Transportation Research Part A*, vol. 94, no. 1, pp. 182-193, 2016.
- [52] N. Zhou, “Volvo admits its self-driving cars are confused by kangaroos,” *The Guardian*, 1 July 2017. [Online]. Available: <https://www.theguardian.com/technology/2017/jul/01/volvo-admits-its-self-driving-cars-are-confused-by-kangaroos>. [Accessed 17 February 2018].
- [53] U. Lee, J. Jung, S. Jung and D. H. Shim, “DEVELOPMENT OF A SELF-DRIVING CAR THAT CAN HANDLE THE ADVERSE WEATHER,” *International Journal of Automotive Technology*, vol. 19, no. 1, pp. 191-197, 2018.
- [54] S. Levin, “Video released of Uber self-driving crash that killed woman in Arizona,” *The Guardian*, 22 March 2018. [Online]. Available: <https://www.theguardian.com/technology/2018/mar/22/video-released-of-uber-self-driving-crash-that-killed-woman-in-arizona>. [Accessed March 30 2018].
-

-
- [55] Backwatch, “Blindspot Detection System,” [Online]. Available: <http://www.backwatch.co.uk/products/blindspot-detection-system/>. [Accessed 2 May 2017].
- [56] Brigade-Electronics, “Ultrasonic Sensor System,” [Online]. Available: <http://brigade-electronics.com/product/ultrasonic-obstacle-detection/overview-uod/>. [Accessed 2 May 2017].
- [57] Fusion Processing, “CycleEye® – cyclist detection and driver alert system for trucks and buses,” [Online]. Available: <http://www.fusionproc.com/products/>. [Accessed 2 May 2017].
- [58] ETA, “Blaze Burner bicycle light aimed at urban riders,” 20 November 2015. [Online]. Available: <https://www.eta.co.uk/2015/11/20/blaze-burner-bicycle-light-aimed-at-urban-riders/>. [Accessed 15 September 2017].
- [59] D. Hoedemaeker, M. Doumen and M. e. a. de Goede, “Model design for blind spot detection and observation systems,” 2010.
- [60] A. Silla, P. Rämä, L. Leden, M. v. Noort, J. Kruijff, D. Bell, A. Morris, G. Hancox and J. Scholliers, “Quantifying the effectiveness of ITS in improving safety of VRUs,” *IET Intelligent Transport Systems*, vol. 11, no. 3, pp. 164-172, 2017.
- [61] A. Silla, L. Leden, P. Rämä, J. Scholliers, M. v. Noort and D. Bell, “Can cyclist safety be improved with intelligent transport systems?,” *Accident Analysis and Prevention*, vol. 105, no. 1, pp. 134-145, 2017.
- [62] Ofcom, “Communications Market Report 2016,” 4 August 2016. [Online]. Available: https://www.ofcom.org.uk/__data/assets/pdf_file/0024/26826/cmr_uk_2016.pdf. [Accessed 11 May 2017].
- [63] T. S. Rappaport, *Wireless Communications: principles and practice*, Prentice Hall, 2001.
- [64] Z. Farid, R. Nordin and M. Ismail, “Recent Advances in Wireless Indoor Localization Techniques and System,” *Computer Networks and Communications*, vol. 2013, p. 12, 2013.
- [65] U.S. Coast Guard Navigation Center, “GPS FREQUENTLY ASKED QUESTIONS,” 09 August 2016. [Online]. Available: <https://www.navcen.uscg.gov/?pageName=gpsFaq>. [Accessed 01 May 2017].
-

-
- [66] G. Blewitt, *Basics of the GPS Technique: Observation Equations*, Newcastle upon Tyne: Swedish Land Survey, 1997.
- [67] N. Rahemi, M. R. Mosavi, A. A. Abedi and S. Mirzakuchaki, "Accurate Solution of Navigation Equations in GPS Receivers for Very High Velocities Using Pseudorange Measurements," [Online]. Available: <https://www.hindawi.com/archive/2014/435891/>. [Accessed 01 May 2017].
- [68] ETSI, "EN 300 328 V1.8.1," June 2012. [Online]. Available: http://www.etsi.org/deliver/etsi_en/300300_300399/300328/01.08.01_60/en_300328v010801p.pdf. [Accessed 05 07 2017].
- [69] M. A. Youssef, . A. Agrawala and A. U. Shankar, "WLAN Location Determination via Clustering and Probability Distributions," *Proceedings of the First IEEE International Conference on Pervasive Computing and Communications*, p. 143–150, 2003.
- [70] Y. Chen and H. Kobayashi, "Signal Strength Based Indoor Geolocation," *IEEE International Conference on Communications*, vol. 1, pp. 436-439, 2002.
- [71] P. Bahl and V. N. Padmanabhan, "RADAR: An In-Building RF-based User Location and Tracking System," *Proceedings of 19th Annual Joint Conference of the IEEE Computer and Communications Societies*, vol. 2, pp. 775-784, 2000.
- [72] O. Katircioglu, H. Isel, O. Ceylan, F. Taraktas and H. B. Yagci, "Comparing Ray Tracing, Free Space Path Loss and Logarithmic Distance Path Loss Models in Success of Indoor Localization with RSSI," in *19th Telecommunications forum TELFOR*, Serbia, Belgrade, 2011.
- [73] K. R. Patel and R. Kulkarni, "Indoor Radio Propagation Model Analysis Wireless Node Distance and Free Space Path Loss Measurements and Using Ultra-wideband (UWB) Technology," *International Journal of Engineering Research and Applications*, vol. 5, no. 6, pp. 20-32, 2015.
- [74] G. Kloos, "Radio-frequency Signal Strength Based Localisation in Unstructured Outdoor Environments," University of Sydney, Sydney, 2007.
- [75] Microsoft, "How 802.11 Wireless Works," 28 March 2003. [Online]. Available: [https://technet.microsoft.com/en-us/library/cc757419\(v=ws.10\).aspx](https://technet.microsoft.com/en-us/library/cc757419(v=ws.10).aspx). [Accessed 02 May 2017].
-

-
- [76] Without the Cat, “Learn about what is on a cell tower,” [Online]. Available: <http://www.withoutthecat.com>. [Accessed 15 June 2017].
- [77] GSM, “Mobile Technology,” [Online]. Available: <https://www.gsma.com/aboutus/gsm-technology/gsm>. [Accessed 15 June 2017].
- [78] M. Miller, “How Mobile Networks Work,” *informIT*, 14 March 2013. [Online]. Available: <http://www.informit.com/articles/article.aspx?p=2021961&seqNum=2>. [Accessed 15 June 2017].
- [79] EndRun Technologies, “CDMA Timing,” [Online]. Available: <http://www.endruntechnologies.com/cdma>. [Accessed 15 June 2017].
- [80] Google Play Store, “Netmonitor,” 29 April 2017. [Online]. Available: <https://play.google.com/store/apps/details?id=com.parizene.netmonitor&hl=en>. [Accessed 15 June 2017].
- [81] Unwired Labs, “The world's largest Open Database of Cell Towers,” [Online]. Available: <https://opencellid.org/>. [Accessed 15 June 2017].
- [82] C. S. Smith, “Cell Phone Triangulation Accuracy Is All Over The Map,” *Search Engine Land*, 22 September 2008. [Online]. Available: <http://searchengineland.com/cell-phone-triangulation-accuracy-is-all-over-the-map-14790>. [Accessed 15 June 2017].
- [83] M. Shimosaka, O. Saisho, T. Sunakawa, . H. Koyasu, K. Maeda and R. Kawajir, “ZigBee based wireless indoor localization with sensor placement optimization towards practical home sensing,” *ADVANCED ROBOTICS*, vol. 30, no. 5, pp. 315-325, 2016.
- [84] Y. Zhuang, J. Yang, Y. Li, L. Qi and N. El-Sheimy, “Smartphone-Based Indoor Localization with Bluetooth Low Energy Beacons,” *Sensors*, vol. 16, no. 5, 2016.
- [85] K. Qiu, F. Zhang and M. Liu, “Visible Light Communication-based Indoor Localization using Gaussian Process,” in *IEEE/RSJ International Conference on Intelligent Robots and Systems (IROS)*, Hamburg, Germany, 2015.
- [86] S. J. Aden, *State-of-the-art review of traffic monitoring infrastructure in London and potential future outlook*, London: City University London, 2013.
- [87] I. Oppermann, J. Linatti and . M. Hämäläinen, *UWB: Theory and Applications*, Chichester: Wiley, 2004.
-

-
- [88] H. N. a. R. Prasad, Introduction to Ultra wideband for wireless communications, London: Springer, 2009.
- [89] ZEBRA, "Dart UWB Technology," 2016. [Online]. Available: <https://www.zebra.com/content/dam/zebra/product-information/en-us/brochures-datasheets/location-solutions/dartuwb-tech-datasheet-en-us.pdf>. [Accessed 18 June 2017].
- [90] Ubisense, "Ubisense Series 7000 IP Sensors," 2013. [Online]. Available: <http://www.ubisense.net/en/>. [Accessed 21 February 2013].
- [91] The Office of Communications, "Electronic Communications, The Wireless Telegraphy (Ultra-Wideband Equipment) (Exemption) Regulation 2009 No. 2517," 16 September 2009. [Online]. Available: http://www.legislation.gov.uk/uksi/2009/2517/pdfs/ukxi_20092517_en.pdf. [Accessed 21 February 2013].
- [92] Y. Zhou, "A closed-form algorithm for the least-squares trilateration problem," *Cambridge University Press*, vol. 29, no. 3, pp. 375-389, 2010.
- [93] S. Pradhan and S.-s. Hwang, "Mathematical Analysis of Line Intersection Algorithm for TOA Trilateration Method," in *15th International Symposium on SCIS & ISIS*, Kitakyushu, Japan, 2014.
- [94] S. M. Cain, *An Experimental Investigation of Human/Bicycle Dynamics and Rider Skill in Children and Adults*, Ann Arbor, Michigan, United States: University of Michigan, 2013.
- [95] D. E. H. Jones, "The stability of the bicycle," September 2006. [Online]. Available: http://www.phys.lsu.edu/faculty/gonzalez/Teaching/Phys7221/vol59no9p51_56.pdf. [Accessed 15 June 2017].
- [96] V. Cossalter, *Motorcycle Dynamics*, 2nd English Edition ed., Morrisville: Lulu, 2006.
- [97] J. Langlely, "What's What On A Bicycle," [Online]. Available: <http://www.jimlanglely.net/wrench/bicycleparts.html>. [Accessed 15 June 2017].
- [98] J. Fajans, "Steering in bicycles and motorcycles," *American Journal of Physics*, vol. 68, no. 7, pp. 654-659, 2000.
- [99] J. Papadopoulos, "PHYSICS ON TWO WHEELS," *Nature*, vol. 353, pp. 338-341, 2016.
-

-
- [100] K. J. Åström, R. E. Klein and A. Lennartsson, "Bicycle dynamics and control: adapted bicycles for education and research," *IEEE Control Systems*, vol. 25, no. 4, pp. 26 - 47, 2005.
- [101] The Fajans Group Website, "How you steer a bicycle," [Online]. Available: <http://socrates.berkeley.edu/~fajans/Teaching/Steering.htm>. [Accessed 15 June 2017].
- [102] M. Doumiati, O. Sename, L. Dugard, J. J. M. Molina, P. Gaspar and Z. Szabo, "Integrated vehicle dynamics control via coordination of active front steering and rear braking," *European Journal of Control*, vol. 19, no. 2, pp. 121-143, 2013.
- [103] M. Canale, L. Fagiano, M. Milanese and P. Borodani, "Robust vehicle yaw control using an active differential and IMC techniques," *Control Engineering Practice*, vol. 15, no. 8, pp. 923-941, 2007.
- [104] C. Voser, R. Y. Hindiyeh and J. C. Gerdes, "Analysis and control of high sideslip manoeuvres," *Analysis and control of high sideslip manoeuvres*, vol. 48, no. 1, pp. 317-336, 2010.
- [105] J. M. Snider, "Automatic Steering Methods for Autonomous Automobile Path Tracking," Carnegie Mellon University, Pittsburgh, Pennsylvania, 2009.
- [106] S. F. Campbell, "Steering control of an autonomous ground vehicle with application to the DARPA urban," 2007.
- [107] T. D. Gillespie, *Fundamentals of Vehicle Dynamics*, Society of Automotive Engineers, 1992.
- [108] A. De Luca and G. Oriolo, "FEEDBACK CONTROL OF A NONHOLONOMIC CAR-LIKE ROBOT," Rome, 2004.
- [109] L. Keo and Y. Masaki, "Trajectory Control for an Autonomous Bicycle with Balancer," *Advanced Intelligent Mechatronics*, pp. 676-681, 2008.
- [110] J. Yi, D. Song, A. Levandowski and S. Jayasuriya, "Trajectory tracking and balance stabilization control of autonomous motorcycles," *Robotics and Automation*, pp. 2583-2589, 2006.
- [111] G. Franke, W. Suhr and F. Riel3, "An advanced model of bicycle dynamics," *European Journal of Physics*, vol. 11, pp. 116-121, 1990.
-

-
- [112] G. Antonelli, S. Chiaverini and G. Fusco, "A Fuzzy-Logic-Based Approach for Mobile Robot Path Tracking," *IEEE Transactions on Fuzzy Systems*, vol. 15, no. 2, pp. 211-221, 2007.
- [113] E. Vans, G. Vachkov and A. Sharma, "Vision based autonomous path tracking of a mobile robot using fuzzy logic," in *Asia-Pacific World Congress on Computer Science and Engineering*, Nadi, Fiji, 2014.
- [114] J. Morales, J. L. Martínez, M. A. Martínez and A. Mandow, "Pure-Pursuit Reactive Path Tracking for Nonholonomic Mobile Robots with a 2D Laser Scanner," *EURASIP Journal on Advances in Signal Processing*, vol. 2008, no. 1, pp. 1-10, 2009.
- [115] C. Wit, C. D. Crane and D. Armstrong, "Autonomous ground vehicle path tracking," *Journal of Robotic Systems*, vol. 21, no. 8, pp. 439-449, 2004.
- [116] D. Hyun, H. S. Yang, H.-S. Park and H.-J. Kim, "Dead-reckoning sensor system and tracking algorithm for 3-D pipeline mapping," *Mechatronics*, vol. 20, no. 2, p. 213-223, 2010.
- [117] H. Andersen, Z. J. Chong, Y. H. Eng, S. Pendleton and M. H. Ang, "Geometric path tracking algorithm for autonomous driving in pedestrian environment," in *IEEE International Conference on Advanced Intelligent Mechatronics*, Banff, Alberta, Canada, 2016.
- [118] u-blox, "3D Automotive Dead Reckoning chip: a new dimension in navigation," 2017. [Online]. Available: <https://www.u-blox.com/en/u-blox-3d-automotive-dead-reckoning-technology>. [Accessed 15 June 2017].
- [119] V. Heine, *Group Theory in Quantum Mechanics: An Introduction to its Present Usage*, New York: Pergamon Press, 1960.
- [120] F. Ramsey, "Understanding the Basis of the Kalman Filter Via a Simple and Intuitive Derivation [Lecture Notes]," *IEEE Signal Processing Magazine*, vol. 29, no. 5, pp. 128-132, 2012.
- [121] G. Welch, "An Introduction to the Kalman Filter," [Online]. Available: http://www.cs.unc.edu/~tracker/media/pdf/SIGGRAPH2001_CoursePack_08.pdf.
- [122] K. Ogata, *Discrete-time Control Systems*, New Jersey: Prentice Hall, 1995.

-
- [123] Ordnance Survey, “The National Grid,” 2017. [Online]. Available: <https://www.ordnancesurvey.co.uk/resources/maps-and-geographic-resources/the-national-grid.html>. [Accessed 15 June 2017].
- [124] J. Verheijen, “World Geodetic System 1984 (WGS84),” Atlassian Confluence, 12 July 2016. [Online]. Available: <https://confluence.qps.nl/pages/viewpage.action?pageId=29855173>. [Accessed 15 June 2017].
- [125] J. Závoti and J. Kalmár, “A comparison of different solutions of the Bursa–Wolf model and of the 3D, 7-parameter datum transformation,” *Acta Geodaetica et Geophysica*, vol. 51, no. 2, pp. 245-256, 2016.
- [126] G. Chang, “On least-squares solution to 3D similarity transformation problem under Gauss–Helmert model,” *Journal of Geodesy*, vol. 89, no. 6, pp. 573-576, 2015.
- [127] Ordnance Survey, “A guide to coordinate systems in Great Britain,” Britain’s mapping agency, Southampton, 2016.
- [128] Ordnance Survey, “Coordinate transformation,” 2017. [Online]. Available: <https://www.ordnancesurvey.co.uk/business-and-government/help-and-support/navigation-technology/os-net/grid-inquest.html>. [Accessed 15 June 2017].
- [129] Cherry, “GEARTOOTH SPEED SENSOR,” [Online]. Available: <http://docs-europe.electrocomponents.com/webdocs/110a/0900766b8110a251.pdf>. [Accessed 18 June 2014].
- [130] RS Components, “NPN Hall Effect Sensor,” [Online]. Available: <http://uk.rs-online.com/web/p/hall-effect-sensors/7659328/>. [Accessed 18 June 2014].
- [131] US Digital, “A2K Absolute Optical Encoder: Kit Version,” [Online]. Available: <https://www.usdigital.com/products/encoders/absolute/rotary/kit/A2K>. [Accessed 19 June 2014].
- [132] US Digital, “SEI Absolute Encoder Communications Protocol,” [Online]. Available: <http://www.usdigital.com/support/user-guides/sei-absolute-encoder-communications-protocol>. [Accessed 19 June 2014].
- [133] US Digital, “A2K Datasheet,” [Online]. Available: http://www.usdigital.com/assets/datasheets/A2K_datasheet.pdf?k=635387676121584284. [Accessed 19 June 2014].
-

-
- [134] STMicroelectronics, "MEMS L3G4200D Gyroscope," STMicroelectronics, 2010.
- [135] M. Efstathios, "The development of the Mathematical Model of an RPV and an Investigation on the Use of an EKF for the Identification of its Aerodynamics Derivatives," Cranfield Institute of Technology , Cranfield, 1987.
- [136] L. Wang and F. Wang, "Intelligent Calibration Method of low cost MEMS Inertial Measurement Unit for an FPGA-based Navigation System," *International Journal of Intelligent Engineering & Systems*, vol. 4, no. 2, pp. 32-41, 2011.
- [137] STMicroelectronics, "MEMS Gyroscope L3G4200D Datasheet," [Online]. Available: <http://www.st.com/web/en/resource/technical/document/datasheet/CD00265057.pdf>. [Accessed 25 July 2015].
- [138] T. Kanesalingam, "Motion Tracking Glove for Human-Machine Interaction: Inertial Guidance," McMaster University, Ontario, 2010.
- [139] ANALOG DEVICES, "ADXL345 Digital Accelerometer Datasheet," [Online]. Available: http://www.analog.com/static/imported-files/data_sheets/ADXL345.pdf. [Accessed 21 June 2014].
- [140] C. J. Fisher, "AN-1057 Application Note - Using an Accelerometer for Inclination Sensing," ANALOG DEVICES, Norwood, 2010.
- [141] R. Mahony, T. Hamel and J.-M. Pflimlin, "Complementary filter design on the special orthogonal group," in *44th IEEE Conference on Decision and Control, and the European Control Conference*, Seville, Spain, 2005.
- [142] B. Batista, C. Silvestre, P. Oliveira and B. Cardeira, "Low-cost Attitude and Heading Reference System: Filter Design and Experimental Evaluation," in *IEEE International Conference on Robotics and Automation Anchorage Convention District*, Anchorage, Alaska, USA, 2010.
- [143] Arduino, "Arduino Mega 2560," [Online]. Available: <http://arduino.cc/en/Main/ArduinoBoardMega2560>. [Accessed 23 June 2014].
- [144] Arduino Forum, "Arduino Mega2560 R3 pinouts photo," 2012. [Online]. Available: <https://forum.arduino.cc/index.php?topic=125908.0>. [Accessed 5 July 2017].
-

-
- [145] Arduino, "Arduino Mini," [Online]. Available: <http://arduino.cc/en/Main/ArduinoBoardMini>. [Accessed 23 June 2014].
- [146] OrCAD, "OrCAD Capture," 2017. [Online]. Available: <http://www.orcad.com/products/orcad-capture/overview>. [Accessed 1 July 2017].
- [147] OrCAD, "OrCAD PCB Designer," 2017. [Online]. Available: <http://www.orcad.com/products/orcad-pcb-designer/overview>. [Accessed 1 July 2017].
- [148] Autodesk, "Inventor 3D CAD software," [Online]. Available: <https://www.autodesk.co.uk/products/inventor/overview>. [Accessed 5 July 2017].
- [149] Arduino, "Arduino IDE," 2017. [Online]. Available: <https://www.arduino.cc/en/main/software>. [Accessed 5 July 2017].
- [150] Arduino, "Libraries," [Online]. Available: <https://www.arduino.cc/en/Reference/Libraries>. [Accessed 15 July 2017].
- [151] Arduino, "Language Reference," [Online]. Available: <https://www.arduino.cc/en/Reference/HomePage>. [Accessed 15 July 2017].
- [152] Google, "Geolocation API," [Online]. Available: <https://developers.google.com/maps/documentation/geolocation/intro>. [Accessed 1 July 2017].
- [153] GSMArena, "Samsung Galaxy S6 edge," [Online]. Available: http://www.gsmarena.com/samsung_galaxy_s6_edge-7079.php. [Accessed 15 July 2017].
- [154] Google Play Store, "Maps - Navigation & Transit," [Online]. Available: <https://play.google.com/store/apps/details?id=com.google.android.apps.maps&hl=en>. [Accessed 16 July 2017].
- [155] Google Play Store, "GPS Logger for Android," [Online]. Available: <https://play.google.com/store/apps/details?id=com.mendhak.gpslogger&hl=en>. [Accessed 15 July 2017].
- [156] Advanced Navigation, "Spatial," 2015. [Online]. Available: <http://www.advancednavigation.com.au/product/spatial>. [Accessed 25 November 2016].
- [157] Advanced Navigation, "Spatial Reference Manual," 30 January 2017. [Online]. Available: http://www.advancednavigation.com.au/sites/advancednavigation.com.au/files/spatial_reference_manual.pdf. [Accessed 30 July 2017].
-

-
- [158] Microsoft, "Surface Pro 4," [Online]. Available: <https://www.microsoft.com/en-gb/store/d/surface-pro-4/8vv4n8vbqg7c/0R3Q>. [Accessed 15 July 2017].
- [159] CNET, "GoPro Hero Specifications," [Online]. Available: <https://www.cnet.com/uk/products/gopro-hero/specs/>.
- [160] J. C. Calvey, M. D. Taylor, J. P. Shackleton and R. Llewellyn, "IntelliBike: a cycle path surface quality assessment tool," in *UTSG*, Newcastle, 2014.
- [161] Transport for London, "Record-breaking year for Santander Cycles," 13 February 2017. [Online]. Available: <https://tfl.gov.uk/info-for/media/press-releases/2017/february/record-breaking-year-for-santander-cycles>. [Accessed 15 July 2017].
- [162] Federal Highway Administration, "Interstate 80 Freeway Dataset," December 2006. [Online]. Available: <https://www.fhwa.dot.gov/publications/research/operations/06137/06137.pdf>. [Accessed 15 July 2017].
- [163] MySQL, "MySQL Workbench," [Online]. Available: <https://dev.mysql.com/doc/workbench/en/>. [Accessed 2 July 2017].
- [164] MathWorks, "MATLAB GUI," [Online]. Available: <https://uk.mathworks.com/discovery/matlab-gui.html>. [Accessed 2 June 2017].
- [165] A. Schneider, "GPS Visualizer," [Online]. Available: <http://www.gpsvisualizer.com/>. [Accessed 2 June 2017].
- [166] Google, "GPX Editor," [Online]. Available: <http://www.gpxeditor.co.uk/>. [Accessed 2 June 2017].
- [167] MATLAB, "MAT-File Format," MathWorks, Natick, 2017.
- [168] MathWorks, "Database Toolbox," 2017. [Online]. Available: <https://uk.mathworks.com/products/database.html>. [Accessed 2 June 2017].
- [169] N. B. Priyantha, "The Cricket Indoor Location System," Massachusetts Institute of Technology, Cambridge, 2005.
- [170] N. B. Priyantha, "The Cricket Indoor Location System," Massachusetts Institute of Technology, Cambridge, 2005.
- [171] B. F. Kavanagh and S. J. Glenn Bird, *Surveying principles and applications*, 5th, Ed., New Jersey: Prentice Hall, 2000.
-

-
- [172] Leica Geosystems, “Leica TPS1100 Professional Series,” Heerbrugg.
- [173] D. Stirling, *Survey Computations*, London: City, University of London, 2016.
- [174] MathWorks, “Documentation: knnsearch,” [Online]. Available: <https://uk.mathworks.com/help/stats/knnsearch.html>. [Accessed 15 July 2017].
- [175] Ordnance Survey, “Triangulation stations,” 2017. [Online]. Available: <https://www.ordnancesurvey.co.uk/gps/legacy-control-information/triangulation-stations>. [Accessed 2 July 2017].
- [176] D. Xia, S. Chen, S. Wang and . H. Li, “Microgyroscope Temperature Effects and Compensation-Control Methods,” *Sensors*, vol. 9, no. 10, pp. 8349-8376, 2009.
- [177] TDK InvenSense, “9 Axis Motion Tracking,” 06 02 2017. [Online]. Available: <file:///C:/Users/shah/Downloads/DS-000189-ICM-20948-v1.3.pdf>. [Accessed 21 July 2017].
- [178] J. Yang and Y. Chen, “Indoor localization using improved RSS-based lateration methods,” in *GLOBECOM'09 Proceedings of the 28th IEEE conference on Global telecommunications*, Honolulu, Hawaii, 2009.
- [179] MATLAB, “Neural Network Toolbox,” [Online]. Available: <https://uk.mathworks.com/products/neural-network.html>. [Accessed 24 July 2017].
- [180] VIVACITY LABS, “Smart Cities,” 2017. [Online]. Available: <http://www.vivacitylabs.com/>. [Accessed 6 July 2017].
- [181] Aralia, “Applications,” 2013. [Online]. Available: <http://aralia.co.uk/pages/applications.htm>. [Accessed 16 July 2017].
- [182] IOTSENS, “Smart Parking Sensor (road surface),” [Online]. Available: http://www.iotsens.com/sensors_en/smart-parking-sensor-road-surface/. [Accessed 6 July 2017].

Appendix A: Additional Materials on the Development of the iBike System

A.1 Brief Operating Principle of iBike Components

The following section studies the operating principle of the required measurement sensors and the Arduino microcontroller board.

A.1.1 Hall Effect Sensor

A Hall Effect sensor is a type of proximate sensor that generates a voltage in response to the proximity of a magnetic field. Hence, it's a transducer that converts a magnetic field to an electrical signal. The word Hall Effect is named after Edwin Hall who discovered it back in the 1870's. The physical principle underlying the Hall Effect is the Lorentz force. To generate a potential difference across the device the magnetic flux lines must be perpendicular to the flow of current and be of the correct polarity, generally a south pole. An illustration diagram is shown in Figure A-1 where the blue arrows represent a magnetic field passing perpendicularly through the conductive plate.

The Hall Effect sensors are widely used in industries for many applications such as proximity switching, speed detection, positioning and current sensing applications. In the simplest form, a Hall Effect sensor operates as an analogue transducer, where it outputs a voltage that is proportional to the strength of the magnetic fields that are detected; hence it is a device which is activated by an external magnetic field and it is an active device. An additional circuitry can be combined with the sensor to allow the device to operate in a digital mode and thus, it can then act as a digital on and off switch. These digital Hall Effect sensors have many uses in consumer equipment. For instance, printers use them to detect missing paper and open covers.

The Hall Effect sensors are highly reliable and durable devices, and therefore they are commonly used to time the speed of wheels and shafts such as for tachometers, internal combustion engine ignition timing and anti-lock braking systems. For this

project, a Hall Effect sensor is used to detect the rotation of the bicycle's rear wheel and to count the spokes in order to calculate the revolution per second.

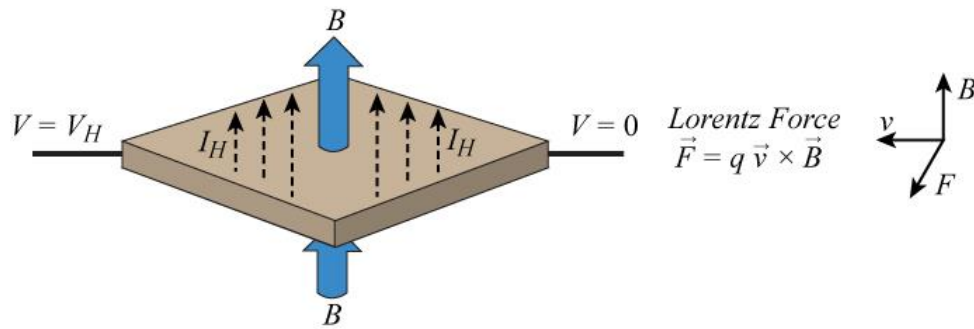


Figure A-1: The Hall Effect and Lorentz force [A1]

Magnetic fields have two important characteristics; flux density (B) and polarity (North and South Poles). As mentioned earlier, the output signal from a Hall Effect sensor is a function of the magnetic field density around it, and when the magnetic flux density around the sensor exceeds a certain pre-set threshold, the sensor detects it and generates an output voltage called the Hall Voltage V_H. Figure A-2 below, shows the operating principle of a Hall Effect sensor, which consists of a thin piece of rectangular p-type semiconductor material such as gallium arsenide (GaAs), and when the device is placed within a magnetic field, the magnetic flux lines exert a force on the semiconductor material, which deflects the charge carriers, electrons and holes to either side of the semiconductor slab. In response to this force, the electrons move in a curved path along the conductor, and a net charge and therefore a voltage develops across the plate.

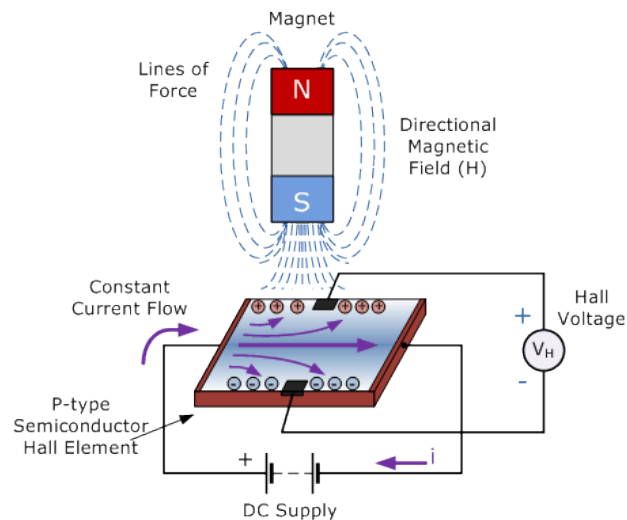


Figure A-2: Hall Effect sensor operation principle diagram [A2]

The Hall voltage, V_H , obeys equation (A.1), which shows that V_H is proportional to the applied field strength, and that the polarity of V_H is determined by the direction, either north or south, of the applied magnetic field, and as a result the Hall Effect is employed as a magnetic sensor.

$$V_H = \frac{IB}{qt\rho} \quad (A.1)$$

where I is the current across the plate length, B is the magnetic field, t is the thickness of the plate, q is the magnitude of the charge of the carriers and ρ is the number of charge carriers per unit volume

A comparator can be used to provide an additional circuit, where a pre-set threshold can be fixed so that the device will only output a digital signal when the input goes above or below a threshold voltage. On the other hand, the detected output voltage from the semiconductor is extremely small, only a few microvolts, and typical Hall Effect sensors would need to have other integrated circuitries to make the device operate smoothly. A typical Hall Effect sensor consists of Hall sensor, DC amplifiers, logic switching circuits, voltage regulators to improve the sensing sensitivity, hysteresis and output voltage. The diagram below represents a typical hall Effect switch that can be used to detect the presence of a magnetic field near the device and it can be used in conjunction with a microprocessor to determine the speed of a moving rotational object.

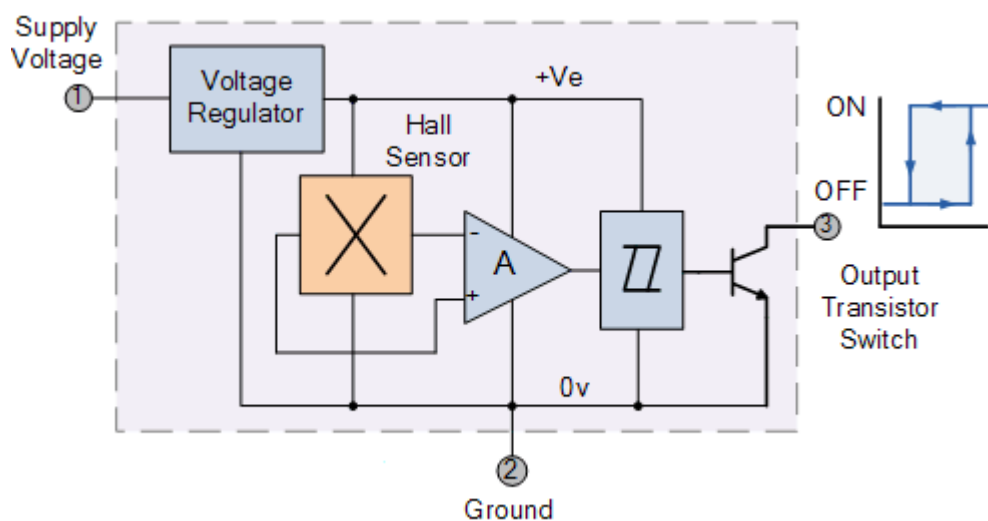


Figure A-3: Typical Hall Effect sensor diagram [A2]

A.1.2 Optical Encoder

An encoder is an electrical mechanical device that converts linear or rotary displacement into a sequence of digital pulses. There are two types of mechanical configurations for optical encoders: rotary and linear encoders, but only the rotary encoders will be discussed here as the linear encoders are outside the scope of this project. The rotary encoders are widely used for many industrial applications which require precise shaft position with unlimited rotation such as robotics, radar and conveyors.

The most popular type of encoder is the optical rotary encoder. It is an electro-mechanical device that converts a rotational motion into an electrical signal. In other words, it is a device that converts the angular position or motion of a shaft to an analogue or digital signal. However, there are two different types of optical rotary encoders: incremental and absolute. The difference between these two types is explained below.

An incremental optical rotary encoder consists of a transparent rotary disk, a light source and a photo-sensor(s). The disk contains a coded pattern of opaque and transparent sectors that are equally spaced to determine the movement of the disk. When the disk rotates, the patterns interrupt the light that is produced by the light source onto the photo-sensor(s). This causes the encoder to generate a train of equally spaced pulses as it rotates; it generates a pulse for each incremental step in its rotation. As a result, the output of the incremental encoder provides information regarding the motion, which is then further processed elsewhere, usually with a microcontroller. The signal is then converted into speed, distance and position. An illustrative diagram of an optical rotary encoder is shown in Figure A-4(a). The incremental encoder can provide a high degree of resolution, but it cannot provide information regarding an absolute position. Furthermore, the output of the single-channel encoder cannot indicate the direction of the rotation. However, this can be overcome by using a two-channel or quadrature encoder which uses two detectors and two code tracks with sectors positioned 90° out of phase. An example output of a two-channel encoder together with code tracks is shown in Figure A-4(b). Most of the optical incremental encoders also include a third channel called an index, which produces a single pulse per revolution of the encoder shaft, and it is often employed as a reference marker for the starting position.

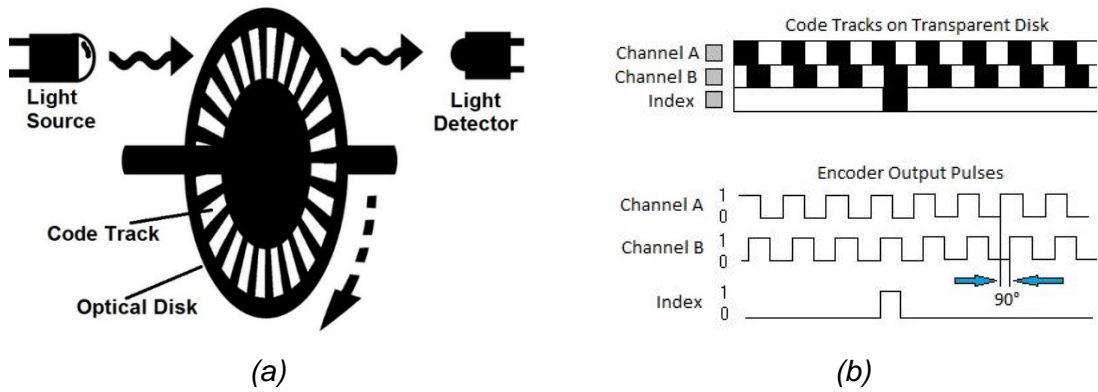


Figure A-4: (a) Optical Rotary Encoder [A3]; (b) Two-Channel Encoder [A4]

A second type of encoder is the absolute optical rotary encoder operating similarly to the incremental one described above, and it also contains similar components. However, there is one exceptional difference between them. An absolute encoder employs a transparent disk with uniquely marked patterns for each position on the optical disk, and thus each position is identified with a unique code from the output of the encoder. The main advantage of absolute encoders is that they maintain position information even when the power is removed from the system and the position information is immediately available again after restoring power. In contrast, the incremental encoders do not maintain position information after the power is removed from the system and position information cannot be retrieved immediately on applying power. The absolute encoder uses one other additional component called the stationary mask or reticle, which is placed in between the photo-detector and the optical disk; an illustration diagram is shown in Figure A-5. The output signal generated from the absolute encoder is in digital bits and they are configured to the light which is received by the photodetector while the disk rotates. Thus, each position has its own unique bit configuration.

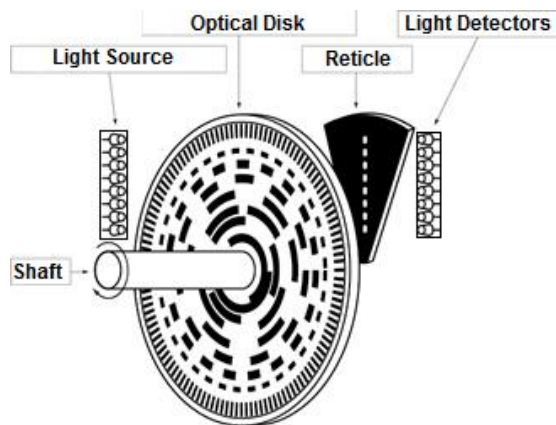


Figure A-5: Absolute Optical Encoder Simplified Structure [A5]

A.1.3 Gyroscope

A gyroscope is usually considered to be a device employed for measuring orientation based on the principle of conservation of angular momentum. A mechanical gyroscope typically consists of a freely spinning disk called a rotor on an axle, which is mounted on a series of gimbals. Each gimbal offers the spinning disk an additional degree of rotational freedom. Thus, as long as the gyroscope is spinning, it will maintain a constant orientation. When external torques or rotations about a given axis are present in these devices, orientation can be maintained, and measurement of angular velocity can be measured due to the phenomenon of precession. Figure A-6 below shows a typical rotary gyroscope with various features. Newton's third law of motion states "a body in motion stays in motion unless it's acted upon by external force". Thus, the same principle can be applied to other moving structures as well and not just spinning bodies. For example, a flying insect uses flapping wing-like structure called halteres, and they vibrate up and down rapidly and function as a gyroscope; informing the insect about the rotation of the body during flights.

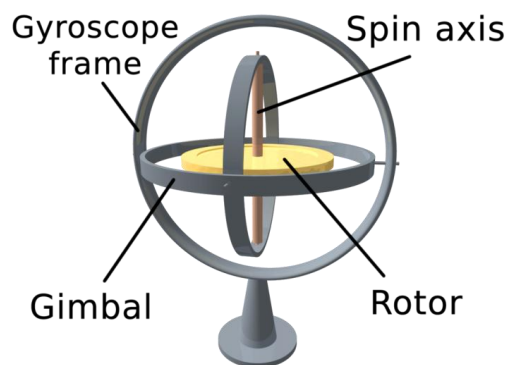


Figure A-6: A typical mechanical Gyroscope [A6]

However, an emerging nano technology related to Micro-Electro-Mechanical Systems (MEMS)-based gyroscopes operates on the same principle. In other words, the MEMS gyroscopes use a similar vibration structure to make an electronic device function as the gyroscope. However, there are also other kinds of gyroscopes available such as Fibre optic gyroscope and they will not be discussed here as they are beyond the scope of this project.

As stated earlier, a vibrating structure gyroscope, standardised by IEEE as Coriolis vibratory gyroscope (CVG), uses solid-state resonators of different shapes that functions much like the halteres of an insect. The MEMS gyroscopes use the same

basic principle; they have a set of microscopic wings that vibrate back and forth with the piezoelectric current. When the gyro springs, the wings want to keep vibrating up and down in the same direction. This causes them to put pressure on the piezoelectric components and generates an electrical signal that can be read by the computer.

A.1.4 Accelerometer

An Accelerometer is a device that can measure the force of acceleration, which is either caused by gravity or by movement. Thus, an accelerometer is an instrument that can measure the acceleration of a moving or vibrating object that it is attached to. A simple accelerometer is a device that measures gravitational pull, which is the acceleration experienced by people and objects whether near earth's surface or in freefall. The essential principle of an accelerometer in the simplest form is shown in Figure A-7. The diagram illustrates that when the device is perpendicular to a horizontal surface on earth, the gravity stretches the spring downward and it is indicated by the mark labelled 1g, which simply means one unit of gravitational acceleration. On the other hand, the device will show 0g if it is laid flat on the surface. In other words, the spring will not experience any gravitational pull and it will not extend. As a result, the device makes it possible to measure acceleration due to gravity. Three of these basic accelerometers set orthogonally to each other could be used to determine the orientation of an object in three-dimensional space. An electronic accelerometer uses the same principle as the simple accelerometer device, but their internal structures are more complex.

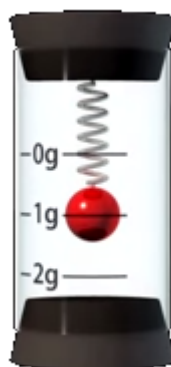


Figure A-7: A simple Accelerometer Device

In a small electronic accelerometer piezoelectric, piezoresistive and capacitive components are commonly used to convert the mechanical motion into an electrical signal. Micro-Electro-Mechanical Systems (MEMS) based accelerometers can

measure the vibration, or the acceleration of motion of a structure. The basic theory behind these accelerometers is similar to the gyroscopes described in the previous section. The force caused by a change in motion or vibration causes the microscopic crystal silicon structures inside the mass to stress and this generates a voltage that is proportional to the force and acceleration. An example of this type of accelerometers made from a slab of silicon is shown in Figure A-8. The housing, which is stationary, is the large block at the base, to which are attached several stationary polysilicon fingers. The seismic mass is the H-shaped object with the 'tongues' extending from it. The mass is secured at the ends so that it can freely move left and right between the stationary fingers. A typical accelerometer with similar structure only occupies an area of 1cm^2 , thus it is very small.

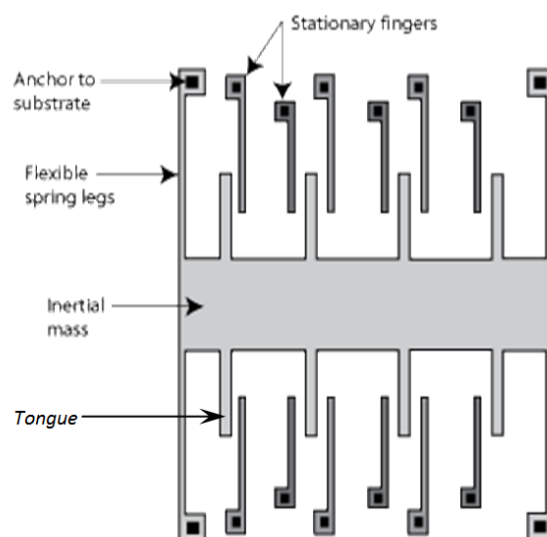


Figure A-8: A sketch of a capacitive MEMS accelerometer [A7]

A.1.5 Arduino Board

An Arduino is a single-board microcontroller that can be employed to sense and control the physical world. Moreover, Arduino is an open-source electronic prototyping platform based on flexible, easy-to-use hardware and software. In comparison with a microprocessor, which is typically found in a desktop PC, a microcontroller in an Arduino board contains all the necessary elements to execute instructions and it also provides external ports that can be used to communicate to the outside world such as SPI, I2C, and UART. In other words, a microcontroller is a standalone single-chip IC that contains all the necessary components which are

normally found in a desktop PC such as a CPU, ROM, RAM and various input and output buses to connect to the outside world.

However, a microcontroller by itself cannot execute any programs without being programmed via an external interface to a PC and some microcontrollers also require an external crystal oscillator to provide a clock for them. The Arduino boards are relevant here. The Arduino hardware consists of an open-source hardware board designed around an 8-bit Atmel AVR microcontroller, or a 32-bit Atmel ARM, and consists of other key components such as a USB port, voltage regulators, an external power jack and easy-to-use input and output female header pins. The Arduino boards provide an inexpensive, easy and fast way to prototype a system that can interact with the outside world using sensors and actuators.

The Arduino also comes with a simple Integrated Development Environment (IDE) [A8] that can run on regular computers such as desktop PCs and laptops and it is written in Java. The IDE comes with a user-friendly “one-click compile and upload” feature; it is designed to be easy to use without being an expert programmer. The IDE allows the programmer to write programs for Arduino using C or C++. However, many of the details are hidden from the user and only two functions are required to make an embedded program continually loops and these functions are called “setup” and “loop”. The IDE also comes with many open-source libraries and one of them is called “Wiring” which makes common input and output operations much easier. A program for Arduino is known as a “sketch”, which is then translated by the IDE into machine code that can then run on the Arduino Boards.

A.2 Configuration of the A2K Encoder

The installation of the optical encoder on the steering hub of the bicycle required a shaft to be inserted into the head tube so that the A2K encoder could be mounted on the steering axis. As a result, custom plates along with a shaft were designed using the CAD software and the mechanical drawings of the CAD design are illustrated in Figure A-9.

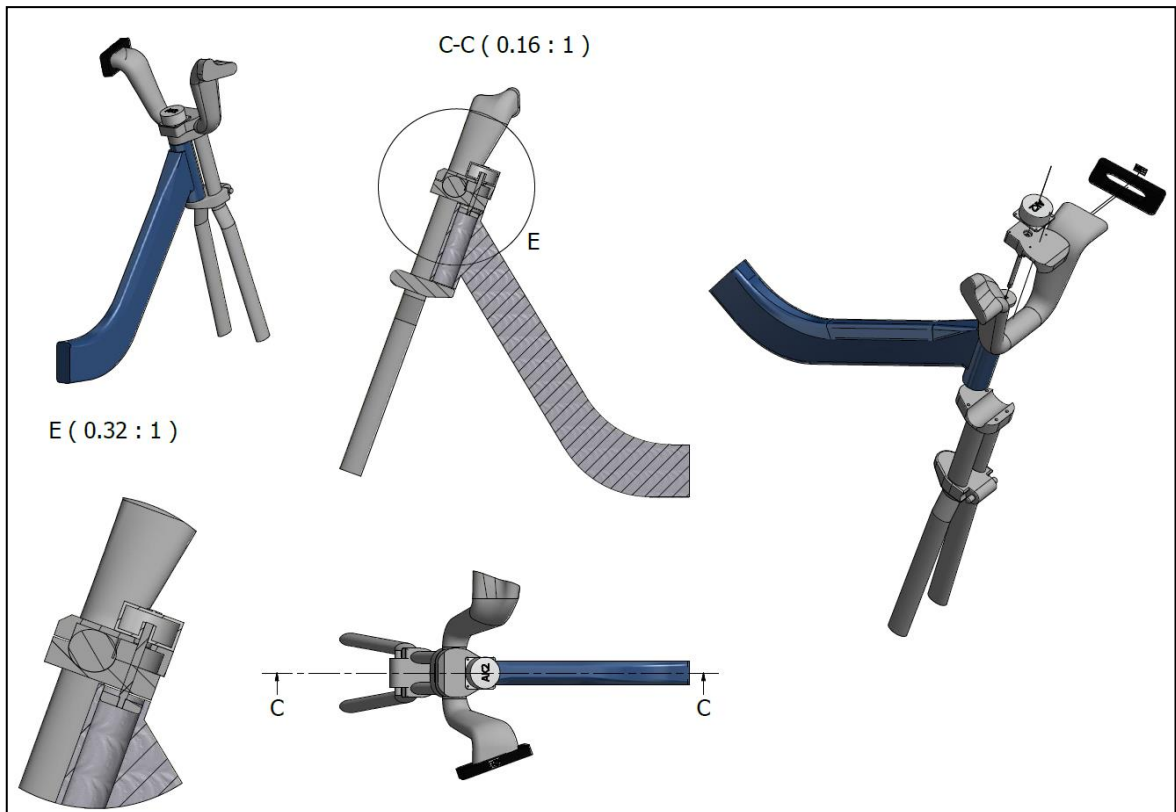


Figure A-9: Mechanical drawings of the steering hub

Figure A-10 below shows the actual plates with the shaft inserted on the steering hub, while Figure A-11 represents the actual configuration of the A2K absolute optical encoder installed on the bicycle.



Figure A-10: Plates and shaft installed on the steering hub of the bicycle

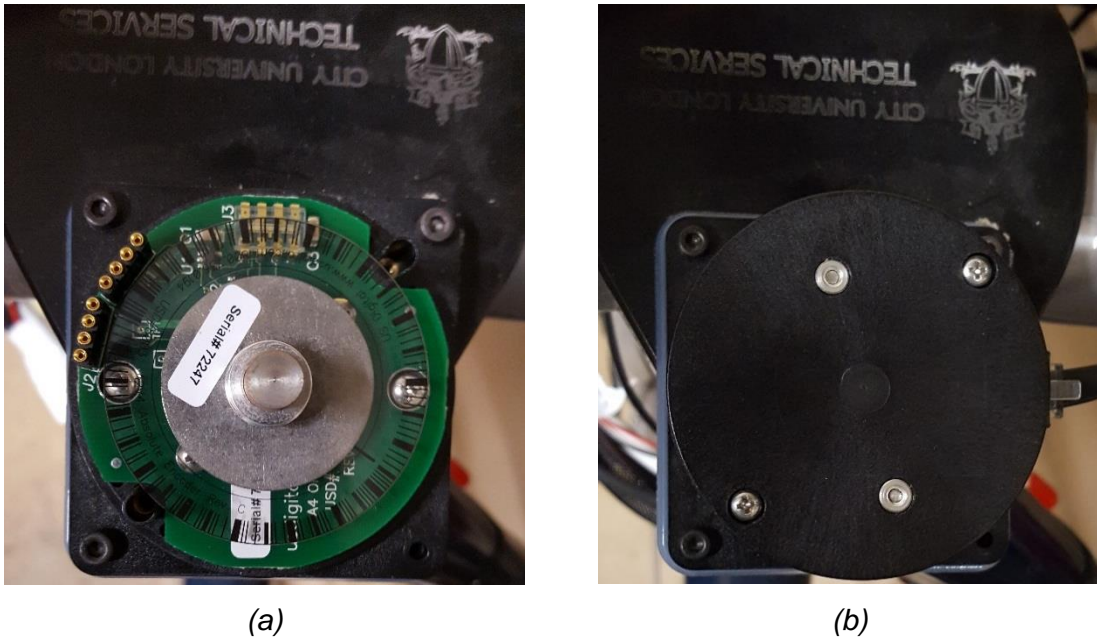


Figure A-11: (a) Installation of the base and the optical disk; (b) top cover of the sensor

A.3 Design and Implementation of the Hardware

A.3.1 Handlebar Sensors

The design and implementation of the handlebar sensors, which house the GY80 breakout board along with the status LED and the push switch, are outlined below.

- 1) Schematic Design – Figure A-12 illustrates the schematic circuit diagram of the handlebar sensors.

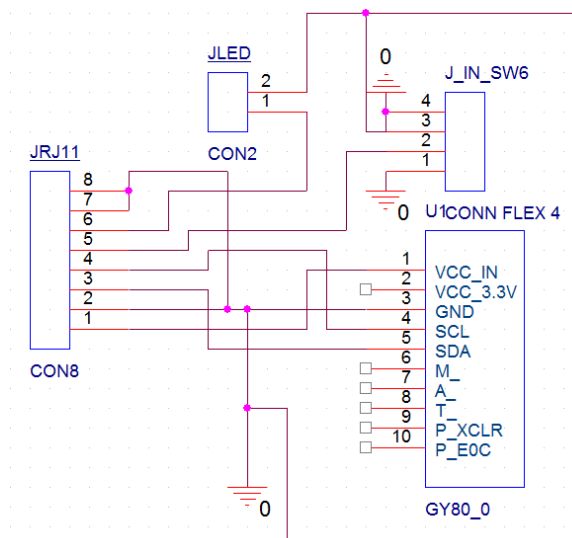


Figure A-12: Schematic circuit diagram of the handlebar sensors.

- 2) PCB Design – Figure A-13 represents the design of the top and bottom layers' wire routing of the above schematic.

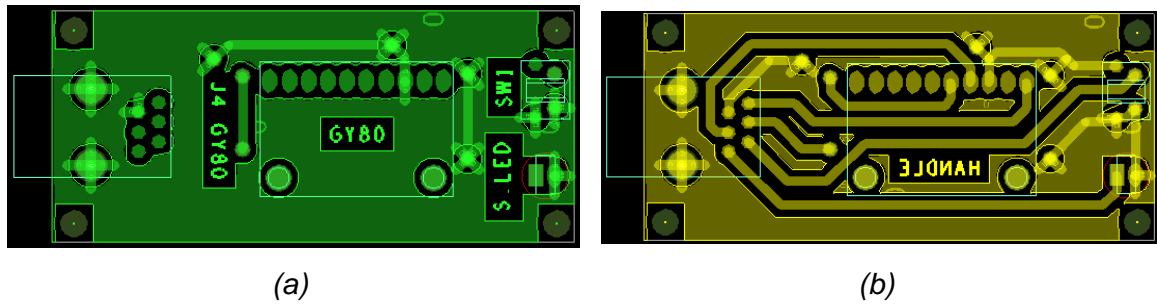


Figure A-13: (a) Design of the top layer routing and (b) the bottom layer routing of the handlebar sensors PCB.

- 3) Manufacturing and Soldering – Figure A-14 shows the actual PCB of the handlebar sensors along with the components and the box.



Figure A-14: (a) Developed PCB with the components

- 4) PCB Enclosure - to house and to install the above PCB on the bicycle, a bespoke 3D part was designed using the CAD software, and then printed with a 3D printer. The developed design and the installation of the parts on the bicycle are shown below.

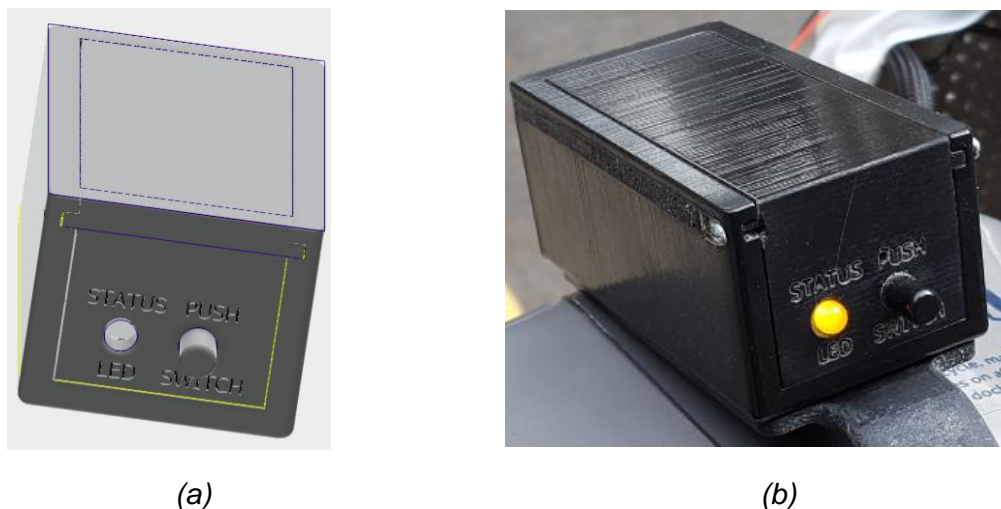


Figure A-15: (a) the CAD design of the housing; (b) the 3D printed part installed on the bicycle.

A.3.2 Main Control Box

The design and implementation of the main control box, which houses the Arduino Mega, Arduino Mini and SD card reader along with various electronic components, are outlined below.

- 4) Schematic Design – Figure 5-15 illustrates the schematic circuit diagram of the main control box.

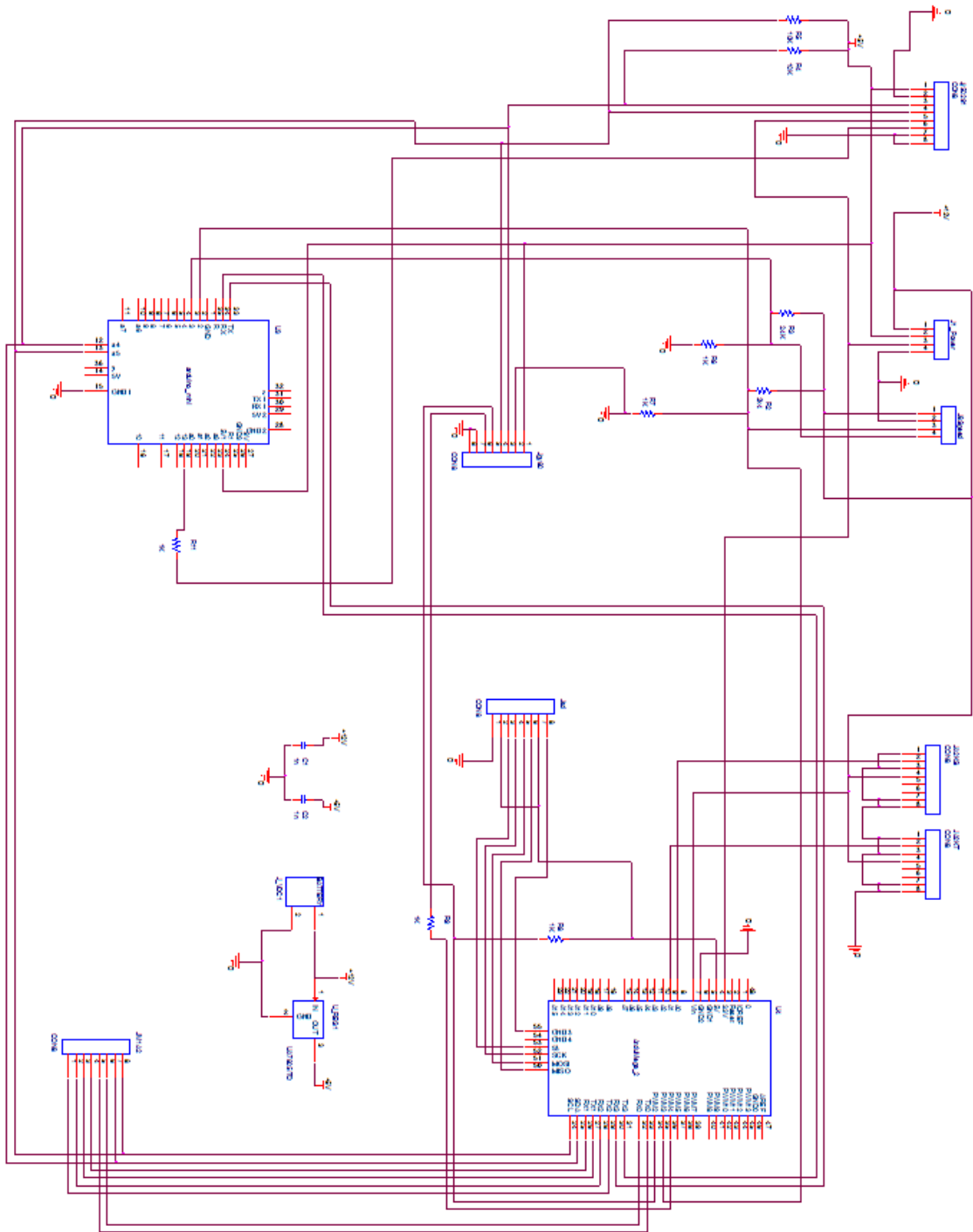


Figure A-16: Schematic circuit diagram of the main control box

- 5) PCB Design – Figure 5-16 represents the design of the top and bottom layers' wire routing of the above schematic.

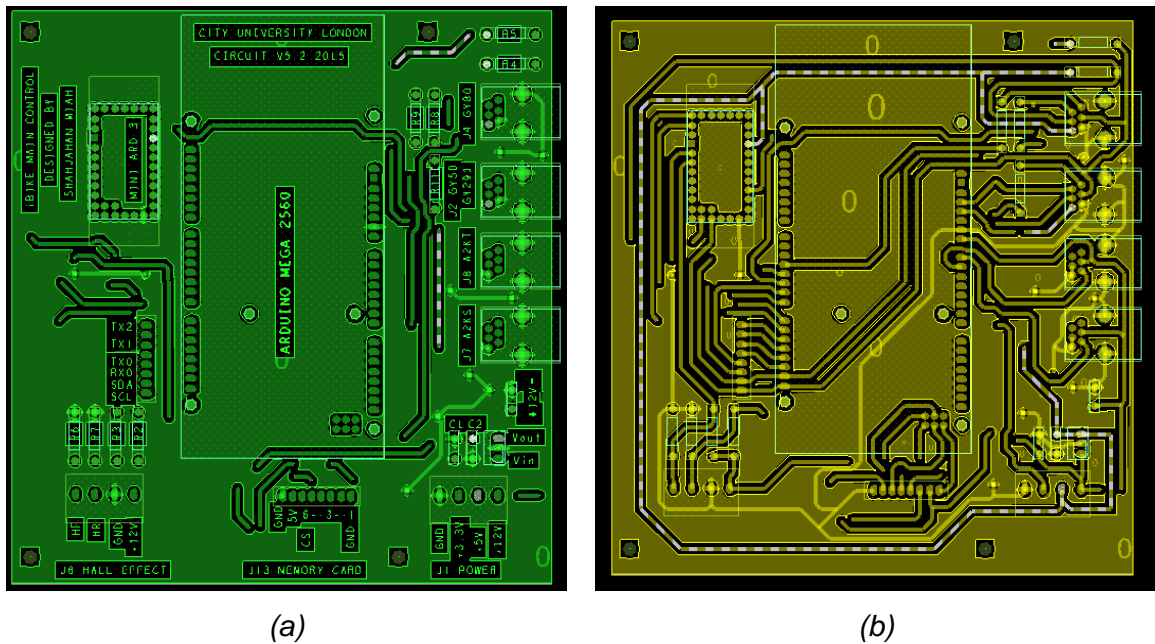


Figure A-17: (a) Design of the top layer routing and (b) the bottom layer routing of the main control box PCB.

- 6) Manufacturing and soldering – Figure 5-17 shows the actual PCB of the main control box.

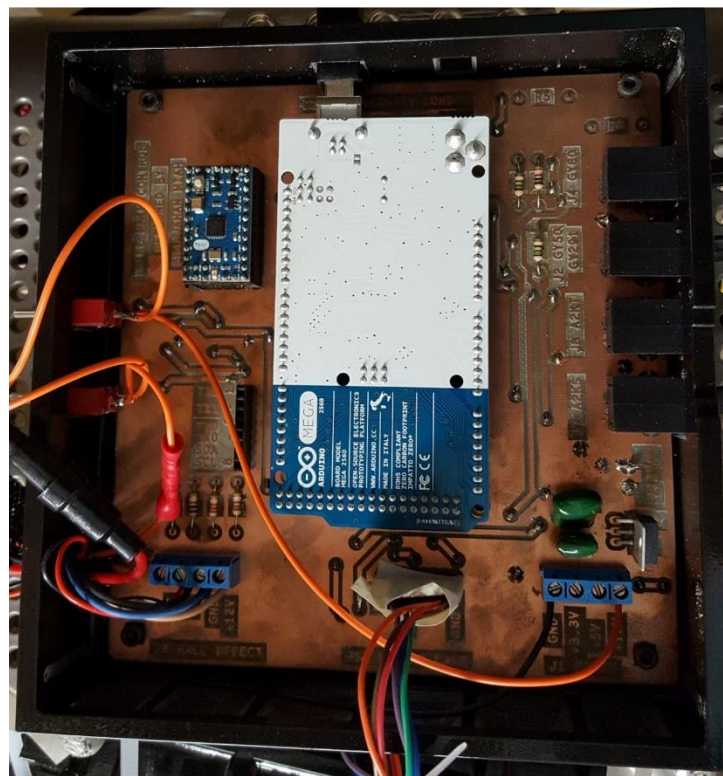


Figure A-18: (a) Developed PCB for the main control box with the components and wiring

- 7) PCB enclosure - to house and to install the above PCB with the components on the bicycle, a bespoke 3D part was designed using the CAD software, and then printed with a 3D printer. The CAD designs of the parts are shown below.

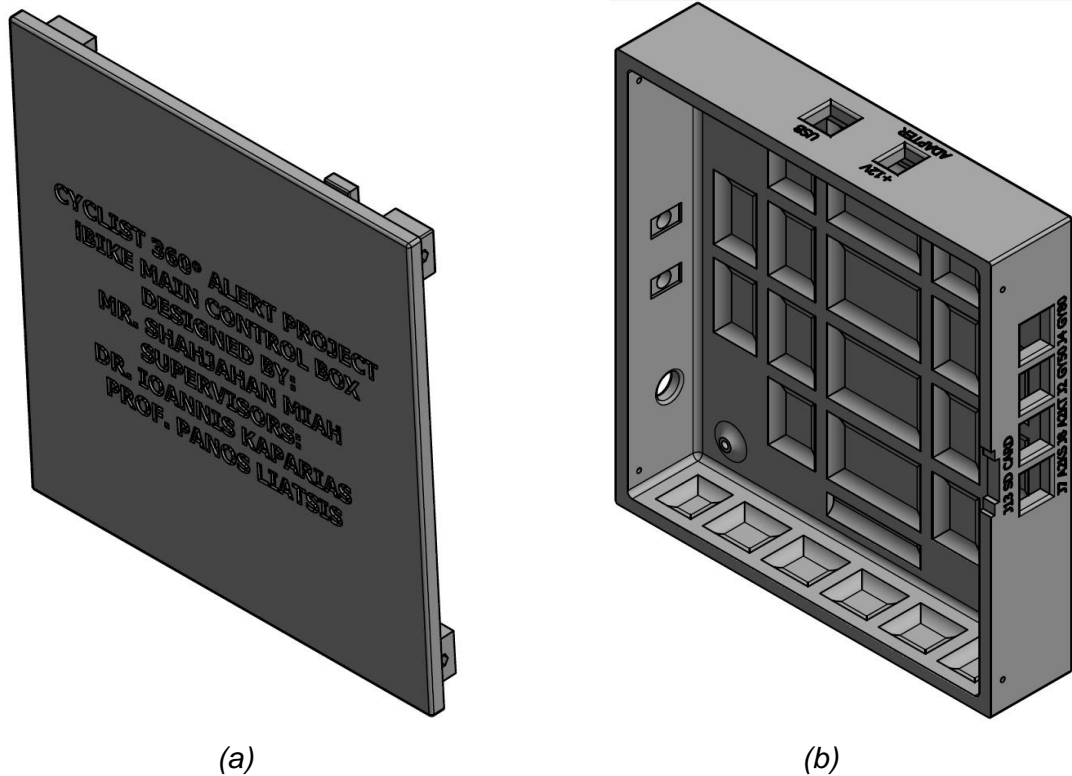


Figure A-19: (a) Top cover and (b) the base of the enclosure for the main control box.

A.3.3 Brackets

Additionally, a number of brackets were also designed using the CAD software and then manufactured so that the enclosures and sensors could be secured to the frame of the bicycle. Two examples of the brackets are shown below:

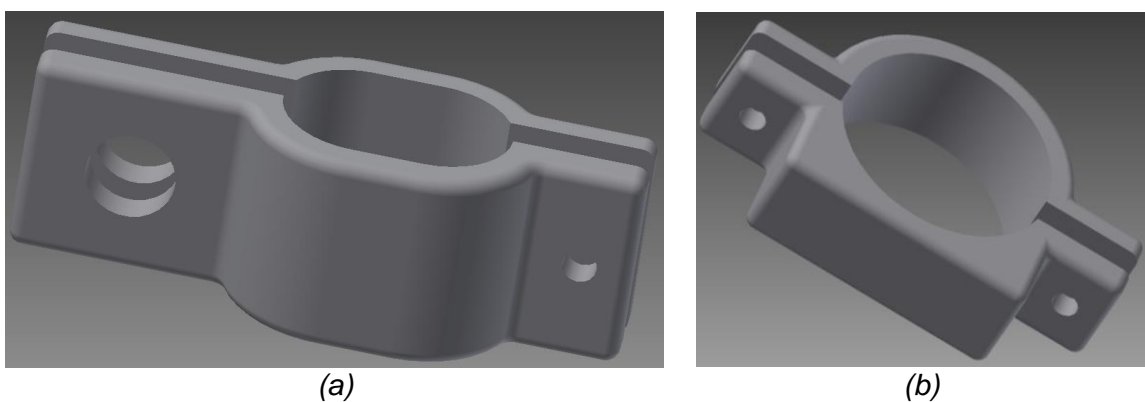


Figure A-20: (a) Hall Effect sensor bracket; (b) Seat tube enclosure brackets

A.4 Electrical Connections of the Complete iBike System

The diagram represents the electrical connections of the entire system installed on the bicycle. As can be seen, the smartphone and the camera are operated as standalone systems, and the other sensors' modules are connected to the main control box either via *RJ11* straight cables or via screw terminals. Moreover, the data from the control box and the INS system are then transferred to the tablet PC via USB cables.

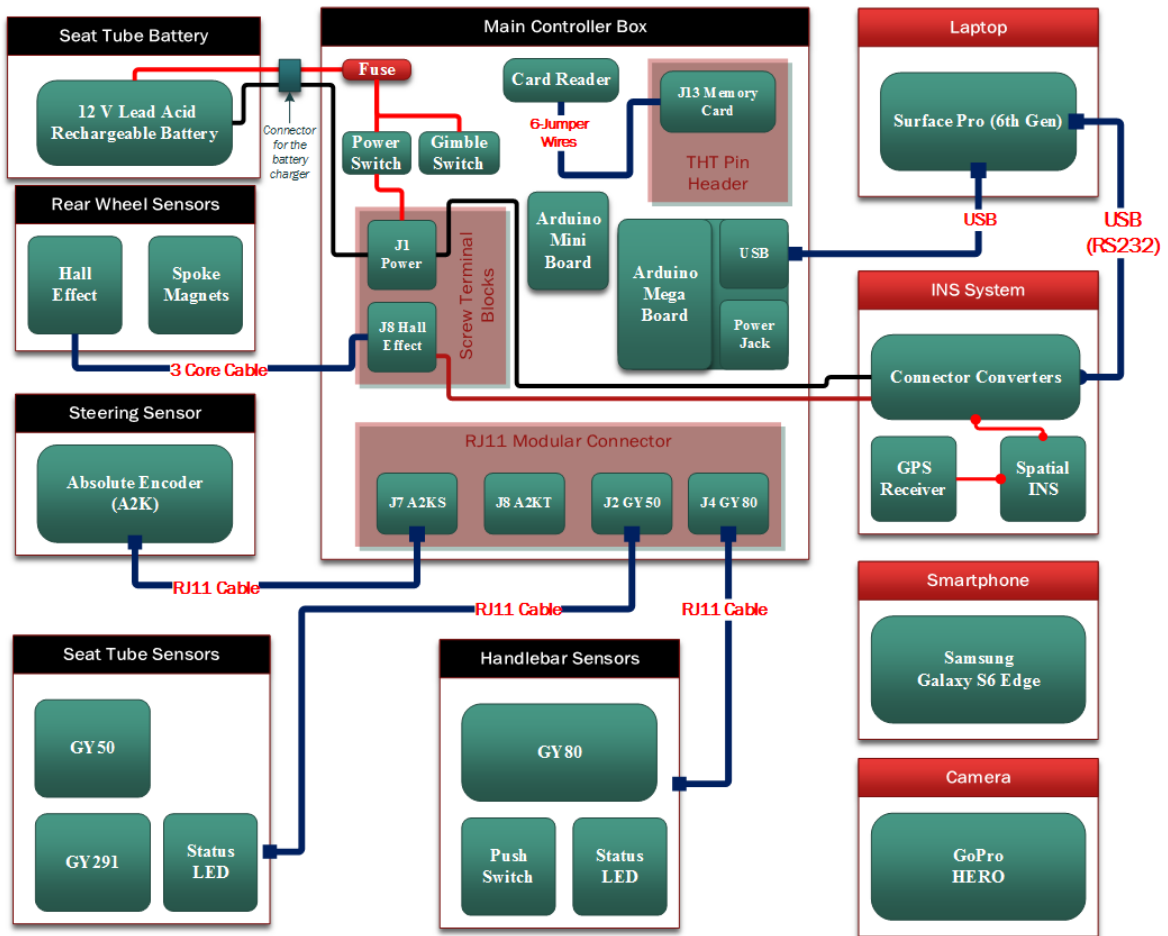


Figure A-21: Electrical connections of the iBike system

Appendix B: Development of Test Rig

B.1 Design of the Test Rig

As discussed previously, the gyroscope sensors do not output “angles” directly. Instead, they provide the instantaneous angular rates, which are caused by the change in motion. Similarly, the accelerometers only provide acceleration due to motion or shock and due to gravity in tilt-sensing applications. Therefore, both sensors’ data need to be transformed for the application of measurements of angles. Moreover, the gyroscopes often provide very accurate angular rates momentarily in dynamic situations, whereas the accelerometers provide accurate acceleration data in static situations. As a result, often these two sensors’ data are combined to obtain more accurate information.

Consequently, to obtain the initial data from the gyroscope and the accelerometer sensors, and to test the measurement accuracy of angles in static and dynamic conditions by simulating the steering behaviour of a bicycle, a two-axis motorised rotational platform was developed using a closed loop motor control system as shown in the block diagram below:

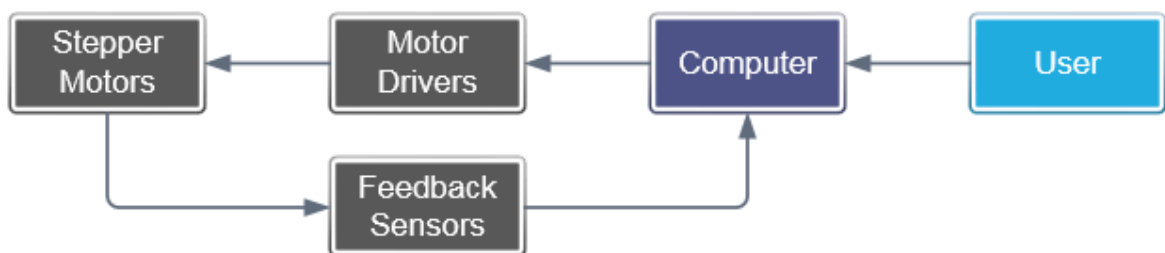


Figure B-1: Closed-loop motor control system

The platform consists of two stepper motors, one for simulating the steering and the other for controlling the tilting motion, and it is also equipped with two absolute encoders. As a result, the platform or the test rig allows data to be fetched from the gyroscope and accelerometer sensors and the absolute encoders, which act as the reference signals, concurrently. The test rig is controlled from a laptop via a USB cable and the angle of rotation and speed is controlled in this way. A block diagram of the complete data acquisition system is shown below:

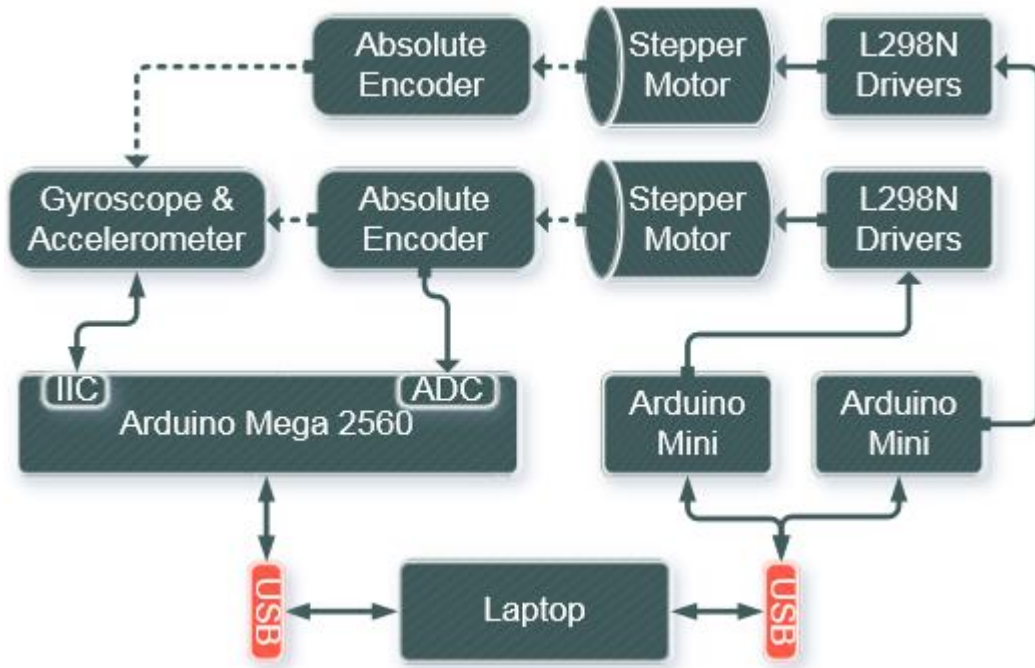


Figure B-2: Block diagram of the control and data acquisition system

The figure below represents the CAD design of the platform assembly with the stepper motors and absolute encoders. Hence, the design was utilised to manufacture the necessary parts of the test rig.

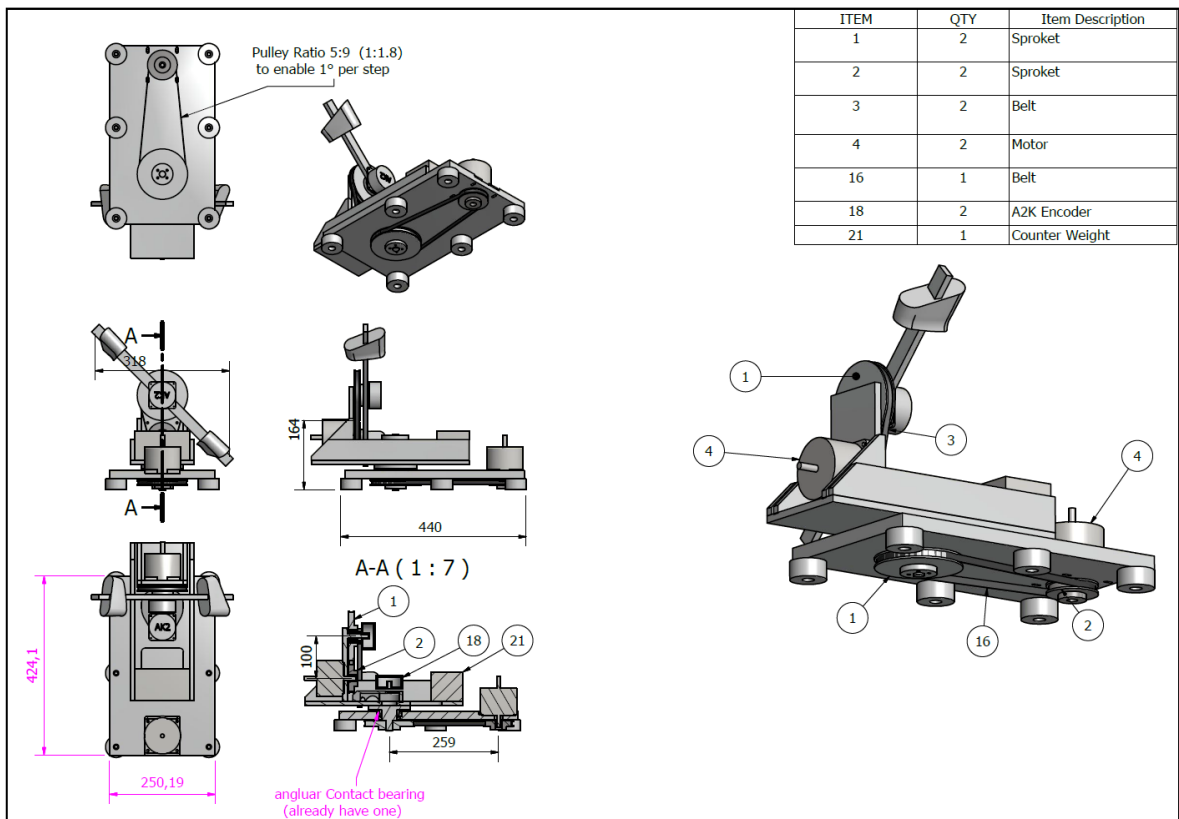


Figure B-3: Mechanical drawings of the test rig

B.2 Implementation of Hardware and Software

Following the design, Figure B-4 below illustrates the developed test rig with the motor control circuits and the power supply mounted on it. The implementation of the hardware system from Figure B-2 was employed to extract the data from the gyroscope and the accelerometer sensors. For this reason, the GY80 breakout board was attached directly onto the bar of the test rig and this made it possible to measure and compare the information about the angles from the encoders and the MEMS sensors.

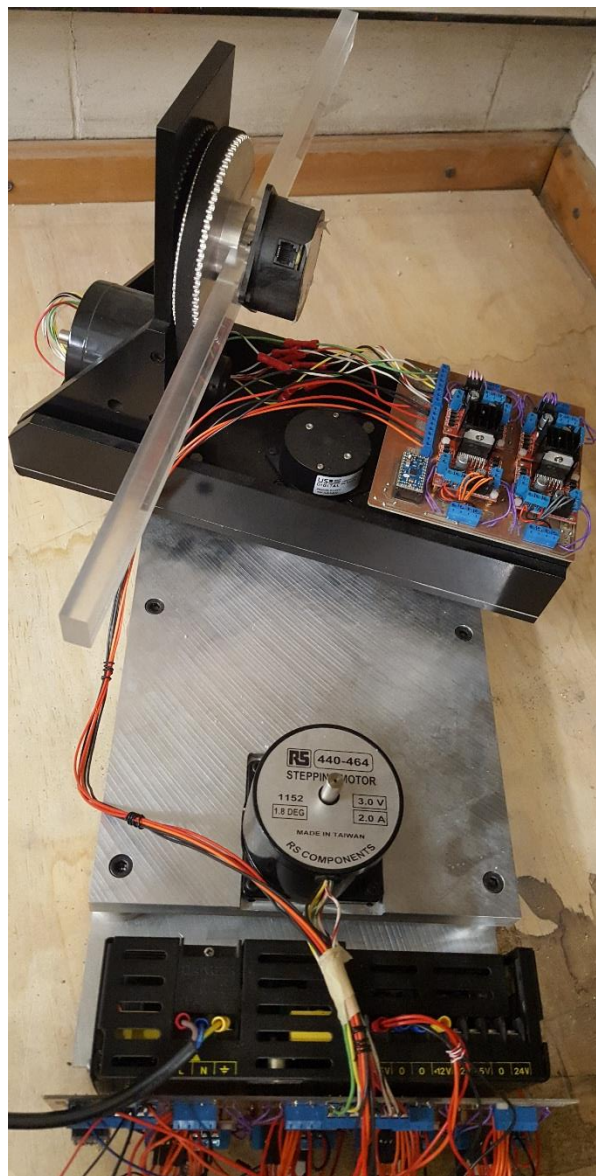


Figure B-4: The developed test rig

Following the implementation of the hardware, two pieces of bespoke software were also developed using the Processing IDE [A9] to control the test rig and to display

the data from the sensors in real-time. Figure B-5 illustrates the interface which was developed to send control commands to the platform and to vary the parameters such as steering angle, transition delays and transition speeds as well as to transmit and receive messages from the Arduino boards.

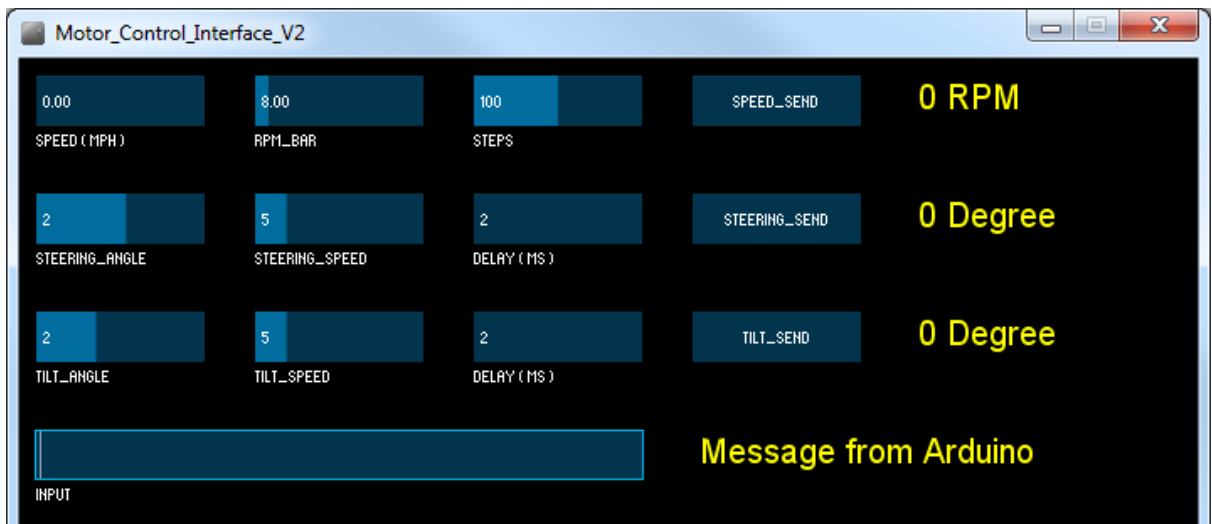


Figure B-5: Motor control interface

Figure B-6 illustrates the interface developed for the data visualisation. Each rectangle cube on the interface represents the sensor modules found within the GY80 breakout board and the interface enabled the behaviour of the sensors to be observed as well as the data to be recorded in a file for further analysis.

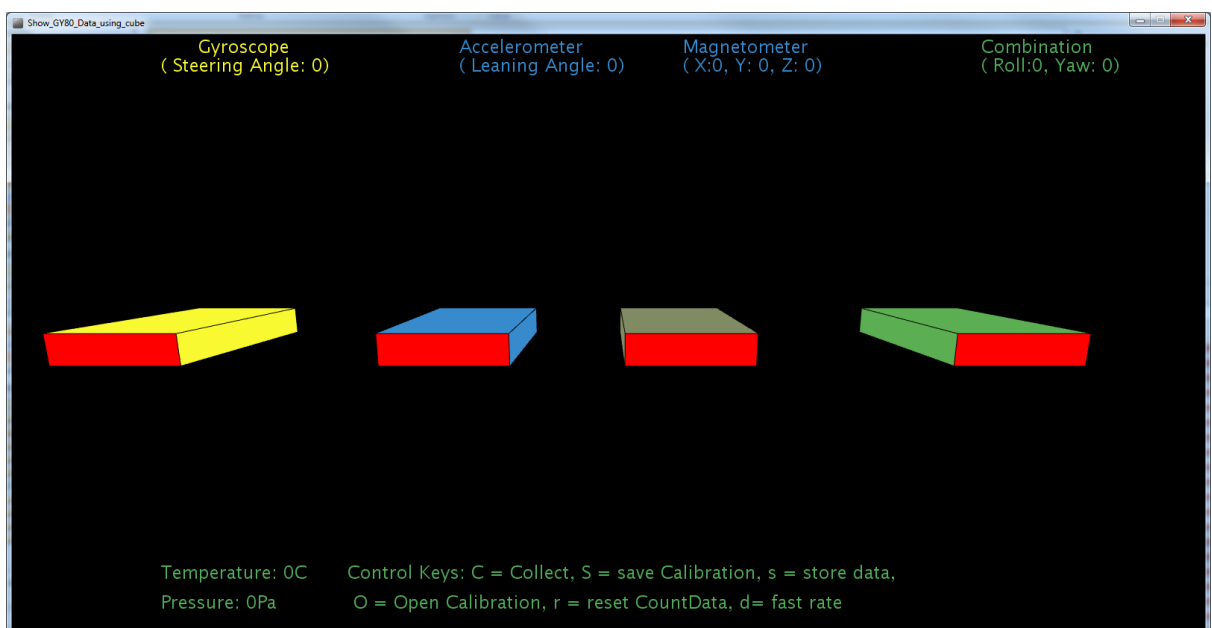
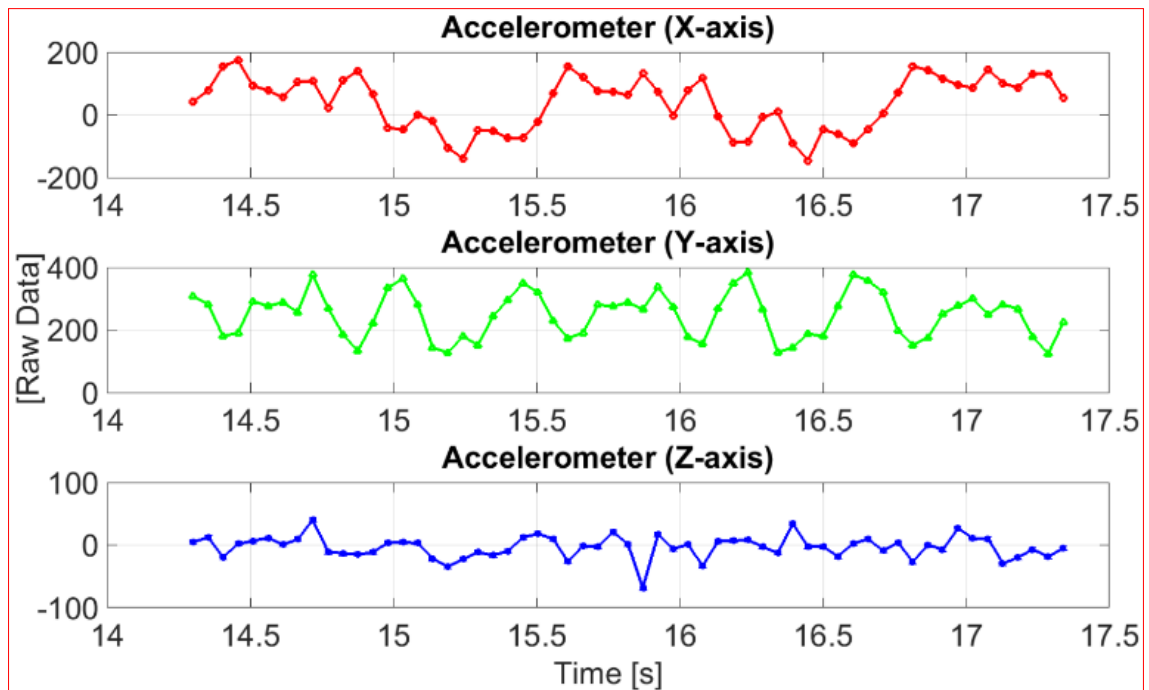


Figure B-6: Data visualisation interface

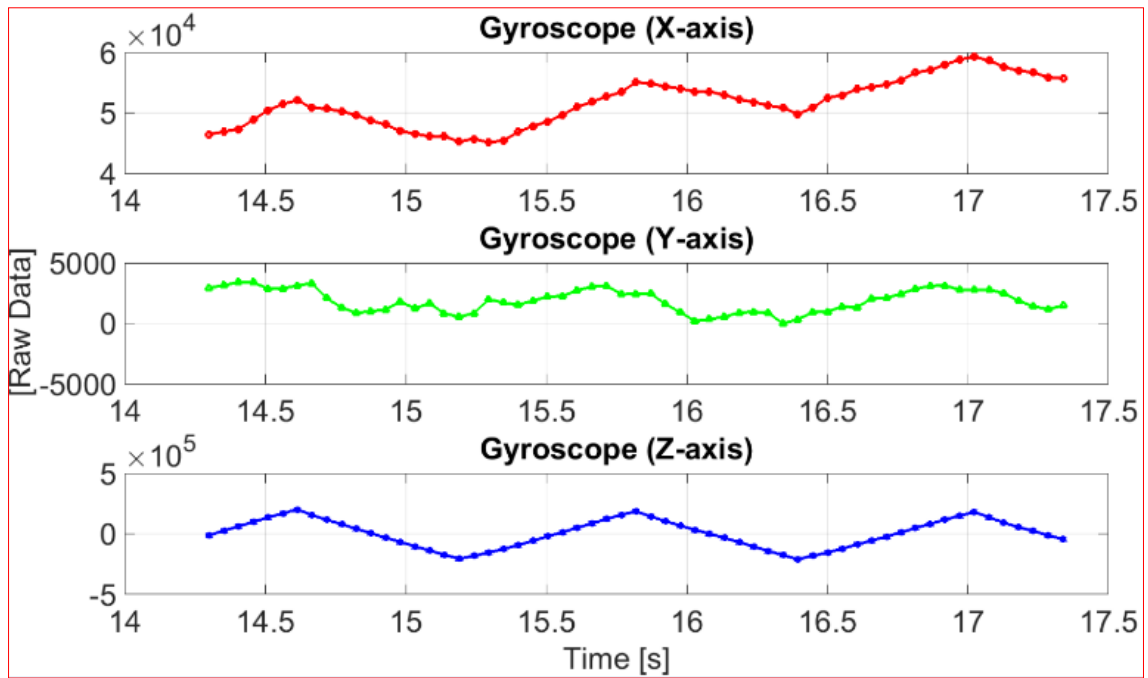
Appendix C: Additional Experimental Results and Field Trial Data

C.1 Experimental Data from the Test Rig

A three-second window was selected to illustrate the result, as visualisation of the entire data set would be difficult. Figure C-1 shows the extracted raw signals from the accelerometer and the gyroscope sensors respectively. In the experiment, the platform was rotated between $\pm 30^\circ$ with angular speed set to 30 revolutions per minute and the sampling rate set to 19Hz. Moreover, the gyroscope measurement range was set to $\pm 250^\circ$ per second and the accelerometer range was set to $\pm 2g$.



(a)



(b)

Figure C-1: (a) Accelerometer raw data; (b) Gyroscope raw data from the test rig

C.2 Sample Data from GPS (GPSLogger app) and Spatial INS

The following screenshot illustrates a sample data set collected via the GPSLogger app during the field trial. The data was pre-processed using Excel in order to filter out the unnecessary data recorded by the app such as the rows where satellites value are zero.

	A	B	C	D	E	F	G	H	I	J	K
1	time	lat	lon	elevation	accuracy	bearing	speed	satellites	provider	hdop	vdop
2	2017-03-2	51.52782	-0.10505		19.814			0	network		
3	2017-03-2	51.52782	-0.10505		19.814			0	network		
4	2017-03-2	51.52783	-0.10467	128.1698	4	216.6183	1.170467	0	gps	99	
5	2017-03-2	51.52783	-0.10467	128.1698	4	216.6183	1.170467	0	gps		
6	2017-03-2	51.52783	-0.1047	123.1059	32			14	gps	3.2	
7	2017-03-2	51.52783	-0.1047	123.1059	32			0	gps		
8	2017-03-2	51.52783	-0.10473	120.9588	24			14	gps	1	
9	2017-03-2	51.52783	-0.10473	120.9588	24			0	gps		
10	2017-03-2	51.52783	-0.10473	118.3006	12			14	gps	0.9	
11	2017-03-2	51.52783	-0.10473	118.3006	12			0	gps		
12	2017-03-2	51.52783	-0.10473	114.6796	12			14	gps	0.8	
13	2017-03-2	51.52783	-0.10473	114.6796	12			0	gps		
14	2017-03-2	51.52783	-0.10473	111.1109	12			15	gps	0.8	
15	2017-03-2	51.52783	-0.10473	111.1109	12			0	gps		
16	2017-03-2	51.52783	-0.10473	106.8852	12			15	gps	0.8	
17	2017-03-2	51.52783	-0.10473	106.8852	12			0	gps		

Figure C-2: A sample GPS data collected via the smartphone app.

The following screenshot shows the filtered data after the pre-processing stage.

Time	GPS_Latitu	GPS_Long	GPS_Eleva	GPS_Accu	GPS_Bear	GPS_Spee	GPS_Satel	GPS_Provi
2017-03-21 13:04:25.265552	51.52783	-0.1047	123.1059	32		0	14	gps
2017-03-21 13:04:25.296800	51.52783	-0.10473	120.9588	24		0	14	gps
2017-03-21 13:04:25.312456	51.52783	-0.10473	118.3006	12		0	14	gps
2017-03-21 13:04:25.344049	51.52783	-0.10473	114.6796	12		0	14	gps
2017-03-21 13:04:25.359307	51.52783	-0.10473	111.1109	12		0	15	gps
2017-03-21 13:04:25.359307	51.52783	-0.10473	106.8852	12		0	15	gps
2017-03-21 13:04:25.375126	51.52783	-0.10473	103.5523	12		0	15	gps
2017-03-21 13:04:25.421848	51.52783	-0.10473	97.08376	12		0	15	gps
2017-03-21 13:04:25.437622	51.52769	-0.10475	93.0596	8		0	16	gps

Figure C-3: Filtered GPS data

The Grid InQuestII software was utilised to transform the coordinates of the GPS and INS data from latitude and longitude to Easting and Northing. Hence, Figure C-4 illustrates the screenshot of a sample data collected from the Spatial INS and loaded onto the software for the transformation.

Sample_ID	Journey_ID	Timestamp	INS_Latitude	INS_Longitude	INS_Elevation	INS_Roll	INS_Pitch	INS_Yaw	INS_PulseCo
93032	10020	13:04:25.265552	51.5277472435057	-0.104872984259569	67.1010131835938	5.63650945216818	-2.70757663322591	256.047426850527	14111
93033	10020	13:04:25.296800	51.5277472435057	-0.104872984259569	67.1010131835938	5.63650945216818	-2.70757663322591	256.047426850527	14111
93034	10020	13:04:25.312456	51.5277472435057	-0.104872984259569	67.1010131835938	5.63650945216818	-2.70757663322591	256.047426850527	14111
93035	10020	13:04:25.344049	51.5277472697211	-0.104873011496852	67.1034851074219	5.62426847251505	-2.71422774337362	256.036088736504	14111
93036	10020	13:04:25.359307	51.5277472697211	-0.104873011496852	67.1034851074219	5.62426847251505	-2.71422774337362	256.036088736504	14111
93037	10020	13:04:25.359307	51.5277472554266	-0.104872976846143	67.1056823730469	5.62859582424107	-2.71489027172311	256.038028510229	14111
93038	10020	13:04:25.375126	51.5277472554266	-0.104872976846143	67.1056823730469	5.62859582424107	-2.71489027172311	256.038028510229	14111
93039	10020	13:04:25.421848	51.5277472647582	-0.104872978194483	67.1064605712891	5.64009743591655	-2.71654552537978	256.025870773506	14111
93040	10020	13:04:25.437622	51.5277472647582	-0.104872978194483	67.1064605712891	5.64009743591655	-2.71654552537978	256.025870773506	14111
93041	10020	13:04:25.453275	51.527747276025	-0.104872981353275	67.1063919067383	5.66232756723083	-2.71880802554235	256.021253565627	14111
93042	10020	13:04:25.500262	51.5277472509015	-0.104872965582017	67.1081924438477	5.68301706400044	-2.71740484855474	256.017838471042	14111
93043	10020	13:04:25.515577	51.5277472509015	-0.104872965582017	67.1081924438477	5.68301706400044	-2.71740484855474	256.017838471042	14111
93044	10020	13:04:25.547046	51.5277472509015	-0.104872965582017	67.1081924438477	5.68301706400044	-2.71740484855474	256.017838471042	14111
93045	10020	13:04:25.547046	51.5277472588811	-0.104872969046078	67.109001159668	5.69674745177946	-2.71745842285104	256.021991226058	14111

Figure C-4: A sample Spatial INS data loaded on the Grid InQuestII software

The following screenshot shows the data settings used for the transformation of the GPS and INS data from ETRS89 Geodetic coordinates system to OSGB36 coordinate system.

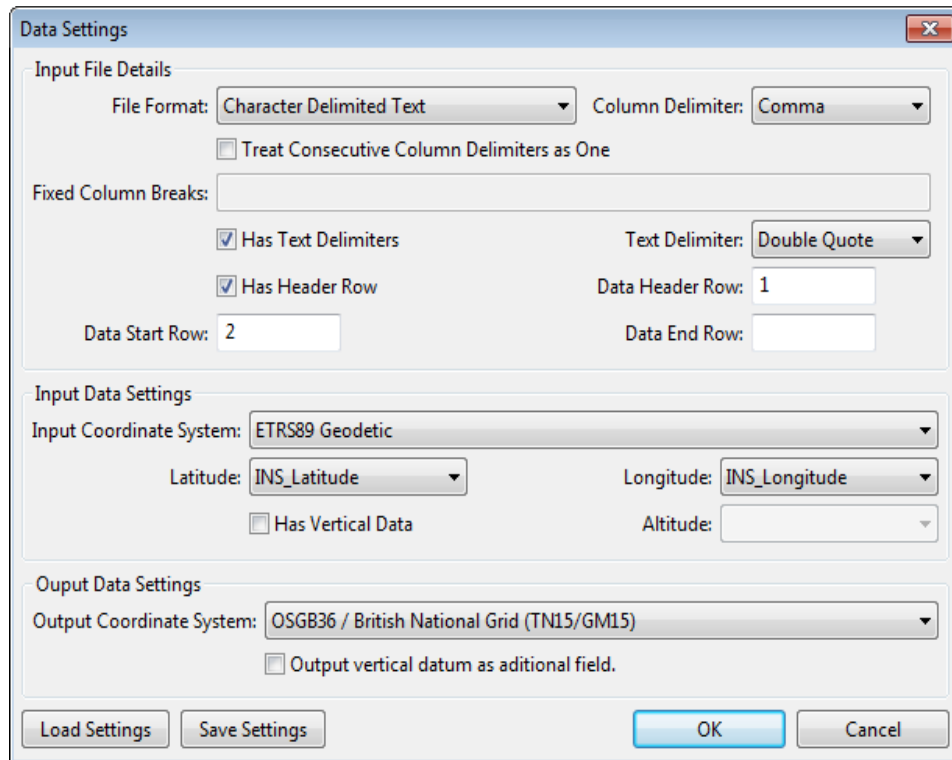


Figure C-5: Data settings used to transform the coordinates

C.3 Sample Data from the Field Trials

The screenshot below represents the sample raw data recorded from the iBike measurement sensors during a field trial. These data were then transformed into the five identified kinematic parameters.

Sample_ID	Journey	Timestamp	iBike_S_A	iBike_S_G	iBike_Acc	iBike_Gyr	iBike_Mag									
93608	10020	04:25.3	255	19	69	-4	-39	52	4	54	227	-232	-140	-49	-78	766
93609	10020	04:25.3	256	20	70	-34	-18	45	0	61	230	-26	-11	-57	-78	766
93610	10020	04:25.3	255	19	69	-68	-56	46	0	60	230	-8	33	-29	-78	766
93611	10020	04:25.3	255	19	67	-15	-126	23	0	64	231	31	42	30	-78	766
93612	10020	04:25.4	255	20	67	-16	-65	31	0	61	228	29	60	57	-78	766
93613	10020	04:25.4	256	20	66	35	-40	0	1	63	227	49	95	72	-78	766
93614	10020	04:25.4	256	18	66	74	-17	-43	0	64	229	63	133	81	-78	766
93615	10020	04:25.4	254	19	65	37	-27	-40	-2	64	228	49	130	58	-78	766
93616	10020	04:25.4	256	23	66	67	-25	-21	-3	64	229	71	132	49	-78	766

Figure C-6: Sample raw data from the iBike measurement sensors

Table C.1 represents the 39 coordinates, which associated with the 39 surveyed points, of trial 1 for each of the respective system, and Table C.2 represents the computed errors at each of the surveyed points for trials 1 to 3 of the systems.

Table C.1: Extracted coordinates of Trial 1

Surveyed points		Trial 1					
		INS		GPS		Fused	
East (x)	North (y)	East (x)	North (y)	East (x)	North (y)	East (x)	North (y)
531558.7	182683	531559.1	182684.3	531552	182680.6	531558.7	182683
531543.2	182681.6	531547	182683.1	531537	182671.4	531543.3	182681.9
531526.5	182675.2	531531.2	182677.9	531520.8	182665.7	531526.2	182676
531513.8	182666.3	531518.9	182669	531506	182658.2	531513.5	182666.8
531504.9	182659.2	531510.5	182661.8	531494.3	182649.4	531504.7	182659.8
531486	182645	531492.2	182647.5	531477.9	182636	531485.7	182645.5
531476.9	182637.3	531483.3	182639.6	531475	182627.7	531476.7	182637.7
531470	182631.6	531476.7	182634.1	531477.1	182621.7	531469.8	182631.9
531469.7	182626.2	531475.9	182628.8	531478.1	182615.9	531469.8	182626.4
531473.7	182619.8	531479.6	182622.7	531482.9	182610.7	531474	182620.2
531479.5	182612.6	531484.5	182615.7	531490.6	182602.8	531479.9	182613.2
531492.5	182599.2	531494.6	182601.2	531503.3	182605.1	531492.8	182599.9
531502.8	182597.1	531503.8	182597.1	531511.5	182611.8	531502.8	182597
531510.2	182603.1	531510.6	182602.2	531517.8	182617.2	531510.1	182602.9
531514.7	182606.9	531514.5	182605.4	531525.1	182623.1	531514.8	182606.8
531519.8	182610.9	531518.4	182608.9	531532.5	182626.8	531519.6	182611
531533.2	182621.8	531528	182617.1	531545	182632.3	531532.9	182622.1
531546.5	182631.9	531538.7	182625.4	531547.4	182634.1	531546.2	182632.5
531555.3	182617.6	531546.8	182611.8	531543.5	182615.3	531554.7	182617.9
531552.9	182610.9	531544.5	182606.6	531542.7	182610.8	531552.3	182611.2
531545.5	182588	531539.2	182590.3	531539.1	182567.1	531545.6	182588.1
531539.5	182563.3	531537.4	182571.8	531533	182554.3	531538.2	182563.8
531536.9	182559.1	531535.5	182570.3	531533	182554.3	531536.1	182560.3
531522.9	182557	531525	182570.1	531521.2	182563.9	531523.7	182558.1
531518.7	182561.9	531522.5	182572.2	531515.6	182569.2	531519.6	182562.5
531504.3	182579.5	531507.1	182584.3	531505.7	182586.5	531504.5	182579.8
531499.8	182583.9	531502.8	182588	531501.9	182590.4	531500.3	182584.3
531494.8	182589.9	531497.8	182593	531495.8	182595.4	531495	182590.3
531473.1	182617.3	531477.1	182618.9	531477.5	182624.5	531472.7	182617.1
531472.4	182640.1	531474.9	182640.3	531487	182638.6	531472	182640.6
531483.9	182647.9	531485.5	182647	531495.9	182649	531483.7	182648.1
531491.6	182653.8	531492.8	182652.7	531502.7	182655	531491.3	182654.2
531509	182666.7	531509	182665.5	531522.3	182672.8	531508.3	182667.5
531515.6	182672.1	531515.2	182670.6	531529.7	182678.7	531515.1	182672.7
531525.5	182679.1	531524.6	182677.5	531541.3	182685.8	531525	182679.8
531533.5	182684.6	531532.4	182682.9	531548.6	182686.7	531533	182685.1
531538.4	182688.3	531536.9	182686.4	531548.6	182686.7	531538.3	182688.9
531541.6	182689	531540.1	182687.2	531548.6	182686.7	531541.5	182689.5
531550.7	182690.7	531549.5	182689.5	531548.6	182686.7	531550.6	182691

Table C.2: Computed errors of the coordinates for Trials 1-3.

Trial 1			Trial 2			Trial 3		
Fused	INS	GPS	Fused	INS	GPS	Fused	INS	GPS
0.00	1.35	7.09	0.00	2.05	17.39	0.00	1.68	11.02
0.31	4.03	11.96	0.16	2.24	18.69	0.41	3.27	10.06
0.88	5.43	11.09	0.33	4.66	12.09	0.72	4.18	6.81
0.62	5.72	11.24	0.09	5.34	9.47	0.54	4.57	8.46
0.58	6.18	14.50	0.44	5.98	8.69	0.21	4.96	10.06
0.63	6.68	12.07	0.21	6.30	9.15	0.20	5.27	5.06
0.47	6.83	9.72	0.33	6.32	7.35	0.13	5.37	3.12
0.32	7.11	12.28	0.19	6.50	6.82	0.36	5.80	4.59
0.30	6.81	13.25	0.14	5.99	8.11	0.53	5.04	5.85
0.51	6.61	12.98	0.14	5.81	6.69	0.59	4.30	5.80
0.67	5.87	14.87	0.38	5.62	5.21	0.62	4.01	4.48
0.77	2.93	12.29	0.21	3.03	4.52	0.55	2.16	4.14
0.14	0.95	17.06	0.11	1.72	4.24	0.09	0.63	3.92
0.20	0.98	15.96	0.21	1.09	4.04	0.35	1.11	6.00
0.18	1.50	19.25	0.32	2.84	4.30	0.36	2.13	5.75
0.18	2.46	20.29	0.47	5.16	3.72	0.37	4.09	4.37
0.40	7.08	15.82	0.27	7.55	2.81	0.36	6.71	1.70
0.75	10.16	2.36	0.13	10.01	4.89	0.48	8.97	5.19
0.71	10.28	12.10	0.27	10.76	20.72	0.15	9.28	14.24
0.61	9.42	10.22	0.06	10.00	24.98	0.33	8.71	31.05
0.12	6.68	21.91	0.55	5.51	33.79	0.93	7.73	23.78
1.38	8.78	11.09	0.70	1.80	11.85	0.60	7.49	19.99
1.46	11.36	6.12	0.37	1.58	12.72	0.59	6.34	21.59
1.41	13.27	7.17	1.53	3.39	7.34	2.25	7.51	13.19
1.08	11.00	8.04	1.27	3.79	12.79	2.16	10.25	8.58
0.36	5.51	7.09	0.62	4.18	15.38	1.07	21.40	9.18
0.61	5.10	6.80	1.26	4.84	16.86	1.54	22.77	11.10
0.48	4.29	5.60	1.12	6.53	18.37	1.38	23.95	12.38
0.43	4.32	8.39	0.35	8.86	18.70	0.10	30.35	11.13
0.61	2.44	14.63	0.38	8.89	12.06	0.36	32.26	8.34
0.25	1.86	12.12	0.47	10.42	12.51	0.38	32.43	8.50
0.52	1.56	11.19	0.54	12.14	10.24	0.68	31.98	5.99
0.97	1.24	14.68	0.32	13.30	7.36	0.25	29.90	7.08
0.85	1.55	15.53	0.42	14.19	5.69	0.23	29.43	9.08
0.94	1.77	17.15	0.34	14.83	6.18	0.05	28.05	12.66
0.74	2.04	15.25	0.39	14.95	6.82	0.45	26.95	10.34
0.60	2.47	10.30	0.50	15.32	6.34	0.15	25.87	8.43
0.47	2.35	7.39	0.23	15.46	4.87	0.24	25.04	9.05
0.41	1.60	4.45	0.44	15.03	7.43	0.12	23.65	12.90

C.4 Approximation of Yaw Rate and Angle for the Kalman Filter

The estimation of yaw rate noise was found through an experiment and in it, the bicycle was kept stationary and held perpendicular to the ground (an inclinometer was used to ensure the frame is orthogonal to the ground contact points). Figure C-7 illustrates the results of this experiment with the mean value.

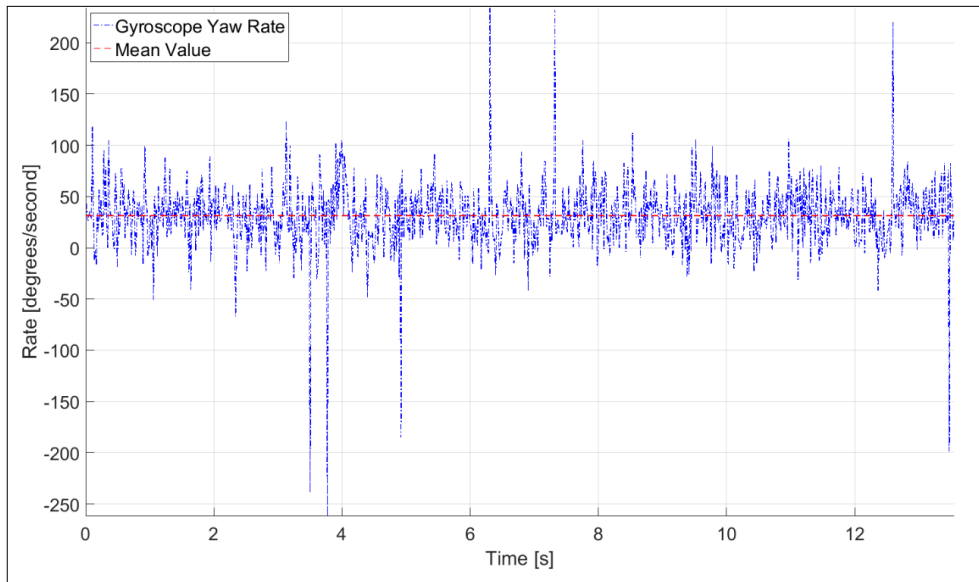


Figure C-7: Gyroscope yaw rate while bicycle is orthogonal to the ground

The estimation of yaw angle noise was found through another experiment, and in this, the bicycle was slowly pushed in a straight path and results of the yaw angle from this experiment is illustrated in Figure C-8 below.

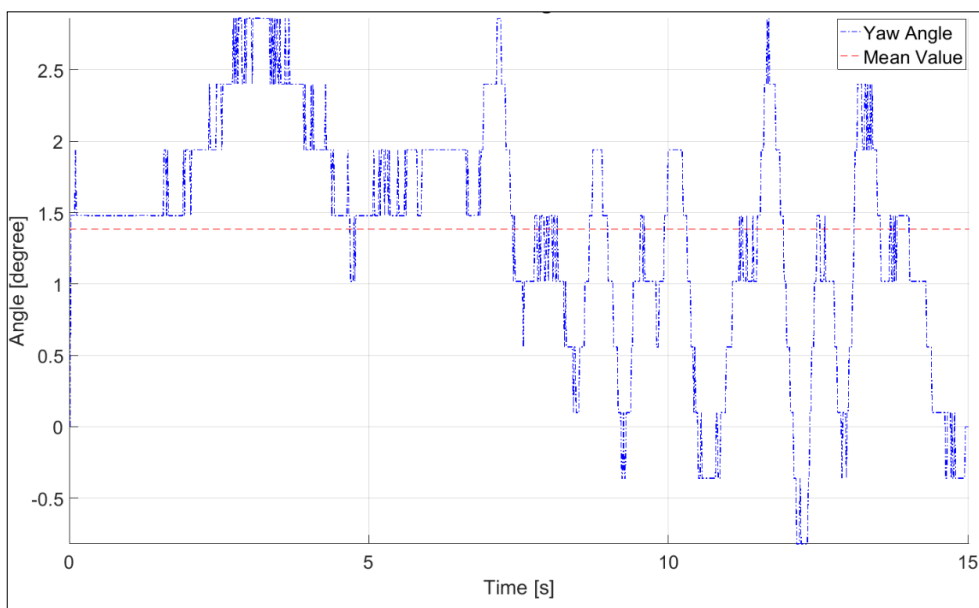


Figure C-8: Yaw Angle while pushing the bicycle in a straight path

C.5 Comparison of Yaw Angles

Figure C-9 shows a comparison between the DR and fused yaw angles with the duration of the experiment, while Figure C-10 illustrates the DR and fused yaw angles of the window between 7 and 8 seconds of the experiment. It was clear from this experiment that the fused angles were more accurate.

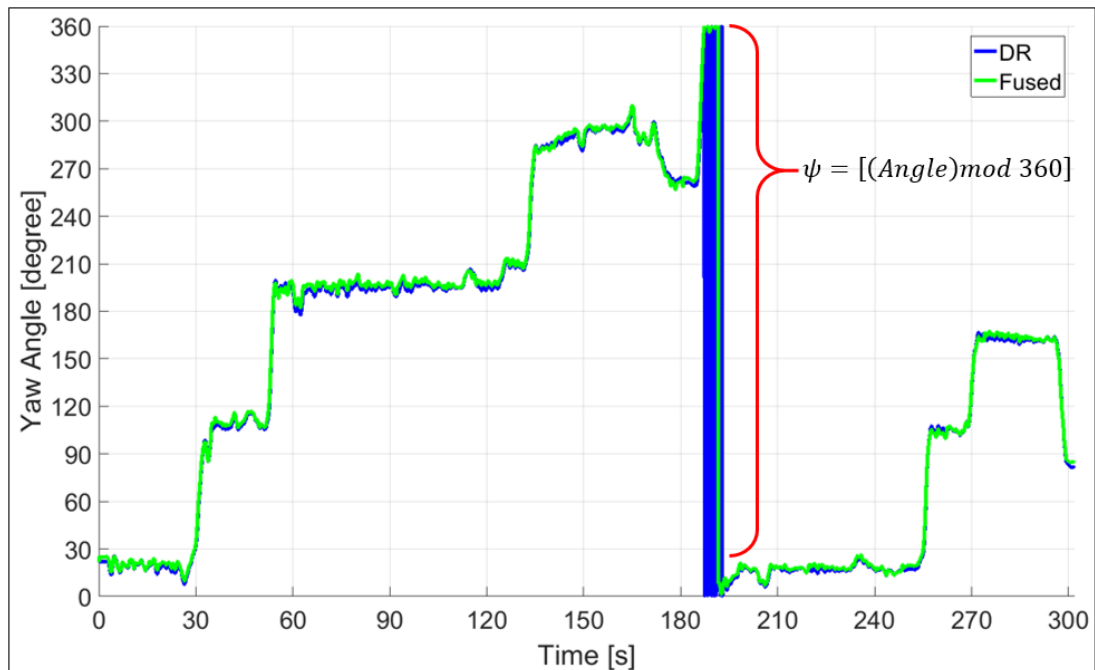


Figure C-9: DR versus Fused yaw angle

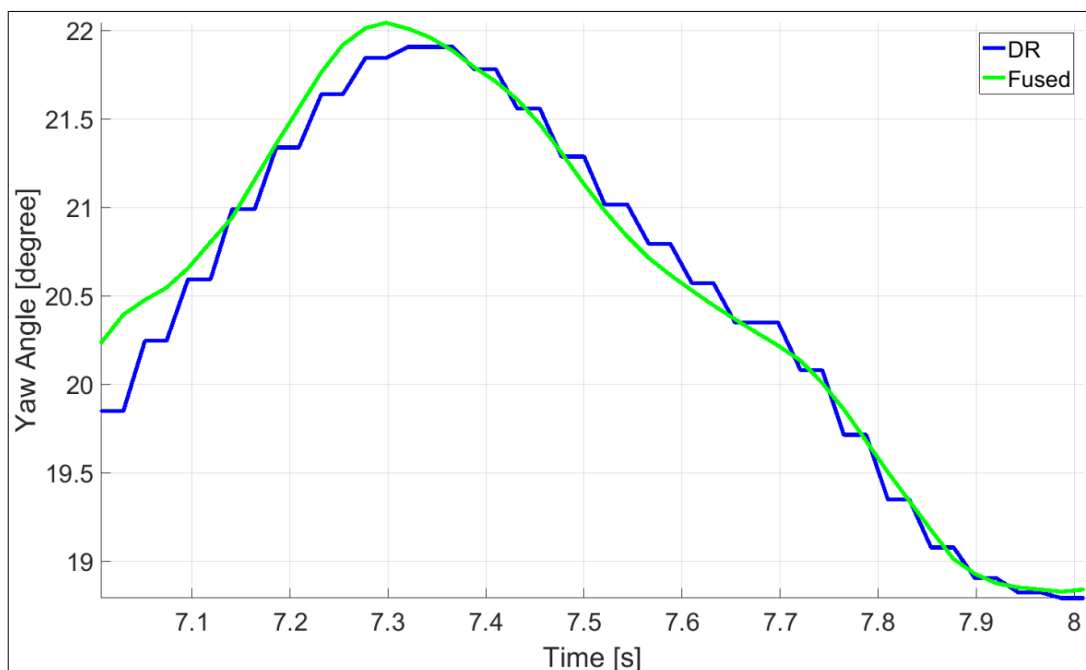


Figure C-10: DR versus Fused yaw angle between 7 and 8 seconds

C.6 Computation of GPS Mean Error

To compute the mean error of the GPS, several points were collected at a known location which was established from the survey using the TS. Figure C-11 illustrates an example of the experimental result for a single location, where the black dot represents the known control point and the pink stars represent the GPS positions over a period at the known location.

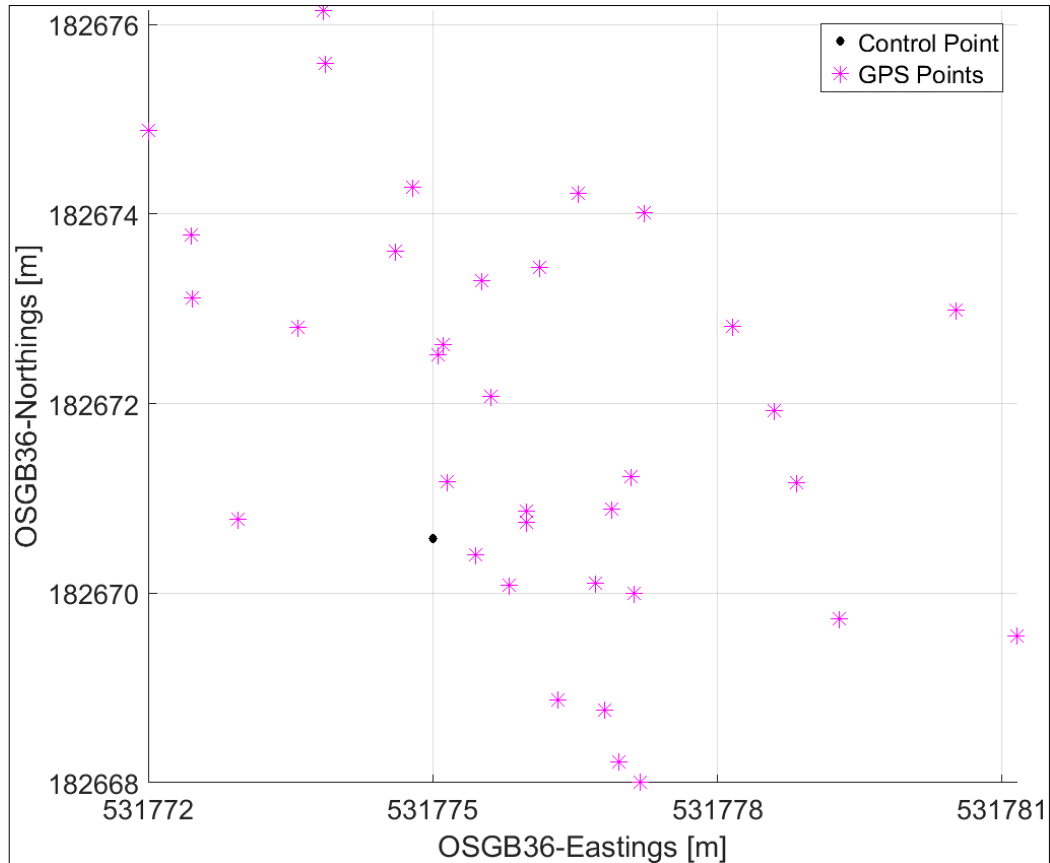


Figure C-11: GPS positions with respect to a known location

Thus, using the dataset and the known position, the displacement or the positional error from the known location can be easily obtained through the Pythagoras theorem as illustrated in the figure below.

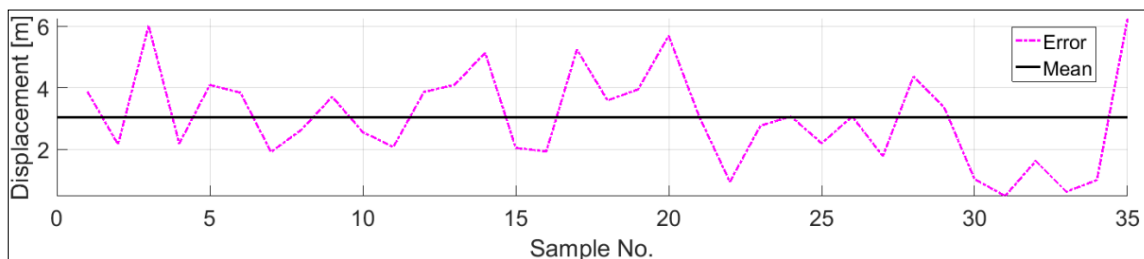


Figure C-12: Displacement from the known location

C.7 Cumulative Distribution of the Localisation Error

The following three graphs represent the unfiltered cumulative distribution of the positional error between the survey points and each of the respective systems. The distribution was computed by ranking the error and dividing by the total number of survey points (observations). It can be seen from the graphs that using the Spatial INS a position can be estimated with an accuracy of 10m or less with 40-90 % probability, whereas, using the GPS alone the same position accuracy can be achieved with 30-90 % probability. On the other hand, illustrated in Figure C-15, the iBike system with the proposed fusion algorithms performed better than the existing enhanced positioning system used for the validation; In fact, with 70-90 % probability a position can be estimated with an accuracy of 1m or less.

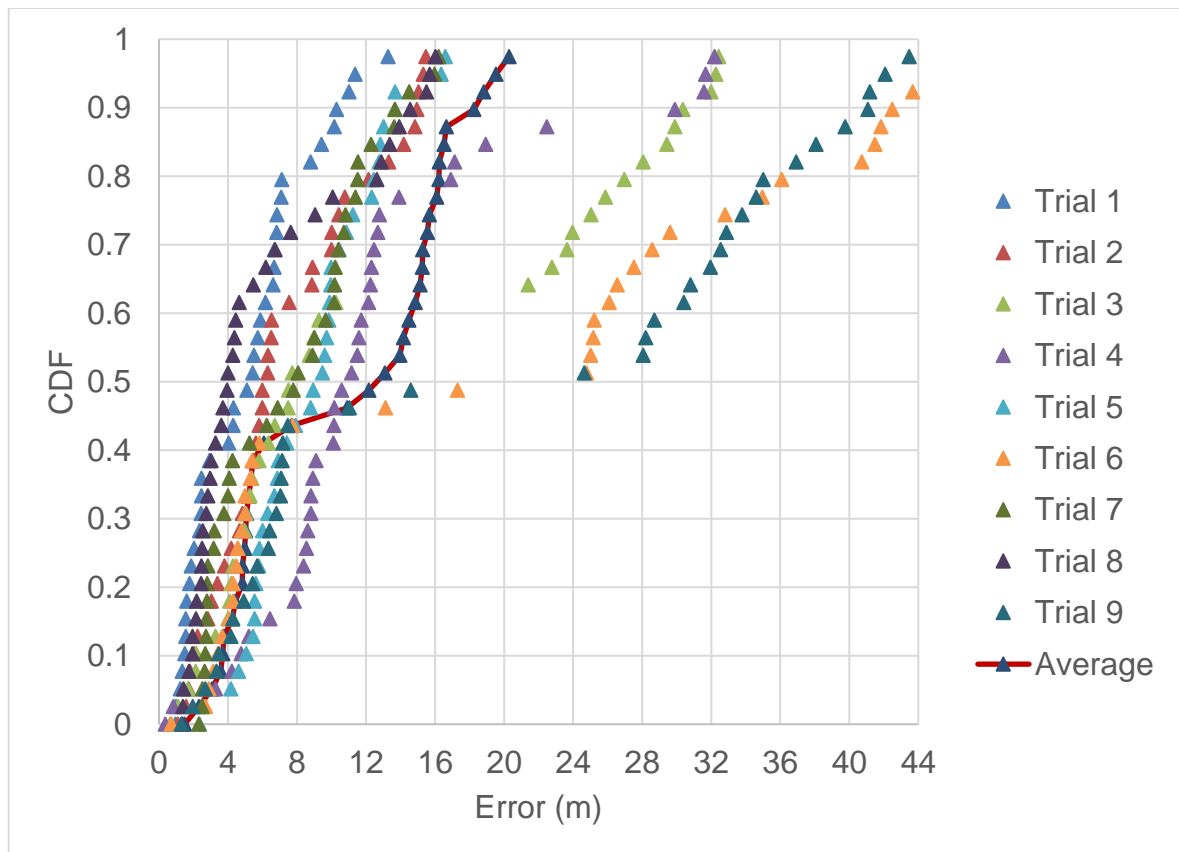


Figure C-13: Comparison of Spatial INS positional error

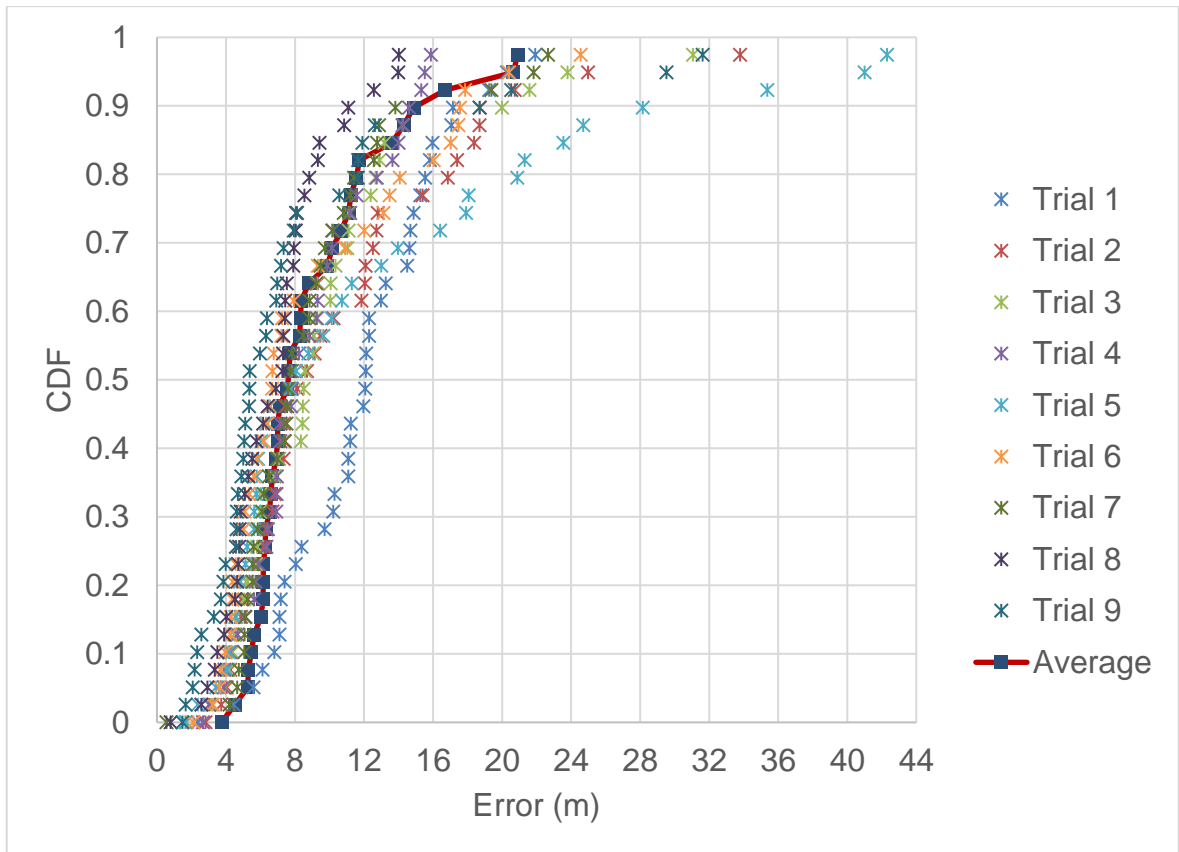


Figure C-14: Comparison of smartphone GPS positional error

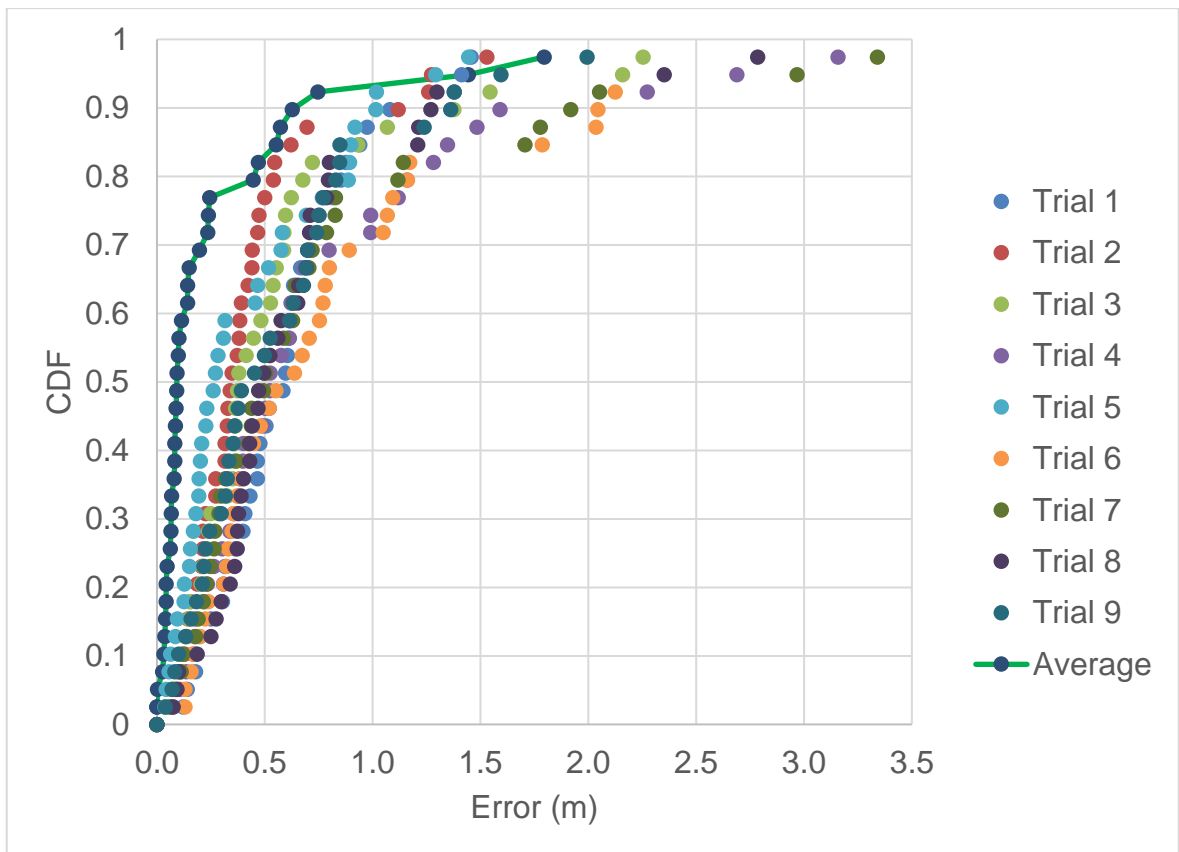


Figure C-15: Comparison of fused positional error

C.8 Cricket System Experimental Setup

The Cricket Indoor Location System [A10] was tried for the ground truth data. In this indoor experiment, one listener connected to the laptop via the USB cable, where MATLAB scripts were running, and six beacons with the arrangement shown in Figure C-16 below were used. The laptop and the listener were attached on the bicycle while the beacons were placed on the ceiling using strings so that the location of the beacons can be adjusted to measured positions prior to the setup.



(a)



(b)

Figure C-16: (a) Listener and laptop; (b) beacons used in the experiment

The following figure illustrates the actual placements of the beacons on the ceiling.



Figure C-17: DR versus Fused yaw angle between 7 and 8 seconds

References

- [A1] Allegro MicroSystems, "Allegro Hall-Effect Sensor ICs," [Online]. Available: <http://www.allegromicro.com/en/Design-Center/Technical-Documents/Hall-Effect-Sensor-IC-Publications/Allegro-Hall-Effect-Sensor-ICs.aspx>. [Accessed 18 June 2017].
- [A2] Electronics Tutorials, "Hall Effect Sensor," [Online]. Available: <http://www.electronics-tutorials.ws/electromagnetism/hall-effect.html>. [Accessed 18 June 2017].
- [A3] ROBOTC, "What is an Encoder?," 2012 August 2012. [Online]. Available: http://www.robotc.net/wikiarchive/Tutorials/Arduino_Projects/Mobile_Robotics/VEX/What_is_an_Encoder. [Accessed 14 July 2017].
- [A4] A. Brown, "Using Encoders," [Online]. Available: http://abrobotics.tripod.com/Ebot/using_encoder.htm. [Accessed 16 July 2017].
- [A5] Tamagawa seiki Co, "ROTARY ENCODERS FA-CODER®," [Online]. Available: <http://www.tamagawa-seiki.com/english/encoder/about-encoder.html>. [Accessed 15 July 2017].
- [A6] Wikipedia, "3D Gyroscope," [Online]. Available: http://en.wikipedia.org/wiki/Gyroscope#mediaviewer/File:3D_Gyroscope.png. [Accessed 17 June 2017].
- [A7] Compliant Mechanisms Research group, "Introduction to Microelectromechanical Systems (MEMS)," [Online]. Available: <http://compliantmechanisms.byu.edu/content/introduction-microelectromechanical-systems-mems#>. [Accessed 21 June 2017].
- [A8] Arduino, "Arduino IDE," 2017. [Online]. Available: <https://www.arduino.cc/en/main/software>. [Accessed 5 July 2017].
- [A9] B. Fry and C. Reas, "Processing," [Online]. Available: <https://processing.org/reference/environment/>. [Accessed 15 July 2017].
- [A10] MIT, "The Cricket Indoor Location System," [Online]. Available: <http://nms.csail.mit.edu/cricket/>. [Accessed 2 June 2017].